



University
of Glasgow

Bain, Hazel M. (2010) *Hard X-ray and radio studies of solar flares*. PhD thesis.

<http://theses.gla.ac.uk/1751/>

Copyright and moral rights for this thesis are retained by the author

A copy can be downloaded for personal non-commercial research or study, without prior permission or charge

This thesis cannot be reproduced or quoted extensively from without first obtaining permission in writing from the Author

The content must not be changed in any way or sold commercially in any format or medium without the formal permission of the Author

When referring to this work, full bibliographic details including the author, title, awarding institution and date of the thesis must be given

Hard X-ray and Radio Studies of Solar Flares

Hazel Miller Bain, M.Sci. Hons.

Astronomy and Astrophysics Group
Department of Physics and Astronomy
Kelvin Building
University of Glasgow
Glasgow, G12 8QQ
Scotland, U.K.



University
of Glasgow

Presented for the degree of
Doctor of Philosophy
The University of Glasgow
April 2010

This thesis is my own composition except where indicated in the text. No part of this thesis has been submitted elsewhere for any other degree or qualification.

Copyright © 2010 by Hazel M. Bain

19 April 2010

Abstract

Combined X-ray and radio observations of the Sun provide powerful diagnostics of particle acceleration and transport effects during solar flares. In this thesis we present observations of two solar flares. In the first event we report what we believe to be the first observation of hard X-ray emission formed in a coronal, flare-related jet. Occurring on the 22nd of August 2002, the event was observed by the Reuven Ramaty High Energy Solar Spectroscopic Imager (RHESSI) and the Nobeyama Radioheliograph (NoRH) and Polarimeters (NoRP). During the impulsive phase RHESSI observed significant hard X-ray emission to energies as high as 30-50 keV in the jet. RHESSI spectroscopy shows a powerlaw spectrum with a spectral index of ~ 4 and NoRH images reveal radio emission at 17 GHz and 34 GHz co-spatial with the hard X-ray emission, thus supporting the evidence for nonthermal emission in the jet.

The second event occurred on the 24th of August 2002 and was also observed by RHESSI and NoRH. The size and orientation of the flare, which occurred on the west limb of the Sun, make it particularly interesting to study. At both NoRH frequencies emission is observed at all points along a flare loop such that the looptop and footpoint emission are clearly separated. We present observations of the flare decay phase to investigate the long term evolution of the event. In particular we follow the evolution of relevant plasma parameters which are used as an input to a 3D gyrosynchrotron model in an attempt to reproduce the observed emission at radio wavelengths.

Contents

1	Introduction	22
1.1	The Sun	22
1.1.1	The Solar Structure	22
1.2	The Corona	27
1.3	Solar Flares	31
1.4	Instruments and Data Analysis	38
1.4.1	RHESSI	38
1.4.2	Nobeyama Radioheliograph and Radiopolarimeters	43
1.4.3	TRACE	44
2	X-ray and Radio Emission	45
2.1	X-ray Emission	46
2.1.1	Coulomb collisions	46
2.1.2	Thermal Bremsstrahlung	47
2.1.3	Non-Thermal Bremsstrahlung	49
2.2	Radio Emission	53
2.2.1	Radio Emission Mechanisms	54
2.2.2	Radiative Transfer	54
2.2.3	Thermal Bremsstrahlung	56
2.2.4	Gyroresonance Emission	58
2.2.5	Synchrotron Emission	60
2.2.6	Gyrosynchrotron Emission	60
2.3	Petrosian-Klein Approximation	63
2.3.1	Solar Plasma Emission	69
3	Hard X-ray Emission From a Flare-Related Jet	72
3.1	Introduction to solar jets	72
3.2	Event overview	75

3.3	Hard X-ray Observations	79
3.3.1	RHESSI Imaging	79
3.3.2	RHESSI Spectroscopy	81
3.4	Radio Observations	84
3.4.1	Nobeyama Radioheliograph	84
3.4.2	Nobeyama Polarimeters	86
3.5	Discussion and Conclusion	91
4	Observations of 24th August 2002 flare	95
4.1	Introduction	95
4.2	Event Overview	97
4.3	Radio Observations	101
4.3.1	NoRH	101
4.3.2	NoRP	118
4.4	Hard X-ray Observations	121
4.4.1	Imaging	121
4.4.2	Spectroscopy	124
4.5	Discussion of plasma parameters	131
4.6	Conclusions	135
5	Modeling of 24th August 2002 flare	141
5.1	Gyrosynchrotron Code	142
5.2	Magnetic Field Model	145
5.2.1	Dipole Field Model	145
5.3	Viewing Angle	148
5.4	Input parameters	151
5.5	Radiative Transfer	152
5.6	Arcade Model	152
5.7	Modeling of 24th August 2002 Event	155
5.8	Thermal distribution	158
5.9	Nonthermal distribution (uniform N)	163
5.10	Nonthermal distribution (Gaussian N)	169
5.11	Thermal/Nonthermal	171
5.12	Effects of δ	178
5.13	Discussion and conclusions	182
6	Conclusions and Future Work	190

A	Wave mode propagation in a magnetised plasma	205
A.1	Wave mode propagation in a Magnetised plasma	205

List of Figures

1.1	Sunspot images from the Solar Optical Telescope (SOT) instrument onboard the Hinode spacecraft. NAOJ/JAXA/NASA. . . .	24
1.2	284 Å EUV images of the Sun over a solar cycle, taken by the Extreme ultraviolet Imaging Telescope (EIT) instrument onboard the Solar and Heliospheric Observatory (SOHO) spacecraft. Courtesy of SOHO/EIT consortium.	26
1.3	Electron density and temperature as a function of height above the photosphere Fontenla et al. (1990); Gabriel (1976); Aschwanden (2004).	28
1.4	Plot shows an example spectrum ranging from soft X-rays to gamma-rays. The relevant energy ranges related to specific emission mechanisms are indicated. The electron-positron annihilation line at 511 keV and the neutron capture line at 2.223 MeV are indicated (Aschwanden 2004).	32
1.5	Cartoon of the CSHKP model from Tsuneta et al. (1997) showing pinching of antiparallel loop legs as they are pinched together resulting in a cusp like structure above closed loops and a plasmoid ejection into interplanetary space, (Tsuneta et al. 1997).	34
1.6	Flare emission at different wavelengths (Benz2002)	36
1.7	Schematic showing RHESSI Rotating Modulation Collimators (Hurford et al. 2002)	39
1.8	Schematic showing arrangement of RHESSI front and rear grids situated in front the corresponding germanium detectors (Hurford et al. 2002)	41

1.9	Plots show examples of modulation profile for an off-axis source. Different panels correspond to different source parameters such as radial offset and source size. Figure taken from (Hurford et al. 2002)	41
2.1	Plots of radio brightness temperature (top) and flux density (bottom) for thermal bremsstrahlung (left), thermal gyrosynchrotron (centre) and nonthermal gyrosynchrotron emission (right) from a homogeneous plasma,(Gary & Hurford 1989)	57
2.2	Gyrosynchrotron emission from mildly relativistic electrons,(Boyd & Sanderson 1969)	60
2.3	Plots of η_ν/BN , $\kappa_\nu B/N$, T_{eff} and r_c against ν/ν_B for the x-mode. These plots are for radiation produced by powerlaw electron distributions with varying spectral indices δ (Dulk & Marsh 1982).	62
2.4	Plots show a comparison of results produced by Ramaty (solid) and Pertosian-Klein (crosses) expressions for viewing angles of (left to right) 80° , 45° and 10° for o-mode (top row) and x-mode (bottom row).(Klein 1987).	69
2.5	Classification of radio bursts (credit HIRAS Solar Observatory).	70
3.1	Cartoon showing the magnetic reconnection jet model (Shimojo & Shibata 2000) adapted from the Heyvaerts et al. (1977) cartoon.	73
3.2	From top to bottom: GOES, RHESSI, TRACE and NoRH lightcurves. Vertical dashed lines represent 32s time intervals used for RHESSI imaging (see Figure 3.6). (See electronic version for colour plots)	76
3.3	TRACE 195Å images for selected times throughout the event showing the evolution of the jet. These images have a time resolution of ~ 9 s and a spatial resolution of $1''$	77
3.4	Velocity timeslice showing jet intensity as a function of height and time. Vertical dash-dot line shows the time at which the jet emission passes out of the TRACE field of view. Dashed lines on insert image show the region used for the analysis. Asterisks and solid line shows a fit to the faint front edge of the jet at the 5% level. Diamonds and dashed line shows a fit to points determined from tracking a brightly emitting source of plasma by eye.	78

3.5	RHESSI lightcurve with logarithmic energy binning. Vertical dashed lines represent 32s time intervals used for RHESSI imaging (see Figure 3.6).	80
3.6	TRACE images with RHESSI image contours overlaid. Rows show time slices at times 01:48:58, 01:50:30, 01:51:02, 01:51:34 and 01:52:06 and columns show contours of RHESSI energy bands at 6–12 (blue), 12–20 (green), 20–30 (magenta) and 30–50 keV (red). The far right column shows all RHESSI contours overlaid. Contour levels are at 90, 75, 50 and 25%.	81
3.7	RHESSI photon spectra obtained from detector 3 for time interval 2. Black lines shows the background subtracted data and grey shows the background. The plot shows two possible fits, isothermal plus thin target (solid lines) and isothermal plus thick target (dashed lines). Green lines show isothermal fits. Blue lines show thick and thin target fits. Red shows the combined fit functions. Orange shows a Gaussian line added to fit a feature seen at 11 keV.	82
3.8	RHESSI image at 29.5–37.5 keV (top left) showing regions chosen for individual spectral analysis. Imaging spectroscopy results for the jet (top right), left footpoint (bottom left) and right footpoint (bottom right). Black lines show the observed photon spectra, green and blue show the isothermal and thick target fit functions respectively. Red shows the combination of fitted functions.	83
3.9	NoRH 17 GHz (top) and 34 GHz (bottom) images at time intervals used for RHESSI imaging. White lines show positive spectral index from 0.5 to 1.5 in steps of 0.5 corresponding to optically thick plasma. Black lines show lines of negative spectral index from –1 to –4 in steps of 1 corresponding to optically thin plasma.	85
3.10	Left : TRACE image with NoRH 17 GHz (dot-dashed black), 34 GHz (solid blue) and RHESSI 30–50 keV (dashed red) contours. Contour levels of 90, 75, 50% for all contours (plus 25% for 17 GHz and 30–50 keV). Right : Map of radio spectral index α with contours of positive α ranging from 0 to 1.5 in steps of 0.25 (solid black) and RHESSI 30–50 keV (dashed red).	86

3.11	Top : NoRP flux (R+L) at 1, 2, 3.75, 9.4, 17 and 34 GHz. Middle : NoRP flux (R-L) showing degree of circular polarisation. Bottom : Brightness temperature calculated at each frequency. The dashed vertical lines show time intervals over which RHESSI images were obtained for Fig. 3.6.	87
3.12	NoRP radio spectra at 15s time intervals. Solid line shows gyrosynchrotron function fitted to the data from 1 to 34 GHz. Dashed line shows the same function fitted to data from 2 to 34 GHz. Corresponding values of α_{tk} and α_{tn} for each fit are displayed on the plot, where 0 and 1 refer to the solid and dashed fits respectively.	88
3.13	Radio spectrogram from the Hiraiso solar observatory (25–2500 MHz) showing Type III radio bursts.	90
3.14	Spectrogram from WAVES on the WIND spacecraft (1.075–13.825 MHz) showing Type III radio bursts	90
4.1	Plot shows, from top to bottom, GOES, RHESSI, TRACE and NoRH lightcurves for the 24th August 2002 flare. Diagonal stripes on TRACE lightcurve indicate data gaps.	97
4.2	TRACE 195 Å evolution of 24th August 2002 flare.	98
4.3	Images of CME associated with flare on 24th August 2002 from the LASCO instrument on SOHO. (a) and (b) Images from C2 at 01:27 and 01:50. (c) Image from C3 at 02:18. Images from the SOHO LASCO CME Catalog.	100
4.4	TRACE 195 Å evolution of 24th August 2002 flare with corresponding NoRH 17 GHz (blue) and 34 GHz (red) image contours overlaid. Image contours are at 8, 16, 32, 64 and 96% of image maximum brightness temperature. Panel (d) has an additional 25% contour for all energy bands.	101
4.5	Plot shows time profiles of T_b for NoRH 17 GHz (blue) and 34 GHz (red) during the flare decay phase. The emission from the looptop and southern footpoint have been separated and shown in top right and bottom right respectively. Vertical lines indicate the time intervals of Stages 2, 3 and 4. Image plot to the left shows an example 17 GHz image at 01:26:41 indicating how the looptop and footpoint emission were separated.	105

4.6	NoRH 34 GHz brightness temperature images in redscale with 17 GHz image contours overlaid at 2, 4, 8, 16, 32, 64 and 96% of image maximum. Ellipses drawn on images are used to determine brightness distribution along the loop. For images at 01:32 and 01:40 the blue ellipse indicates the outer loop and green the inner loop.	106
4.7	Plots of T_b as a function of θ for 17 GHz (top) and 34 GHz (bottom) around an ellipse fitted to the loop for each time interval in Stage 2.	107
4.8	Plots of radio spectral index α as a function of θ around an ellipse fitted to the NoRH radio loop for each time interval in Stage 2.	107
4.9	Plot shows radio mean spectral index α for the southern footpoint. Vertical lines indicate the separation of Stages 2, 3 and 4.	109
4.10	Ratios of T_b peaks along loop for Stage 2 (top left), Stage 3 outer (top right) and inner loops (bottom left) and Stage 4 (bottom right). Blue lines represent ratios taken at 17 GHz and red lines the ratios taken at 34 GHz. Solid lines show the ratio SFP:LT, dotted show the ratio SFP:AS and dashed lines show the ratio AS:LT.	111
4.11	Plots of T_b as a function of θ for 17 GHz (top) and 34 GHz (bottom) around an ellipse fitted to the outer loop for each time interval in Stage 3.	112
4.12	Plots of T_b as a function of θ for 17 GHz (top) and 34 GHz (bottom) around an ellipse fitted to the inner loop for each time interval in Stage 3.	112
4.13	Plots of radio spectral index α as a function of θ around an ellipse fitted to the NoRH radio loop for each time interval in Stage 3.	113
4.14	Plot showing line profile of brightness at 17 GHz (dashed) and spectral index (solid) as a function of X through the loop apex at 01:30 taken from Karlický (2004).	114

4.15	Plots showing line profiles of brightness and spectral index as a function of X through the loop apex. Top: plot of T_b at 34 GHz (redscale) with 17 GHz contours at 2, 4, 8, 16, 32, 64, 96% of image maximum at 01:30. Horizontal lines shows line profiles through loop apex at $Y = 86''$ (solid), $92''$ (dotted) and $100''$ (dashed). Corresponding plots of T_b at 17 GHz (blue), 34 GHz (red), and α (black) are shown below.	115
4.16	Plots of T_b as a function of θ for 17 GHz (top) and 34 GHz (bottom) around an ellipse fitted to the loop for each time interval in Stage 4.	117
4.17	Plots of radio spectral index α as a function of θ around an ellipse fitted to the NoRH radio loop for each time interval in Stage 4.	118
4.18	Plots of flux (top) and polarisation (bottom) at 1, 2, 3.75, 9.4, 17 and 34 GHz from the Nobeyama Radiopolarimeters. Black vertical lines indicate the separation between stages as before.	119
4.19	NoRP fitted radio spectra for times corresponding to images in Figure 4.6.	120
4.20	Peak flux (top left), peak frequency (top right), α_{tk} (bottom left), α_{tn} (bottom right) parameters from fitted NoRP spectra as a function of time.	121
4.21	TRACE 195Å evolution of 24th August 2002 flare with corresponding RHESSI 16 s image contours overlaid with energy bands 6-12 keV (blue), 12-25 keV (green) and 25-50 keV (red). Times indicated are the start of the RHESSI time integration. Image contours are at 50, 75 and 90% of image maximum intensity. Panel (d) has an additional 25% contour for all energy bands.	122
4.22	Plots show NoRH 34 GHz (redscale) brightness temperature images with NoRH 17 GHz contours overlaid (black) at 2, 4, 8, 16, 32, 64 and 96% of image maximum. RHESSI 6-12 keV (blue), 12-25 keV (green) and 25-50 keV (white) image contours are overlaid for a comparison of radio and X-ray sources during the decay phase. RHESSI contours are at 25, 50, 75 and 90% of image maximum.	123

-
- 4.23 RHESSI photon spectra for time intervals corresponding to panels b, c, d, j, k, l, m, n and o of Figures 4.2 and 4.21. Black lines show the background subtracted data and pink the background emission. Plots show an isothermal (green) plus a broken powerlaw (blue) fit to the data. Red shows the overall fit function. Below each fitted spectrum the fit residuals are show. 125
- 4.24 Plot shows evolution of RHESSI spectroscopy temperature, emission measure (top) and γ (bottom) fit parameters for the decay phase of 24th August 2002. The combined fit function was an isothermal plus broken power law. 126
- 4.25 RHESSI photon spectra for 24th August 2002 for time intervals corresponding to panels b, c, d, j, k, l, m, n and o of Figures 4.2 and 4.21. Black lines show the background subtracted data and pink the background emission. Plots show two isothermal (light and dark green) plus a broken powerlaw (blue) fit to the data. Red shows the overall fit function. 129
- 4.26 Plot shows evolution of RHESSI spectroscopy temperature, emission measure (top) and γ (bottom) fit parameters for the decay phase of 24th August 2002. The combined fit function was two isothermals plus a broken power law. 130
- 4.27 Thermal electron density calculated from RHESSI (right) and GOES (left). Orange shows the thermal density from RHESSI isothermal plus broken powerlaw fit. Pink solid shows thermal density from low temperature, high EM component of the double isothermal plus broken powerlaw fit. Pink dashed shows the corresponding thermal density from the high temperature, low EM component. . . 131
- 4.28 From top to bottom plots show T_b , α , δ , N_{nontherm} for looptop (dashed) and southern footpoint (solid) determined from observations with $\nu = 17$ GHz. Top plot also shows T_b for the arcade source (dotted). The looptop N_{nontherm} was calculated using $B = 150$ G. The southern footpoint N_{nontherm} was calculated using $B = 800$ G (black) and $B = 1000$ G (blue). Values of N_{nontherm} are calculated using $E_0 = 50$ keV. 134

- 5.1 Left shows thermal electron distributions for $n = 3 \times 10^{10} \text{ cm}^{-3}$ and $T = 3 \times 10^6 \text{ K}$ (dashed), $T = 3 \times 10^7 \text{ K}$ (solid) and $T = 3 \times 10^8 \text{ K}$ (dash-dot). Non-thermal electron distribution (over kinetic energy) for $N = 1 \times 10^7 \text{ cm}^{-3}$, $E_{\text{min}} = 0.1 \text{ MeV}$, $E_{\text{max}} = 10 \text{ MeV}$ and $\delta_1 = 2$ (dashed) $\delta_1 = 4$ (solid) and $\delta_1 = 6$ (dash-dot). Right shows the resulting radio emission from these spectra (credit GF). 144
- 5.2 Left shows double powerlaw over kinetic energy for $E_{\text{break}} = 1 \text{ MeV}$, $\delta_1 = 4$ and $\delta_2 = 2$ (dashed), $\delta_2 = 6$ (solid) and $\delta_2 = 9$ (dash-dot). The dotted line shows a single powerlaw where $\delta_1 = \delta_2 = 4$. Right shows the resulting radio emission from these spectra (credit GF). 144
- 5.3 Left shows thermal/nonthermal electron distributions for a thermal with $T = 3 \times 10^7 \text{ K}$ and nonthermal powerlaw over kinetic energy with $\delta_1 = 4$ and $\epsilon = 0.1$ (solid), $\epsilon = 0.03$ (dashed) and $\epsilon = 0.02$ (dash-dot). Right shows the resulting radio emission from these spectra (credit GF). 145
- 5.4 Magnetic dipole field from a buried dipole (Aschwanden 2004). . . 146
- 5.5 Definition of loop apex cross section in the yz-plane for a magnetic dipole model with dipole buried at depth, D . Circular cross section of radius r_0 centred at height H , the height above the dipole origin. Green cross shows loop central axis and red crosses show points at which field lines pass through the apex. 147
- 5.6 Magnetic dipole model field lines for $H = 32''$, $D = -16''$ and $r_0 = 5''$. Top left: xz-plane. Bottom left: xy-plane. Right: yz-plane. Arrows indicates the line of sight of the observer ($\hat{\mathbf{v}}$). In the case of the xz-plane $\hat{\mathbf{v}}$ is pointing into the page. The red circle in the yz-plane represents the cross section at the loop apex. . . . 148
- 5.7 Magnetic dipole model field lines for $H = 32''$, $D = -16''$ and $r_0 = 5''$. The model has been rotated around the z axis ($\gamma = 15^\circ$) Top left: xz-plane. Bottom left: xy-plane. Right: yz-plane. Arrows indicates the line of sight of the observer ($\hat{\mathbf{v}}$). In the case of the xz-plane $\hat{\mathbf{v}}$ is pointing into the page. 149

- 5.8 Magnetic dipole model field lines for $H = 32''$, $D = -16''$ and $r_0 = 5''$. The model had been rotated around the z and y axes ($\gamma = 15^\circ$ and $\beta = 20^\circ$) Top left: xz-plane. Bottom left: xy-plane. Right: yz-plane. Arrows indicates the line of sight of the observer (\hat{v}). In the case of the xz-plane \hat{v} is pointing into the page. 150
- 5.9 Magnetic dipole model for $H = 32''$, $D = -16''$, $r_0 = 5''$ and $B_0 = 100$ G. Top row shows an xz-plane slice at step 6 through the 3D mesh. Bottom row shows an xz-plane slice half way through the 3D mesh. From left to right, plots show B_x , B_y , B_z magnetic field components and far right shows B_{tot} . The dynamic range is scaled to the maximum and minimum values of each component for the entire model. 152
- 5.10 Arcade field model for $k = 1$, $l = 1$. Left shows an xz-plane. Right row shows an xy-plane. Arrows indicates the line of sight of the observer (\hat{v}). In the case of the xz-plane \hat{v} is pointing into the page. 154
- 5.11 Arcade model for $k = 1$, $l = 1$ which has been rotated the z-axis ($\gamma = 15^\circ$). Left shows an xz-plane. Right row shows an xy-plane. Arrows indicates the line of sight of the observer (\hat{v}). In the case of the xz-plane \hat{v} is pointing into the page. 155
- 5.12 Arcade model for $k = 1$, $l = 1$ which has been rotated around the y-axis ($\beta = 10^\circ$). Left shows an xz-plane. Right row shows an xy-plane. Arrows indicates the line of sight of the observer (\hat{v}). In the case of the xz-plane \hat{v} is pointing into the page. 156
- 5.13 Arcade model magnetic field components for $k = 1$, $l = 1$ and $B_0 = 100$ G for the “straight on” view. Left shows B_x , middle shows B_z and right shows B_{tot} . The dynamic range is scaled to the maximum and minimum values of each component. Note also that $B_y = 0$ 156
- 5.14 Thermal GS emission from the dipole model with $T = 1.0 \times 10^7$ K and $n_0 = 1.0 \times 10^9$ cm $^{-3}$ ($\gamma = 0^\circ$, $\beta = 0^\circ$). Left: 17 GHz image (S.F.U). Right: looptop spectrum (green), footpoint spectrum (red), total spectrum (blue). 159
- 5.15 Thermal GSFF emission from the dipole model with $T = 1.0 \times 10^7$ K and $n = 1.0 \times 10^9$ cm $^{-3}$ ($\gamma = 0^\circ$, $\beta = 0^\circ$). Left: 17 GHz image (S.F.U). Right: looptop spectrum (green), footpoint spectrum (red), total spectrum (blue). 159

- 5.16 Thermal GSFF emission from the dipole model with $T = 5.0 \times 10^7$ K and $n = 1.0 \times 10^9 \text{ cm}^{-3}$ (black), $n = 5.0 \times 10^9 \text{ cm}^{-3}$ (red), $n = 1.0 \times 10^{10} \text{ cm}^{-3}$ (green), $n = 5.0 \times 10^{10} \text{ cm}^{-3}$ (blue) ($\gamma = 0^\circ$, $\beta = 0^\circ$). 160
- 5.17 Thermal GSFF emission from the dipole model with $T = 5.0 \times 10^7$ K and $n = 5.0 \times 10^{10} \text{ cm}^{-3}$ ($\gamma = 0^\circ$, $\beta = 0^\circ$). Top: total dipole spectrum (blue), total looptop (solid green), looptop o-mode (dotted) and x-mode (dashed). Bottom: total dipole spectrum (blue), total footpoint emission (solid red), footpoint o-mode (dotted) and x-mode (dashed). The frequencies ranges of relevant cut offs are over plotted. 161
- 5.18 Thermal GSFF emission from the arcade model with $T = 1.0 \times 10^7$ K and $n = 1.0 \times 10^9 \text{ cm}^{-3}$ ($\gamma = 15^\circ$, $\beta = 0^\circ$). Left: 17 GHz image (S.F.U). Right: looptop spectrum (green), footpoint spectrum (red), total spectrum (blue). 162
- 5.19 Nonthermal GS emission from the dipole model with $\delta = 4$ and $N = 1.0 \times 10^4 \text{ cm}^{-3}$ ($\gamma = 0^\circ$, $\beta = 0^\circ$). Top left: 17 GHz image (S.F.U.). Top middle: 34 GHz image (S.F.U.). Top right: looptop spectrum (green), footpoint spectrum (red), total spectrum (blue). Bottom left: T_b profiles as a function of distance s along the loop at 17 GHz (blue) and 34 GHz (red). Bottom right: alpha calculated from 17 and 34 GHz images as a function of distance s along the loop. Path s along the loop is shown in green on 17 and 34 GHz images (top left and middle). 163
- 5.20 (a) Nonthermal GS total flux spectrum from the dipole model with $\delta = 2$ (black), 3(blue), 4(red) and $N = 1.0 \times 10^4 \text{ cm}^{-3}$ (solid), $N = 1.0 \times 10^5 \text{ cm}^{-3}$ (dashed) ($\gamma = 0^\circ$, $\beta = 0^\circ$). (b) Corresponding alpha calculated from 17 and 34 GHz images as a function of distance s along the loop. (c) alpha as a function of frequency for total spectrum (solid), looptop (dashed) and footpoint (dotted) for selected input parameters indicated on plot. 166

5.21	Nonthermal GS emission from the arcade model with $\delta = 3$ and $N = 1.0 \times 10^4 \text{ cm}^{-3}$ ($\gamma = 15^\circ, \beta = 0^\circ$). Top left: 17 GHz image (S.F.U.). Top middle: 34 GHz image (S.F.U.). Top right: looptop spectrum (green), footpoint spectrum (red), total spectrum (blue). Bottom left: T_b profiles as a function of distance s along the loop at 17 GHz (blue) and 34 GHz (red). Bottom right: α calculated from 17 and 34 GHz images as a function of distance s along the loop. Path s along the loop is shown in green on 17 and 34 GHz images (top left and middle).	167
5.22	(a) Shows nonthermal GS total flux spectrum from the arcade model with $\delta = 2$ (black), 3(blue), 4(red) and $N = 1.0 \times 10^4 \text{ cm}^{-3}$ (solid), $N = 1.0 \times 10^5 \text{ cm}^{-3}$ (dashed). Green shows reduction of arcade volume by 25% (solid) and 50% (dashed) for $\delta = 3$ and $N = 1.0 \times 10^4 \text{ cm}^{-3}$ ($\gamma = 0^\circ, \beta = 0^\circ$). (b) Shows comparison of arcade and dipole spectra for $\delta = 3$ and $N = 1.0 \times 10^4 \text{ cm}^{-3}$ for the arcade (black solid), arcade with 50% volume reduction (black dotted) and dipole (blue).	169
5.23	Plots of loop T_b profile at 17 GHz and 34 GHz for a series of input parameters (indicated on each plot) from a nonthermal GS distribution. FP:LT ratio can be seen in Table 5.5.	170
5.24	Plots of total GS emission from the dipole field model for a series of nonthermal electron distributions, with input parameters indicated on the plot, corresponding to the plots of T_b in Figure 5.23. . . .	172
5.25	Thermal density profile as a function of distance s along the loop which models progression to greater values of n when approaching the footpoints.	174
5.26	Plots show total GS spectra using a thermal/nonthermal electron distribution (red) for three sets of input parameters indicated on the plot.	175

- 5.27 Plots show comparison of GS emission from TNT and nonthermal models with the same input parameters $\delta = 3$, $N_{\text{LT}} = 5.0 \times 10^5 \text{ cm}^{-3}$ and $N_{\text{FP}} = 5.0 \times 10^4 \text{ cm}^{-3}$ i.e. solid lines on Figure 5.26. The looptop and footpoint sources are separated out. The top row shows the spectra from the TNT model and the bottom row shows the nonthermal model. Plots to the left the looptop spectra are plotted in dark green with separated into total (solid), x-mode (dashed) and o-mode (dotted) components. Plots to the right show the equivalent footpoint spectra in red. For comparison the total loop emission is plotted in blue. For the top row, the thermal spectrum is also plotted (light green), and split into its various components. 176
- 5.28 Plots of loop T_b profile at 17 GHz and 34 GHz for a series of input parameters (indicated on each plot) from a thermal/nonthermal GS distribution. 177
- 5.29 GS emission from a thermal/nonthermal electron distribution with $\delta_{\text{LT}} = 3$, $\delta_{\text{FP}} = 4$, $N_{\text{LT}} = 1.0 \times 10^4 \text{ cm}^{-3}$, $N_{\text{FP}} = 1.0 \times 10^3 \text{ cm}^{-3}$ and $T = 1.5 \times 10^7 \text{ K}$. The thermal electron density is the same as is shown in Figure 5.25 ($\gamma = 15^\circ$, $\beta = 0^\circ$). Top left: 17 GHz image (S.F.U.). Top middle: 34 GHz image (S.F.U.). Top right: looptop spectrum (Green), footpoint spectrum (red), total spectrum (blue). Bottom left: T_b profiles as a function of distance s along the loop at 17 GHz (blue) and 34 GHz (red). Bottom right: alpha calculated from 17 and 34 GHz images as a function of distance s along the loop. Path s along the loop is shown in green on 17 and 34 GHz images (top left and middle) 178
- 5.30 Total GS spectra from thermal/nonthermal and nonthermal electron distributions for different sets of input parameters (indicated on each plot). The values of N and δ are varied along the loop. For black TNT spectra $T = 1.5 \times 10^7 \text{ K}$ and red TNT $T = 2.5 \times 10^7 \text{ K}$. n is varied as shown in Figure 5.25 ($\gamma = 15^\circ$, $\beta = 0^\circ$). 180
- 5.31 Plots of loop α profile for a series of input parameters (indicated on each plot) corresponding to spectra in Figure 5.30 from a thermal/nonthermal and nonthermal electron distributions. 181

-
- 5.32 Plots of loop T_b profile at 17 GHz and 34 GHz for a series of input parameters (indicated on each plot) corresponding to spectra in Figure 5.30 from thermal/nonthermal and nonthermal electron distributions. 182
- 5.33 Plots of alpha as a function of frequency. Left shows the comparison of two nonthermal electron distributions which have the same spatial distribution of nonthermal electron density and have a low energy cut off at 50 keV. Plotted in black are the results for a model with a constant value of α along the loop and plotted in red are the results for a model with $\alpha_{LT} = 3$ and $\alpha_{FP} = 4$. Solid lines represent α calculated from the total loop spectrum and dashed and dotted represent α from the looptop and footpoint spectra respectively. Right shows a comparison between a TNT model (blue) and a nonthermal model (red). 183
- 5.34 Left shows looptop (green) and footpoint (red) and total (blue) thermal GS spectra for temperatures ranging from 1.0×10^7 K to 2.5×10^7 K for $B_0 = 150$ G. Right shows thermal spectra from increased magnetic field models from $B_0 = 150$ G to $B_0 = 200$ G for a temperature of $T = 1.5 \times 10^7$ K. 183

List of Tables

1.1	RHESSI grid parameters	40
4.1	24th August 2002 Flare evolution	99
4.2	24th August 2002 - Peaks along loop	110
4.3	Energy Loss Time (τ)	137
5.1	Input Parameters	142
5.2	Electron Distribution	143
5.3	NoRP times	160
5.4	Arcade model FP:LT brightness ratios (17 GHz/34 GHz)	169
5.5	Dipole nonthermal model FP:LT brightness ratios (17 GHz/34 GHz)	171
5.6	Dipole TNT model E_{\min} (LT/FP)	175
5.7	Dipole TNT vs nonthermal model FP:LT T_b ratio (17 GHz/34 GHz)	177
5.8	Dipole TNT vs nonthermal model FP:LT T_b ratio (17 GHz/34 GHz) .	179

Preface

Chapter 1 consists of an introduction to the Sun, giving details of the solar structure from the core to the corona. In particular an overview is given of the processes occurring in solar flares, covering relevant observations and theoretical work. Also included is a description of each the main instruments used for the work contained in the thesis.

Chapter 2 covers the relevant theory behind X-ray and radio emission which will be called upon in the following Chapters. The processes of thermal and non-thermal bremsstrahlung emission, for soft and hard X-ray emission, are explained and the assumptions behind thick and thin-target emission are presented. Details of thermal bremsstrahlung emission at radio wavelengths is also covered along with a description of the gyroresonance, gyrosynchrotron and synchrotron emission processes. In the complex case of gyrosynchrotron emission, a discussion is presented of different approximations that can be used.

In Chapter 3 we report what we believe to be the first observation of hard X-ray emission formed in a coronal jet. The event occurred on the 22nd of August 2002 and its evolution was observed by a number of instruments. In particular we study the pre-impulsive and impulsive phase of the flare using data from the RHESSI and TRACE spacecrafts. The event was also observed by the ground-based Nobeyama Radioheliograph and Polarimeters. Together these observations cover the X-ray, extreme ultraviolet (EUV) and radio regimes. During this period RHESSI observed significant hard X-ray emission to energies as high as 30-50 keV in the jet suggesting the presence of nonthermal electrons in the jet. NoRH observations at 17 and 34 GHz are seen to be co-spatial with the hard X-ray emission during this time and a value for the radio spectral index α is found to be ~ 0.75 corresponding to optically thick emission by non-thermal electrons, reinforcing our claim that X-rays are directly revealing the presence of these particles in the jet. We calculate an apparent jet velocity of $\sim 500 \text{ km s}^{-1}$ which is consistent with model predictions for jet material accelerated by the $\underline{J} \times \underline{B}$

force resulting in a jet velocity of the order of the Alfvén speed.

From the work carried out in Chapter 3, a growing interest in solar radio emission from flares led to another project involving the combination of X-ray and radio observations. In Chapter 4 we present observations of a GOES X3.1 class flare which occurred on the 24th August 2002. This event was also observed by RHESSI, TRACE and NoRH and occurred on the west limb of the Sun. At both NoRH frequencies, 17 GHz and 34 GHz, we are able to resolve a loop structure where the looptop is clearly separated from the footpoints and the loop apex exhibits an optically thin source. In addition to exhibiting a spatially resolved distribution of brightness along the loop, this flare also shows a temporal distribution of radio brightness where, in particular, the dominant emission varies between the looptop and one footpoint over time. In particular we concentrate on the decay phase of the flare. We follow the evolution of parameters such as the thermal and nonthermal electron density, plasma temperature and electron spectral index δ to understand the processes occurring in the decay phase and to determine the physical parameters of the flaring plasma.

Following the work in Chapter 4, we use the determined flare parameters to try and reproduce the emission at radio wavelengths in Chapter 5. We use a computational code written by Dr Gregory Fleishman (NJIT) which calculates the thermal and nonthermal gyrosynchrotron and free-free radio emission at a range of frequencies. Details of the construction of a 3D magnetic field model are presented, in particular we concentrate on two magnetic field models, a dipole and an arcade. From the spatial variation of the plasma parameters used as input to the calculation and from the choice of a thermal, nonthermal or a single combined thermal/nonthermal electron distribution, a number of possible scenarios are created and the results presented.

In Chapter 6 we summarise the work contained in each of the previous Chapters and discuss possible improvements and future directions which follow on from this body of work.

Acknowledgements

“All men dream: but not equally. Those who dream by night in the dusty recesses of their minds wake in the day to find that it was vanity: but the dreamers of the day are dangerous men, for they may act their dreams with open eyes, to make it possible”. - TE Lawrence, The Seven Pillars of Wisdom

I wasn't intending on using any quotes in my thesis but I like this one. It's used at the start of *Touching The Void* by Joe Simpson. In some ways a PhD is a bit of a survival story in itself. At no point was I left for dead on 'Thesis Mountain' and thanks are due to many folk who helped get me out alive.

Firstly, the biggest thanks to my parents, Morag and George Bain. Thanks for supporting and encouraging me from day one. I could not have done this without you both.

Secondly, a massive thank you to my primary supervisor Lyndsay Fletcher. Thank you for always taking the time to answer my "quick questions" and being so enthusiastic about all things solar, it certainly helped (even when the statement 'I've had enough of this!' prompts the answer 'You should write a paper!'). Thank you also to my second supervisor John Brown, who got me interested in solar physics by offering me a summer project between my third and fourth year of undergraduate. Thanks to Joe Khan for making that project interesting enough for me to want to do a PhD in solar physics. A big thank you to Gregory Fleishman for letting me loose on his code and for answering a stream of questions over the last year.

Throughout my PhD I tried to stick to the motto "Work hard. Play hard". There are a number of people who I would like to thank for helping me uphold the second part of that. Thanks firstly to Ross Galloway, an excellent officemate, who welcomed me in and showed me the ropes. Thanks to Iain Hannah, who also turned out to be a pretty good officemate. Thanks for tolerating my head bobbing when I was listening to music that made me want to dance. To the

wonderful variety of people that occupied that third desk, thanks for putting up with the occasional surf board in the office. Thank you to Morag Casey and Marina Battaglia for the weekly ‘climb and whine’ sessions down at the Ibrox Climbing Centre. Much PhD frustration was worked out on those nights. To the astro folk old and new, thanks for always having an open door and for being eager to help with any problems or just willing to chat for a bit. In particular the astro coffee core should be mentioned, Craig Stark, Robert McKay, Fiona Speirits, Procheta Mallik, Hamish Reid, Hugh Potts and Norman Gray for some absolutely bizarre topics of conversation. Thanks to the Solar Self Help group for a much needed, safe place to ask the really stupid questions. To the physics crowd, Bob Taylor, Matt Pitkin, Ellie Chalkley, John Veitch, James Clark, Richard Codling, Jen Toher, David Crooks, Bryan Barr, Siong Heng and Erin Macdonald, thank you for loving curry as much as me and for keeping me laughing. Thanks also to Mr India’s West End Balti and Dosa House for providing excellent curry. To Ed Bloomer, with whom I shared a flat in the second half of my PhD. Thanks for putting with my nocturnal thesis writing and general prowling around the flat in the wee hours of the morning.

To my non-physicists, Kimberley, Sean, Lucy and Rutoria. Thank you so much for keeping me firmly grounded in the real world and reminding me that not everyone must know that the Sun is more than a ‘big ball of fire in the sky’. Thank you to Claire for always being there to listen, keeping me thinking positive and for giving me something to smile about when all else failed.

Thanks finally to the Glasgow University surf club. There really is no better cure for a saturated brain (and a hangover) than the cold, wintery waves of Scotland.

Right, so now I’ve thanked you all, you are encouraged to read what you helped me achieve. Or maybe I’ll just let you all away with buying me a celebratory beer/curry.

Chapter 1

Introduction

1.1 The Sun

The Sun is our nearest star and is situated at the centre of our solar system. Given our close proximity to such an object is hardly surprising that the Sun has a considerable influence on our life here on Earth. Our orbital path around the Sun, in addition to the Earth's tilted rotational axis, results in our yearly seasons. The heat from the Sun warms our atmosphere and drives our weather systems, and its light is used in the process of plant photosynthesis which provides us with vegetation. In addition to the more obvious everyday processes, the Sun's influence is also felt as a result of its extended magnetic field. When the solar wind, a flow of charged particles propagating out from the Sun along the interplanetary magnetic field, interacts with the Earth's magnetic field, particles are accelerated. These particles stream down towards our polar regions creating displays of coloured light known as the aurora borealis in the north and the aurora australis in the south. With such a connection to the Sun it is no wonder that scientists are interested in trying to understand the processes occurring on our nearest star.

1.1.1 The Solar Structure

The Sun is a main sequence star with spectral classification G2V. It is around 4.5 billion years old and is approximately half way through its lifetime. The visible solar disc has a diameter of 1.4×10^9 m such that when viewed from Earth the Sun subtends an angle of about 0.5° . Its mass is 1.989×10^{30} kg and its luminosity is 3.85×10^{26} W (Stix 2004).

The Sun's energy is generated by nuclear fusion of hydrogen by the proton-

proton chain in the core, which extends out to around $0.2 R_{\odot}$. The core has a temperature and electron density of around 15 MK and 10^{34} cm^{-3} . The energy generated then travels outwards through the Sun's interior. Initially the temperature gradient and opacity are low enough for the energy to be transported by radiation. However at roughly $0.7 R_{\odot}$ the temperature has cooled to 1MK and a steep temperature gradient causes the Schwarzschild criterion to be broken. This instability leads to the onset of convection. In the convection zone hot material rises upwards to the visible solar surface, or photosphere. The effects of this can be seen on the photosphere as granulation cells which are around 1,000 km in diameter. The centres of these cells are bright where hot material rises. At the cell boundaries cooler, down-flowing material appears darker. The process is similar to that of boiling water. Larger scale convection effects can be seen as supergranulation cells which have diameters of around 30,000 km.

The photosphere is the thin layer of plasma, roughly 100 km deep, that marks the change between the optically opaque solar interior and the transparent solar atmosphere. More precisely the photosphere is marked by the condition that $\tau_{500\text{nm}} = 1$. The reason for this opacity is the absorption of visible light by abundant H^- ions in the process of photoionisation. The sharp change in opacity is due to the decrease in H^- ions. The vast majority of the Sun's radiation and heat is emitted from the photosphere. The plasma here emits and absorbs radiation almost like a blackbody resulting in a photospheric temperature of around 5,700 K. The plasma number density of the photosphere is roughly 10^{17} cm^{-3} .

A distinctive feature of the photosphere is the sunspot pattern. These features are the result of processes occurring below the photosphere. Observations show a differential rotation of the solar surface with an equatorial rotation period of around 27 days compared to around 34 days at the poles. At the base of the convection zone this differential rotation meets the solid-body rotation of the radiative zone. The region through which this steep velocity gradient occurs is called the tachocline.

The magnetohydrodynamic (MHD) induction equation describes a magnetic field in a plasma.

$$\frac{\partial B}{\partial t} = \nabla \times (v \times B) + \eta \nabla^2 B \quad (1.1)$$

where

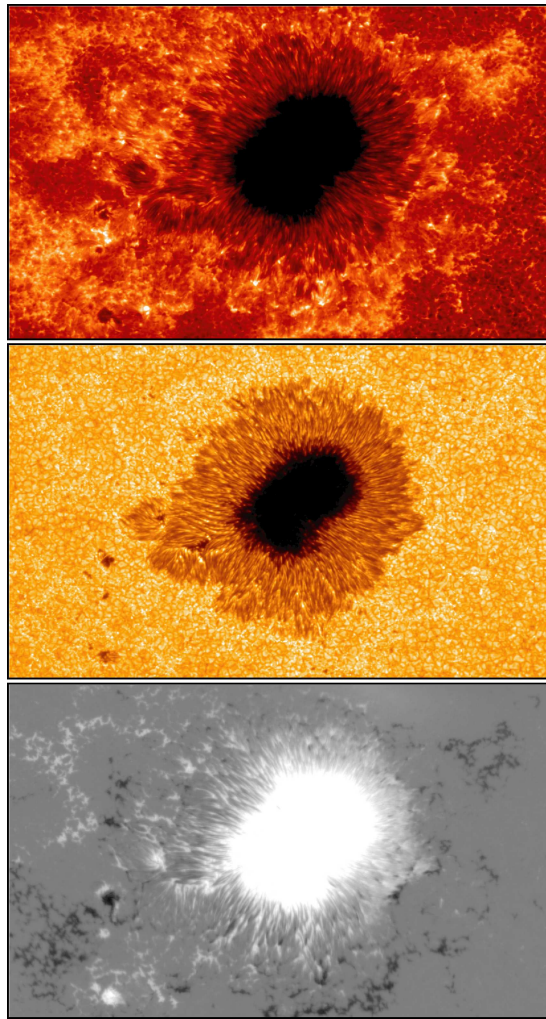


Figure 1.1: Sunspot images from the Solar Optical Telescope (SOT) instrument onboard the Hinode spacecraft. NAOJ/JAXA/NASA.

$$\eta = \frac{c^2}{4\pi\sigma} \quad (1.2)$$

is the magnetic diffusivity. When $\partial B/\partial t \approx \nabla \times (v \times B)$ then we are in the advective limit meaning that the magnetic field is frozen-in to the plasma and can be distorted by the motion of the plasma. When $\partial B/\partial t \approx \eta \nabla^2 B$ then we are in the diffusive limit and the magnetic field is able to slip through the plasma, a condition that is required at the reconnection point in the theory of magnetic reconnection. The ratio of the advective to diffusive terms is given by the magnetic Reynolds number, R_m . Often the plasma beta parameter is used to describe conditions in the Sun, the ratio of gas to magnetic pressure, $\beta = \frac{8\pi p}{B^2}$. For $\beta < 1$ the magnetic pressure dominates and the plasma is frozen-in to the

magnetic field, prohibiting cross field plasma transport. Conversely, in the case of $\beta > 1$ the gas pressure dominates and the plasma dynamics dominate the field dynamics.

Below the photosphere $R_m \gg 1$ and the magnetic field is influenced by the sub-photospheric plasma flows. The shearing process in the tachocline is believed to be the key to magnetic dynamo which generates the solar magnetic field. As a result of the Sun's differential rotation, poloidal magnetic field is altered to become toroidal field. Perturbations in the plasma motion can result in bundles of twisted magnetic field, called flux ropes, rising through the photosphere and up into the corona due to magnetic buoyancy, forming pairs (also groups) of sunspots which have opposite polarity. Sunspot pairs are linked by large magnetic loops which are anchored at their base in regions of opposite polarity. Subphotospheric plasma motion at the loop footpoints can cause a build up in shear and twist along the loop. The central portion of the sunspot, the umbra, appears dark. Here strong vertical field (1,000-4,000 G) rises out of the photosphere impeding convection to the surface and hence appearing dark. The outer penumbra appears lighter where the field has a larger horizontal component. Figure 1.1 shows images of a sunspot taken by the Solar Optical Telescope (SOT: Tsuneta et al. 2008) instrument onboard the Hinode spacecraft. Images are CaII H (top), G-band (middle), and a magnetogram (bottom). The Sun has a periodic cycle of approximately 11 years where solar activity passes through a phase of solar minimum and maximum due to the twisting of the magnetic field. Figure 1.2 shows 284 Å EUV images of the Sun over a solar cycle, taken by the Extreme ultraviolet Imaging Telescope (EIT: Delaboudinière et al. 1995) instrument onboard the Solar and Heliospheric Observatory (SOHO) spacecraft. This trend is also observed in the number of sunspots present on the photosphere. At the start of each cycle sunspots appear at high latitudes in both hemispheres. As the global magnetic field becomes increasingly twisted sunspot formation occurs closer to the equator. At the end of each cycle the Sun's polarity flips giving a 22 year magnetic cycle.

Above the photosphere is the chromosphere which derives its name from the Greek word 'chromos' meaning color. This is in reference to its deep red appearance caused by the dominant hydrogen Balmer α emission line at 6563 Å. The reddish glow of the chromosphere can be seen as a thin ring around the Sun during a solar eclipse when the photosphere is obscured from sight by the moon. In addition to H α there are a large number (> 3500) of other emission and absorp-

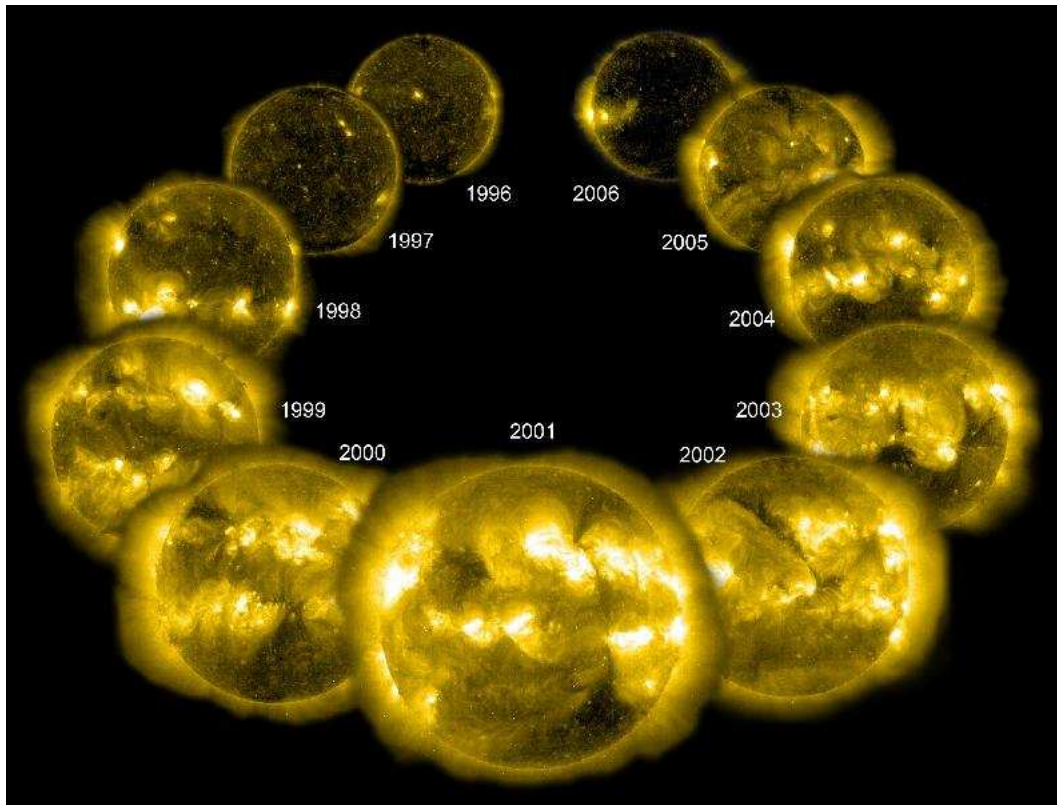


Figure 1.2: 284 Å EUV images of the Sun over a solar cycle, taken by the Extreme ultraviolet Imaging Telescope (EIT) instrument onboard the Solar and Heliospheric Observatory (SOHO) spacecraft. Courtesy of SOHO/EIT consortium.

tion lines. The chromosphere is roughly 2,500 km thick. At around 500 km above the photosphere the temperature reaches a minimum value of $\sim 4,300$ K before gradually increasing to a value of $\sim 20,000$ K at the upper boundary. Figure 1.3 shows a plot of electron density, and temperature as a function of height above the photosphere. Cool dense chromospheric material can often be seen suspended at greater heights in the hot tenuous corona, usually along polarity inversion lines in active regions. When viewed in $H\alpha$ these features appear dark (when situated above the disk) and are known as filaments, or appear bright (when viewed over the limb) and are known as prominences. Filament, or prominence, disruption is often observed in the pre-flare phase of a solar flare or coronal mass ejection (CME).

Above the chromosphere there exists a thin 'layer' around a few hundred km thick named the transition region where the temperature rapidly increases up to a few million Kelvin. The emission from this region is predominantly at ultra

violet (UV) wavelengths, for example Lyman α at 1216 Å.

1.2 The Corona

Above the transition region the corona extends out to around $3 R_{\odot}$. The name comes from the Latin word for ‘crown’, referring to the bright halo of white light seen during a solar eclipse. This white light is photospheric light that has been scattered into the line of sight by Thompson scattering off free electrons. The corona can be separated into three components based on the dominant emission mechanism. The K-corona is defined at heights, $h \lesssim 0.3 R_{\odot}$ and is dominated by the Thompson scattering of photospheric continuum emission. The L-corona at heights $h \lesssim 0.5 R_{\odot}$ is dominated by line emission from highly ionised ions. Finally the F-corona extending to heights $h \gtrsim 0.5 R_{\odot}$ shows Fraunhofer absorption lines caused by dust particles diffracting photospheric radiation.

For conditions in the corona $\beta < 1$ and thus the plasma traces out the magnetic field structure in the corona. We observe that the corona is highly dynamic. Large loops and arc-like structures are present at all locations on the Sun i.e. in areas of quiet Sun, active regions and also in flare sites. Above the closed loops we often observe coronal streamers or helmet streamers (structures which resemble a Prussian soldier’s spiked helmet) that stretch out and connect to the interplanetary field. We also observe large regions of unipolar magnetic field, where “open” field lines reach out into interplanetary space. These locations appear darker and are termed coronal holes. At times of solar minimum the coronal holes are located at the solar poles, however at the solar maximum these regions of open field can be seen extending down towards the equator. The coronal holes are thought to be the origin of the fast solar wind ($\approx 800 \text{ km s}^{-1}$), a stream of electrons and ions that flows from the Sun out into interplanetary space. Parker (1958) proposed that there must exist a solar wind, as the corona could not be in hydrostatic equilibrium. The Parker model has one critical solution that starts with a subsonic wind close to the Sun that becomes supersonic at a critical radius r_c . This simple model does not explain the fast and slow solar winds. The slow solar wind ($\approx 400 \text{ km s}^{-1}$) is thought to originate in closed field regions where the magnetic field becomes “open” only at greater heights in the corona.

Emission in the corona from highly ionised species such as iron, implies temperatures of $\gtrsim 1 \text{ MK}$. At these temperatures hydrogen is fully ionised (in contrast to the chromosphere which contains only partially ionised hydrogen). This is seen

Figure has been removed due to Copyright restrictions.

Figure 1.3: Electron density and temperature as a function of height above the photosphere Fontenla et al. (1990); Gabriel (1976); Aschwanden (2004).

in the sudden drop off in the density of neutral hydrogen in Figure 1.3. We can see the rapid increase in temperature that occurs in the transition region reaching temperatures of a few MK. In flares the coronal plasma can be heated to tens of MK. At greater distances the temperature gradually decreases. At 1 AU the temperature reaches a value of around 10^5 K.

Why the corona is so much hotter than the photosphere and chromosphere has puzzled scientists for many years and is known as the coronal heating problem. When considering this problem one must identify an energy source which, when released, can heat the surrounding plasma and also one must consider the response of the solar atmosphere to the release of such energy. There are two main candidates for storing the energy. 1) Energy stored in stressed magnetic field (DC heating). 2) Energy stored in plasma wave oscillations (AC heating).

It is thought that stress added to the magnetic field required for DC heating is generated by turbulent convective motions below the photosphere where the magnetic field is anchored. Estimates suggest there is ample energy contained in the magnetic field as a result of stressing, however the process in which this energy is released is still being investigated. In a model first suggested by Parker (1983, 1988), individual magnetic strands contained within a flux tube could become

tangled due to the continual footpoint motion. As the stress in these strands increases and current sheets form between neighboring strands small reconnection events could occur. In the “field line” scenario, this process involves the reconnection of magnetic field lines resulting in an altered magnetic connectivity. The reconnecting field lines allow the release of energy stored within the magnetic field as it allows the field to relax to a lower energy configuration. In order to maintain the coronal temperatures we observe and balance the energy release and energy losses from radiation and conduction, requires a minimum number of these ‘nanoflare’ events. Hudson (1991) investigates the relation between the peak flux and number of reconnection events. As expected there are a greater number of small events and fewer large events. The powerlaw fit to this trend suggests a critical powerlaw index of two in order to match the number of nanoflare occurrences needed to account for the require energy input into the corona.

The constant motion of photospheric plasma causing the continual restructuring of the magnetic field required for DC heating is also responsible for launching a variety of plasma wave modes. It is unclear whether the energy content in these waves modes is great enough to be the dominant process in heating the corona. The concept works on the basis that the plasma waves propagate up into the corona where they dissipate their energy in ways as yet unknown. However for wave modes generated low down in the atmosphere, only a small fraction of the energy flux is able to propagate into the corona. A large number of wave modes are unable to pass through the chromosphere and transition region as a result of the steep density and temperature gradients. One possibility is wave modes originating in the corona as the result of reconnection. These waves would then transport energy to regions of the corona not immediately associated with the primary event. A full discussion of the coronal heating problem and DC and AC heating mechanisms is discussed in a review by Klimchuk (2006) and references therein.

Somewhat related to the coronal heating problem is the question of temperature gradient observed in the chromosphere from a temperature minimum of $\sim 4,600$ K at around 500 km above the photosphere to the million degree plasma when rising through the transition region to the corona. One suggestion is that acoustic wave modes transport mechanical energy that is generated by turbulent motion in the subphotosphere. These waves then propagate up into the chromosphere where they dissipate their energy in the form of acoustic shocks caused by the steep density gradient, (Carlsson 2007; Wedemeyer-Böhm et al. 2007).

The corona is highly inhomogeneous with varying values of ambient plasma temperature. In the coronal holes we find the temperature to be $T \lesssim 1$ MK. Quiet Sun regions have slightly higher temperatures of $T \approx 1 - 2$ MK and active regions can be much hotter with $T \approx 2 - 6$ MK (Aschwanden 2004). There is also a variation in the plasma density for different structures observed in the corona. For example, at the base of the corona ($\approx 2,500$ km above the photosphere) the coronal hole density is $\approx (0.5 - 1.0) \times 10^8 \text{ cm}^{-3}$. Quiet Sun values are $\approx (1 - 2) \times 10^8 \text{ cm}^{-3}$. The density is greatest for active regions, with values $\approx 2 \times 10^8 - 2 \times 10^9 \text{ cm}^{-3}$. The density is seen to drop to values of $\approx 10^6 - 10^7 \text{ cm}^{-3}$ for heights greater than $1R_{\odot}$ Aschwanden (2004). EUV and soft X-ray observations reveal the brightly emitting plasma situated along coronal loops.

It is difficult to measure coronal magnetic field strengths. One method uses photospheric field measurements and applies a model-dependent extrapolation to estimate the coronal field strength. To determine the field strength in the photosphere we can use the Zeeman effect which describes the splitting of a spectral line in the presence of an external magnetic field. The magnitude of the splitting is proportional to the strength of the field. From the Stokes' parameters I, V, Q and U we can determine polarisation. Using these and taking into account the radiative transfer effects we can determine the intensity and magnetic field vector components in the photosphere. At this point a model for the coronal currents is applied and upper and transverse boundary conditions applied for extrapolation to the coronal field. Assuming a stationary state where forces due to gravity and pressure (i.e. low plasma β) are negligible then the MHD force balance equation

$$\rho \frac{dv}{dt} = \mathbf{j} \times \mathbf{B} - \nabla \mathbf{p} + \rho \mathbf{g} \quad (1.3)$$

can be reduced to $\underline{j} \times \underline{B} = 0$. Hence a so-called force 'free' model. A potential (current-free) field ($\nabla \times \underline{B} = 0$) is the lowest state of energy in which the magnetic field can reside. However potential field models do not describe well the field before or during a flare. As mentioned previously, free magnetic energy can be built up by shearing or twisting the field. Twisting of magnetic field lines produce current, $\mathbf{j} = \nabla \times \mathbf{B}/4\pi$. For cases where a current is present we can rearrange to find $\nabla \times \underline{B} = \alpha \underline{B}$, where the function α is constant along the field line and for all field lines i.e. a linear force free field model. A further extension to nonlinear

force free field models allows α to vary for different field lines, see Sturrock (1994) for details.

1.3 Solar Flares

The first solar flare was observed in white light by R.C. Carrington and R. Hodgson in 1859, (Carrington 1859). Flares are sudden violent eruptions in which large amounts of magnetic energy ($10^{29} - 10^{33}$ ergs) are released. These events can last from a few minutes up to a few hours. Flares have been observed to occur at all points on the Sun. However large flares are usually associated with large active regions which exhibit a complex, rapidly evolving, 3D magnetic field configuration (Régnier & Canfield 2006), with sources of mixed polarity such that the footpoints of flaring loops straddle the line of sight photospheric magnetic polarity inversion line and are seen to be anchored in regions of opposite polarity.

The energy is thought to be released high in the corona and produces emission across the entire EM spectrum, from radio to gamma ray energies and heats the surrounding plasma to tens of MK. Roughly 50% of the energy released in a flare goes into accelerating particles (electrons, protons and heavy ions). It is thought that the energy required for a flare is stored as ‘free’ magnetic energy (i.e. the excess energy contained within the force free field in comparison to the potential field) in the corona in the form of a current. As mentioned before, this free magnetic energy can be built up and stored over the course of several hours or days as the result of photospheric or sub-photospheric disturbances.

It is not fully understood how the energy is released and converted into thermal heating and into nonthermal particle acceleration energy. There are many complex models which propose how this occurs, however most models at some point invoke magnetic reconnection. There are several models that use this idea of magnetic reconnection, each with different configurations of magnetic field. There are also other models which do not feature magnetic reconnection as the main cause of energy release.

One particular model suggests electrons are accelerated in the corona to energies of up to 10 - 100’s of keV. These electrons then propagate down the newly connected field lines. Upon reaching the loop footpoints the electrons encounter an increased plasma density where they undergo Coulomb collisions and emit hard X-ray emission. This process is described by the thick target model (Brown 1971) and will be discussed in detail in Chapter 2 on X-ray and Radio emission.

Figure has been removed due to Copyright restrictions.

Figure 1.4: Plot shows an example spectrum ranging from soft X-rays to gamma-rays. The relevant energy ranges related to specific emission mechanisms are indicated. The electron-positron annihilation line at 511 keV and the neutron capture line at 2.223 MeV are indicated (Aschwanden 2004).

This nonthermal hard X-ray emission at the flare footpoints was first spatially resolved by Hoyng et al. (1981). Kane (1983) showed that 95% of emission \gtrsim 150 keV is situated at altitudes of \lesssim 2500 km, i.e. in the chromosphere where the density is high enough to completely thermalise the accelerated electrons.

In addition to footpoint hard X-ray sources, observations have also shown a third source located in the corona at heights of 6000 - 25,000 km. Probably the most famous of these occurred during a flare on the 13th January 1992 (Masuda et al. 1994) (note that the Masuda flare is a very rare type of a coronal source), see also Krucker et al. (2008a) for a review of such sources. These coronal sources often exhibit a nonthermal component which can be associated with thin target emission of electrons propagating in a collisionless plasma (Datlowe & Lin 1973; Mariska & McTiernan 1999; Krucker & Lin 2008). In the thin target scenario, the electrons only lose a small fraction of their energy and continue towards the footpoints where they produce thick target hard X-ray emission through Coulomb collisions mentioned above. We discuss thin target emission in more detail in Chapter 2.

Protons and other atomic nuclei are also accelerated in the energy release

process. These particles are accelerated to energies of $\gtrsim 100$ MeV and, like the electrons, propagate down magnetic field lines to the chromosphere where they undergo collisions with ambient nuclei, producing neutrons. These neutrons are then captured within $\sim 1,000$ km by ambient protons and produce gamma-ray emission at 2.223 MeV, i.e. the neutron capture gamma ray line. RHESSI images taken at 2.223 MeV reveal gamma-ray footpoint emission indicating the location of ion precipitation in the flare. Hurford et al. (2006) presented observations of flare hard X-ray and gamma ray footpoints showing that the centroid positions of the footpoints in hard X-rays and 2.223 MeV are not co-spatial. This could suggest that the electrons and ions are undergoing separate acceleration processes or that they originate in separate loop systems (Emslie et al. 2004). Figure 1.4 shows a spectrum from soft X-rays to gamma-rays. The neutron capture line at 2.223 MeV is indicated. In addition to neutron capture there are a number of other gamma-ray emission mechanisms. Firstly, the gamma-ray continuum can be seen up to hundreds of MeV, caused by electron bremsstrahlung emission. A number of narrow and broad band emission lines arise as the result of de-excitation of chromospheric species caused by the precipitation of flare accelerated protons and heavier atomic nuclei. These lines are observed for energies in the range 0.5 - 8 MeV. A strong line is observed at 511 keV caused by positron annihilation with free electrons. Gamma-rays are also produced by the decay of neutral pions, which are created by proton/ion collisions in the chromosphere.

The exact geometry of the magnetic field structure in a solar flare is unclear and may in fact not be restricted to one particular model. One suggestion is the single loop model which is defined in 2D or an arcade of loops in 3D. The CSHKP model named after the contributors to the model, Carmichael (1964), Sturrock (1966), Hirayama (1974) and Kopp & Pneuman (1976). Here the reconnection occurs between the antiparallel field in the loop legs as they are pinched together, resulting in a cusp-like structure above closed loops and the ejection of a plasmoid into interplanetary space, see Figure 1.5 (Tsuneta et al. 1997). Observational evidence for this is presented in Tsuneta et al. (1997); Shibata (1999). The model in Figure 1.5 has been adapted by Tsuneta et al. (1997) to include slow and fast shocks.

In the chromosphere bright ribbons are observed in UV, EUV and $H\alpha$ marking the anchored field lines of a magnetic arcade. It is thought that the bright ribbons could arise from thermal conduction or weak particle precipitation. Flares which exhibit reconnection between multiple loops systems can result in more than two

Figure has been removed due to Copyright restrictions.

Figure 1.5: Cartoon of the CSHKP model from Tsuneta et al. (1997) showing pinching of antiparallel loop legs as they are pinched together resulting in a cusp like structure above closed loops and a plasmoid ejection into interplanetary space, (Tsuneta et al. 1997).

ribbons occurring: this is particularly evident at the start of the flare during a period of rapid reconnection and field restructuring. The positioning of the flare ribbons provides clues to the overarching magnetic topology. Also observed are hard X-ray and white light footpoints which appear in localised compact sources at points along the ribbons. Spatial and temporal correlation of hard X-ray and white light footpoint sources suggests that they are formed by a similar process of energy deposition. White light emission has been observed in large and small flares and represents a significant fraction of the flare energy in order to be observed over and above the photospheric flux. Whilst the hard X-ray emission can be described in terms of the thick target model, it is as yet unclear how the white light sources are produced. For energy to be deposited in the photosphere places a high energy budget on the energy contained in electron beams. A number of other alternatives have been suggested including beams of protons of energy 10-20 MeV penetrating deep into the atmosphere (Švestka 1970), or radiative ‘back-warming’ caused by energy deposition in the chromosphere which heats the lower atmosphere (Metcalf et al. 1990). See Fletcher et al. (2010) and references therein for a fuller discussion. The differences in the morphology of ‘footpoints’

and ‘ribbons’ suggests that only select field lines involved in the reconnection act as conduits for the propagation of accelerated particles to the lower atmosphere. How the emission at hard X-ray and EUV energies is related is also still unclear. As the flare progresses the ribbons can be seen to move apart, in a motion parallel to the polarity inversion line, as the reconnection site moves to greater heights in the corona due to subsequent reconnection Krucker et al. (2003). The cusp shape and closed loops also move to higher altitudes. The motion of the hard X-ray footpoints is more complex, often showing perpendicular motion (with respect to the inversion line) along the ribbons and also a motion in the parallel direction. For more details concerning the extensive work regarding flare footpoints/ribbons see Fletcher et al. (2010) and references therein.

Other flare models consider reconnection between two separate loop systems where two antiparallel magnetic field lines meet and reconnect. An example of this is the emerging flux model, Heyvaerts et al. (1977), which is used to describe the observations of a flare related jet presented in Chapter 3 and will be discussed in more detail at that point.

From the release site in the corona, energy is transported down the newly reconnected field lines to the chromosphere where the accelerated electrons precipitate and in turn heat the surrounding footpoint plasma. The chromosphere responds dynamically through the process of chromospheric evaporation (Dosc hek et al. 1980; Feldman et al. 1980). As the plasma is heated to tens of MK, the thermal pressure becomes greater than that of the surrounding plasma. This results in a pressure gradient which drives the heated plasma up the loop legs and into the corona, where the loop is seen emitting at soft X-ray and EUV wavelengths. Observations have shown that the density in the coronal loop is greatly increased to values as high as 10^{11} cm^{-3} , (Tsuneta et al. 1997). By studying blue shifts observed in chromospheric spectral lines, such as Caxix, upflow velocities of 300 - 400 km s^{-1} have been observed (Antonucci 1989; Milligan et al. 2006). At times of immense particle acceleration the heating occurs rapidly in response to the increased nonthermal electron flux in what is known as ‘explosive’ heating. In addition to heating by energetic electrons it is expected that there will be a contribution from thermal conduction which can be dominant at times before and after the intense electron acceleration (Battaglia et al. 2009; Zarro & Lemen 1988) when the heating can be considered as ‘gentle’. Fisher et al. (1985) showed that for explosive evaporation, the heating timescale should be less than the timescale for hydrodynamic expansion and estimated that explosive heating

Figure has been removed due to Copyright restrictions.

Figure 1.6: Flare emission at different wavelengths (Benz2002)

would need a flux of nonthermal electrons greater than 3×10^{10} ergs $\text{cm}^{-2} \text{s}^{-1}$. Hot loops that are observed at locations which are not flaring could be explained by gentle chromospheric evaporation.

Flare emission at different energies as a function of time is summarised in Figure 1.6 (Benz 2008). The flare three main phases are, preflare, impulsive and decay. The impulsive phase marks the period over which the main energy release occurs and during which there is intense particle acceleration. This is reflected in the bursty profile of the hard X-ray emission through to radio wavelengths. As the accelerated electrons propagate towards the footpoints they emit gyroemission at radio wavelengths as they orbit the magnetic field. A full discussion of flare radio emission mechanisms is given in Chapter 2.

In the case where hot soft X-ray emitting plasma is driven into the corona in response to the precipitation of nonthermal electrons in the chromosphere there is, as is expected, a relation between the soft and hard X-ray fluxes. It was found that the soft X-ray flux can be approximated as the integral of hard X-ray flux over time. This finding is known as the Neupert effect (Neupert 1968).

$$F_{SXR}(t) \propto \int_{t_0}^t F_{HXR}(t') dt' \quad (1.4)$$

For flares which display this feature, the soft X-ray peak occurs at the end of the impulsive phase. The end of the impulsive phase represents a move from rapid energy release to a more gentle release. Many flares deviate from the Neupert relation (Veronig et al. 2002). This could be explained by efficient loop cooling or that the initial plasma heating resulted from thermal conduction as opposed to nonthermal electron precipitation, or ongoing slow heating after the impulsive phase.

In addition to the Neupert effect, the hard X-ray emission can be seen to follow what is known as a ‘soft-hard-soft’ trend, where the spectral index of the hard X-ray spectrum decreases i.e. hardens as the flux increases before increasing again i.e. softening as the flux decreases. This trend can be seen for individual hard X-ray bursts during the main rise phase, but the trend is also observed spanning the entire flare time range. Individual sources such as footpoints and looptop sources have been seen to follow the soft-hard-soft behaviour (Battaglia & Benz 2006). In addition to soft-hard-soft there are also a number of events which follow a ‘soft-hard-harder’ trend in which the hard X-ray spectral index gradually increases over time. This has been seen for coronal sources and is thought to occur due to trapping of higher energy particles (Krucker et al. 2008b). The trapping time is shorter for lower energy electrons which are more likely to be scattered into the loss cone and lost from the trap. Another suggestion would be continuation of particle acceleration beyond the main energy release phase.

Flares are classified by the peak soft X-ray flux (0.1-0.8 nm) recorded by the Geostationary Operational Environmental Satellite (GOES) spacecraft giving A,B,C,M or X type flares. Each class of flare is an order of magnitude apart, the highest being an X class flare (10^{-4} W m^{-2}). Each class is also split into 9 linear subcategories.

During the impulsive phase $H\alpha$ line emission increases in intensity and the line width is broadened. After the main release of energy the flare enters a decay phase where the overall emission returns to background levels.

In addition to solar flares there are other eruptive events occurring on the Sun. Coronal mass ejections, eruptive events in which around $10^{14} - 10^{16}$ g of magnetised ‘blobs’ of plasma are expelled from the corona into interplanetary space at speeds of $1,000 - 3,000 \text{ km s}^{-1}$, are sometimes associated with flares and filament disruptions. It should be noted that not all flares have an associated CME and equally not all CMEs are associated with a flare. However most large CMEs are associated with a flare and vice versa. The energy release in a CME is

mechanical in contrast to a flare in which the energy is converted into heat and particle acceleration. At metric radio wavelengths, emission can still be observed far into the decay phase as the result of shock front particle acceleration, occurring as the ejected plasma propagates outwards into interplanetary space.

The standard flare model describes the general evolution of a flare from energy release in the corona to the coupled response of the chromosphere. Although many observations show strong agreement, there are many observations which deviate from the standard model. No two flares are the same and as new technologies and instrumentation develop providing better spatial, temporal and spectral information more and more new and interesting features are uncovered.

1.4 Instruments and Data Analysis

1.4.1 RHESSI

The (Reuven) Ramaty High Energy Solar Spectroscopic Imager (RHESSI) is one of NASA's Small Explorer missions (Lin et al. 2002). Launched in February 2002, its objectives are to study particle acceleration and energy release in solar flares. The single instrument is designed to perform both separate and combined imaging and spectral analysis. With superb spatial resolution of $2.3''$ ($\approx 1660\text{km}$) and spectral resolution of $\approx 1\text{-}10\text{ keV}$ FWHM, RHESSI can observe photon energies ranging from 3 keV (soft X-rays) to 17 MeV (γ -rays). This encompasses the thermal and nonthermal X-ray up to gamma-ray energies including the 2.223 MeV line of neutron capture by hydrogen and 0.511 MeV line by electron-positron annihilation.

The implementation of protective shutters or attenuators ensures a wide dynamic range and makes it possible to observe both microflares and large flares. For large count rates, two shutters can be put in place (thin and thick) giving three attenuator states, A0, A1 and A3 where A0 is the open state. The effect of the attenuator state is energy dependent and is more significant at lower energies where the counts are highest whilst still allowing higher energy photons to penetrate. When count rates are high the instrument can be affected by pileup. The detector requires a finite time to register a photon. If two photons arrive during this time then the detector will record an energy equal to the sum of the two photons. This can become a problem in large flares before the shutters are introduced.

Figure has been removed due to Copyright restrictions.

Figure 1.7: Schematic showing RHESSI Rotating Modulation Collimators (Hurford et al. 2002)

RHESSI Imaging

Considering the energy range which RHESSI detects, telescope designs using grazing incidence mirrors are unsuitable as the photons have high enough energy to penetrate the mirror or are scattered by its surface at low energies. Instead the best imaging solution currently available is Fourier-transform imaging, Hurford et al. (2002). The instrument consists of 9 bi-grid rotating modulation collimators.

As seen in Figure 1.7, each collimator consists of two grids (front and rear) separated by 1.5m. Each grid is made up of an array of X-ray opaque slats equally spaced by X-ray transparent slits. The slits on the corresponding front and rear grids are parallel and have identical pitches. The pitch is altered for each grid ranging from 34 μm to 2.75 mm in steps of $\sqrt{3}$, see Table 1.1 (Hurford et al. 2002).

The rotation of the spacecraft every 4s causes modulation of the transmission of photons within each collimator, giving information on the photon incidence angle. Behind each collimator resides a cryogenically-cooled germanium detector, which records the photon's arrival time and energy (Smith et al. 2002). Figure 1.8 shows the arrangement of the nine collimators, showing the front and rear

Table 1.1: RHESSI grid parameters

Subcollimator number	Pitch (mm)	slit width (mm)	FWHM resolution (")
1	0.034	0.02	2.26
2	0.059	0.035	3.92
3	0.102	0.061	6.79
4	0.177	0.106	11.76
5	0.306	0.184	20.36
6	0.530	0.318	35.27
7	0.918	0.477	61.08
8	1.590	0.811	105.8
9	2.754	1.487	183.3

grids situated in front of the corresponding germanium detectors. The spatial resolution depends on the slit width. Grids with a finer slit width are able to resolve the modulated signal from two adjacent finite sources. However, larger sources will show no modulation in the finer grids and so a coarser slit width is required. The FWHM resolution for each collimator is shown in Table 1.1 (Hurford et al. 2002). Note that sources that are situated at centre of the rotation axis are therefore not modulated. During each rotation the amplitudes and phases for $\sim 10^3$ Fourier components are recorded (Hurford et al. 2002). A combination of the time-modulated flux from different detectors provides information required for effective image construction.

Figure 1.9 shows examples of the time-modulated flux for an off-axis source with varying parameters. Panel one shows the modulation pattern for one rotation for an off-axis point source. Panel two shows the same point source but half the flux thus reducing the amplitude of the modulated signal by half. Panel three shows another point source, at the same radial distance from the rotation axis centre, but at a different position on the Sun. The effect of this is a phase shift in the modulated signal. Panel four shows a point source at a greater radial distance from the rotation centre. This is reflected in the frequency of the modulated pattern as the slit passes across the source in a shorter time. Panel 5 shows a source with finite size which results in the trough of each period occurring at a finite value instead of the signal dropping to zero. Panel 6 shows an even larger source size which enhances the effect shown in panel 5. Panel 7 shows a more realistic modulation pattern which contains a mixture of all the previously mentioned features.

RHESSI images can be made for user-defined time and energy ranges and with

Figure has been removed due to Copyright restrictions.

Figure 1.8: Schematic showing arrangement of RHESSI front and rear grids situated in front the corresponding germanium detectors (Hurford et al. 2002)

Figure has been removed due to Copyright restrictions.

Figure 1.9: Plots show examples of modulation profile for an off-axis source. Different panels correspond to different source parameters such as radial offset and source size. Figure taken from (Hurford et al. 2002)

a combination of detectors which optimises the resolution of the source image. Firstly, in order to reconstruct RHESSI images from the time-modulated signal an inverse Fourier transform is required to retrieve the spatial information. This process is known as back projection and is the starting point for all images reconstruction algorithms. However a back projection image contains a contribution from the instrumental response causing side lobes in the image. A number of algorithms have been developed to remove these instrumental effects and return the true source. A full discussion of these algorithms is given in Hurford et al. (2002), however we mention here the CLEAN algorithm, which has been used for RHESSI images in later chapters.

The CLEAN algorithm was originally developed for radio astronomy, (Högbom 1974). The method works on the basis that the source is made up of individual point sources convolved with the instrument response. The CLEAN algorithm works in an iterative fashion by identifying the bright pixel in the back projected image and deconvolving with the instrument point spread function. This pixel is then subtracted from the image. The process continues until the level of the background noise is reached. The subtracted deconvolved point sources are then convolved with a clean, gaussian point spread function, known as the CLEAN beam or CLEAN point spread function, with a FWHM that is equal to the spatial resolution of the collimators.

RHESSI Spectroscopy

Spectral Analysis for RHESSI is carried out using an object orientated program called OSPEX developed by R. Schwartz (Schwartz et al. 2002). OSPEX uses a method of forward fitting in which model spectra are used to fit the count spectrum recorded by the detector. The count spectrum does not have a simple one-to-one relation with the emitted photon spectrum. The photons arriving at the spacecraft can be absorbed by the grids or undergo Compton scattering in the Earth's atmosphere, and in and out of the detectors. To correct for this, a time dependent Detector Response Matrix is used which relates the energy of incoming photons to that of the measured counts detected. A linear photons-to-counts response is represented by the diagonal elements of this matrix, whilst off-diagonal elements represent photon energies caused by scattering etc. A background subtraction is required to remove the solar background and a contribution from instrumental noise.

$$\mathbf{C} = \mathbf{B} + \mathbf{DRM} \times \mathbf{I} \quad (1.5)$$

The counts recorded are related to the incident photons as shown in Equation 1.5 where \mathbf{C} is the recorded counts, \mathbf{B} is background subtraction and \mathbf{I} is the incident photon flux.

OSPEX offers a choice of parametric model spectra to fit the data. The lower energy soft X-rays can be fitted with an isothermal (or multithermal) Maxwellian distribution characterised by a temperature and an emission measure. At higher hard X-ray energies a single, broken or triple power law photon distribution characterised by spectral power law index γ can be used. Alternatively one can assume a thick or thin-target source. In this case model electron spectra are used, characterised by a power law fit to nonthermal electrons between an electron low and high energy cut off. The fitting routine convolves the model spectrum with the DRM and converts to count space to compare with the recorded observations and obtain a good fit.

1.4.2 Nobeyama Radioheliograph and Radiopolarimeters

The Nobeyama Radioheliograph (NoRH) is a ground-based, solar-dedicated, radio interferometer situated in Japan (Nakajima et al. 1994). Full disk images of flux density (brightness) are made at 17 and 34 GHz microwave frequencies with good spatial resolution of 10" and 5" respectively and excellent temporal resolution of 0.1s during flare events. Measurements of polarisation are also made at 17 GHz. At these frequencies, NoRH observes gyrosynchrotron, free-free and (for high temperatures and magnetic field strengths) gyroresonance emission. From the flux at 17 GHz and 34 GHz it is possible to determine a radio spectral index α from $F(\nu) \sim \nu^\alpha$, where $F(\nu)$ is the flux at frequency ν . Combined observations from NoRH and RHESSI provide useful diagnostics of plasma properties in the flaring region.

The Nobeyama Polarimeters (NoRP) observe the Sun at 1, 2, 3.75, 9.4, 17, 35 and 80 GHz radio frequencies recording flux and polarisation at each frequency (Torii et al. 1979). NoRP has no imaging capabilities but instead provides the spatially integrated radio spectrum. From this spectrum we have information about whether the source is optically thick or thin. The value of spectral index at optically thin frequencies provides a clue as to what the dominant emission

mechanism is, see Chapter 2 for more details. The combination of NoRP spectra and NoRH images provide necessary information to recover the physical parameters of the flaring plasma and the source of radio emission in a flare.

1.4.3 TRACE

TRACE is another of NASA's Small Explorer missions (Handy et al. 1999). Launched in 1998, the spacecraft consists of a single instrument, a 30cm Cassegrain Telescope. TRACE observes the solar photosphere, transition region and corona with a high spatial resolution of 1" and temporal resolution of less than a minute. The telescope is split into quadrants which record 171Å, 195Å and 284Å EUV passbands and a range of UV passbands between 1200-7000Å, selected by multilayer coatings on the primary and secondary mirrors and by the use of 2 filter wheels. At these wavelengths TRACE can observe atmospheric emission at temperatures between 6000K and 10MK.

Chapter 2

X-ray and Radio Emission

The previous Chapter gave an overview of the evolution of a solar flare from energy release high in the corona, which heats plasma and accelerates particles, and the corresponding response of the chromosphere. The flare can be split into separate phases and each phase characterised by the evolution of emission at different wavelengths. It was found that temperatures vary considerably from the solar surface, where photospheric sunspot umbrae have temperatures as low as 4,400 K, to flaring plasma which can be heated to tens of MK. For coronal temperatures the thermal emission falls into EUV and soft X-ray wavelengths. The observations of the Sun in these energy regimes were obtained from balloon rocket flights in the 1940's and 1950's. However these flights provided only snapshots of the Sun with rocket flight times lasting less than 10 minutes. The first spacecraft observations came from the Orbiting Solar Observatory satellites which were launched between 1962 and 1975. There have since been a number of space missions which have observed the Sun at a number of wavelengths each providing better and better observations with the improvement of technology.

The work presented in later Chapters focuses on observations and modeling of eruptive solar events at X-ray and Radio energies. This Chapter aims to give a review of the relevant X-ray and radio emission mechanisms which we later rely on for diagnostics of the physical properties of the flaring plasma and for identifying particle acceleration in these events.

2.1 X-ray Emission

2.1.1 Coulomb collisions

In the solar atmosphere particles undergo collisions. From classical electrodynamics, (Jackson 1962), it can be shown that an incident particle with charge ze , mass m and velocity v will be deflected from its initial trajectory by the Coulomb field of a stationary target particle with charge Ze and mass M . The angle of deflection Ψ is

$$\tan\left(\frac{\Psi}{2}\right) = \frac{Zze^2}{\mu bv^2} \quad (2.1)$$

where μ is the reduced mass

$$\mu = \frac{mM}{(m+M)} \quad (2.2)$$

Following the method in Emslie (1978) and Tandberg-Hanssen & Emslie (1988), for electron collisions with an effectively stationary target of electrons and protons with equal number density n , the mean rate of change of electron energy E and parallel velocity v_{\parallel} are

$$\frac{dE}{dt} = \frac{-C}{E}nv \quad (2.3)$$

$$\frac{dv_{\parallel}}{dt} = \frac{-3C}{2E^2}nv^2 \quad (2.4)$$

where, for a fully ionised electron-proton plasma

$$C = 2\pi e^4 \ln \Lambda \quad (2.5)$$

Here we define $\ln \Lambda$ as the Coulomb logarithm

$$\ln \left[\left(\frac{\mu_0 b_0 v^2}{Zze^2} \right)^2 \right] = 2 \ln \Lambda \quad (2.6)$$

where b_0 is an upper cutoff on the value for the impact parameter. Several values of b_0 can be considered. Due to charge shielding the Coulomb force

is not felt by an incident particle at distances greater than the Debye length λ_D and so $b_0 = \lambda_D$. If we consider an electron gyrating around a magnetic field line then b_0 will be confined to length scales on the order of the gyroradius r_B and $b_0 = r_B$. Thirdly if we take into account plasma oscillations then Coulomb interactions are required to take place in a timescale of $\tau < \nu_p^{-1}$, where $\nu_p = \left(\frac{e^2 n_e}{\pi m_e}\right)^{1/2} \approx 9000\sqrt{n_e}$ is the plasma frequency and hence $b_0 = v\nu_p^{-1}$. A choice of b_0 will be dependent on the target temperature, density and magnetic field strength.

After a number of successive collisions the incident electron will be stopped or thermalised in the target plasma. The column depth N_{stop} required to stop an electron is

$$N_{\text{stop}} = \frac{\mu_0}{3C} E_0^2 \approx 10^{17} \mu_0 [E_0(\text{keV})]^2 \quad (2.7)$$

where E_0 and μ_0 are the initial electron energy and cosine of electron pitch angle with respect to the magnetic field, when the electron enters the collisional target.

2.1.2 Thermal Bremsstrahlung

One of the most prevalent emission mechanisms in the solar atmosphere is bremsstrahlung emission from Coulomb collisions between charged particles. The incident particle will emit “braking radiation” as it is deflected from its initial trajectory by the Coulomb field of a stationary target particle. The energy of the emitted photon ϵ is proportional to the difference in the incoming and outgoing energy E of the incident particle and to the impact parameter, b , the distance between the target particle and the trajectory of the incident particle.

The soft X-ray energy range ($\sim 1 - 10$ keV) is dominated by thermal free-free (bremsstrahlung) emission from Coulomb collisions between electrons in a Maxwellian particle distribution and an ambient ion distribution in hot (tens of MK) plasma, where $E_{\text{electron}} \approx E_{\text{ambient plasma}}$. For large values of b where the electron undergoes small deflections and emission is in the EUV and soft X-ray regime, it is adequate to consider only non-relativistic classical collisions. For emission at higher photon energies quantum mechanical corrections are required.

From Jackson (1962) and Kramers (1923) it can be shown that the power emitted by a single electron with velocity v interacting with an effectively stationary

ion of charge Z is

$$P = \frac{2}{3} \frac{e^2}{c^3} \left(\frac{dv}{dt} \right)^2 \quad \text{erg s}^{-1} \quad (2.8)$$

To calculate the total bremsstrahlung intensity we first define a differential cross-section for bremsstrahlung interaction which describes the rate of collisions. For X-ray energies it is possible to use the non-relativistic Bethe-Heitler cross-section σ_B which is a function of ϵ , the photon energy and E , the electron energy but integrates over all possible directions of the outgoing photon. For $\epsilon > E$, σ_B becomes zero, a necessary condition since we cannot attain a photon with energy greater than that of the incident electron. When the ratio of ϵ to E is high i.e. when $\epsilon \approx E$ this approximation will not hold as the cross-section is highly anisotropic.

$$\sigma_B(\epsilon, E) = \frac{8\alpha}{3} r_0^2 \frac{m_e c^2 \bar{Z}^2}{\epsilon E} \ln \frac{1 + (1 - \epsilon/E)^{1/2}}{1 - (1 - \epsilon/E)^{1/2}} \quad (2.9)$$

Here $\alpha = 2\pi e^2/hc$ is the fine structure constant and $r_0 = e^2/m_e c^2$ is the classical electron radius. Z is the atomic number of the stationary ion, giving \bar{Z}^2 to be the atomic number of scattering ions weighted by abundance. For the chromosphere this is roughly 1.8 (Fletcher et al. 2007). Now we can determine the total free-free intensity by integrating over a volume V with uniform electron density n_e and over all particles in a Maxwell-Boltzmann distribution $f_e(E)$ for a hot plasma with temperature T (typically tens of MK), Equations 2.10 and 2.13.

$$f_e(E) = \frac{2n_e}{\pi^{1/2} (k_B T)^{3/2}} E^{1/2} \exp(-E/k_B T) \quad \text{electrons cm}^{-3} \text{ erg}^{-1} \quad (2.10)$$

$$I(\epsilon) = n_e V \int_{\epsilon}^{\infty} f_e(E) v(E) \sigma_B(\epsilon, E) \quad (2.11)$$

$$= \left(\frac{8}{\pi m_e k_B T} \right)^{1/2} \kappa_{BH} \bar{Z}^2 (n_e^2 V) \frac{1}{\epsilon} \exp(-\epsilon/k_B T) g(\epsilon/k_B T) \quad (2.12)$$

$$\text{photons s}^{-1} \text{ erg}^{-1} \quad (2.13)$$

where $v(E) = \sqrt{E/m}$ and $g(\epsilon/k_B T)$ is the gaunt factor (see Tandberg-Hanssen & Emslie (1988)) a term which describes the difference between a classical and a quantum mechanical cross-section by taking into account maximum and minimum values for the impact parameter.

$$g(a) = \int_0^{\infty} \frac{e^{ax} dx}{[x(1-x)]^{1/2}} \quad (2.14)$$

Equation 2.13 also shows a proportional dependance on the total emission measure $EM = \int n_e^2 dV$. The emission measure can also be considered as a function of temperature and so it is common to see an expression for differential emission measure $EM(T) = n_e^2 dV/dT$, which gives a measure of the amount of emitting plasma at temperature T . From 2.13 we can see that the form of the bremsstrahlung spectrum is defined by $\frac{1}{\epsilon} \exp(-\epsilon/k_B T)$ i.e. for a high temperature plasma, a few tens of MK, the profile will be broad and conversely for a lower temperature plasma, at a few MK, the spectrum will drop off quicker.

From the optical through to X-ray energies free-free emission in the corona is optically thin. It should be noted that there is also a contribution to the thermal continuum from free-bound Coulomb interactions. Until recently it was thought that free-free emission was the dominant emission process, however Brown & Mallik (2008, 2009) show that free-bound emission can be important at low soft X-ray energies, especially for interactions with highly ionised species of iron. Further to the thermal continuum process there is also line emission from a number of highly ionised species such as iron, an example of such emission lines is the iron and nickel complex seen in RHESSI spectra at 6.7 keV and 8 keV. The line ratios of these two peaks in the RHESSI spectrum can be used for temperature diagnostics (Phillips 2004).

2.1.3 Non-Thermal Bremsstrahlung

In contrast to the bremsstrahlung emitted by thermal plasma at soft X-ray energies, the hard X-ray energy range ($\sim 10 - 100$ keV) is dominated by nonthermal bremsstrahlung emission where accelerated beams of electrons undergo Coulomb collisions with a ‘cool’ target of ambient plasma i.e. $E_{\text{beam}} \gg E_{\text{ambient plasma}}$. The photon flux $I(\epsilon)$ (photons $\text{s}^{-1} \text{cm}^{-2} \text{keV}^{-1}$) seen at earth due to the injection of a beam of accelerated electrons $F(E_0)$ (electrons $\text{s}^{-1} \text{cm}^{-2} \text{keV}^{-1}$) depends on whether the injected electron distribution is in a collisionally ‘thick’ or ‘thin’ target. For a thin target model the electrons are injected into a collisionless plasma where they undergo few collisions, leaving the injected distribution mostly unchanged. In the thick target model electrons precipitate or thermalise in a collisional plasma due to Coulomb collisions.

The thin target photon flux at Earth can be related to the injected electron spectrum by (Tandberg-Hanssen & Emslie 1988)

$$I(\epsilon) = \frac{S\Delta N}{4\pi R^2} \int_{\epsilon}^{\infty} F(E_0)\sigma_B(\epsilon, E)dE_0 \quad (2.15)$$

where $R = 1\text{AU}$ and $\Delta N = \int_{source} n(s)ds$ is the column density of the source. For a thin target ΔN will be less than the column depth required to completely stop an electron of energy E . n is the ambient target density which is a function of s , the distance along the path of the injected electron.

For a thick target we are required to replace $F(E_0)$ in 2.15 with an target-averaged electron distribution $F(E)$ which reflects the alteration of the injected distribution due to electron energy losses (Brown 1971). However, to understand how particles are accelerated in flares and other solar eruptive events it is essential to determine $F(E_0)$. We do this by relating $F(E)$ to $F(E_0)$ by firstly considering a single electron that undergoes energy loss by Coulomb collisions with ambient electrons in a thick target. Note here that the largest fraction of the incident electrons energy is lost through electron-electron interactions in comparison to only a small fraction of energy ($\sim 10^{-5}$) lost in electron-proton interactions. However it is the interaction with the ambient protons that cause the large-angle scattering which results in hard X-ray emission Benz (2002). This in turn constrains the energy content of the incident electron beam that is needed to match the observed hard X-ray flux. The rate of energy loss of the electron is given by

$$\frac{dE}{dt} = \sigma_E(E)nv(E)E \quad (2.16)$$

where σ_E is the cross section for energy loss and $v(E)$ is the electron velocity. The number of photons emitted per unit energy centred on ϵ from an electron with a starting energy of E_0 is then

$$m(\epsilon, E_0) = \int_{\epsilon}^{E_0} \frac{\sigma_B(\epsilon, E)}{E\sigma_E(E)}dE \quad (2.17)$$

From this we can integrate $m(\epsilon, E_0)$ over the entire electron injection distribution and over the flare area S to find

$$I(\epsilon) = \frac{S}{4\pi R^2} \int_{E_0=\epsilon}^{\infty} F(E_0) m(\epsilon, E_0) dE_0 \quad (2.18)$$

$$= \frac{S}{4\pi R^2} \int_{E_0=\epsilon}^{\infty} F(E_0) \int_{\epsilon}^{E_0} \frac{\sigma_B(\epsilon, E)}{E \sigma_E(E)} dE dE_0 \quad (2.19)$$

For Coulomb collisions the energy loss rate can be defined as

$$\frac{dE}{dt} = \left(\frac{-C}{E} \right) nv \quad (2.20)$$

and rearranging we find

$$\sigma_e(E) = \frac{C}{E^2} \quad (2.21)$$

where $C = 2\pi e^4 \ln \Lambda$. Combining 2.19 and 2.20 gives

$$I(\epsilon) = \frac{S}{4\pi R^2} \frac{1}{C} \int_{E_0}^{\infty} F(E_0) \int_{\epsilon}^{E_0} E \sigma_B(\epsilon, E) dE dE_0 \quad (2.22)$$

From Equations 2.15 and 2.22 we see that for the thin-target photon flux the bremsstrahlung cross section, $\sigma_B(\epsilon, E_0)$, is a function of the initial electron energy E_0 whereas for the thick-target photon flux the bremsstrahlung cross section, $\sigma_B(\epsilon, E)$ is weighted by the electron energy and takes into account energy losses experienced by the electrons.

From observations of the hard X-ray photon flux at Earth we can invert $I(\epsilon)$ in order to attain $F(E_0)$ (Kontar et al. 2004). An alternative to inversion is forward fitting. Here we assume a model injection spectrum. Hard X-ray observations show a power law trend and so an assumption is made that $F(E_0)$ is also in the form of a power law distribution

$$F(E_0) = A E_0^{-\delta} \quad (2.23)$$

which is characterised by A , a normalisation factor and δ , the injected electron spectral index. Following the working in Tandberg-Hanssen & Emslie (1988) it can be shown that a thin target photon flux will be

$$I(\epsilon) = a\epsilon^{-\gamma} \quad (2.24)$$

which is characterised by a , the photon flux normalisation factor and γ the hard X-ray photon flux where $\gamma = \delta + 1$. For the thick target

$$I(\epsilon) = a\epsilon^{-\gamma} \quad (2.25)$$

where $\gamma = \delta - 1$. For more details on forward fitting see the section on RHESSI spectroscopy, Section 1.4.1.

From these equations we can determine the total number of electrons present in the source above a cutoff energy E_c . For a thick target scenario

$$F(E > E_c) = \int_{E_c}^{\infty} F(E_0) dE \quad (2.26)$$

$$f_e(E) = 3.28 \times 10^{33} \frac{b(\gamma)}{\gamma} A E_c^{-\gamma} \quad (2.27)$$

$$b(\gamma) = \gamma^2 (\gamma - 1)^2 B\left(\gamma - \frac{1}{2}, \frac{3}{2}\right) \approx 0.27\gamma^3 \quad (2.28)$$

where $F(E_0)$ (electrons $\text{keV}^{-1} \text{s}^{-1}$) is the electron injection spectrum, E_c is the electron energy cutoff, B is the Beta function, and A is the photon flux at 1 keV determined by fitting a power law to the photon spectrum where $I(\epsilon_x) = A\epsilon_x^{-\gamma}$ (Brown 1971; Hudson et al. 1978).

Alternatively for a thin target model we define an instantaneous number of electrons above a cutoff energy E_c .

$$f_e(E) = 1.05 \times 10^{42} C(\gamma) A \frac{1}{n_0 E^{-(\gamma-1/2)}} \quad (2.29)$$

$$C(\gamma) = \frac{(\gamma - 1)}{B\left(\gamma - 1, \frac{1}{2}\right)} \approx (\gamma - 1.5)^{1.2} \quad (2.30)$$

where $F(E_0)$ (electrons keV^{-1}) is the thin target electron spectrum and n_0 is the target density.

2.2 Radio Emission

Radio emission from the Sun was first observed by an English radar station during World War II. It was soon discovered that the solar radio flux density S_ν ($\text{W m}^{-2} \text{ Hz}^{-1}$) is correlated with the solar activity. Radio wave propagation is governed by the local electron density which in turn defines a local plasma frequency, $\nu_p \approx 9000\sqrt{n_e}$. For an unmagnetised plasma the refractive index $n = \sqrt{1 - \frac{\nu_p^2}{\nu^2}}$. When $\nu = \nu_p$ the radiation is reflected and the source becomes optically thick. For a magnetised plasma the refractive index is different for x and o-mode wave propagation and cutoffs and resonances occur under specific conditions, see Appendix A for more details. A decreasing electron density with height results in higher frequency (GHz) radio observations being needed to probe the lower corona whilst lower frequency (MHz) observations map out the upper corona. A consequence of this is that the solar radio limb occurs at a greater height in the atmosphere than for optical or EUV observations.

In radio astronomy measurements are made of the source surface brightness or specific intensity I_ν ($\text{W m}^{-2} \text{ Hz}^{-1} \text{ Sr}^{-1}$), i.e. the flux density per solid angle $S_\nu = \int_\Omega I_\nu d\Omega$. For a blackbody the surface brightness is uniform and is dependent only on ν and T and is described by the Planck function

$$I_\nu = \frac{2h\nu^3}{c^2} \frac{1}{e^{h\nu/k_B T} - 1} \quad (2.31)$$

where k_B is Boltzmann's constant and h is the Planck constant. At long wavelengths where $h\nu \ll k_B T$ the Planck function can be simplified to give the Rayleigh Jeans approximation.

$$I_\nu = \frac{2k_B T \nu^2}{c^2} \quad (2.32)$$

We can therefore describe radio source with a spatially varying surface brightness as

$$\begin{aligned} S_\nu &= \int_\Omega I_\nu(\theta, \phi) d\Omega \\ &= \frac{2k_B \nu^2}{c^2} \int_\Omega T_b(\theta, \phi) d\Omega \end{aligned}$$

where T_b is the brightness temperature, the temperature of a blackbody with the same surface brightness as the observed source.

2.2.1 Radio Emission Mechanisms

Radio emission from the Sun can be characterised as (1) incoherent emission: continuum processes such as thermal bremsstrahlung, gyroresonance (cyclotron) emission and mildly relativistic gyrosynchrotron emission or (2) coherent emission: nonlinear plasma instabilities from unstable particle distributions which result in plasma emission, electron cyclotron maser and a number of radio bursts. The dominant emission mechanism depends on the observing frequency, local plasma properties and in particular the optical depth for each emission process. Details of solar radio emission mechanisms and the associated characteristic properties can be found in review articles such as Dulk (1985) and Bastian et al. (1998).

2.2.2 Radiative Transfer

To interpret radio observations it is important to understand the various emission and absorption processes and take into account radiative transfer effects as the emitted radiation propagates along the line of sight s . The energy emitted from a source surface dA at angle θ from the normal, in time dt , over frequency range $d\nu$ and over solid angle $d\Omega$ is shown in Equation 2.33.

$$dE_\nu = I_\nu dt dA \cos \theta d\nu d\Omega \quad (2.33)$$

From this the energy emitted from each volume element is a function of the line of sight s ($dV = dsdA$)

$$dE_\nu(s) = \epsilon_\nu(s) dt dV d\nu d\Omega \quad (2.34)$$

where $\epsilon_\nu(s)$ is the local emission coefficient for a volume element centred at s . Therefore the emitted intensity at each position s is simply

$$dI_{\nu,em}(s) = \epsilon_\nu(s) ds \quad (2.35)$$

As well as the emitted radiation from each volume element we must also determine the absorption from dV at position s along the line of sight.

$$dI_{\nu,abs}(s) = -\alpha_{\nu}(s)I_{\nu}(s)ds \quad (2.36)$$

Where α_{ν} is the absorption coefficient. The optical depth τ_{ν} at position s is defined as

$$d\tau_{\nu} = \alpha_{\nu}(s)ds \quad (2.37)$$

The combination of Equations 2.35 and 2.36 results in the equation of radiative transfer that can be applied along the line of sight.

$$\frac{dI_{\nu}(s)}{ds} = -\alpha_{\nu}(s)I_{\nu}(s) + \epsilon_{\nu}(s) \quad (2.38)$$

$$\epsilon_{\nu}(s) = \frac{2\alpha_{\nu}(s)k_B T \nu^2}{c^2} \quad (2.39)$$

Using 3.1 and assuming $T = \text{const}$, 2.39 gives the expression for Kirchoff's Law which relates the emission and absorption coefficients. We also define the ratio of the emission to the absorption coefficient to be the source function S_{ν} . Using Kirchoff's Law we can rewrite in terms of T_{eff} , the effective temperature, in the case that the plasma is not a blackbody.

$$S_{\nu} = \frac{\epsilon_{\nu}(s)}{\alpha_{\nu}(s)} \quad (2.40)$$

$$= \frac{2k_B T_{\text{eff}} \nu^2}{c^2} \quad (2.41)$$

For a Maxwellian distribution $T = T_{\text{eff}}$ regardless of the emission mechanism or observation frequency of polarisation mode. Inserting S_{ν} and τ into Equation 2.38 gives

$$\frac{dI_{\nu}(s)}{d\tau} = -I_{\nu}(s) + S_{\nu}(s) \quad (2.42)$$

We can then solve the radiative transfer equation by multiplying by an integration factor $e^{-\tau}$ and integrating with respect to τ to get a general solution.

$$I_\nu = e^{-\tau_\nu} I_{\nu_0} + S_\nu(1 - e^{-\tau_\nu}) \quad (2.43)$$

For an optically thick source where $\tau_\nu \gg 1$ we find

$$I_\nu = S_\nu \quad (2.44)$$

Conversely for an optically thin source where $\tau_\nu \ll 1$

$$I_\nu = I_{\nu_0} + \tau_\nu(S_\nu - I_{\nu_0}) \quad (2.45)$$

Alternatively if we express Equation 2.42 in terms of T_b and T_{eff} using Equations 3.1 and 2.41.

$$\frac{dT_b}{d\tau} = -T_b + T_{\text{eff}} \quad (2.46)$$

Equation 2.46 can be solved and for a source with constant T_{eff} , and we find (Dulk & Marsh 1982)

$$\begin{aligned} T_b &= T_{\text{eff}} \quad (\text{for } \tau_\nu \gg 1) \\ &= T_{\text{eff}}\tau_\nu \quad (\text{for } \tau_\nu \ll 1) \end{aligned}$$

It is important to note that the equations defined above for radiative transfer effects are only applicable in plasma with a low density such that the refraction index of the medium is close to 1. In a plasma where this condition does not hold Razin-Tsytovich suppression must be considered i.e. when $\nu < 20n/B$ (Ginzburg & Syrovatskii 1965).

2.2.3 Thermal Bremsstrahlung

An introduction to thermal bremsstrahlung emission at soft X-ray energies was discussed in a previous section on X-ray emission. For thermal bremsstrahlung emitted at radio frequencies a non-relativistic approach can be used. Figure 2.1 taken from (Gary & Hurford 1989) shows the form of the radio spectra for a homogenous source. The top row shows plots of T_b and the bottom shows S_ν .

Figure has been removed due to Copyright restrictions.

Figure 2.1: Plots of radio brightness temperature (top) and flux density (bottom) for thermal bremsstrahlung (left), thermal gyrosynchrotron (centre) and nonthermal gyrosynchrotron emission (right) from a homogeneous plasma, (Gary & Hurford 1989)

The vector arrows shown on the plot show how the peak of the spectrum is altered by increasing the labeled parameters by a factor of 2. Typical spectra for thermal bremsstrahlung emission are shown in the left plot. At radio frequencies thermal bremsstrahlung emission typically becomes optically thick for frequencies $\nu \lesssim 1 \text{ GHz}$. This can be seen clearly in the T_b spectrum where the profile flattens to a constant at lower frequencies to the left of the peak and $T_b = T_e$. The position of the turnover between optically thick and thin emission is dependent on temperature T and density n . The flux density spectrum shows $S_\nu \propto \nu^2$ for optically thick emission. This is due to $I_\nu \propto \nu^2$, see Equation 2.33.

Dulk (1985) gives a simplified expression for the absorption coefficient for thermal bremsstrahlung emission which assumes a fully ionised hydrogen-helium plasma.

$$\kappa_\nu \approx 0.2n_e^2 T^{-3/2} \nu^{-2} \quad (2.47)$$

The drop-off in T_b for optically thin emission $T_b \propto \nu^{-2}$ is due to a dependence of the brightness temperature on the absorption coefficient. In contrast the flux

density becomes constant for optically thin emission.

Discussion so far has ignored the effect of the magnetic field on the emitted bremsstrahlung emission. A magnetised plasma results in o-mode and x-mode wave propagation, Appendix A. The presence of a magnetic field changes the refractive index $n_\nu(B)$ and alters the propagation of the o-mode and x-mode by different amounts. A change in the absorption coefficient for each mode results in a difference in the T_b for each mode. A measure of this effect can be seen in the degree of circular polarisation r_c

$$r_c = \frac{(T_{b,x} - T_{b,o})}{(T_{b,x} + T_{b,o})} \quad (2.48)$$

When both modes are optically thick the polarisation tends to zero for a thermal plasma. For the case where both modes are optically thin the polarisation can be expressed in terms of the emission coefficient

$$r_c = \frac{(\eta_{\nu,x} - \eta_{\nu,o})}{(\eta_{\nu,x} + \eta_{\nu,o})} \quad (2.49)$$

and for bremsstrahlung emission the polarisation is in the x-mode. For more details concerning the polarisation see Dulk & Marsh (1982) and Dulk (1985). Care should be taken with regard to interpretations of polarisation, any change in parameters such as B , θ or T_{eff} along the line of sight will alter the polarisation. It is also important to note that polarisation is a function of brightness temperature and not flux density, as this is integrated over the source and will give an average weighted by T_b .

2.2.4 Gyroresonance Emission

In the corona where the $\beta < 1$ the electrons are “frozen-in” to the magnetic field. The Lorentz force, acting perpendicular to the directions of the magnetic field and the particle motion, causes the electrons to precess around the field in gyro orbits with a Larmor radius r_L and an electron gyrofrequency of $\nu_B/\gamma = eB/2\pi m_e c = 2.8B/\gamma$ MHz, where B is in units of Gauss. Gyroemission is produced as a result of this Lorentz acceleration.

For non-relativistic electron energies (i.e. low temperature Maxwellian distribution) where $\gamma \sim 1$ the emission produced is named gyroresonance or cyclotron emission. It occurs as “line” emission at the electron gyrofrequency ν_B and its

harmonics s where $s \lesssim 10$. Taking into account Doppler shifts this line emission is seen at frequencies

$$\nu = \frac{s\nu_B}{1 - \beta_{\parallel} \cos(\theta)} \quad (2.50)$$

separated by an interval ν_B and where θ is the angle between the line of sight and the magnetic field. Note here $\beta_{\parallel} = \frac{v_{\parallel}}{c}$. The power emitted at each harmonic is given by (Boyd & Sanderson 1969).

$$P_s = \frac{2e\omega_B^2}{c} \frac{(s+1)s^{2s+1}}{(2s+1)!} \beta_{\perp}^{2s} \quad (2.51)$$

Note $\omega_B = 2\pi\nu_B$. The power emitted at each harmonic is proportional to β_{\perp}^2 giving

$$\frac{P_{s+1}}{P_s} \sim \frac{v_{\perp}^2}{c^2} \quad (2.52)$$

so as we move to higher values of s the power decreases. The majority of gyroresonance emission is therefore emitted at the fundamental ($s = 1$). The intensity of observed gyroresonance emission is highly dependent on the observing angle θ . The power emitted per unit solid angle for emission over one harmonic is

$$\frac{dP}{d\Omega} \simeq \frac{e^2\omega_B^2\beta_{\perp}^2}{8\pi c} (1 + \cos(\theta)) \quad (2.53)$$

Thus for an observer at $\theta = 0$ the intensity is twice that for an observer at $\theta = \pi/2$.

So far we have considered the gyroresonance emission to be discrete “line” emission however in practise the emission line will have a finite line width, Lorentzian in shape, due to natural broadening. Collisional broadening (Lorentzian shape) and Doppler broadening (Gaussian shape) or a combination of both (Voigt profile) will also effect the line width. From the line width and shape it is possible to gather information on the electron-ion collision frequency (collisional broadening) or on the electron temperature (Doppler broadening).

Figure has been removed due to Copyright restrictions.

Figure 2.2: Gyrosynchrotron emission from mildly relativistic electrons, (Boyd & Sanderson 1969)

2.2.5 Synchrotron Emission

At highly relativistic energies where $\gamma \gg 1$ and $s > 100$ the emission mechanism is referred to as synchrotron emission. For this scenario the “line” emission is no longer separated by ω_B . Instead the line peaks are separated by $\omega_B(1 - \beta^2)^{1/2}$. At these energies the line width of each harmonic increases due to relativistic broadening. The power emitted is now expressed as a function of frequency.

$$\frac{dP}{d\omega} = \frac{\sqrt{3}e^2\omega_B}{2\pi c} \frac{\omega}{\omega_c} \int_{\omega/\omega_c}^{\infty} K_{5/3}(t) dt \quad (2.54)$$

where $\omega_c = \frac{3}{2}\omega_B\gamma^2$ and $K_{5/3}(t)$ is a modified Bessel function. For synchrotron emission it is no longer possible to distinguish individual harmonic peaks in the emission. An example is shown in Figure 2.2. At higher values of s the spectrum appears smooth and can be approximated by a power law.

2.2.6 Gyrosynchrotron Emission

At intermediate, mildly relativistic energies ($\gamma \approx 2$ or 3) radio emission is seen at harmonics $10 < s < 100$. At these energies there is a contribution from electrons in both thermal and nonthermal distributions. The definitions for emissivity

and absorption are complex. Ramaty (1969) approaches the problem by summing the contribution from each harmonic in the range of interest. The derived expressions are numerically complex. A number of authors have worked towards simplifying these definitions. Petrosian (1981) replaces the sum over harmonics with an integral. Other authors have provided semi-empirical approximations for gyrosynchrotron emission (Dulk & Marsh 1982). These approximations suffer from inaccuracies outside specific parameter regimes and only consider specific electron distributions. From Dulk & Marsh (1982) (and corrections detailed in Dulk (1985)) the authors chose to derive expressions for gyrosynchrotron emission in terms of the collective variables η_ν/BN and $\kappa_\nu B/N$ as $\eta_\nu \propto BN$ and $\kappa_\nu \propto N/B$. Hence we can rewrite T_{eff} as

$$T_{\text{eff}} = \frac{c^2}{k_B \nu^2} \frac{\eta_\nu}{\kappa_\nu} \quad (2.55)$$

$$= \frac{c^2}{k_B} \frac{(\eta_\nu/BN) B^2}{(\kappa_\nu B/N) \nu^2} \quad (2.56)$$

$$= 8.33 \times 10^{23} \frac{(\eta_\nu/BN)}{(\kappa_\nu B/N)} \left(\frac{\nu^2}{\nu_B} \right)^{-2} \quad (2.57)$$

The authors present expressions for the four variables mentioned above for electrons with a Maxwellian electron distribution and an isotropic pitch angle distribution. These expressions are valid for $s > 5$ and is found to be accurate to greater than 20% for $\nu/\nu_B > 5$, $\theta \gtrsim 10^\circ$ and $T \gtrsim 10^7$ K. However the expressions is long and complex and the reader is referred to the original paper for details.

The authors also present expressions for the case of nonthermal electrons. For the contribution from a nonthermal distribution we assume a powerlaw electron energy distribution and an isotropic pitch angle distribution. The electron energy distribution is

$$n(E) = K E^{-\delta} \quad (2.58)$$

where δ is the electron spectral index and K is a normalisation constant

$$K = (\delta - 1) E_0^{\delta-1} N \quad (2.59)$$

where N is the number of electrons per cubic centimeter with $E > E_0$, the low energy electron cutoff. E_0 is usually in the range $10 < E_0 < 100$ keV. Figure 2.3 shows plots of η_ν/BN , $\kappa_\nu B/N$, T_{eff} and r_c against ν/ν_B for the x-mode. These plots are for radiation produced by powerlaw electron distributions with varying spectral indices, δ .

Figure has been removed due to Copyright restrictions.

Figure 2.3: Plots of η_ν/BN , $\kappa_\nu B/N$, T_{eff} and r_c against ν/ν_B for the x-mode. These plots are for radiation produced by powerlaw electron distributions with varying spectral indices δ (Dulk & Marsh 1982).

From these plots it can be seen the trend above $\nu/\nu_B \gtrsim 10$ is roughly a power law. From this the following equations can be derived which hold in the range $2 \lesssim \delta \lesssim 7$, $\theta \gtrsim 20^\circ$ and $10 \lesssim \nu/\nu_B \lesssim 100$. Note that these expressions have been found to be better than 30% accurate. However for $\delta \gtrsim 6$ the accuracy decreases in particular for large values of θ and ν/ν_B .

$$\frac{\eta_\nu}{BN} \approx 3.3 \times 10^{-24} 10^{-0.52\delta} (\sin \theta)^{-0.43+0.65\delta} \left(\frac{\nu}{\nu_B} \right)^{1.22-0.90\delta} \quad (2.60)$$

$$\frac{\kappa_\nu B}{N} \approx 1.4 \times 10^{-9} 10^{-0.22\delta} (\sin \theta)^{-0.09+0.72\delta} \left(\frac{\nu}{\nu_B} \right)^{-1.30-0.98\delta} \quad (2.61)$$

$$T_{\text{eff}} \approx 2.2 \times 10^9 10^{-0.31\delta} (\sin \theta)^{-0.36-0.06\delta} \left(\frac{\nu}{\nu_B} \right)^{0.50+0.085\delta} \quad (2.62)$$

$$r_c \approx 1.26 10^{0.035\delta} 10^{-0.071 \cos \theta} \left(\frac{\nu}{\nu_B} \right)^{-0.782+0.545 \cos \theta} \quad (\tau_\nu \ll 1) \quad (2.63)$$

$$\nu_{\text{peak}} \approx 2.72 \times 10^3 10^{0.27\delta} (\sin \theta)^{0.41+0.03\delta} (NL)^{0.32-0.03\delta} B^{0.68+0.03\delta} \quad (2.64)$$

Of particular use is the expression for ν_{peak} which can be used to estimate a magnetic field strength for the observed source. Note however Razin suppression effects can alter the frequency of the peak.

2.3 Petrosian-Klein Approximation

As mentioned previously work has been carried out to simplify the expressions presented in (Ramaty 1969). Here we give details of the Petrosian-Klein approximation which will be used for modeling gyrosynchrotron flare radiation in Chapter 5.

In a cold, collisionless magnetoactive plasma wave propagation is possible for the ordinary (o) and extraordinary (x) modes. The refractive indices and polarisation coefficients are given as (Ginzburg & Syrovatskii 1964; Ramaty 1969)

$$n_{\pm}^2(\theta) = 1 + \frac{2\nu_p^2(\nu_p^2 - \nu^2)}{\pm[\nu^4\nu_B^4 \sin^4 \theta + 4\nu^2\nu_B^2(\nu_p^2 - \nu^2)^2 \cos^2 \theta]^{1/2} - 2\nu^2(\nu_p^2 - \nu^2) - \nu^2\nu_B^2 \sin^2 \theta} \quad (2.65)$$

$$a_{\theta\pm}(\nu, \theta) = -\frac{2\nu(\nu_p^2 - \nu^2) \cos \theta}{-\nu^2\nu_B \sin^2 \theta} \pm [\nu^4\nu_B^2 \sin^4 \theta + 4\nu^2(\nu_p^2 - \nu^2)^2 \cos^2 \theta]^{1/2} \quad (2.66)$$

$$a_{k\pm}(\nu, \theta) = -\frac{\nu_p^2\nu_B\nu \sin \theta - a_{\theta\pm}\nu_p^2\nu_B^2 \cos \theta \sin \theta}{\nu_p^2(\nu_B^2 \cos^2 \theta - \nu^2) - \nu^2(\nu_B^2 - \nu^2)} \quad (2.67)$$

where ν_p is the plasma frequency, ν_B is the electron gyrofrequency and + and - correspond to the o-mode and x-mode respectively. θ is the angle between

the wave vector \mathbf{k} and the magnetic field \mathbf{B} . The polarisation coefficients can be written in terms of \mathbf{E}

$$ia_\theta = E_\theta/E_x \quad (2.68)$$

$$ia_k = E_k/E_x \quad (2.69)$$

where E_x and E_θ are the transverse electric field vectors, with E_θ in the plane of \mathbf{B} and \mathbf{k} . E_k is the longitudinal component of \mathbf{E} in the direction of the wave vector \mathbf{k} . The emitted radiation as a result of the longitudinal oscillations is negligible and unless coupled with the transverse waves the energy will not be seen to escape the source. We can therefore set $a_k = 0$.

For a single electron performing gyro-orbits in a magnetised plasma then the emissivity η_\pm (ergs s⁻¹ sterad⁻¹ Hz⁻¹) of the electron per unit frequency $d\nu$ and solid angle $d\Omega$ is (Trulsen & Fejer 1970; Klein & Trotter 1984)

$$\begin{aligned} \eta_\pm(\nu, \theta, \gamma, \phi) &= \frac{2\pi e^2}{c} \nu^2 \frac{n_\pm}{1 + a_{\theta\pm}^2} \\ &\times \sum_{s=-\infty}^{\infty} \left[-\beta \sin \phi J'_s(x_s) \right. \\ &\quad \left. + a_{\theta\pm} \frac{\cos \theta - n_\pm \beta \cos \phi}{n_\pm \sin \theta} J_s(x_s) \right]^2 \delta[f(\nu)] \end{aligned} \quad (2.70)$$

where

$$x_s = \gamma\nu/\nu_B n_\pm \beta \sin \phi \sin \theta \quad (2.71)$$

and

$$f(\nu) = (1 - n_\pm \beta \cos \phi \cos \theta)\nu - s\nu_B/\gamma \quad (2.72)$$

Here ϕ is the electron pitch angle, γ is the lorentz factor where $\gamma = (1-\beta^2)^{-1/2}$, J_s is a Bessel function of order s and δ is the Dirac function. For frequencies that this expression is intended i.e. $\nu > \nu_p$ and $\nu > (\nu_p^2 + \frac{1}{4}\nu_B^2)^{1/2} + \frac{1}{2}\nu_B$ the value

of s is always positive and represents the Doppler effect. To obtain the volume emissivity $j_{\pm}(\nu, \theta)$ and absorption coefficient $K_{\pm}(\nu, \theta)$ from a population of mildly relativistic electrons, with momentum $f(p)d^3p$ centred on p , in a unit volume, we use expressions from Befki (1966); Melrose (1968) and Ramaty (1969).

$$j_{\pm}(\nu, \theta) = \int \eta_{\pm}(\nu, \theta, \gamma, \phi) f(p') d^3p' \quad (2.73)$$

$$K_{\pm}(\nu, \theta) = (c^2/nv^2) \int \eta_{\pm}(\nu, \theta, \gamma, \phi) \frac{1}{h\nu} [f(p) - f(p')] d^3p' \quad (2.74)$$

Here the electron momentum changes from p' to p as it emits a photon of energy $h\nu$. For a volume V with N electrons the electron distribution can be written as

$$f(p) = \frac{N}{V} \frac{1}{p^2} \frac{d\gamma}{dp} u(\gamma) g(\phi) \quad (2.75)$$

where $f(p)$ can be represented by electrons with an energy distribution $u(\gamma)$ and a pitch angle distribution $g(\phi)$. Following the working in Ramaty (1969) the total emissivity and absorption coefficient for o and x-mode waves from a source of radio emitting electrons are

$$j_{\pm}(\nu, \theta) = \frac{BN}{V} \frac{e^2}{mc^2} G_{\pm}\left(\frac{\nu}{\nu_B}, \theta\right) \quad (2.76)$$

$$K_{\pm}(\nu, \theta) = \frac{N}{BV} (2\pi)^2 e H_{\pm}\left(\frac{\nu}{\nu_B}, \theta\right) \quad (2.77)$$

Formulae for G_{\pm} and H_{\pm} can be found in Ramaty (1969) Equations 17-21 and corrections in Trulsen & Fejer (1970). The approach taken by Ramaty (1969) sums the contribution from each harmonic over the frequency range of interest. This approach is numerically time consuming over a harmonic number of around 10. As we move to higher frequencies the peaks for each harmonic move closer together. Petrosian (1981) presents a simplification to the expressions present in Ramaty (1969) which can be applied to frequencies at which the emitted radiation is optically thin, i.e. at $\nu > \nu_B$ such that $\nu/\nu_B \gg 1$. To do this Petrosian (1981) replaces the summation over harmonics with an integral.

$$\begin{bmatrix} G \\ H \end{bmatrix} = 2\pi n \int_1^\infty d\gamma \int_{-1}^1 d\mu \gamma u(\gamma) g(\mu) \Phi_s^2 \begin{bmatrix} \left[\frac{\nu}{\nu_B} \right]^2 \\ \frac{k}{n^2} H \end{bmatrix} \quad (2.78)$$

$$\Phi_s = \frac{-\beta(1-\mu^2)^{1/2}}{(1+a_\theta^2)^{1/2}} J'_s(Sx) + \frac{a_\theta}{(1+a_\theta^2)^{1/2}} \frac{\cos\theta - n\beta\mu}{n \sin\theta} J_s(Sx) \quad (2.79)$$

$$S = \gamma \frac{\nu}{\nu_B} (1 - n\beta\mu \cos\theta) \quad (2.80)$$

$$x = \frac{n\beta(1-\mu^2)^{1/2} \sin\theta}{1 - n\beta\mu \cos\theta} \quad (2.81)$$

$$\kappa = \frac{\beta\gamma^2}{u(\gamma)} \frac{d}{d\gamma} \frac{u(\gamma)}{\beta\gamma^2} + \frac{\beta n \cos\theta - \mu}{\beta^2\gamma} \frac{1}{g(\mu)} \frac{dg(\mu)}{d\mu} \quad (2.82)$$

The full working can be found in Petrosian (1981) (the equations below follow the layout in Klein (1987)). For the case of mildly relativistic electrons the Bessel function $J_s(Sx)$ and $J'_s(Sx)$ are approximated by Wild & Hill (1971)

$$J_s(Sx) = \frac{1}{\sqrt{2\pi S}} \frac{Z^s}{a(S, x)} \quad (2.83)$$

$$J'_s(Sx) = F(S, x) \frac{J_s(Sx)}{x} \quad (2.84)$$

where

$$Z = \frac{x \exp[(1-x^2)^{1/2}]}{1 + (1-x^2)^{1/2}} \quad (2.85)$$

$$a(S, x) = \left[[1-x^2]^{3/2} + \frac{A}{S} \right]^{1/6}, \quad A = 0.503297 \quad (2.86)$$

$$b(S, x) = \left[[1-x^2]^{3/2} + \frac{B}{S} \right]^{1/6} \left[1 - \frac{1}{5S^{2/3}} \right], \quad B = 1.193000 \quad (2.87)$$

$$F(S, x) = a(S, x)b(S, x) \quad (2.88)$$

To perform the integration over the pitch angle distribution Petrosian (1981) uses the method of steepest decent. Equations for G_{\pm} and H_{\pm} can be written as

$$\begin{bmatrix} G \\ H \end{bmatrix} = \frac{1}{n \sin^2 \theta} \frac{\nu}{\nu_B} \int_1^{\infty} d\gamma u(\gamma) g(\mu_0) Y_0^2 Z_0^{2S_0} \left[-\frac{2\pi}{h''(\mu_0)} \right]^{1/2} \begin{bmatrix} 1 \\ \left[\frac{\nu_B}{\nu} \right]^2 \frac{\kappa_0}{n} \end{bmatrix} \quad (2.89)$$

where

$$Y_0 = \frac{-(1 - n\beta\mu_0 \cos \theta)F(S_0, x_0) + a_{\theta}(\cos \theta - n\beta\mu_0)}{[1 - n\beta\mu_0 \cos \theta]^{1/2} a[S_0, x_0][1 + a_{\theta}^2]^{1/2}} \quad (2.90)$$

is a slowly varying component with respect to μ the cosine of pitch angle. On the contrary the rapidly varying $Z_0^{2S_0}$ component quickly becomes 0 as we move away from the maximum value of μ and thus dominates the equations for G_{\pm} and H_{\pm} . Parameters marked with a subscript 0 represent the value that parameter has when $h(\mu)$ is at it's maximum value.

$$h(\mu) = \ln(g(\mu)Z^{2S}) \quad (2.91)$$

Petrosian (1981) also used this method to perform the integration over the energy distribution. However we continue here to follow the layout of Klein (1987). At this point Klein (1987) expands on the work in Petrosian (1981) to include the effects of the medium through which the emitted radiation passes to give

$$\begin{aligned} \begin{bmatrix} G \\ H \end{bmatrix} &= \left[\frac{\pi\nu}{\nu_B} \right]^{1/2} \int_1^{\infty} d\gamma \frac{[-F(S_0, x_0)(1 + \tau^2) + a_{\theta} \cos \theta]^2}{n \sin^2 \theta (1 + a_{\theta}^2) a^2(S_0, x_0)} \\ &\times \frac{u(\gamma)g(\mu_0)Z_0^{2S_0}}{\gamma^{1/2}\epsilon^3[1 + \tau^2]^{1/4}} \begin{bmatrix} 1 \\ \left[\frac{\nu_B}{\nu} \right]^2 \frac{\kappa_0}{n} \end{bmatrix} \end{aligned} \quad (2.92)$$

where

$$\frac{\mu_0}{n\beta \cos \theta} = 1 - \frac{1 - \mu_0^2}{(1 - x_0^2)^{1/2}} \left[\ln Z(\mu_0) - \frac{\nu_B}{2\gamma\nu n\beta \cos \theta} \frac{d}{d\mu} \ln g(\mu_0) \right] \quad (2.93)$$

and

$$\epsilon = (1 - n^2\beta^2)^{-1/2} \quad (2.94)$$

$$\tau = \epsilon\beta n \sin \theta \quad (2.95)$$

It is important to note that since $a_{\theta+} = \infty$ for $\theta = \pi/2$ and hence $Y_0 = 0$ for a maximum value of component Z^{2S} then this simplification cannot be used for values of θ around $\pi/2$ when considering o-mode propagation.

When considering the propagation of wave modes through an ionised plasma, the medium can have the effect of suppressing the emission. Razin suppression can effect the emissivity at low frequencies and is characterised by the parameter a .

$$a = \frac{3}{2}\nu_B/\nu_p \quad (2.96)$$

The emission will be suppressed if $a\gamma < 1$, where γ is the Lorentz factor of the emitting electron. If $a\gamma > 1$ the emission is unaffected, (Ramaty 1968)

Figure 2.4, taken from Klein (1987), shows a comparison of results produced by Ramaty (solid) and Petrosian (crosses) expressions for viewing angles of (left to right) 80° , 45° and 10° for o-mode (top row) and x-mode (bottom row). These were made assuming an isotropic electron distribution with $\delta = 3$ above 100 keV. The calculations were made using cold plasma refractive indices and polarisation coefficients and for a tenuous source where Razin suppression dominates at low frequencies ($a = 3.0$).

From these plots we can see that the Petrosian-Klein method provides a good approximation for calculating gyrosynchrotron emission above the 3rd or 4th harmonic for intermediate viewing angles. But the approximation is less good for small viewing angles in the presence of a medium. And as mentioned before this method is unable to calculate o-mode emission for a viewing angle of $\pi/2$.

Figure has been removed due to Copyright restrictions.

Figure 2.4: Plots show a comparison of results produced by Ramaty (solid) and Pertosian-Klein (crosses) expressions for viewing angles of (left to right) 80° , 45° and 10° for o-mode (top row) and x-mode (bottom row).(Klein 1987).

2.3.1 Solar Plasma Emission

Figure 2.5 shows the typical structures of the phenomena known as radio bursts that appear in solar spectrograms at radio frequencies. The different features in the spectrogram are thought to be produced by difference processes. Historically the bursts were named as Type I, Type II and so on to distinguish their different characteristics.

In the solar corona where the plasma can be considered to be quasi-collisionless, beams of accelerated particles are permitted to stream along field lines either down towards the chromosphere or out along “open” field lines into interplanetary space. Fast electrons stream ahead of slower moving electrons causing a bump-in-tail in the velocity distribution. If we consider the velocity distribution parallel to the magnetic field then $\partial f / \partial v_{\parallel} > 0$. This leads to an instability producing longitudinal Langmuir waves which undergo nonlinear wave-particle interactions and resulting in electromagnetic radiation at the local plasma frequency or its harmonics (Melrose 1986). These bursts occur in the radio regime. As the local plasma frequency is dependent on the local plasma density, emission at radio frequencies requires a density of $\sim 10^8 - 10^{10} \text{ cm}^{-3}$, plasma emission is a diagnostic

of the density and hence gives an estimate of height at which the burst is being produced. In the case of an outward propagating, mildly relativistic beam of electrons the density and hence the local plasma frequency quickly decreases. Observations of plasma emission, or Type III radio bursts, can therefore be seen in radio spectrograms as bright bursts which rapidly decay in frequency see Figure 2.5.

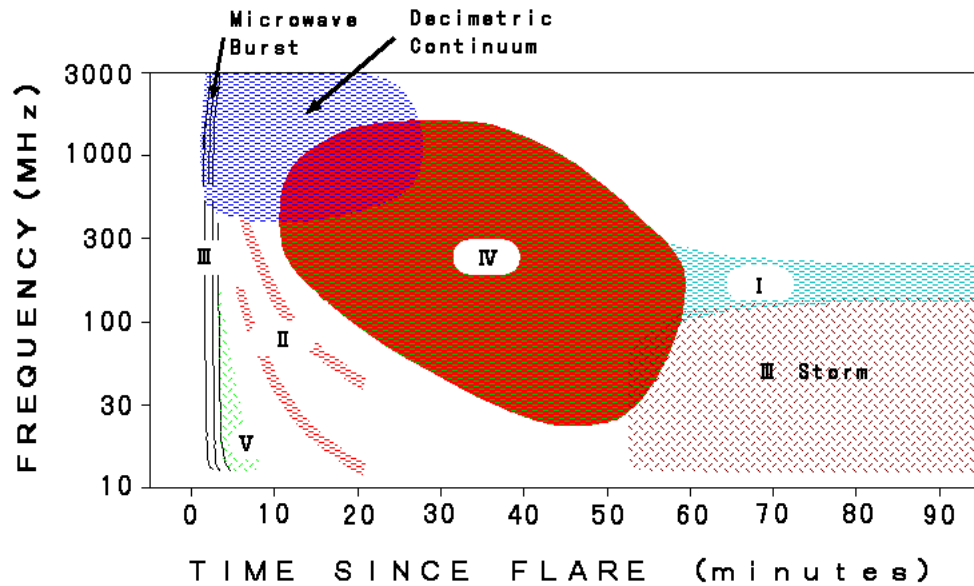


Figure 2.5: Classification of radio bursts (credit HIRAS Solar Observatory).

Downward propagating beams will in turn produce reverse slope (RS) bursts and beams trapped in closed loops will produce Type J and Type U bursts. U and J type bursts represent beams which travel initially in one direction, are mirrored and then propagate in the opposite direction, hence giving a U or J shape to the burst frequency versus time.

In addition there are a number of other radio bursts: Type I, thought to be produced by Langmuir wave interaction with low frequency waves; Type II, produced by Fermi acceleration leading to beams of particles streaming out of shock fronts; moving Type IV caused by trapped electrons in a moving magnetic structure such as a plasmoid; flare continuum Type IV due to electrons trapped in large coronal loops; and Type V bursts which are seen to follow Type III bursts and are thought to be caused by the same Type III producing electrons (Dulk 1985). More details of solar radio bursts can be found in the review paper Dulk

(1985) and references therein.

Chapter 3

Hard X-ray Emission From a Flare-Related Jet

3.1 Introduction to solar jets

Solar X-ray jets (transient bursts of collimated flows of plasma) were first observed by the Yohkoh Solar X-ray Telescope (SXT: Tsuneta et al. 1991) (Shibata et al. 1992; Strong et al. 1992). It has been shown that jets are spatially correlated with active regions, X-ray bright points and regions of emerging flux and can be associated with small footpoint flares (Shibata et al. 1992, 1994). Several studies of X-ray jets (Shimojo et al. 1996; Canfield et al. 1996) yielded characteristic properties such as length and width observed to be in the range of a few 10^4 – 10^5 km and 5×10^3 – 10^5 km respectively. Apparent jet velocities of 10–1000 km s⁻¹ (average ~ 200 km s⁻¹) are observed and the kinetic energy of the jet is thought to be 10^{25} – 10^{28} ergs. Shimojo & Shibata (2000) analysed a number of jets and their footpoint flares finding values for jet temperature and density of 3–8 MK (average 5.6 MK) and 0.7 – 4.0×10^9 cm⁻³ (average 1.7×10^9 cm⁻³) respectively. More recently observations of solar X-ray jets have been made using data from the Hinode X-ray Telescope (XRT: Golub et al. 2007) (Shimojo et al. 2007; Chifor et al. 2008; Savcheva et al. 2007). The results are generally consistent with the previous studies however XRT's improved spatial and temporal resolution has revealed many smaller X-ray jet events.

It has been observed that in general there are two kinds of jet; 1) the anemone-shaped jet, consistent with emerging photospheric field interacting with pre-existing coronal field which is vertical or oblique, 2) the two-sided-loop type where the interaction occurs with overlying horizontal coronal magnetic field (Shimojo et al. 1996). Observational properties such as the jet velocity are an important

Figure has been removed due to Copyright restrictions.

Figure 3.1: Cartoon showing the magnetic reconnection jet model (Shimojo & Shibata 2000) adapted from the Heyvaerts et al. (1977) cartoon.

diagnostic of the jet acceleration mechanism. Several jet models have been suggested, most models at some stage invoke magnetic reconnection as the source of a rapid injection of energy. The magnetic reconnection jet model (Heyvaerts et al. 1977; Shimojo et al. 1996; Shimojo & Shibata 2000) describes a bundle of emerging photospheric field reconnecting with a pre-existing overlying coronal magnetic field, see Figure 3.1. As the result of the reconnection, surrounding plasma is heated to X-ray emitting temperatures and subsequently ejected out along the direction of the reconnected field. Plasma propagating downwards forms X-ray emitting loops at the foot of the jet. Observations have shown that $H\alpha$ surges are often associated with X-ray jets (Canfield et al. 1996). In the reconnection model this is as a result of a ‘magnetic sling-shot’ effect caused by magnetic tension as the previously highly stressed emerging field straightens out. This results in the ejection of cool plasma (10,000 K) that had been supported by the field. Magnetohydrodynamic simulations of this scenario describe the observations well (Yokoyama & Shibata 1995; Nishizuka et al. 2008; Moreno-Insertis et al. 2008). Ejected jet material accelerated by the $\underline{J} \times \underline{B}$ force will have a velocity of the order of the Alfvén speed.

There have been observations of jets with a helical twisted shape. The ‘mag-

netic twist' model explains this as the result of reconnection between twisted and untwisted magnetic field (Shibata & Uchida 1986; Shibata et al. 1992; Alexander & Fletcher 1999). The ejected material is accelerated by the $\underline{J} \times \underline{B}$ force as the twisted magnetic field relaxes. As with the magnetic reconnection model, the ejected material will have a velocity of the order of the Alfvén speed. Magnetic islands of cool plasma form within the twisted field, described by the 'melon-seed' model for spicules (Uchida 1969), which propagate out as the field relaxes. This also occurs at the Alfvén speed. A paper by Pariat et al. (2009) an MHD simulation describes the interaction between a vertical dipole and open coronal field. The reconnection occurs between two flux systems which are separated by a separatrix surface. The footpoints of the inner flux system are slowly rotated at the photospheric boundary adding twist to the closed field lines which slowly increases the energy stored in the system. Eventually the system becomes unstable and a kink-like instability triggers reconnection with the open field. As twist, previously stored in the closed field lines, propagates along the newly reconnection field lines a large fraction of the free energy is released in the form of a nonlinear torsional Alfvén wave. The pressure gradient of the Alfvén wave accelerates the plasma along the open field lines as the wave propagates outwards. The wave also compresses the plasma causing an increase in density and temperature. We note that the jet described here could be compared with jets observed in EUV, where the bright jet emission is the result of a density enhancement. However in addition to this there is also hot plasma ejected as the direct result of the reconnection (Moreno-Insertis et al. 2008).

Other models suggest that the acceleration mechanism is related to gas pressure. Evaporation flows occur as the result of a rapid release of energy in the corona. In this situation the jet velocity will be of the order of the sound speed (Shibata et al. 1992; Sterling et al. 1993). Figure 3.1 shows that there is an evaporation jet associated with the magnetic reconnection model which is separate to plasma heated directly from the reconnection.

Type III radio bursts, caused by unstable beams of accelerated electrons, are often associated with jets. Electrons accelerated in association with jets have been detected in space (Christe et al. 2008). Another diagnostic of fast electrons is bremsstrahlung X-ray emission which can be observed with RHESSI. However until now no evidence of hard X-ray emission has been observed directly from the jet in the corona. This could be because it is rare to find a coronal jet dense enough to provide a bremsstrahlung target for the electrons, or hot enough

to generate high energy thermal emission. In this Chapter we report what we believe to be the first observation of hard X-ray emission formed in a coronal jet. We observe a flare-related jet which occurred on the 22nd August 2002. Observations from TRACE and RHESSI satellite missions are presented. The event was also observed by the ground-based Nobeyama Radioheliograph and Polarimeters. Together these observations cover the X-ray, extreme ultraviolet (EUV) and radio regimes.

3.2 Event overview

The jet occurred on the 22nd of August 2002 preceding a GOES M5.4 class flare. Time profiles from GOES, RHESSI, TRACE and NoRH can be seen in Fig. 3.2. Vertical dashed lines represent 32s time intervals used for RHESSI imaging (see Fig. 3.6 later). At 01:40 GOES, RHESSI and NoRH 17 GHz show an increase in the signal above background levels. This is due to a small source slightly north of the jet region, centred at $(825'', -225'')$ which does not appear to be related to the jet. The evolution of the event can be followed best using high resolution TRACE observations (see Fig. 3.3), only available for the 195\AA passband during the event. These images have a time resolution of $\sim 9\text{s}$ and a spatial resolution of $1''$. Dark black areas show regions of saturation. This is particularly noticeable later in the event when the hot loops form. The high contrast is to allow faint features to be visible. Under normal active region conditions this wavelength is dominated by FeXII line emission at $1.4 \times 10^6\text{ K}$. During flares it will be dominated by higher temperature plasma, providing both FeXXIV and CaXVII line emissions ($5 \times 10^6\text{ K}$ and $(1-2) \times 10^7\text{ K}$) and a significant thermal continuum due to free-free and free-bound emission, which is in fact dominant at temperatures of around 10^7 K (Feldman et al. 1999). The images were exposure normalised using the Solarsoft routine `trace_prep`. Cosmic ray spikes were also removed using this routine.

Preflare activity can be seen in the region as early as $\sim 01:25$ (Fig. 3.3a). From $\sim 01:27$ a complex system of twisted loops begin to brighten (Fig. 3.3b–f) and appears to rise. At 01:35 part of this system becomes twisted in a configuration similar to that found in models of the kink instability (Török & Kliem 2005). This can be seen best a few minutes later when it is at its brightest in Fig. 3.3e (see arrow). Although faint, this feature is present right up until the main ejection. To the north-west, at the right foot of the twisted field $(820'', -270'')$,

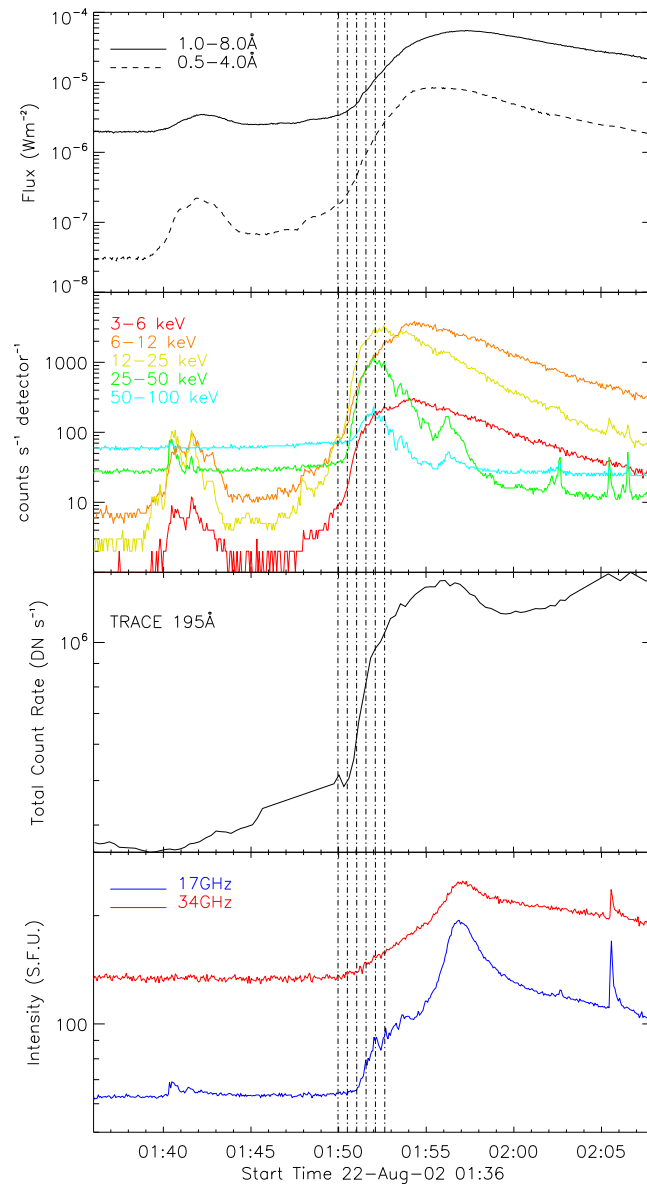


Figure 3.2: From top to bottom: GOES, RHESSI, TRACE and NoRH lightcurves. Vertical dashed lines represent 32s time intervals used for RHESSI imaging (see Figure 3.6). (See electronic version for colour plots)

faint material starts to move outward, starting at 01:31, along a separate large scale loop or possibly even open interplanetary field. This is seen at its brightest in Fig. 3.3d (see arrow). Small amounts of faint material continue to move in this direction for several minutes before the main ejection, becoming more obvious at 01:42 (see Fig. 3.3e and f). Unfortunately a gap in the TRACE data between 01:45:49 and 01:49:44 prevents us following this material with TRACE. For the purpose of understanding this complex event, we label pre-jet activity, including

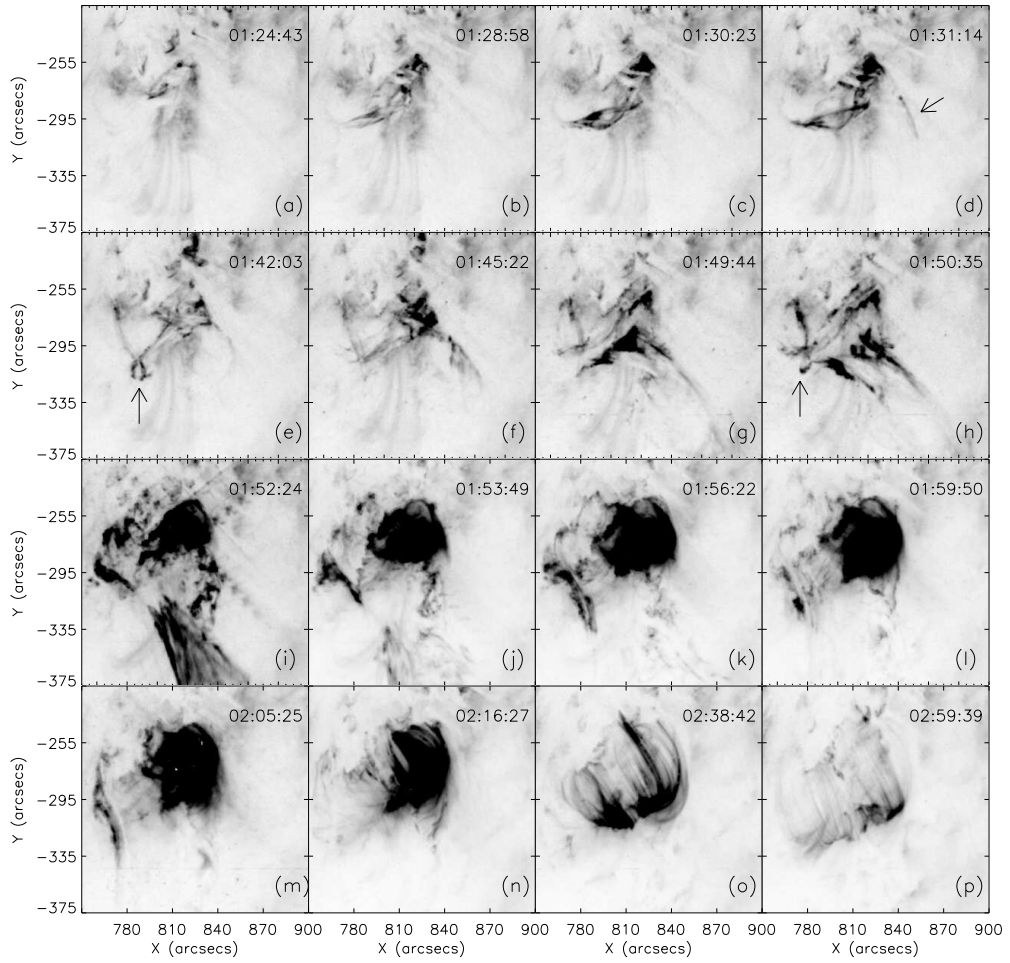


Figure 3.3: TRACE 195Å images for selected times throughout the event showing the evolution of the jet. These images have a time resolution of ~ 9 s and a spatial resolution of $1''$.

the ejection missed by TRACE up to 01:49:44, as “pre-gap”.

During the data gap increased amounts of material are ejected. This can be seen, in images immediately after the data gap, as plasma at greater heights in the corona (Fig. 3.3g and h). Also from the images immediately after the data gap (Fig. 3.3g and h) we can see that the rising twisted loops appear to have opened to the right of the kink feature, which is still visible (see arrow in Fig. 3.3h). This results in a large amount of plasma being ejected, beginning at $\sim 01:50:35$. The feature to the left of the jet can then be seen to straighten out. The ejected material appears to untwist slightly as the twist from the emerging field is transferred to the “open” field lines of the jet as a result of reconnection. The material then passes out of the TRACE field of view after $\sim 01:52$.

Material continues to be ejected until $\sim 02:09$ (Fig. 3.3g–m). The total du-

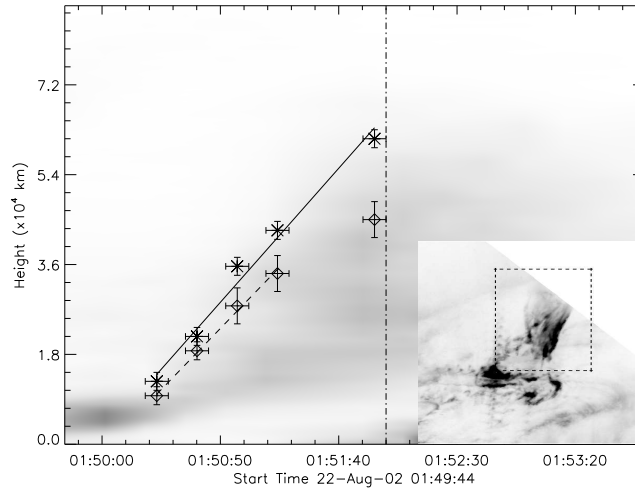


Figure 3.4: Velocity timeslice showing jet intensity as a function of height and time. Vertical dash-dot line shows the time at which the jet emission passes out of the TRACE field of view. Dashed lines on insert image show the region used for the analysis. Asterisks and solid line shows a fit to the faint front edge of the jet at the 5% level. Diamonds and dashed line shows a fit to points determined from tracking a brightly emitting source of plasma by eye.

ration of jetting material is therefore around 40 minutes. Hot loops can be seen forming between EUV ribbons, roughly ($820''$, $-260''$), as early as $\sim 01:51:30$. These loops brighten, expand and then fade away over the course of an hour (Fig. 3.3n-p). Activity from 01:49:44 onwards, including the main ejection, is labelled “post-gap”. In this Chapter we concentrate on the impulsive and rise phase of the event i.e. post-gap times when the main ejection of material occurs.

Due to the jet extending beyond the TRACE field of view we were unable to determine its full length. However an estimate of jet width was found to be $(2.32 \pm 0.2) \times 10^4$ km. This was determined by eye and assigned an error of ± 5 pixels. To calculate the apparent velocity of the jet during the main ejection a timeslice image was created using post-gap images (Fig. 3.4). These images were rotated such that the ejected material moves in a vertical direction. A subregion, through which the ejected material moves, was then chosen, shown by dashed lines on the inserted TRACE image in Fig. 3.4. Note that the TRACE insert is cut off at the top right corner due to the edge of the TRACE field of view. For each image, intensity was summed over rows to give a 1D array of intensity as a function of height. These were then combined to make Fig. 3.4, showing how the jet intensity varies in height as a function of time. The faint front edge of the jet was determined to be at the 5% level of the maximum timeslice

intensity (asterisks). By fitting these points we obtain an apparent jet velocity of $540 \pm 45 \text{ km s}^{-1}$ (solid line Fig. 3.4). It should be noted that this is the apparent jet velocity, there will be some degree of uncertainty due to the material following a curved trajectory and also due to the overall projection effects. However this method provides a ball-park figure which is consistent with previous jet studies and is on the order of the Alfvén velocity in the corona in accordance with a jet accelerated by the magnetic $\underline{J} \times \underline{B}$ force. To further check this value a source of brightly emitting plasma was followed by eye throughout the main ejection (diamonds). Fitting points 1 to 4 we obtain a value of $493 \pm 96 \text{ km s}^{-1}$ (dashed line Fig. 3.4). Here the 5th point has not been included in the fit as at the time of the image the material appeared to follow field that curved away from the vertical and our technique thus underestimates the distance travelled.

3.3 Hard X-ray Observations

3.3.1 RHESSI Imaging

Unlike for most large flares the RHESSI data for this period was not interrupted by movements of the spacecrafts attenuators. Note the RHESSI thin attenuator (A1) is in place throughout the entire event. A series of 32s RHESSI images (times shown as vertical dashed lines in Fig. 3.2) were reconstructed using detectors 3 to 9 providing a spatial resolution of $\sim 7''$. Energy bins of 6–12 keV, 12–20 keV, 20–30 keV and 30–50 keV were used. It is hoped that by using these energy bands it will be possible to distinguish sources of thermal and nonthermal emission. A more detailed RHESSI lightcurve is shown in Fig. 3.5. Here the lightcurve is split into 10 logarithmic energy bins between 3 keV and 100 keV. Looking at the trend of the lightcurve in each energy band we can see that the emission above $\sim 17 \text{ keV}$ follows a very similar profile to that of higher energies suggesting that the emission is nonthermal in nature above this energy. RHESSI spectroscopy (see Section 3.3.2) also confirms the turnover between thermal and nonthermal emission to be $\sim 20 \text{ keV}$. Therefore we consider the 20–30 and 30–50 keV bands to be free of thermal emission during these time intervals, to a first approximation.

Figure 3.6 shows RHESSI image contours overlaid on the corresponding TRACE images. Rows show times 01:48:58, 01:50:30, 01:51:02, 01:51:34 and 01:52:06 and columns show contours of RHESSI energy bands at 6–12 (blue), 12–20 (green), 20–30 (magenta) and 30–50 keV (red). The far right column shows all RHESSI

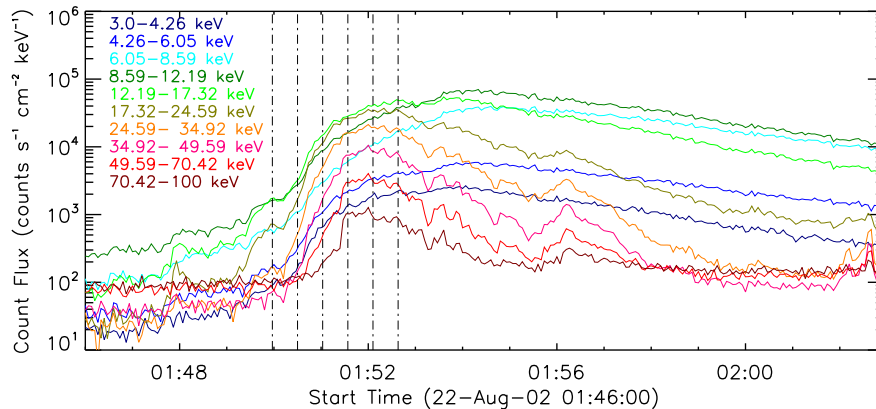


Figure 3.5: RHESSI lightcurve with logarithmic energy binning. Vertical dashed lines represent 32s time intervals used for RHESSI imaging (see Figure 3.6).

contours overlaid. TRACE pointing is controlled by an Image Stabilization System (ISS) which is accurate to roughly $5''$ – $10''$. A pointing drift on the order of $\pm 1''$ as a result of temperature fluctuations can cause some additional offset (Aschwanden et al. 2000). Correction to the alignment can be done using image cross correlation with other instruments. However for this event no TRACE pointing correction was carried out. From the images in Fig. 3.6 it is clear that the RHESSI contours align well with bright TRACE features.

From row 2 of Fig. 3.6, at time 01:50:30 (hereafter interval 2), emission as high as the RHESSI 30–50 keV energy band can be seen to be co-spatial with the jet around $(820'', -300'')$. From the TRACE images this is the region in which we think the twisted magnetic field became unstable, resulting in the ejection of plasma. These observations indicate the presence of hard X-rays and hence nonthermal electrons in the jet, and we believe this to be the first observation of its kind. Although not shown here, RHESSI images at these energies with better time resolution have been studied to see how this source evolves, and on this basis the question of whether the emission could be from a coronal loop can be dismissed: the hard X-ray jet emission can be seen to propagate out on a similar time scale to the ejected material and does not behave like a coronal loop. In general coronal loops are not present in the early impulsive phase of the event.

As the event continues (rows 3, 4 and 5 of Fig. 3.6) compact footpoint sources are seen forming at higher energies from 20–50 keV. In the low energy bands sources begin to form, co-spatial with the hot loops faintly visible in TRACE (see also Fig. 3.3 (i) onwards), seen as the right hand source in Fig. 3.6 rows 4

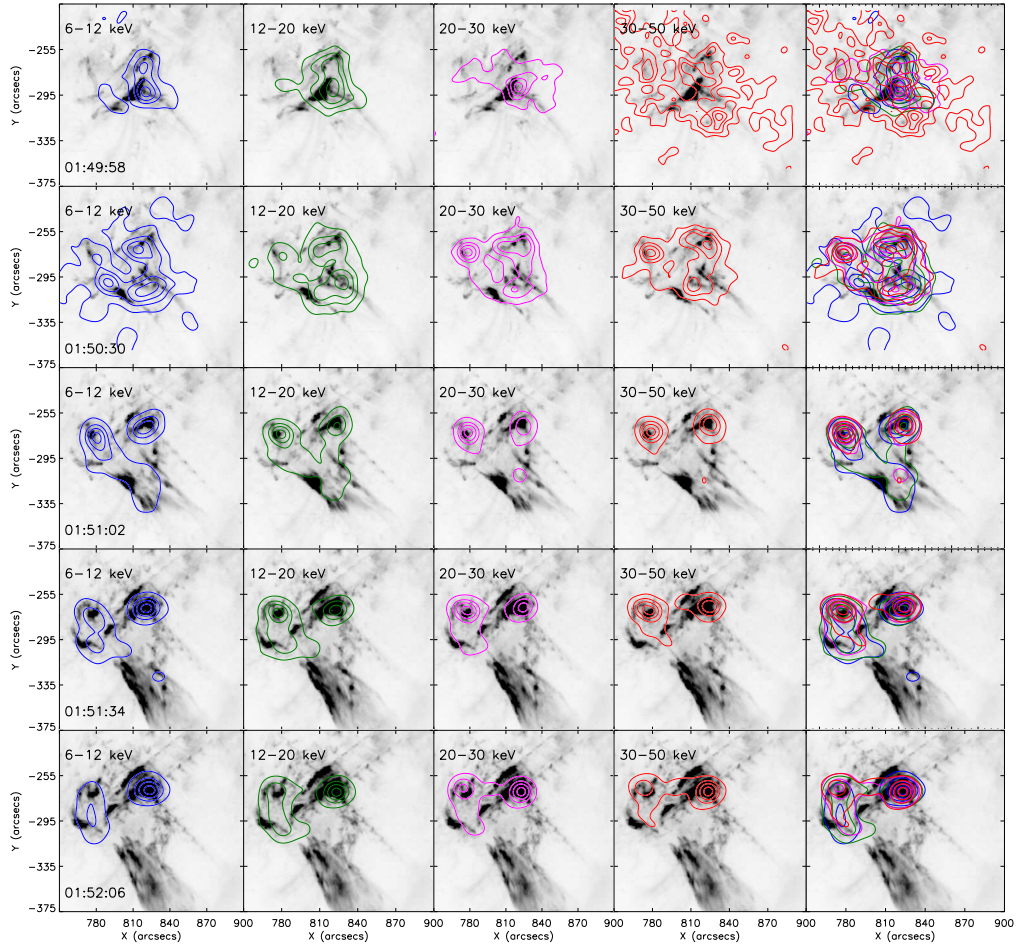


Figure 3.6: TRACE images with RHESSI image contours overlaid. Rows show time slices at times 01:48:58, 01:50:30, 01:51:02, 01:51:34 and 01:52:06 and columns show contours of RHESSI energy bands at 6–12 (blue), 12–20 (green), 20–30 (magenta) and 30–50 keV (red). The far right column shows all RHESSI contours overlaid. Contour levels are at 90, 75, 50 and 25%.

and 5 at roughly $(820'', -260'')$. Note that although these sources appear to be cospatial with the higher energy sources this is thought to be just a projection effect. In this Chapter we concentrate primarily on the emission present in the jet at 01:50:30.

3.3.2 RHESSI Spectroscopy

Figure 3.7 shows the fitted RHESSI spectra obtained from detector 3 for time interval 2. Energy bins of 0.33 keV at lower energies (6–12 keV) were used to properly fit the iron and nickel lines at 6.7 and 8.0 keV. Above 12 keV energy binning of 1 keV was used. The black line shows the background subtracted

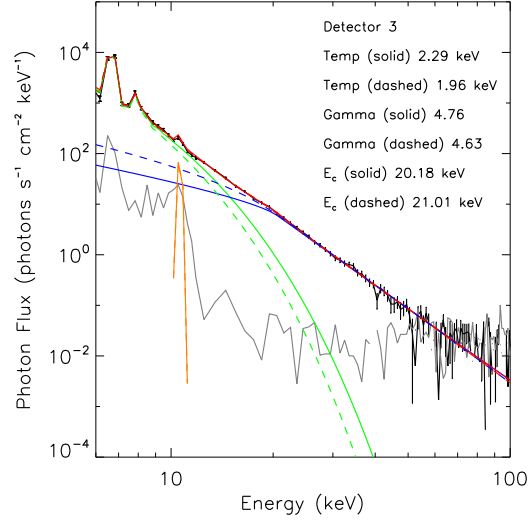


Figure 3.7: RHESSI photon spectra obtained from detector 3 for time interval 2. Black lines shows the background subtracted data and grey shows the background. The plot shows two possible fits, isothermal plus thin target (solid lines) and isothermal plus thick target (dashed lines). Green lines show isothermal fits. Blue lines show thick and thin target fits. Red shows the combined fit functions. Orange shows a Gaussian line added to fit a feature seen at 11 keV.

data and grey the background emission. Figure 3.7 shows two possible fits to the data between 6–100 keV. Fit 1 is an isothermal (green solid) plus thin target (blue solid) fit to the electron spectrum. Fit 2 is an isothermal (green dashed) plus thick target (blue dashed) fit. The thermal component is characterised by temperature and emission measure parameters which are allowed to vary. For thick and thin target components the electron spectral index and low energy cut off were allowed to vary. Figure 3.7 shows the conversion to photon spectra and values of temperature, photon spectral index and electron low energy cut off are stated in each plot. An additional Gaussian line (orange) was added to fit the line feature seen at 11 keV. It is thought that this is an instrumental feature but it is not fully understood what is producing this (Dennis 2009, private communication). Red shows the overall combination of fitted functions. Spectral fitting was carried out for individual detectors 1, 3, 4, 6, 8, and 9 and average parameters values calculated. The thermal component is characterised by a temperature of 24 MK and 26 MK for fit 1 and 2 respectively. The hard X-ray spectral index obtained was 4.67 and 4.77 for fit 1 and 2 respectively, thus supporting the evidence for nonthermal electrons present in the event. However using only spatially integrated spectra it is not possible to separate the contribution from the jet and

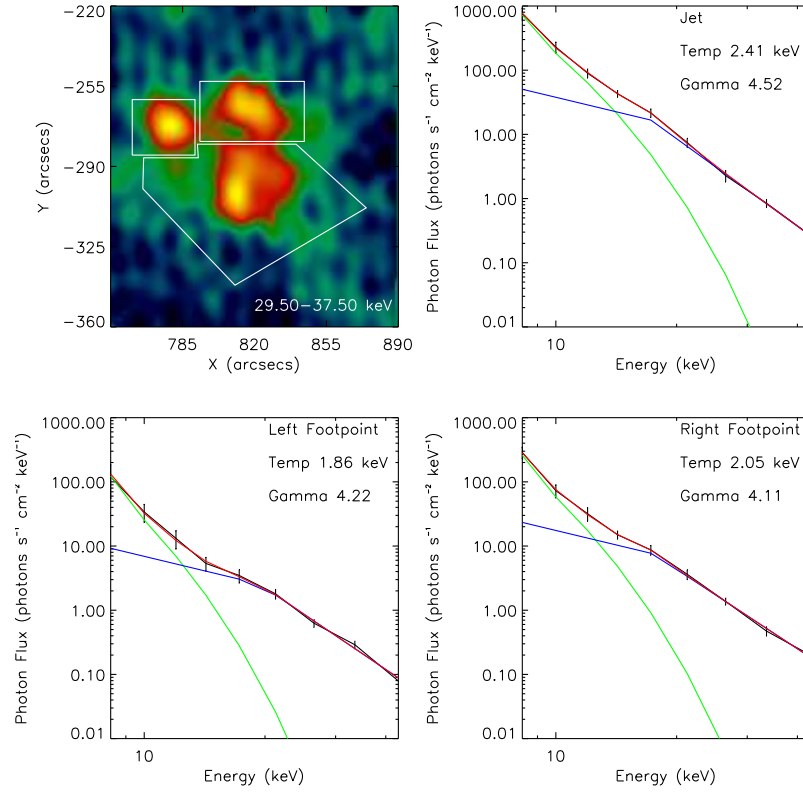


Figure 3.8: RHESSI image at 29.5–37.5 keV (top left) showing regions chosen for individual spectral analysis. Imaging spectroscopy results for the jet (top right), left footpoint (bottom left) and right footpoint (bottom right). Black lines show the observed photon spectra, green and blue show the isothermal and thick target fit functions respectively. Red shows the combination of fitted functions.

the footpoints and hence it is impossible to determine the spectral parameters resulting from the jet alone, therefore we have carried out imaging spectroscopy.

To perform imaging spectroscopy for time interval 2, images were made using pseudo-logarithmic energy binning from 7.5 keV to 48.5 keV. Despite summing counts from detectors 1, 3, 4, 6, 8 and 9 there were not enough counts for image synthesis above this energy to allow fitting to higher energies. Figure 3.8 (top left) shows a RHESSI image at 29.5–37.5 keV. Marked on the image are the regions chosen for individual spectral analysis to separate the emission from the jet and the footpoints. Here we fit an isothermal plus broken power fit components to the photon spectrum. For the broken power law component the spectral index below a variable break energy is fixed at 1.5. Above the break the spectral index is allowed to vary. The results are shown in Fig. 3.8. Black lines show the observed photon spectra, green and blue show the isothermal and broken power

law fit functions respectively. Red shows the combination of fitted functions. Stated on each plot are the values obtained for temperature and photon spectral index. We draw particular attention to Fig. 3.8 (top right) which shows the fitted photon spectrum for the jet characterised by a power law with a spectral index of 4.5 (slightly softer than the value obtained for the footpoints) confirming a nonthermal hard X-ray component in the jet, in turn implying the presence of nonthermal electrons. An estimate of jet temperature was found to be 28 MK. Temperature estimates for the hard X-ray footpoints are stated in each plot. However it should be noted that thermal footpoint emission could be subject to contamination as a result of the bright coronal source contributing to the flux. This is due to side lobes (Krucker & Lin 2002).

3.4 Radio Observations

3.4.1 Nobeyama Radioheliograph

NoRH images at 17 GHz (top) and 34 GHz (bottom) are shown in Fig. 3.9 for the same time intervals as with RHESSI. Note the field of view here is larger than that of Fig. 3.6 and shows an active region to the north-west of the jet. As time progresses, ejected material can be seen moving southwest away from the footpoint region. From the flux at 17 GHz and 34 GHz it is possible to determine a radio spectral index α from $F(\nu) \sim \nu^\alpha$, where $F(\nu)$ is the flux at frequency ν . Overlaid on the NoRH images are contours of spectral index α . White lines show positive spectral index from 0 to 2 in steps of 0.5, corresponding to optically thick emission. Black lines show lines of negative spectral index from -1 to -4 in steps of 1 corresponding to optically thin emission. As the event progresses footpoints can be seen forming. At 01:51:34 and onwards these regions become optically thin. Confirmation of this can be seen in Fig. 3.12 which shows spectra from the Nobeyama Polarimeters from 01:51 onwards. The turnover in the spectrum occurs at lower frequencies than those observed by NoRH indicating optically thin emission at 17 GHz and 34 GHz. See section 4.2 for more details. At these frequencies we can assume that the microwave emission is gyrosynchrotron radiation from particles at even higher energies than those observed via RHESSI hard X-rays, and hence definitely nonthermal in nature.

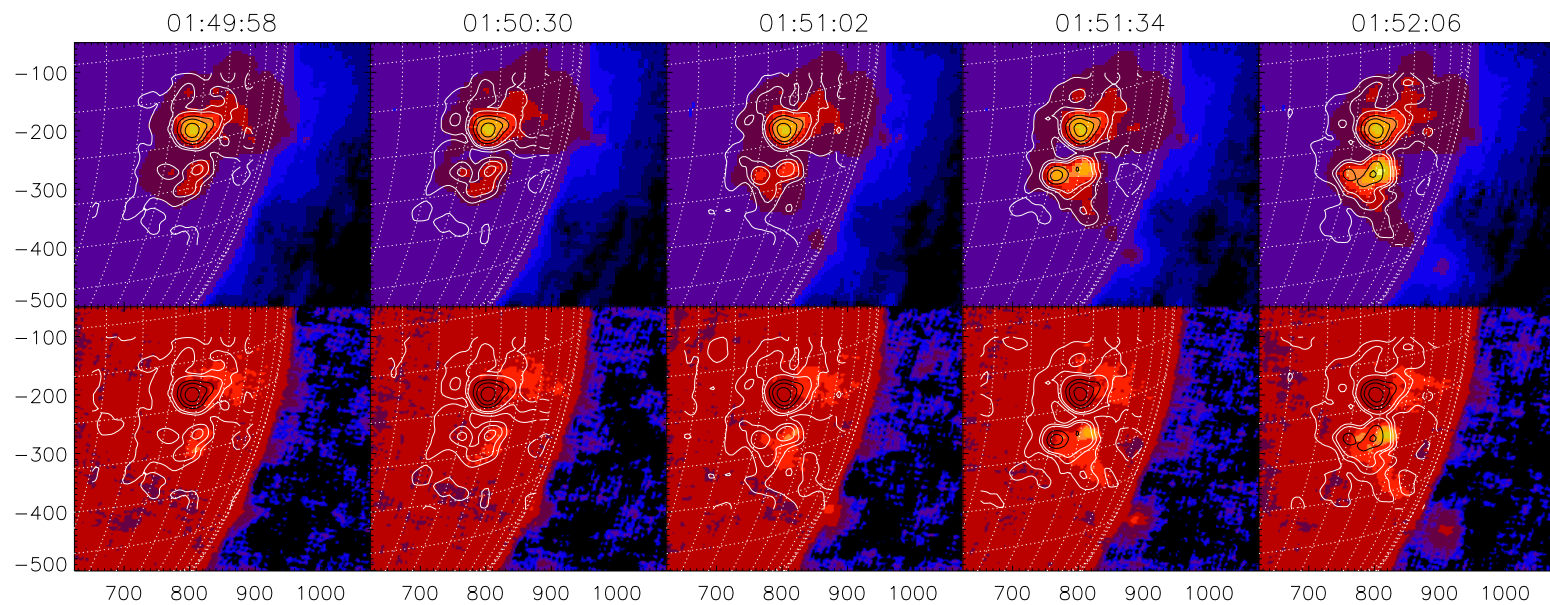


Figure 3.9: NoRH 17 GHz (top) and 34 GHz (bottom) images at time intervals used for RHESSI imaging. White lines show positive spectral index from 0.5 to 1.5 in steps of 0.5 corresponding to optically thick plasma. Black lines show lines of negative spectral index from -1 to -4 in steps of 1 corresponding to optically thin plasma.

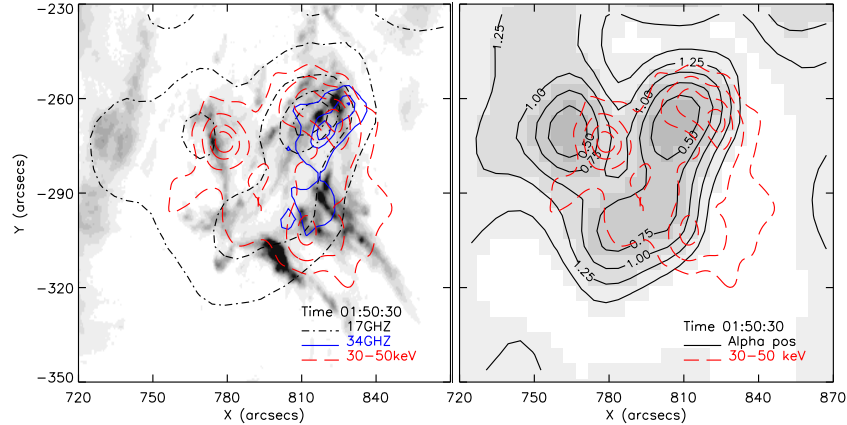


Figure 3.10: Left : TRACE image with NoRH 17 GHz (dot-dashed black), 34 GHz (solid blue) and RHESSI 30–50 keV (dashed red) contours. Contour levels of 90, 75, 50% for all contours (plus 25% for 17 GHz and 30–50 keV). Right : Map of radio spectral index α with contours of positive α ranging from 0 to 1.5 in steps of 0.25 (solid black) and RHESSI 30–50 keV (dashed red).

We pay particular attention to the images at 01:50:30 (see Fig. 3.10). On the left the contours of NoRH 17 GHz (dot-dashed black), 34 GHz (solid blue) and RHESSI 30–50 keV (dashed red) are overlaid on TRACE. It is important to note that NoRH images are subject to pointing errors due to random fluctuations of the Earth’s troposphere, particularly during a flare. Observing the left footpoint at 17 GHz and 30–50 keV suggests a displacement of $10''$ in the E-W direction. Despite this the emission seen by NoRH and RHESSI are well correlated with each other and with the EUV jet supporting the evidence for nonthermal particles in the jet at this time. Fig. 3.10 (right) shows a contour map of spectral index α with contours of positive α , ranging from 0 to 1.5 in steps of 0.25. The value of α for the jetting region is ~ 0.75 corresponding to optically thick emission from the fast-moving electrons.

3.4.2 Nobeyama Polarimeters

In addition to data from the Nobeyama Radioheliograph, radio flux and polarisation at 1, 2, 3.75 9.4, 17 and 34 GHz are obtained from the Nobeyama Polarimeters. For this event the flux at 80 GHz remained at the background level and was excluded. Figure 3.11 (top) shows a plot of total flux (R+L) and Fig. 3.11 (middle) shows the degree of circular polarisation (R-L), R and L denote the right and left circular polarisation. Note that NoRP records flux from the full disk,

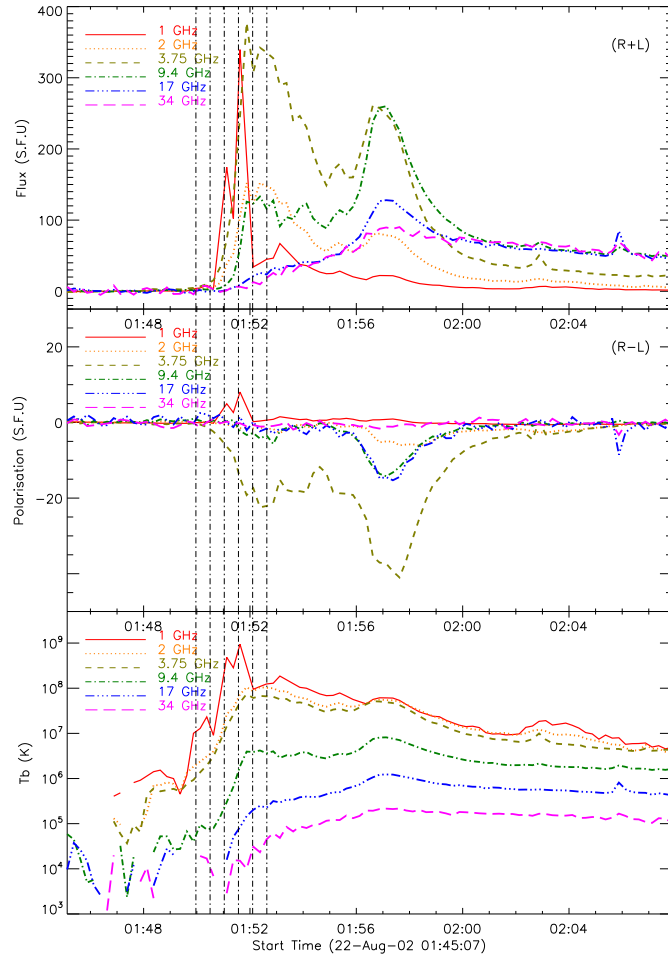


Figure 3.11: Top : NoRP flux (R+L) at 1, 2, 3.75, 9.4, 17 and 34 GHz. Middle : NoRP flux (R-L) showing degree of circular polarisation. Bottom : Brightness temperature calculated at each frequency. The dashed vertical lines show time intervals over which RHESSI images were obtained for Fig. 3.6.

however as there appears to be no other significant activity on the disk during this time interval, the emission recorded is likely to be from the jet event. It is interesting to note that the spiky bursts between 01:51:00 and 01:52:00 seen at the lower frequencies during the impulsive phase have no counterpart at higher radio frequencies. At 1 GHz these bursts are thought to be due to plasma emission at the local plasma frequency and its harmonics caused by a beam of electrons producing Langmuir waves due to a bump-in-tail instability. The non-linear nature of Langmuir wave-particle interactions results in the increased flux at 1 GHz. This effect will also be reflected in the brightness temperature T_b , which can be calculated using the Rayleigh-Jeans law (Equation 3.1, see also Chapter 2).

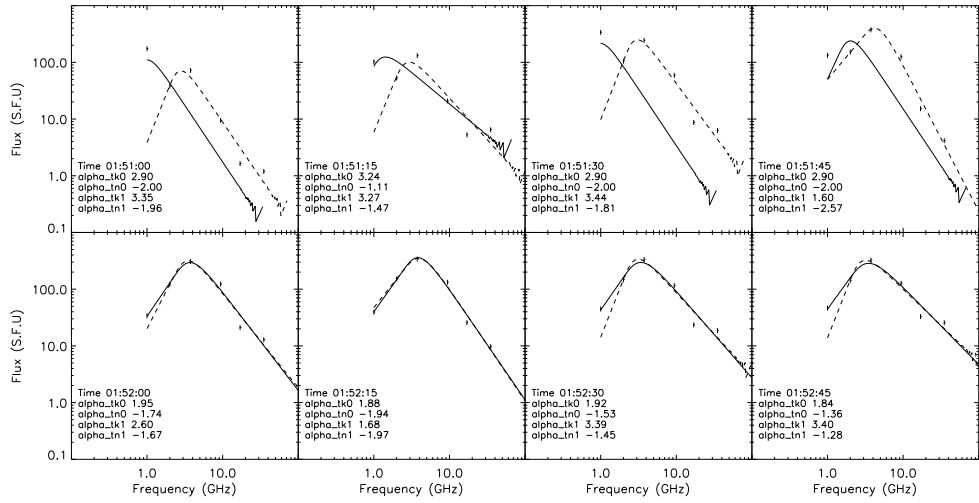


Figure 3.12: NoRP radio spectra at 15s time intervals. Solid line shows gyrosynchrotron function fitted to the data from 1 to 34 GHz. Dashed line shows the same function fitted to data from 2 to 34 GHz. Corresponding values of α_{tk} and α_{tn} for each fit are displayed on the plot, where 0 and 1 refer to the solid and dashed fits respectively.

$$I_\nu = \frac{2k_b T_b \nu^2}{c^2} \quad (3.1)$$

$$S_\nu = \int_{source} I_\nu(\theta, \phi) P_n(\theta, \phi) d\Omega \quad (3.2)$$

Rearranging Equation 3.2 where S_ν is the spectral flux density received by NoRP, $I_\nu(\theta, \phi)$ is the surface brightness for a source subtending $d\Omega$. $P_n(\theta, \phi)$ is the antenna power pattern. For sufficiently small source size, compared with the NoRP beam size, we can set $P_n(\theta, \phi) \simeq 1$ across the source. By subtracting a background flux we assume that emission observed results from an emitting source size $d\Omega$, taken to be $50'' \times 100''$, roughly the extent of the jet region visible from NoRH images at 17 and 34 GHz thus an upper limit of $d\Omega$. We obtain an estimate for the brightness temperature T_b in units of K. Plots of T_b are shown in Fig. 3.11 (bottom). It can be seen at the time of the spikes at 1 GHz T_b reaches $\sim 10^9$ K. This is too hot to plausibly be thermal and so implies non-linear, nonthermal plasma emission.

Figure 3.12 show plots of NoRP radio spectra following the evolution of the event beginning 01:51:00. Before this the flux at higher frequencies is still at the level of the background. The spectra are made by summing the flux

over 15s time intervals and normalising. Error bars at the 10% level are assigned to the data points as an estimate of errors due to atmospheric effects and local weather conditions. The spectra were then fitted using a function for gyrosynchrotron emission (Equation 3.3) allowing for four fit parameters (see <http://solar.nro.nao.ac.jp/norp/> for details): α_{tk} , the positive power index at low frequencies (corresponding to optically thick plasma), α_{tn} is the negative power index at high frequencies corresponding to optically thin plasma, $\hat{\nu}$ the turn-over frequency and \widehat{F}_ν the turn-over flux density.

$$F_\nu = \widehat{F}_\nu \left(\frac{\nu}{\hat{\nu}}\right)^{\alpha_{tk}} \left\{ 1 - \exp \left[- \left(\frac{\nu}{\hat{\nu}}\right)^{\alpha_{tn} - \alpha_{tk}} \right] \right\}$$

$$\approx \begin{cases} \widehat{F}_\nu (\nu/\hat{\nu})^{\alpha_{tk}} & \text{for } \nu \ll \hat{\nu} \\ \widehat{F}_\nu (\nu/\hat{\nu})^{\alpha_{tn}} & \text{for } \nu \gg \hat{\nu} \end{cases} \quad (3.3)$$

To fit the data we used the standard NoRP software which first chooses $\hat{\nu}$ to be the datapoint for which there is the greatest flux, and \widehat{F}_ν is assigned this value. The parameters are then varied to find the best fit. Figure 3.12 shows fits to the data from 1 to 34 GHz (solid line) and also a second fit excluding the flux at 1 GHz (dashed line). Corresponding values of α_{tk} and α_{tn} for each fit are displayed on the plot, where 0 and 1 refer to the solid and dashed fits respectively. However as can be seen from the first three plots of Fig. 3.12, the flux peaks at 1 GHz and the fit incorrectly tries to fit a spectrum which turns over at low frequencies. A second attempt excluding the flux at 1 GHz provides a more acceptable fit. We conclude from this that the flux from the burst at 1 GHz can not be described by a function for gyrosynchrotron emission and thus supports our case for the production of plasma emission at this time.

Plasma emission is at the local electron plasma frequency ω_p or its second harmonic $2\omega_p$ which is dependent on the plasma density n . Figure 3.13 (<http://sunbase.nict.go.jp/solar/denpa/hirasDB/Events/>) shows a radio spectrogram from the Hiraiso Solar Observatory (HiRAS) which observes in the range 25–2500 MHz. The spectrogram shows faint type III bursts starting $\sim 01:50:50$ followed by more intense bursts at $\sim 01:51:30$. The spectrogram shows high frequency type III bursts which have a duration of about a minute during which the frequency drifts from ≈ 1800 MHz to ≈ 400 MHz due to decreasing plasma density as the beam propagates out. This confirms that the bursts detected at 1 GHz by NoRP is indeed plasma emission. At lower frequencies, more intense type

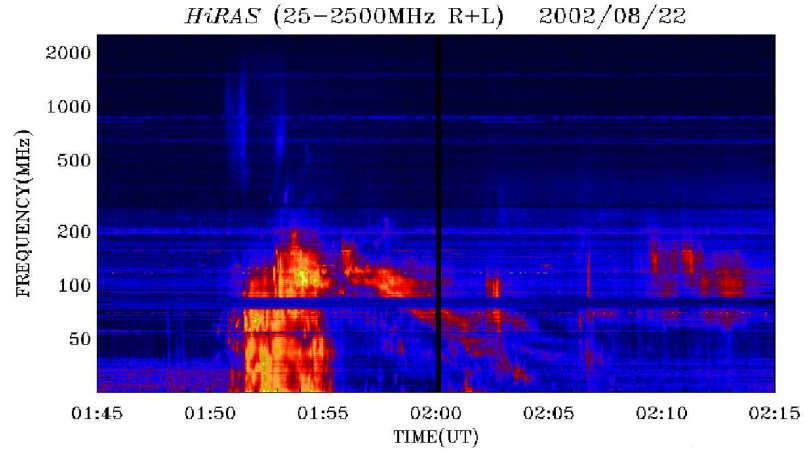


Figure 3.13: Radio spectrogram from the Hiraiso solar observatory (25–2500 MHz) showing Type III radio bursts.

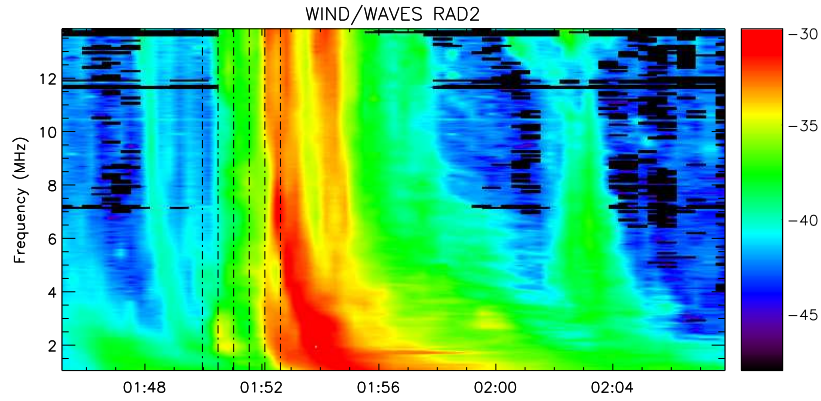


Figure 3.14: Spectrogram from WAVES on the WIND spacecraft (1.075–13.825 MHz) showing Type III radio bursts

III emission can be seen lasting around $4\frac{1}{2}$ minutes which drifts to frequencies below the observing range of HiRAS. Figure 3.14 shows a spectrogram obtained from RAD2 on the WAVES experiment on the WIND satellite which observes in the range 1.075–13.825 MHz (Bougeret et al. 1995). Figure 3.14 shows that the type III emission continues to drift to frequencies as low as 1 MHz. From the starting frequency of the radio bursts it is possible to determine the local plasma density n and from this estimate a height at which the burst was emitted. Using $\nu_p \approx 1500$ MHz as an approximate starting frequency of the plasma emission, then we can estimate n to be a few 10^{10} cm^{-3} . If we assume that the Type III radio burst is caused within the jet this suggests that the jet density is consistent with low coronal density.

3.5 Discussion and Conclusion

The evolution of the jet observed on the 22 August 2002 is similar to that of events described by Shimojo et al. (2007) in which a twisted loop rises prior to the jet. Reconnection with the overlying coronal field results in field reconfiguration and the ejection of hot X-ray emitting plasma. As the event progresses TRACE observations show loops forming at the base of the jet as expected by the magnetic reconnection model. In addition to this the ejected material appears to untwist slightly as twist from the emerging field is transferred to the “open” field lines of the jet. We found an apparent jet velocity of $\sim 500 \text{ km s}^{-1}$ which is consistent with predictions of velocities on the order of the Alfvén speed for this model. Calculating the Alfvén speed, $v_A = B/(4\pi\rho)^{1/2}$ for $B=10 \text{ G}$ and $n = 10^{10} \text{ cm}^{-3}$ we obtain $v_A \approx 200 \text{ km s}^{-1}$. However it should be noted that for plasma temperatures such as those found from RHESSI spectroscopy the sound speed in the corona will be in the range of $640 - 780 \text{ km s}^{-1}$.

At the time of the main ejection RHESSI imaging shows hard X-rays to as high as 30–50 keV present in the jet. This is the first time that hard X-rays coming from the jet location have been reported. Sui et al. (2006) have reported an event which may demonstrate hard X-ray emission from a jet region, a 6–12 keV coronal source was observed in the vicinity of a cusp-like, possibly jetting, structure above the apex of a compact flare loop. However without imaging spectroscopy it was not possible to determine if the source was thermal or nonthermal. Krucker et al. (2008d) found evidence for nonthermal coronal X-rays in the 14–30 keV range at the onset time of an interplanetary Type III radio burst, suggesting emission by escaping fast electrons, however there was no radio or other coronal imaging of a jet or other feature supporting this interpretation. By contrast, our observations show a clear spatial as well as temporal association of the jet with the nonthermal emission in both radio and hard X-rays, and therefore we believe this to be the first clear observation of nonthermal emission from flare-accelerated escaping electrons. RHESSI imaging spectroscopy includes a broken power law fit function which yields a spectral index of ~ 4.5 confirming the presence of nonthermal jet electrons.

If the nonthermal emission is bremsstrahlung caused by electrons propagating in a thick target coronal source in the jet then we can estimate the number of electrons above 20 keV using Equations 3.4, 3.5 and 3.6

$$F(E > E_c) = \int_{E_c}^{\infty} f_e(E) dE \quad (3.4)$$

$$f_e(E) = 3.28 \times 10^{33} \frac{b(\gamma)}{\gamma} A E_c^{-\gamma} \quad (3.5)$$

$$b(\gamma) = \gamma^2 (\gamma - 1)^2 B\left(\gamma - \frac{1}{2}, \frac{3}{2}\right) \approx 0.27 \gamma^3 \quad (3.6)$$

where $f_e(E)$ (electrons $\text{keV}^{-1} \text{ s}^{-1}$) is the electron injection spectrum, E_c is the electron energy cutoff, B is the Beta function, and A is the photon flux at 1 keV determined by fitting a power law to the photon spectrum where $I(\epsilon_x) = A \epsilon_x^{-\gamma}$ (Brown 1971; Hudson et al. 1978). We find this to be 1.5×10^{35} electrons s^{-1} . The thick target model is the most efficient method of converting energy from the electrons into photons (apart from thermal bremsstrahlung emission in a confined source). Taking a jet length of $40''$ (2.9×10^9 cm) suggests a total column depth of $\sim 2.9 \times 10^{19} \text{ cm}^{-2}$, which is collisionally thick to electrons of 10 keV. Therefore we consider also a hard X-ray emitting thin target through which the electrons are being ejected. From Equations 3.4, 3.7 and 3.8

$$f_e(E) = 1.05 \times 10^{42} C(\gamma) A \frac{1}{n_0 E^{-(\gamma-1/2)}} \quad (3.7)$$

$$C(\gamma) = \frac{(\gamma - 1)}{B(\gamma - 1, \frac{1}{2})} \approx (\gamma - 1.5)^{1.2} \quad (3.8)$$

where $f_e(E)$ (electrons keV^{-1}) is the thin target electron spectrum and n_0 is the target density. We estimate the instantaneous number of radiating electrons to be 1×10^{35} electrons. An electron of 30 keV will have a residence time of 0.29s in the jet. For a thin target interpretation the number of ejected electrons is then 3×10^{35} electrons s^{-1} .

In addition, RHESSI spectral fitting suggests a jet temperature of ~ 28 MK. As no hot loops are seen in this region with TRACE at this time or slightly after we are confident that this indeed the temperature of the jet. As suggested by Feldman et al. (1999), at these high temperatures the thermal continuum from

free-free and free-bound emission will be significant. From this it is plausible to suggest that TRACE images reveal free-free emission in the jet similar to that observed with RHESSI. NoRH observations at 17 and 34 GHz are seen to be co-spatial with the hard X-ray emission during this time and α is found to be ~ 0.75 corresponding to optically thick emission by nonthermal electrons, reinforcing our claim that X-rays are directly revealing the presence of these particles in the jet. Further radio observations from NoRP and HiRAS show simultaneous bursts of plasma emission at 1 GHz. If we assume this results from a beam of electrons accelerated in the jet, we calculate $n = 10^{10} \text{ cm}^{-3}$ which is a reasonable jet density. We note however, for a density of $n = 10^{10} \text{ cm}^{-3}$ and an estimated coronal magnetic field of $B = 10 \text{ G}$, Razin suppression effects are likely to occur at frequencies of around 20 GHz, shifting the peak of the spectrum to higher frequencies. Thus the positive value for α therefore may not indicate optically thick plasma, but could be explained by medium suppression effects.

From our estimates of jet velocity it is not conclusive as to whether the jet is moving at the Alfvén speed in the corona, a jet at the sound speed cannot be completely ruled out. However the evolution can be compared to that described by the magnetic reconnection jet of e.g. Heyvaerts et al. (1977); Shimojo et al. (1996) where rising magnetic field interacts with the overlying corona field. In this scenario the jet emission would be produced around the reconnection region where the plasma is heating and particles are accelerated. Another thing to consider is the model by Pariat et al. (2009) where twist from closed magnetic field lines is transferred to the open field lines as a result of the reconnection. As this twist relaxes and propagates outwards torsional Alfvén waves compress the plasma and enhances the jet density and temperature as it propagates outwards. From the TRACE images we observe a helical twist in the jet and it is plausible to suggest that the cooler TRACE material could be produced by the compression of the jet plasma. In this scenario the TRACE and RHESSI hard X-ray jet emission result from different processes and may explain why emission at 30-50 keV is not observed for longer. Although we cannot rule out that the jet emission is simply unobservable due to dynamic range effects caused by and increased footpoint emission. If this scenario were true, it should also be noted that we are therefore measuring the velocity of the propagation of the Alfvén wave compression and not necessarily the bulk motion of the jet, or indeed the velocity of the accelerated electrons. One interesting thought is that tens of seconds before the main ejection there is evidence of smaller ejection events, if these pre-jet events were to result

in an enhancement of the plasma density around the jetting region, could this provide a thick-target for the accelerated electrons which results in observable hard X-ray emission? We believe this to be a rare observation, but one lending strong support to a model involving coronal electron acceleration in a relatively dense plasma and in close association with the magnetic reconfiguration that launches the jet.

Chapter 4

Observations of 24th August 2002 flare

4.1 Introduction

Radio observations of solar flares can be used to determine important information regarding particle acceleration and transport effects, and can be used to determine a number of physical parameters of the flaring plasma. In addition the morphology of radio brightness can provide constraints on magnetic field models in flares due to the dependence of gyrosynchrotron emission on the magnetic field and the orientation of the field with respect to the observer.

When the first spatial information was achieved, using data from the Westerbork Synthesis Radio Telescope, the Very Large Array, and with the Nobeyama Radioheliograph, radio emission was often found either as a compact source at the flare looptop or as multiple sources at the flare footpoints (Dulk (1985); Bastian et al. (1998); Nindos et al. (2008) and references therein, in particular (Marsh & Hurford 1980)). These findings agreed well with theoretical models (Alissandrakis & Preka-Papadema 1984; Klein & Trotter 1984). Initial images from NoRH were at a single frequency, 17 GHz and the addition of a second high frequency at 34 GHz provided information on the radio spectrum at these frequencies and on the optical depth of the emitted radiation. In general it was found that at higher frequencies the radio emission was optically thin and emission dominated in the footpoints. Conversely, lower frequency emission was optically thick and was concentrated at the looptop. However a number of observations showed dominant optically thin emission at the flare looptops that could not be explained by the existing theoretical models (Kundu et al. 2001; White et al. 2002; Melnikov et al. 2002a,b). Tzatzakis et al. (2006) showed that roughly half of the flares where

the footpoint and looptop emission can be spatially resolved show optically thin emission occurring between the footpoint sources. Kundu et al. (2001) suggested that in order to achieve an optically thin looptop source the magnetic field along the loop would need to vary slowly or remain constant. However modeling a constant magnetic field along the loop they were only able to partly match the flux and morphology of the observations. Melnikov et al. (2002b) suggested that the presence of a dominant, optically thin looptop source is caused by an enhancement of energetic electrons at the top of the loop occurring as the result of a transverse pitch angle anisotropy or pancake distribution caused by the accelerating mechanism. Trapping of particles in the looptop or loss of trapped particle in the flare legs, for example due to Coulomb collisions, could also account for an increase in the number density at the looptop.

In this Chapter we present observations of a GOES X3.1 class flare which occurred on the 24th August 2002. The event, which was observed by a number of instruments including RHESSI, TRACE and NoRH, occurred on the west limb of the Sun. Observations from NoRH are available for the entire event and show the evolution of a flaring arcade of coronal loops. At both NoRH frequencies, 17 GHz and 34 GHz we are able to resolve a loop structure where the looptop is clearly separated from the footpoints. Like the observations mentioned above, this flare exhibits an optically thin looptop source. Such flare observations, where the footpoints and looptop can be easily separate and exhibit an optically thin looptop source are infrequent and thus, combined with its size and intensity at radio frequencies, this flare is of particular interest. In addition to exhibiting a spatially resolved distribution of brightness along the loop, this flare also shows a temporal distribution of radio brightness where, in particular, the dominant emission varies between the looptop and one footpoint over time.

In this Chapter we present observations of the August 24th event. We will carry out detailed radio modeling of the event in the following Chapter. Firstly we present a detailed description of the evolution of the flare using images from TRACE. Following this radio observations from NoRH are presented, and also observations from RHESSI which are used to constrain values for flare parameters such as temperature and emission measure.

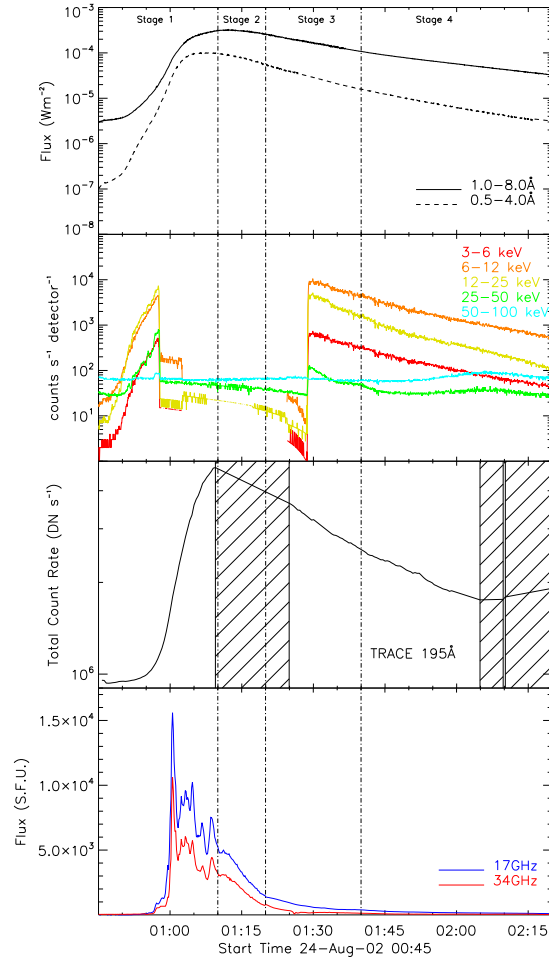


Figure 4.1: Plot shows, from top to bottom, GOES, RHESSI, TRACE and NoRH lightcurves for the 24th August 2002 flare. Diagonal stripes on TRACE lightcurve indicate data gaps.

4.2 Event Overview

On the 24th August 2002 a GOES X3.1 class flare was observed on the west limb of the Sun. The event was observed by a number of instruments. Figure 4.1 shows time profiles from GOES, RHESSI, TRACE and NoRH. A gradual rise phase is seen by GOES, TRACE and RHESSI 6-50 keV energy bands. Unfortunately both RHESSI and TRACE suffer data gaps around times of peak flux (RHESSI: 00:57-01:30, TRACE: 01:09-01:24 (diagonal stripes)). However a rough estimate taken from the GOES lightcurves suggests a soft X-ray and EUV flux peak around 01:09. In contrast to this, NoRH shows a number impulsive bursts, seen at both frequencies 17 GHz and 34 GHz, the largest of which occurs around 01:00. Before RHESSI enters a period of spacecraft night, the 50-100 keV energy

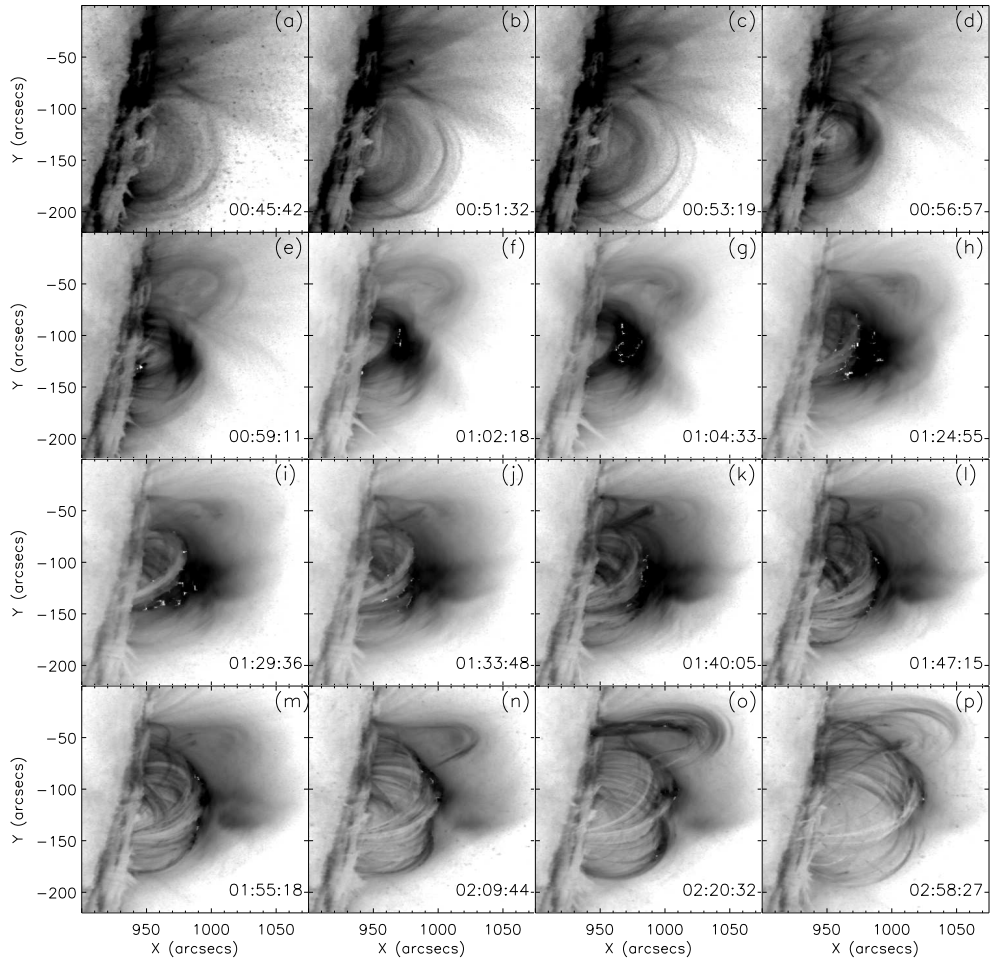


Figure 4.2: TRACE 195 Å evolution of 24th August 2002 flare.

band shows an increase in flux at 00:56 which corresponds with the timing of the impulsive bursts seen by NoRH. Due to spacecraft night it was not possible to investigate further the temporal correlation between the radio and RHESSI hard X-ray emission. When RHESSI comes out of night emission in the 50-100 keV energy band had returned to background levels. However it is of interest to point out observations presented in Reznikova et al. (2009) from the SONG detector onboard CORONAS-F which show the hard X-ray time profiles in the 64-180 keV and 180-600 keV energy bands. The SONG lightcurves show that for each impulsive radio burst there is a corresponding hard X-ray peak. They find time delays between the peaks of the radio and hard X-ray bursts of 6 s (± 2 s) and 8 s (± 2 s) for 17 GHz and 34 GHz respectively.

The evolution of the associated flare can be followed using images from TRACE. For this event images were only available for the TRACE 195Å passband. The

images have a 19.5 s exposure and a cadence of roughly 27 s. Figure 4.2 shows a selection of images which cover the entire flare. The images have been exposure normalised using the Solarsoft routine `trace_prep`. Cosmic ray spikes were also removed using this routine. To clarify the progression of the flare we have divided the temporal evolution into four stages, see Table 4.1 for a summary. Note that no TRACE data is available for Stage 2. These time ranges were chosen with observations from RHESSI and NoRH in mind. The selected time ranges will become apparent in the following Sections.

Table 4.1: 24th August 2002 Flare evolution

Stage	Time Range	Fig. 4.2 Panel	Brief Description
1	00:45 - 01:10	a - g	Impulsive phase and peak Filament Eruption/CME Arcade formation
2	01:10 - 01:20		Decay phase TRACE data gap
3	01:20 - 01:40	h - k	Arcade forming at greater heights
4	01:40 - 02:20	l - p	Arcade forming at greater heights

Stage 1 covers the flare rise and peak times from 00:45 - 01:10. Preflare images reveal large coronal loops present above the active region. From images a to c it is thought that the base of the TRACE loops, seen to the north and hereafter known as ‘farside’ footpoints, are occulted. It is difficult to determine whether the conjugate TRACE loop footpoints seen to the south, ‘nearside’ footpoints, are also occulted. Throughout the event there is no bright ribbon seen at the base of the farside loops, supporting occultation. At the nearside loop footpoints the very edge of the EUV limb brightens slightly suggesting that the footpoints are right on the limb. In the run up to the flare a prominence can be seen above the limb, see panels a to c. The reverse colour table is such that the filament appears white. At 00:45:42 the outer loops begin to expand outward, see panels a to c. Learmonth Observatory showed that a prominence eruption occurred at 00:55. Observations also show a CME associated with the flare. Figures 4.3(a), 4.3(b) and 4.3(c) show images from the Large Angle Spectrometric Coronagraph (LASCO) instrument on the SOHO spacecraft. The two working coronagraphs C2 and C3 image the solar corona out to $6 R_{\odot}$ and $12 R_{\odot}$ respectively. Figures 4.3(a) and 4.3(b) show images at 01:27 and 01:50 from the C2 and 4.3(c) shows a later image at 02:18 from C3, taken from the SOHO LASCO CME catalog. The

catalog states an estimated launch time of around 00:50 at a speed of around $1,900 \text{ km s}^{-1}$

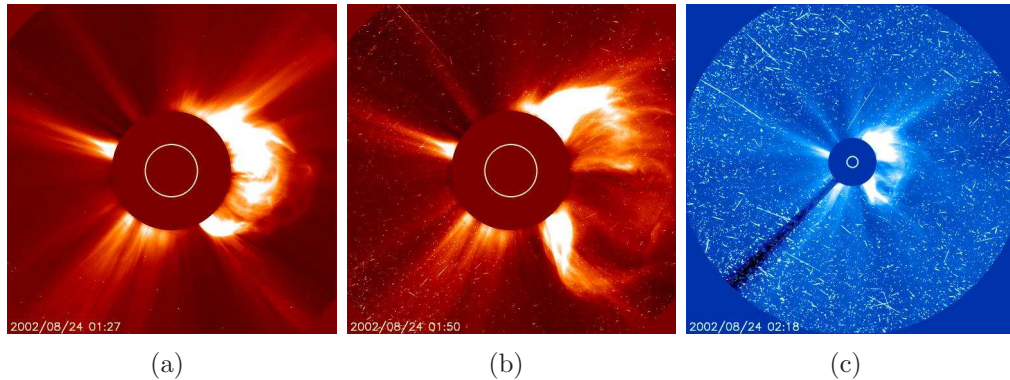


Figure 4.3: Images of CME associated with flare on 24th August 2002 from the LASCO instrument on SOHO. (a) and (b) Images from C2 at 01:27 and 01:50. (c) Image from C3 at 02:18. Images from the SOHO LASCO CME Catalog.

From around 00:57 an arcade of loops begins to form at lower heights in the corona, see panels d to g. Although difficult to see in still images, a movie of the event clearly shows that the arcade forms from west to east i.e. right to left in the TRACE images. We speculate that subsequent bright loops form as a result of a systematically moving reconnection region or ‘unzipping’ due to the liftoff of the filament (Grigis & Benz 2005). A TRACE data gap prevents us following the evolution of the flare between 01:09 and 01:24 i.e. Stage 2. However after the data gap (panel h and onwards) we can see arcade loops occurring at greater heights in the corona due to subsequent reconnection occurring at greater heights. Under normal active region conditions this wavelength is dominated by FeXII line emission at $1.4 \times 10^6 \text{ K}$. During flares it is often dominated by higher temperature plasma, providing both FeXXIV and CaXVII line emissions ($5 \times 10^6 \text{ K}$ and $(1-2) \times 10^7 \text{ K}$) and a significant thermal continuum due to free-free and free-bound emission, which is in fact dominant at temperatures of around 10^7 K (Feldman et al. 1999). The higher 10^7 K component can be seen in TRACE images as a source which is diffuse in comparison to the well delineated emission at lower temperatures. From panel h to m we see such a source present above the well-defined arcade emission. We associate this with plasma emitting at the higher temperature. Another TRACE data gap occurs between 02:04:53 and 02:09:44 and also again between 02:10:11 and 02:20:21 during which another large loop feature slightly to the north of the arcade begins to brighten and expand, see

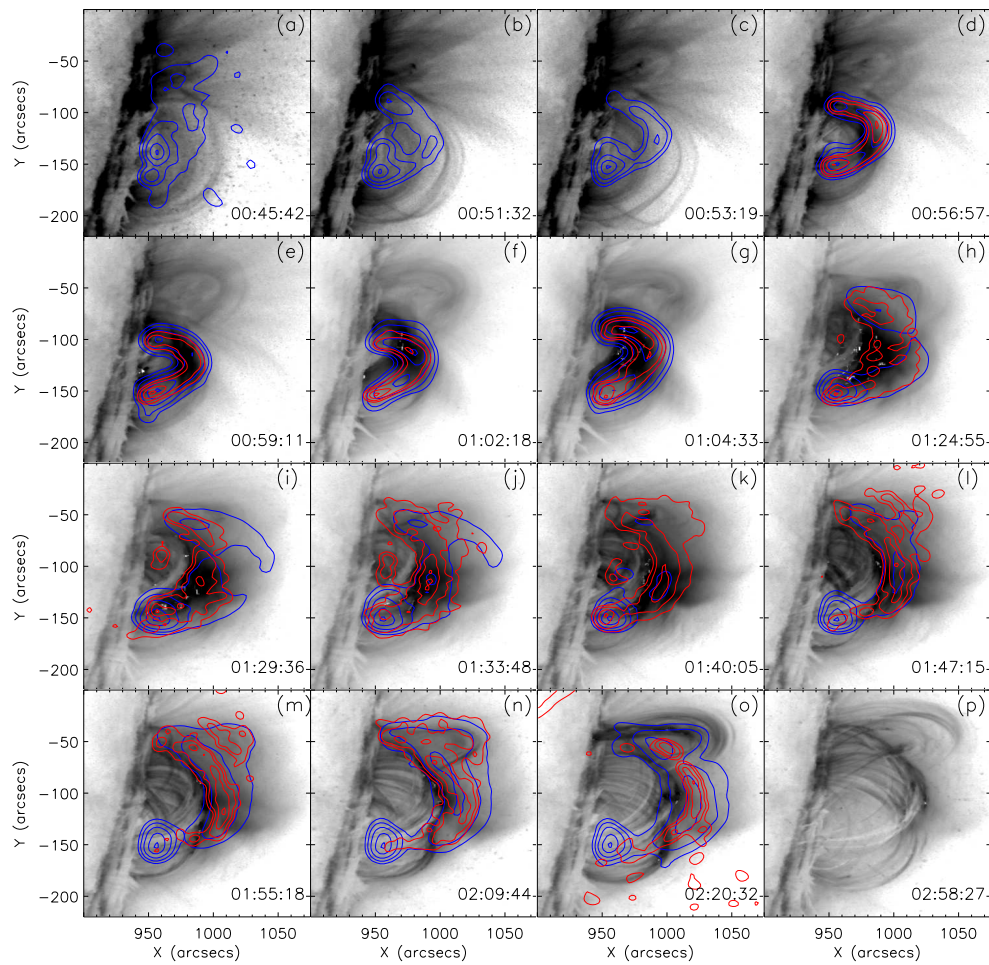


Figure 4.4: TRACE 195 Å evolution of 24th August 2002 flare with corresponding NoRH 17 GHz (blue) and 34 GHz (red) image contours overlaid. Image contours are at 8, 16, 32, 64 and 96% of image maximum brightness temperature. Panel (d) has an additional 25% contour for all energy bands.

panels n to p.

A number of authors have presented observations of six radio bursts seen around the flare peak, see later for details. For this Chapter we concentrate our analysis on the decay phase of the event with the intention of studying the overall evolution of the flare.

4.3 Radio Observations

4.3.1 NoRH

Figure 4.4 shows TRACE images with corresponding NoRH image contours at 17 GHz (blue) and 34 GHz (red) overlaid. Radio images are in units of brightness

temperature (K) and contours are at 8, 16, 32, 64 and 96% of image maximum. Panel (d) has an additional 25% contour for all energy bands. These 17 and 34 GHz images were made using CLEAN image algorithm and coaligned by Dr Stephen White using the NRAO AIP software package developed by T. S. Bastian, S. M. White, K. Shibasaki and S. Enome (Greisen 2003) (see also (Nindos et al. 1999) for some details). Images were made every 10 s from 00:45-01:20 and every 20 s from 01:20-02:20. The image pixel size is 3'' for 17 GHz and 2'' for 34 GHz with CLEAN beam sizes of 12'' and 8'' respectively. As NoRH is a ground based instrument, image pointing can be affected by atmospheric disturbances. To align the images the 17 GHz southern footpoint was kept fixed and the 34 GHz loop aligned with the 17 GHz loop. Due to the nature of this event, where the distribution of brightness changes considerably throughout the event, alignment is tricky. It is possible that the southern footpoint is not fixed in reality however we believe the alignment to be accurate to a first approximation. These images were then aligned with MDI white light and magnetogram images taken during the preflare and again in the decay phase. Errors due to alignment are roughly $\pm 5\text{-}10''$ for both 17 GHz and 34 GHz.

In addition to alignment the images are subject to uncertainties in intensity scaling. This problem can occur for strong flares when NoRH records a signal greater than ~ 500 S.F.U. This occurs for two reasons. Firstly limited dynamic range causes the disk to disappear in the presence of a strong flare, resulting in deviation from the normal scaling. Secondly the fringe correlation coefficient for the correlated data becomes close to unity in strong flares. Normally the correlation coefficient should be much smaller indicating that the flare is only a small fraction of the quiet sun flux. This results in the compression of bright image features. The later effect was corrected by forcing the NoRH fluxes to match those obtained from the Nobeyama Polarimeters. This was also performed by Dr Stephen White.

Stage 1

At 00:45 NoRH 17 GHz images show two distinct sources at low heights in the corona, Figure 4.4 (a). These appear to be roughly cospatial with the filament observed in TRACE and have a brightness temperature, T_b , of around 3×10^5 K. At 00:50 an additional 3rd source appears to the north cospatial with the farside loop ‘footpoints’ with $T_b \approx 3 \times 10^5$ K. Note here we refer to the point where

the farside TRACE loops meet the limb, not the true footpoints as we believe these to be occulted. By this time the sources to the south have increased to $T_b \approx 6 \times 10^5$ K. By 00:51:50 emission at 17 GHz can be seen all along the loop. Contours at the looptop also suggest a source at the loop apex. At 00:52 the two sources at the southern footpoint can be seen to either merge (or the one slightly to the north disappears) to form a source with $T_b \approx 2 \times 10^6$ K. Until this time emission at 34 GHz has been faint and only slightly above the background level and images appear noisy, so contours are not shown in Figure 4.4 a to c. Despite this the radio brightness seems in general to be concentrated around the region of the 17 GHz loop. At 00:54 emission at 34 GHz is sufficiently bright to image and can be seen all along the loop. The higher contour values show an increase in brightness at the southern footpoint and at the loop top, found to be cospatial with the 17 GHz and TRACE 195 Å emission, see Figure 4.4d.

In agreement with the looptop evolution present in the TRACE observations, the radio looptop source appears to move from west to east following the formation of an arcade of loops from 00:56 - 01:04. The looptop emission remains cospatial with the bright arcade looptops observed with TRACE. During this time the brightness temperature at 17 GHz increases from 4×10^6 K at 00:56 to 2×10^8 K at 01:04, peaking at 5×10^8 K at around 01:00. A similar trend is seen at 34 GHz with an increase from 1×10^6 K to 4×10^7 K. Beyond this time we cannot say if the radio source follows a similar evolution to the TRACE arcade due to the data gap. However from NoRH images alone during this time range, and up until 01:10, the distribution of brightness temperature along the loop varies back and forth from footpoint to looptop on timescales on the order of 10's of seconds to 1 minute. These times coincide with the impulsive bursts seen in the NoRH lightcurves, Figure 4.1.

Detailed observations of the impulsive radio bursts occurring in Stage 1 are presented by Melnikov et al. (2005); Tzatzakis et al. (2006) and in particular in Reznikova et al. (2009). Here we quickly summarise the key observational features pointed out by Reznikova et al. (2009). 1) At the peak of each sub burst the source with the maximum brightness temperature at 34 GHz is found in the footpoints whilst in the valley between sub bursts the brightness at 34 GHz increases away from the footpoints in a source slightly to the north of the looptops i.e. along the farside loop leg. 2) The brightness temperature at the footpoint source varies drastically between the peak of each sub burst and the corresponding valley whilst

the brightness temperature away from the footpoints remains largely unchanged between each sub burst peak and corresponding valley. 3) At 17 GHz, for the first three sub bursts, the emission at the peak of each burst is already present towards the looptop source instead of being situated in the footpoint as at 34 GHz. 4) By examining the main peak in particular, the peak of the burst at the looptop is delayed with respect to the peak at the footpoint for both frequencies ($6 \text{ s} \pm 2 \text{ s}$ for northern source, $8 \text{ s} \pm 2 \text{ s}$ for southern footpoint). The delay is greater at 34 GHz. 5) There is a delay between the overall timing of the burst at 34 GHz with respect to 17 GHz. The peak is also wider and has a longer decay for emission at 34 GHz than for 17 GHz. 6) Comparison of spectral index α for the southern, northern and looptop sources reveals a negative (but increasing) value for α over the course of the main burst corresponding to optically thin emission at the looptop and northern footpoint. For the southern footpoint α increases from negative to positive values on the rise and at the peak before decreasing in the decay phase of the burst. This is interpreted as optically thick nonthermal gyrosynchrotron emission at 17 GHz. See Reznikova et al. (2009) Figures 4 to 7 for more details.

Each of the three papers mentioned above attempt to model the radio emission observed during these impulsive bursts using a Fokker-Planck approach to describe the evolution of energetic electrons in the loop over time. Details of these attempts are presented in the following Chapter. As previously mentioned we concentrate our investigation on the decay phase of the flare.

Stage 2

Figure 4.5 shows time profiles of NoRH brightness temperature at 17 GHz (blue) and 34 GHz (red) during the flare decay phase. The emission from the looptop and southern footpoint have been separated and shown in top right and bottom right respectively. An example image of 17 GHz emission at 01:26:41 shows how the looptop and footpoint emission were separated. These regions are kept constant for all images. The lightcurves were plotted using the maximum pixel value in each region for each time interval. The evolution of the looptop is complex as the loop morphology changes and increases in size. This will be described in more detail in the following sections. We try here to simply show the difference between the footpoint emission and the looptop emission. As we believe the loop northern footpoint to be occulted, we consider all sources of emission outside of

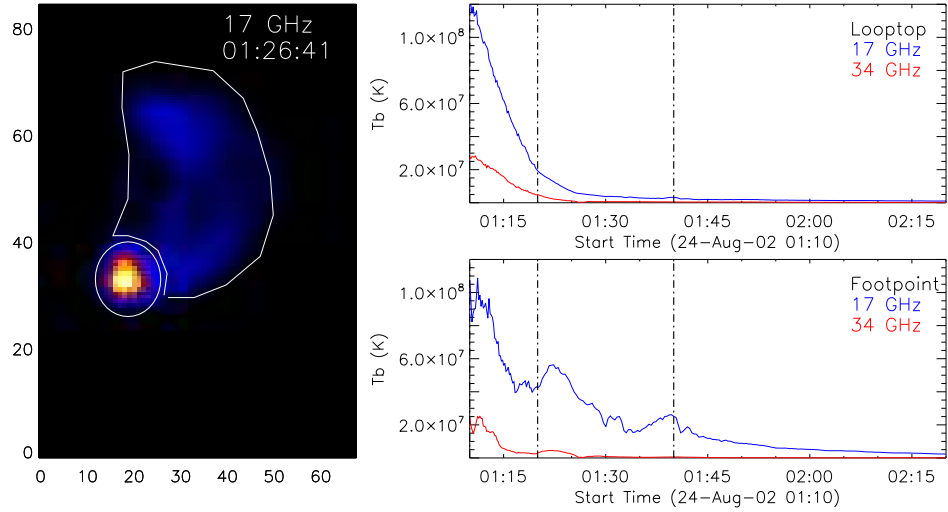


Figure 4.5: Plot shows time profiles of T_b for NoRH 17 GHz (blue) and 34 GHz (red) during the flare decay phase. The emission from the looptop and southern footpoint have been separated and shown in top right and bottom right respectively. Vertical lines indicate the time intervals of Stages 2, 3 and 4. Image plot to the left shows an example 17 GHz image at 01:26:41 indicating how the looptop and footpoint emission were separated.

the southern footpoint region as looptop. A variety of polygon shapes were tried and it was found that combining these sources of emission under this heading did not significantly alter the general trend of the lightcurve. We can see straight away that the footpoint profile fluctuates considerably over time, with several cotemporal bursts seen at 17 GHz and 34 GHz, in comparison to the smoother decay of the looptop emission.

Vertical lines on the time profiles in Figure 4.5 indicate time intervals for Stages 2, 3 and 4. Stage 2 was chosen to commence at 01:10 which marks the end of the impulsive radio bursts. Over this period the maximum brightness temperature in the looptop decreases from 1.2×10^8 K to 2×10^7 K at 17 GHz and from 3×10^7 K to 5×10^6 K at 34 GHz. The footpoint shows a decreasing brightness temperature from 1×10^8 K to 4×10^7 K at 17 GHz and 2×10^7 K at 34 GHz.

As mentioned previously we have simply taken the value of the brightest pixel as a proxy of the evolution of the looptop and footpoint emission. However we also know that there is a spatial variation of brightness along the loop over time. Figure 4.6 shows a series of NoRH images throughout the decay phase. Brightness temperature images at 34 GHz are shown in redscale and 17 GHz image contours

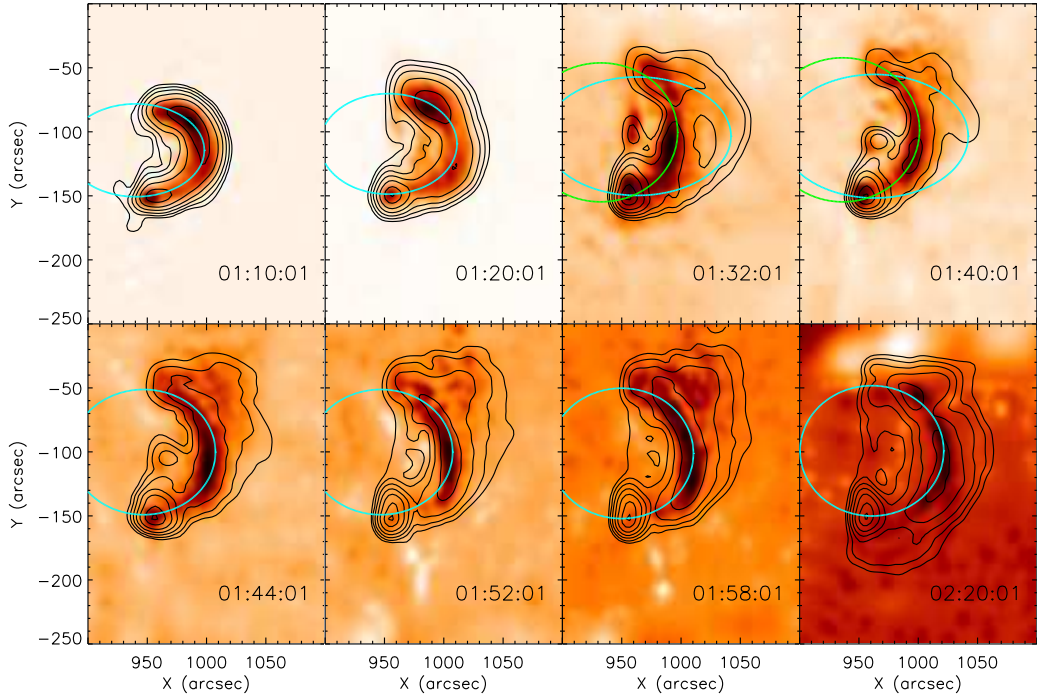


Figure 4.6: NoRH 34 GHz brightness temperature images in redscale with 17 GHz image contours overlaid at 2, 4, 8, 16, 32, 64 and 96% of image maximum. Ellipses drawn on images are used to determine brightness distribution along the loop. For images at 01:32 and 01:40 the blue ellipse indicates the outer loop and green the inner loop.

are overlaid at 2, 4, 8, 16, 32, 64 and 96% of image maximum. NoRH images at 01:10 and 01:20, i.e. the start and end of Stage 2, are shown in first two panels on the top row.

To investigate the spatial variation of brightness, an ellipse was used to fit the loop at 2 minute intervals. The ellipse was fitted by eye with the help of image contours. The ellipse centre, semi-major and semi-minor axes altered to pass through bright sources along the loop. Thus we get an estimate of brightness as a function of θ around the ellipse, where θ is the angle joining the ellipse centre to a point on the ellipse. The centre was chosen such that a point on the ellipse with θ equal to 0° (or 360°) is placed roughly at the loop apex. One set of ellipse parameters are chosen to fit the loop at both 17 GHz and 34 GHz. By doing this we are assuming that both frequencies have similar morphology and that the main bright sources lie along the same loop axis. As expected, for some time intervals this is not the case. To evaluate the error this produced we also attempted to independently fit an ellipse to each frequency and then compared the results. It

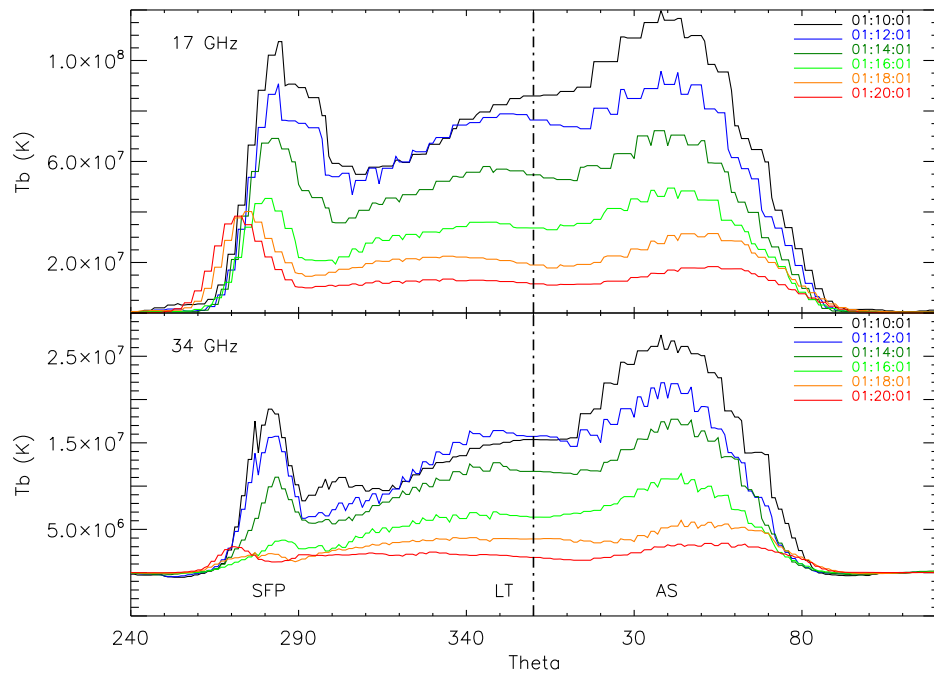


Figure 4.7: Plots of T_b as a function of θ for 17 GHz (top) and 34 GHz (bottom) around an ellipse fitted to the loop for each time interval in Stage 2.

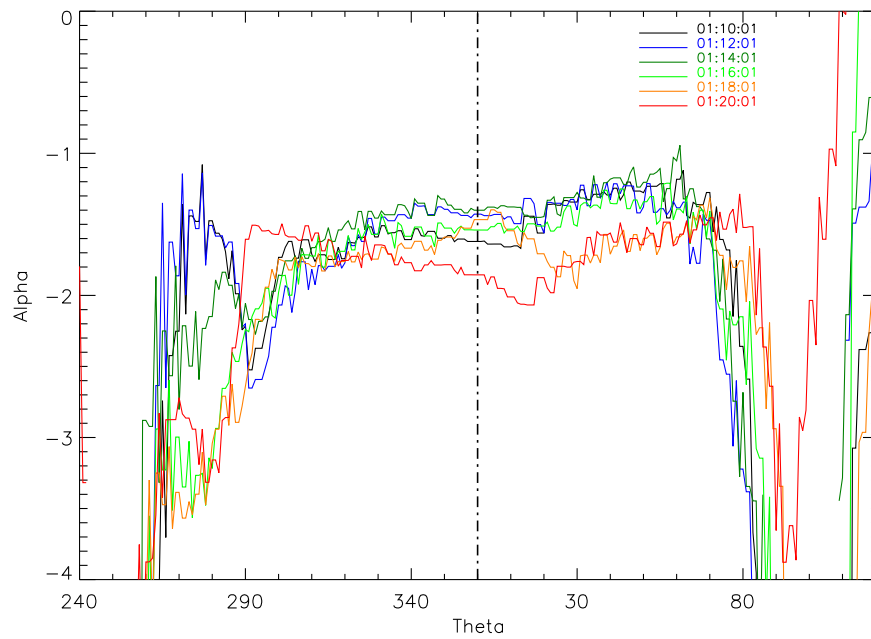


Figure 4.8: Plots of radio spectral index α as a function of θ around an ellipse fitted to the NoRH radio loop for each time interval in Stage 2.

was found that the ellipses were cospatial to within $\sim \pm 6''$ (± 2 pixels at 17 GHz and ± 3 pixels at 34 GHz). It was found that this method was more successful and less time consuming than attempting to fit a spline function to a number of points selected along each individual loop. As mentioned the ellipse parameters are unique to each time interval, as the loop expands and changes in shape over time. As the loop increases in height this results in the emission at the base of the loops moving further round the ellipse (i.e. to greater values of θ for the farside loop legs and to smaller values of θ on the nearside loop legs) caused by moving the centre of the ellipse to keep the point at 0° in place at the loop apex. The loop also widens over time which requires us to alter the semi-major and semi-minor axes to ensure the ellipse fits the shape of the loop. A consequence of these alterations is that the emission at the base of the loops shows a shift in θ over time. With some simple calculations it would be possible to acquire information about the true height and width of the loop. However we wish here to simply show the overall shape of brightness along the loop and the ratio between different bright sources. We point out here, that for panels 3 and 4 on the top at 01:32 and 01:40 we plot two ellipses which fit two loops which can be observed during this period, see details in Stage 3 section. The green ellipse fits the inner of these two loops and blue the outer loop.

Figure 4.7 shows how T_b varies as a function of θ around the ellipse for Stage 2. Plots are shown for values of θ between $\pm 120^\circ$ where the main loop emission is concentrated. The vertical dash-dotted lines show where θ is 0° . Nearside loop legs have values of θ between 240° and 360° and are seen to the left of the vertical line. Emission from the farside loop legs have values of θ between 0° and 120° and are seen to the right of the vertical line. Time increases as the colors move from blue to red. The jagged appearance at small scales along the profile is caused by pixel to pixel variation in brightness temperature, which gives an idea of the variation in magnitude between neighboring pixels. Hence a rough estimate in the error of the brightness can be obtained. The pixel resolution at 17 GHz will result in a large pixel to pixel variation in comparison to that at 34 GHz.

In addition to the profile of T_b along the loop is possible to determine the radio spectral index α along the loop. We first of all convert from T_b to flux and then use the relation

$$\alpha = \frac{\log(F_{17}/F_{34})}{\log(17/34)} \quad (4.1)$$

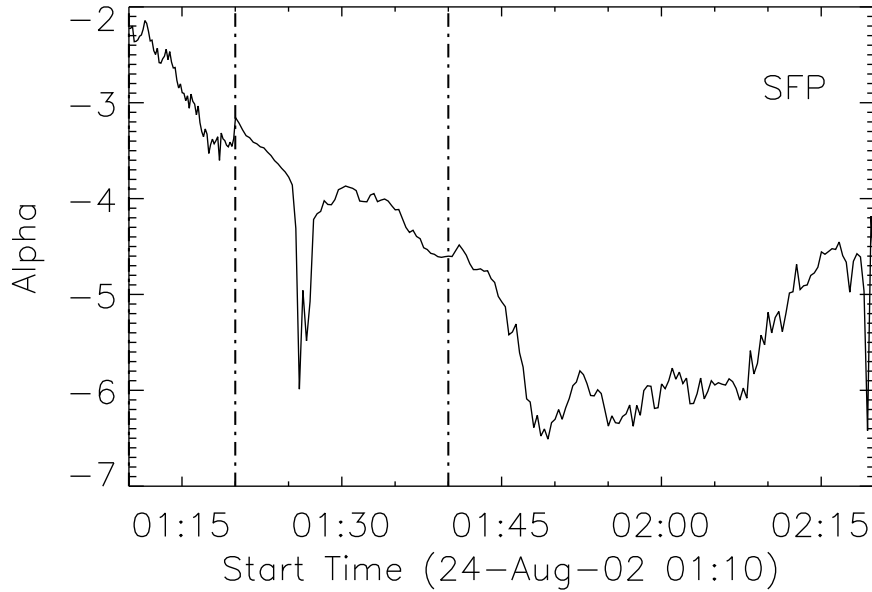


Figure 4.9: Plot shows radio mean spectral index α for the southern footpoint. Vertical lines indicate the separation of Stages 2, 3 and 4.

to determine the radio spectral index α . Figure 4.8 shows plots of α as a function of θ . Between around 300° and 70° α has a value of around -1.5 for all time intervals indicating that the loop is optically thin. There seems to be a slight increase in α as along the farside loop legs such that α is increased by a few decimal places. As we move down the loop legs to where the loop footpoints meet the much fainter disk, the values of α head off to extremes and it is difficult to follow the value of α for the footpoints. To make things simpler we return to the circle defined in Figure 4.5, and find the mean α for the southern footpoint, see Figure 4.9.

From these plots we can see that there is strong emission from southern footpoint, ‘SFP’ ($270^\circ - 310^\circ$). From the profiles of T_b and also from Figure 4.6 that the footpoint source appears more compact at 34 GHz compared to at 17 GHz. This could be the result of radio limb effects or due to thermal gyroresonance, the effect of which would be more prominent at 17 GHz than 34 GHz. There is also a broader peak in brightness along the farside loop from $15^\circ - 65^\circ$ where the emission is copatial with the arcade source, ‘AS’. From the orientation of the TRACE loops we can see that the arcade is not observed straight on, and we are not observing in the plane of the loop. From the orientation of the arcade

Table 4.2: 24th August 2002 - Peaks along loop

Stage	Time Range	Peak	Range
2	01:10 - 01:20	SFP	$260^\circ - 300^\circ$
		LT	$300^\circ - 10^\circ$
		AS	$10^\circ - 70^\circ$
3 (Outer)	01:20 - 01:40	SFP	$250^\circ - 280^\circ$
		LT	$310^\circ - 360^\circ$
		AS	$30^\circ - 95^\circ$
3 (Inner)	01:20 - 01:40	SFP	$275^\circ - 330^\circ$
		LT	$330^\circ - 20^\circ$
		AS	$20^\circ - 60^\circ$
4	01:40 - 02:20	SFP	$260^\circ - 300^\circ$
		LT	$300^\circ - 30^\circ$
		AS	$30^\circ - 70^\circ$

the brightness of the optically thin foreground loops could be enhanced by radiation emitted from background loops. This could account for the broad peak seen along the farside loop leg. We can see that between the farside source, associated with the top of the foreground arcade loops, and the southern footpoint there is another faint source. The brightness of this source increases only slightly along the loop, peaking around 350° , ‘LT’. This source could account for emission that is not enhanced by line of sight effects. Initially the source on the farside loop dominates. As time progresses the brightness decreases for all sources following the trend we observed in Figure 4.5. A more rapid decline is seen for the farside source, resulting in the southern footpoint dominating the emission.

To clarify the relative brightness of each source as a function of time the loop was split into specific ranges of θ corresponding to the maximum brightness of each source. See Table 4.2 for the range of θ chosen for each peak throughout the course of the decay phase. Over the course of the flare three main sources or peaks in brightness were seen along the loop length. These can be separated out quite clearly for Stage 2 as 1) the southern footpoint source (SFP), 2) a faint looptop source appearing mainly around the apex of the loop (LT) and 3) a bright source cospatial with the top of the arcade, which is situated on the farside loop leg (AS). As a quick estimate of the ratio of peak brightness in each source relative to the other two sources, the maximum value of T_b for each peak was found. The results are plotted in Figure 4.10. Blue lines represent ratios taken at 17 GHz and red lines the ratios taken at 34 GHz. Solid lines show the ratio SFP:LT, dotted show the ratio SFP:AS and dashed lines show the ratio AS:LT.

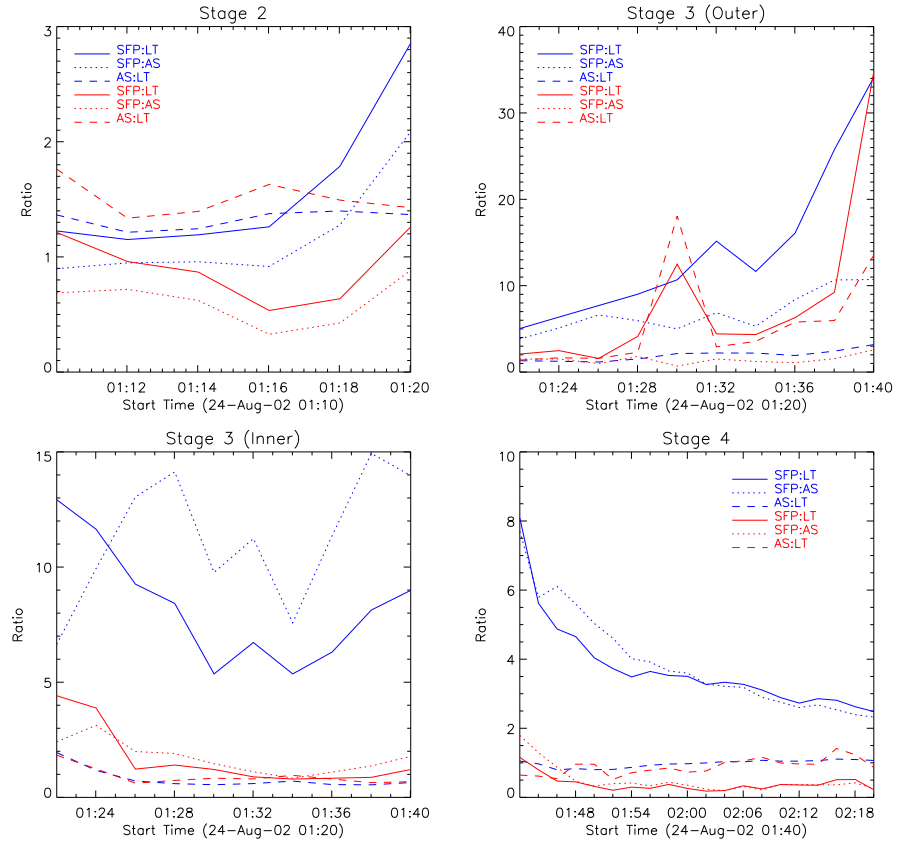


Figure 4.10: Ratios of T_b peaks along loop for Stage 2 (top left), Stage 3 outer (top right) and inner loops (bottom left) and Stage 4 (bottom right). Blue lines represent ratios taken at 17 GHz and red lines the ratios taken at 34 GHz. Solid lines show the ratio SFP:LT, dotted show the ratio SFP:AS and dashed lines show the ratio AS:LT.

If we start first with the comparison of the arcade source with the looptop source, (AS:LT dashed), we see in general the ratio remains around 1.3 for 17 GHz and slightly higher at around 1.5 for 34 GHz. This could suggest that a similar process is affecting the emission in both the arcade and looptop sources. For 17 GHz the ratios SFP:LT (solid) and SFP:AS (dotted) are roughly equal with values of 1.2 and 0.9 respectively from 01:10-01:16. After this the footpoint source becomes relatively strong and the ratios increase to 2.9 and 2.1 respectively. At 34 GHz the footpoint source weakens slightly between 01:10 and 01:16 in comparison to the looptop and arcade sources resulting in a dip in the ratios SFP:LT and SFP:AS from 1.2 to 0.3 and 0.7 to 0.3 before rising to 1.3 and 0.9 respectively. As Figures 4.5 and 4.7 show that the decline in the looptop and arcade sources is smooth and on a similar timescale to one another, this suggests that the evolution of the footpoint source is dominant term of the ratio.

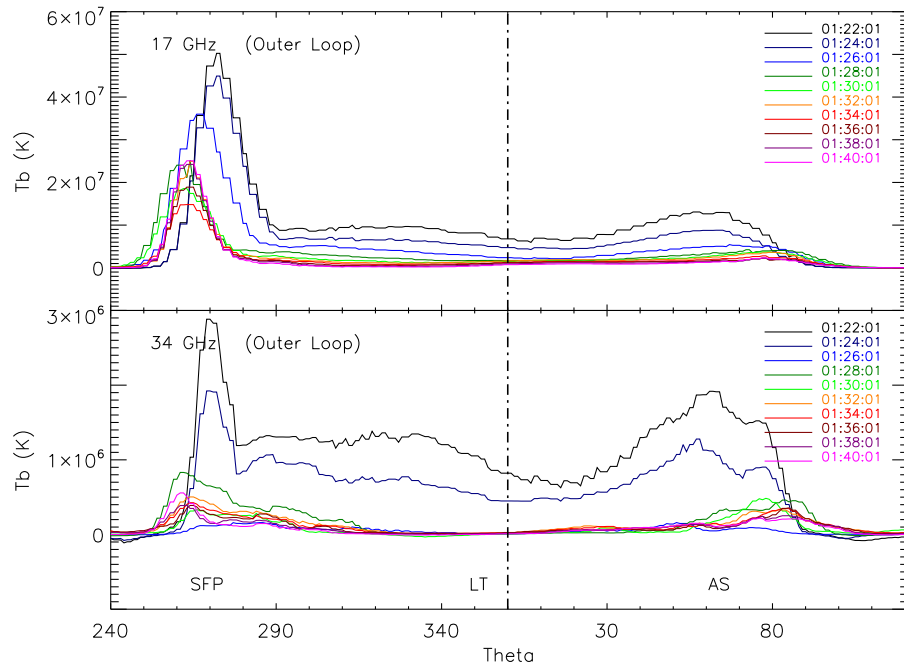


Figure 4.11: Plots of T_b as a function of θ for 17 GHz (top) and 34 GHz (bottom) around an ellipse fitted to the outer loop for each time interval in Stage 3.

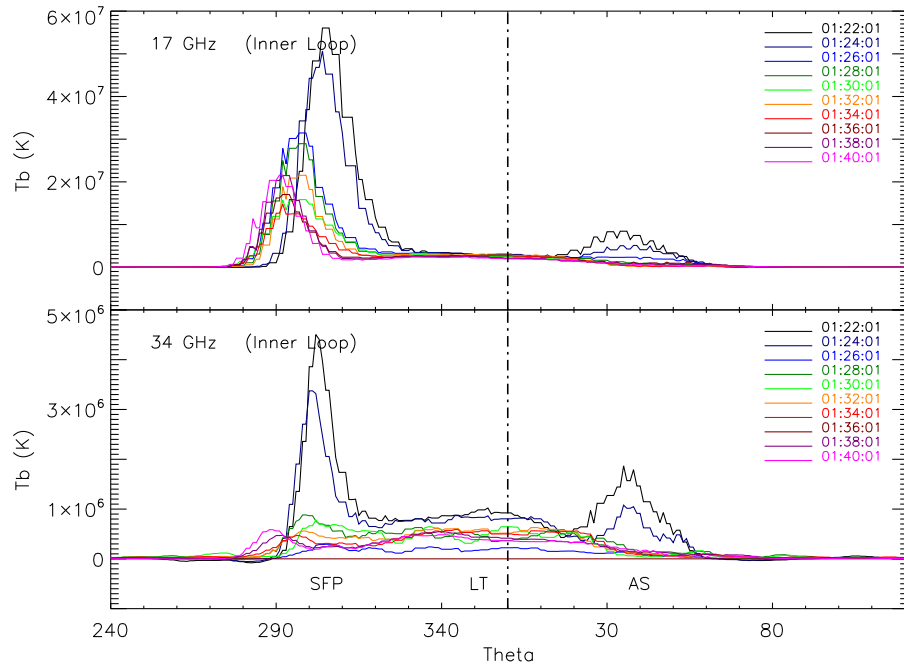


Figure 4.12: Plots of T_b as a function of θ for 17 GHz (top) and 34 GHz (bottom) around an ellipse fitted to the inner loop for each time interval in Stage 3.

Stage 3

During Stage 3 we see a considerable change in the overall morphology of the radio loop at both 17 GHz and 34 GHz. At 01:20 the loop has similar features

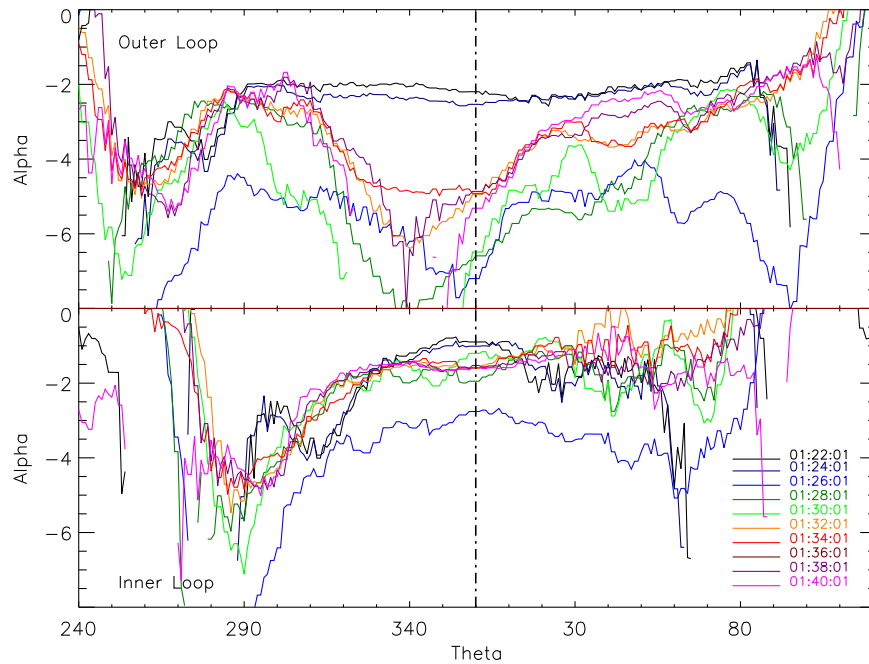


Figure 4.13: Plots of radio spectral index α as a function of θ around an ellipse fitted to the NoRH radio loop for each time interval in Stage 3.

to that in Stage 2, i.e. SFP, LT and AS, see Table 4.2. At 01:24 a second loop appears at lower heights in the corona at around $985''$. This can be seen as early as 01:21 in 34 GHz, as faint emission below the dominant “outer” loop. The “inner” loop begins to dominate first at 34 GHz around 01:25. Meanwhile at 17 GHz the outer loop can be seen to expand out to as far as $1050''$ and is still visible at 01:38. Emission from the inner loop can be seen at 17 GHz from around 01:26. Figure 4.6 shows images at 01:32 and 01:40 showing both inner and outer loops. The blue ellipse drawn on the plots indicates a fit to the outer loop used to create the brightness profile seen in Figure 4.11 and the green ellipse defines a fit to the inner loop used to make Figure 4.12.

For 17 GHz the ratio of AS:LT increases slightly from 1 to 3 as emission in both sources gradually decreases. The looptop emission fades more rapidly than the arcade source. This results in a steeper increase in the ratio of SFP:LT than in SFP:AS which increase from 5 to 35 and 4 to 11 respectively. A similar trend is seen at 34 GHz with ratios of AS:LT increasing 1 to 2, SFP:LT increasing 1 to 35 and SFP:AS increasing 1 to 13. By the end of Stage 3 the outer loop is only just visible at 17 GHz and is at the background level for 34 GHz.

For the inner loop the 17 GHz emission is concentrated predominantly in the footpoint with significantly less looptop and arcade source emission, thus the

Figure has been removed due to Copyright restrictions.

Figure 4.14: Plot showing line profile of brightness at 17 GHz (dashed) and spectral index (solid) as a function of X through the loop apex at 01:30 taken from Karlický (2004).

ratios of SFP:LT and SFP:AS range between 5 and 15. At 34 GHz SFP:LT and SFP:AS gradually decrease from 4 to 1 and 3 to 2.

Note that the inner and outer ellipse fits both pass through the southern footpoint and therefore show a similar profile. From the footpoint/looptop lightcurves in Figure 4.5 we see that there are several peaks of emission at 01:22, 01:27, 01:32 and 01:40. We note that the first peak occurs roughly around the time that the second loop appears.

Figure 4.13 shows the variation of α along the outer and inner loops as time progresses. From the plot for the outer loop the drop in the value of α between 01:24 and 01:26 at the loop apex confirms the rapid decrease of emission at 34 GHz at this position. A gradual decrease of α at the broad peak of emission at 60° shows that for this region the brightness at 34 GHz decreases more quickly than at 17 GHz but is not as rapid as the drop off at the loop apex. At the apex of the inner loop α has a value of around -1. The value of α for the southern footpoint can be followed in Figure 4.9 where it decreases over time indicating a steeper spectrum and less relative flux at 34 GHz. At 01:27 there is a sudden drop in the footpoint emission at 34 GHz and hence a much steeper slope.

A paper by Karlický (2004) also investigates the brightness and spectral index

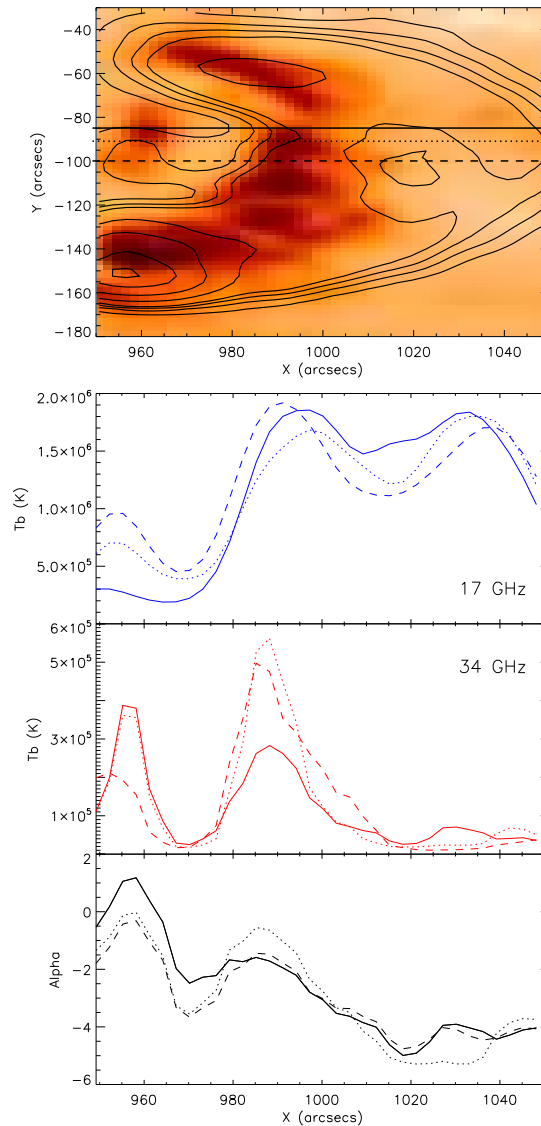


Figure 4.15: Plots showing line profiles of brightness and spectral index as a function of X through the loop apex. Top: plot of T_b at 34 GHz (redscale) with 17 GHz contours at 2, 4, 8, 16, 32, 64, 96% of image maximum at 01:30. Horizontal lines shows line profiles through loop apex at $Y = 86''$ (solid), $92''$ (dotted) and $100''$ (dashed). Corresponding plots of T_b at 17 GHz (blue), 34 GHz (red), and α (black) are shown below.

α in the post-maximum phase of this flare. The analysis concentrates on the looptop emission during the time interval 01:22 - 01:30 i.e. at the times when the second loop appears. A line profile is used with cuts across the width of the loop at the apex from $X = 950$ - $1050''$ at $Y = 86''$. The brightness and spectral index are followed as a function of distance along the line (i.e. as a function of X). At 01:30, the author finds that $\alpha = \sim 0$ for 950 - $990''$ which is interpreted as

free-free emission. For 990-1050'' α is negative, reaching a minimum of -1.31 at 1020'' which is interpreted as optically thin gyrosynchrotron emission, see Figure 4.14. It is suggested that the optically thin gyrosynchrotron looptop source results from a decrease in looptop density such that the gyrosynchrotron emission at 1020'' dominates over the free-free component. The values of α presented in this paper differ from those obtained from our investigation, in that we find that at all points along the loop the emission is optically thin with values of ~ -1 or less.

In order to check that that this is not related to the positioning of the ellipse line profiles for the inner and outer loops, similar line profiles to that in Karlický (2004) were made showing how brightness and spectral index vary as a function of X through the loop apex. Figure 4.15 shows a plot of T_b at 34 GHz (redscale) with 17 GHz contours at 2, 4, 8, 16, 32, 64, 96% of image maximum at 01:30. The solid horizontal line shows $Y = 86''$. Corresponding plots of T_b at 17 GHz (blue), 34 GHz (red), and α (black) are shown below. All points along the loop, i.e. for $X > 980''$, show $\alpha < -1$ indicating the presence of optically thin gyrosynchrotron emission. Around 960'' a small 'footpoint' source is observed, which TRACE images reveal to be from the base of a brightly emitting loop seen at the back of the arcade. A line profile passing through this point (solid line) results in $\alpha \approx 0$. However it appears that there is an offset between the 17 GHz and 34 GHz images, seen most prominently for the background footpoint and around the southern footpoint. In order to align these footpoint sources requires a shift of around 15'', which is greater than our upper limit of alignment error and results in the misalignment of contours along the loop. Considering that it is apparent there are two loop structures present during this time interval, an outer loop which is dominant in 17 GHz and an inner loop 34 GHz, there is no stipulation to say that they should be aligned and in any case realigning the footpoints does not result in a $\alpha = 0$ at any point in the loop. One suggestion could be a difference in overall vertical alignment in comparison to that used by Karlický (2004). At 34 GHz the loop emission does not vary smoothly along the loop but instead is broken into smaller sources. Additional line profiles were also taken at 92'' (dotted) and 100'' (dashed). Regardless, $\alpha < 0$ for all points across the loop. One final suggestion for the discrepancy could be due to the way in which the images were synthesised. As mentioned earlier our images were corrected for instrumental effects caused by such a large radio flux recorded by NoRH. We can infer from Figures 4.14 and 4.15 that our values of T_b are around

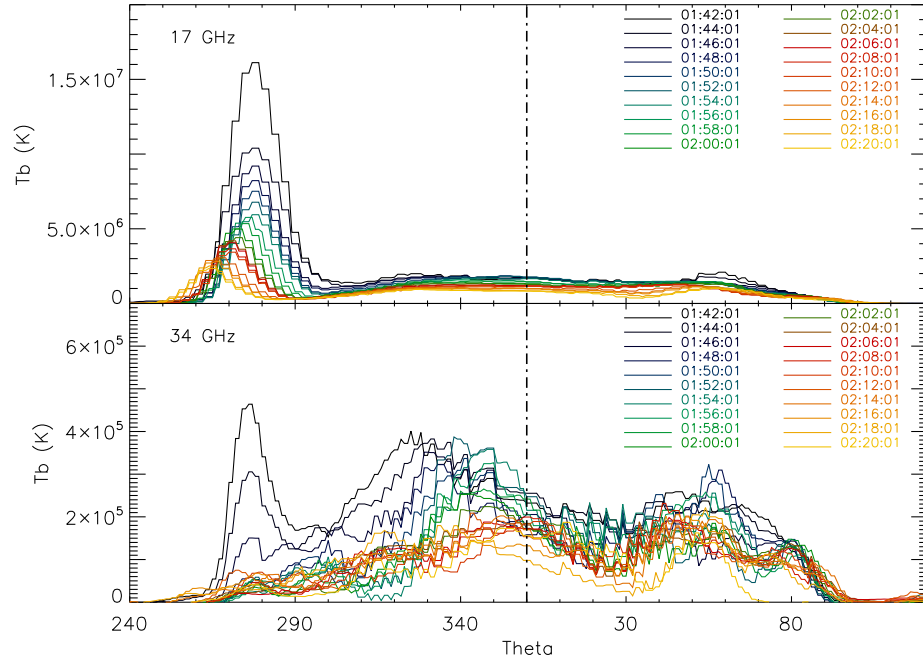


Figure 4.16: Plots of T_b as a function of θ for 17 GHz (top) and 34 GHz (bottom) around an ellipse fitted to the loop for each time interval in Stage 4.

a factor of 2 greater than those from Karlický (2004).

Stage 4

From 01:40 onwards the inner loop forms at greater heights and gradually fades. Images at 01:44, 01:52, 01:58 and 02:20 are shown in Figure 4.6 with blue lines showing the fitted ellipse used to determine the brightness and α profiles shown in Figures 4.16 and 4.17. The dominating feature in the T_b profile at 17 GHz is once again at the southern footpoint. Over time the value of T_b decreases from 2×10^7 K at 01:42 to 3.5×10^6 K 02:20. At 17 GHz the looptop emission varies smoothly along the loop and over time. As the footpoint fades the loop emission is seen more clearly. At 34 GHz the footpoint fades away after 01:46 and emission from the looptop source dominates. As time progresses the peak of this loop emission gradually shifts from the nearside loop leg to the loop apex. From around 01:42 the brightening of an additional loop at both frequencies, to the north of the arcade (mentioned earlier when detailing the TRACE images, see Figure 4.2 and 4.4). It is likely that the bumps in the brightness profile at 34 GHz at 50° and 80° are related to this additional feature and are not attributed to the emission from the flaring arcade. In addition, the distribution of small compact

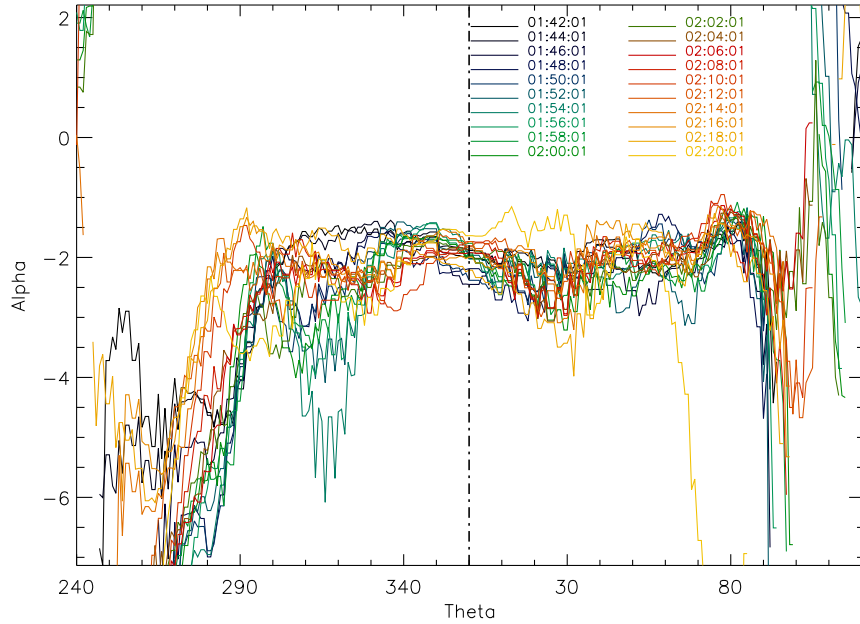


Figure 4.17: Plots of radio spectral index α as a function of θ around an ellipse fitted to the NoRH radio loop for each time interval in Stage 4.

peaks of brightness along the loop could be related to the bright tips of the arcade seen in TRACE images, see Figure 4.2 panels m to p. There is a variation in height of loops along the arcade, which result in the emission from the tip of the arcade occurring at different heights. In TRACE images the loop legs appear to be in absorption (in reverse colour images this appears bright) indicating that the loops are cooling and that the arcade is draining of plasma.

The plots of α show that the loop remains optically thin for all sources. An initial drop in the value of α around 310° to 320° is a result of the unsmooth distribution of 34 GHz emission along the loop. However from around 02:00 the value of α is roughly -2 along the entire loop. The value of α in the footpoint had a value of around -4 indicating a very steep spectrum as the 34 GHz emission is concentrated at the looptops.

4.3.2 NoRP

Images from the Nobeyama Radioheliograph can provide information on the radio spectrum at high frequencies. To determine the spectral shape below these frequencies we require data from the Nobeyama Radiopolarimeters. Figures 4.18 shows plots of flux (top) and polarisation (bottom) at 1, 2, 3.75, 9.4, 17 and

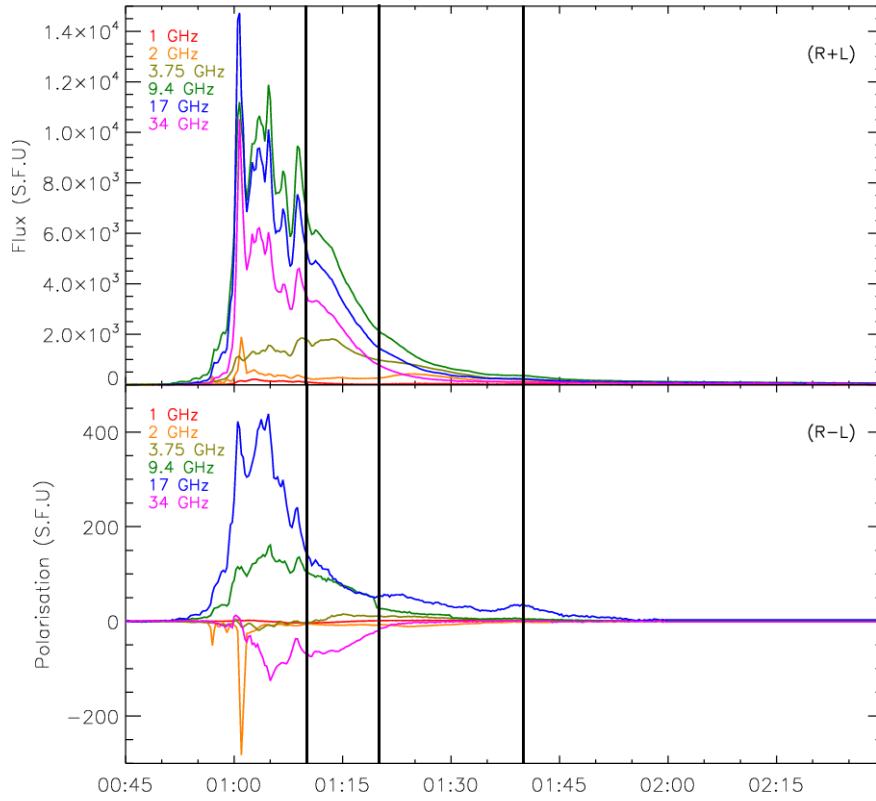


Figure 4.18: Plots of flux (top) and polarisation (bottom) at 1, 2, 3.75, 9.4, 17 and 34 GHz from the Nobeyama Radiopolarimeters. Black vertical lines indicate the separation between stages as before.

34 GHz from NoRP. Black vertical lines indicate separation between stages as before. We can see that the impulsive bursts between 01:00 and 01:10 are also observed at the lower frequencies. Taking this data we can then fit these points using the standard NoRP software. The spectra are made by summing over time intervals equal to those used for NoRH imaging (10s up until 01:20 and 20s thereafter) and normalising. The fitting routine uses the function shown in Equation 4.2, with four fitting parameters (see <http://solar.nro.nao.ac.jp/norp/> for details): α_{tk} , the positive power index at low frequencies (corresponding to optically thick plasma), α_{tn} is the negative power index at high frequencies corresponding to optically thin plasma, $\hat{\nu}$ the turn-over frequency and \widehat{F}_{ν} the turn-over flux density.

$$\begin{aligned}
F_\nu &= \widehat{F}_\nu \left(\frac{\nu}{\widehat{\nu}} \right)^{\alpha_{tk}} \left\{ 1 - \exp \left[- \left(\frac{\nu}{\widehat{\nu}} \right)^{\alpha_{tn} - \alpha_{tk}} \right] \right\} \\
&\approx \begin{cases} \widehat{F}_\nu (\nu/\widehat{\nu})^{\alpha_{tk}} & \text{for } \nu \ll \widehat{\nu} \\ \widehat{F}_\nu (\nu/\widehat{\nu})^{\alpha_{tn}} & \text{for } \nu \gg \widehat{\nu} \end{cases} \quad (4.2)
\end{aligned}$$

Figure 4.19 shows the fitted spectra corresponding to the eight NoRH images in Figure 4.6, taken during the decay phase. As expected the NoRP spectra confirm optically thin emission at the highest frequencies.

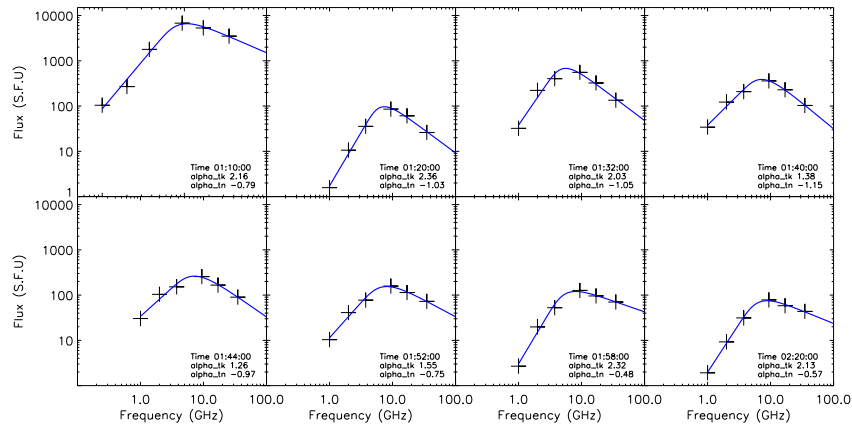


Figure 4.19: NoRP fitted radio spectra for times corresponding to images in Figure 4.6.

Figure 4.20 shows how the four fit parameters vary over time. Firstly note that for all four plots there are certain points which lie off the general trend, most noticeable on the plot for α_{tn} where they have a value of -2.0. These points show times for which the spectral fitting failed to converge on a result. The fitting routine assumes an initial guess for each parameter and when the fit fails to converge the initial guess is returned as the fitted value. Having inspected these individual spectra these points can be discounted from the overall trend. The spectral distribution of points does not appear to vary widely in comparison to time intervals immediately before and after. It is unclear why the fit fails, but as the general trend is upheld we do not strive to remove the points or spend time forcing a fit.

The top left plot shows the peak flux which declines over time, although we note two small bumps in the downward trend occurring around 01:20 - 01:25

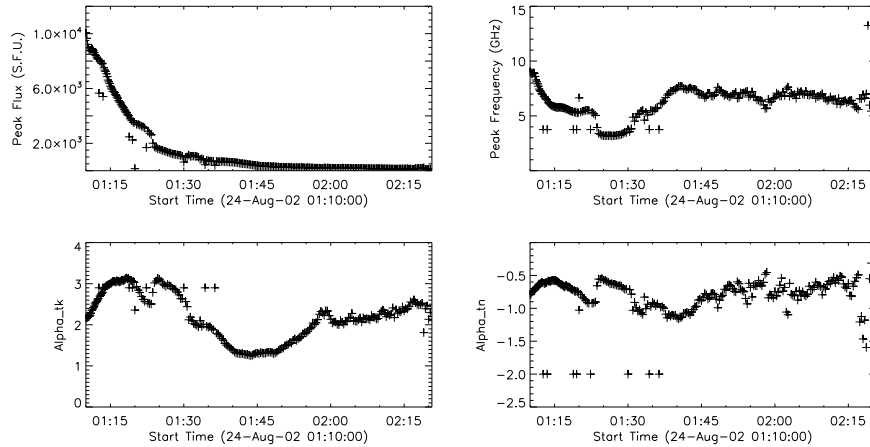


Figure 4.20: Peak flux (top left), peak frequency (top right), α_{tk} (bottom left), α_{tn} (bottom right) parameters from fitted NoRP spectra as a function of time.

and 01:30 - 01:35. These bumps also correspond to features in the position of the peak frequency (top right). In general the peak frequency between 01:10 and 01:28 moves to lower values from 9 GHz to around 3 GHz, before increasing again between 01:28 and 01:40, where it increases to around 7 or 8 GHz. After this the peak frequency shows a very gradual decrease to around 5 or 6 GHz. The two bumps in peak flux also result in dips in the value of α_{tk} and α_{tn} (bottom left and right respectively). For α_{tk} the general trend, excluding the dips, increases from 2 to 3 from 01:10 to 01:20 and then decreases to around 1.3 at 01:45 before increasing again to roughly 2.5 at 02:20. A similar trend is seen for α_{tn} although the change in magnitude varies only between -0.5 and -1.0.

It is possible that the bump observed in the peak flux trend is related to another small injection of energetic particles. Karlický (2004) report the presence of a Type III radio burst occurring at 01:25 in the range 250-450 MHz which could indicate the injection of energetic particles. Using a starting frequency of 450 MHz gives an estimate of local electron density $n = 2.5 \times 10^9 \text{ cm}^{-3}$ where the Type III occurred. At this time RHESSI is still in spacecraft night.

4.4 Hard X-ray Observations

4.4.1 Imaging

In order to model the radio emission from the flare it is important to have an understanding of the physical conditions in the flaring region by obtaining esti-

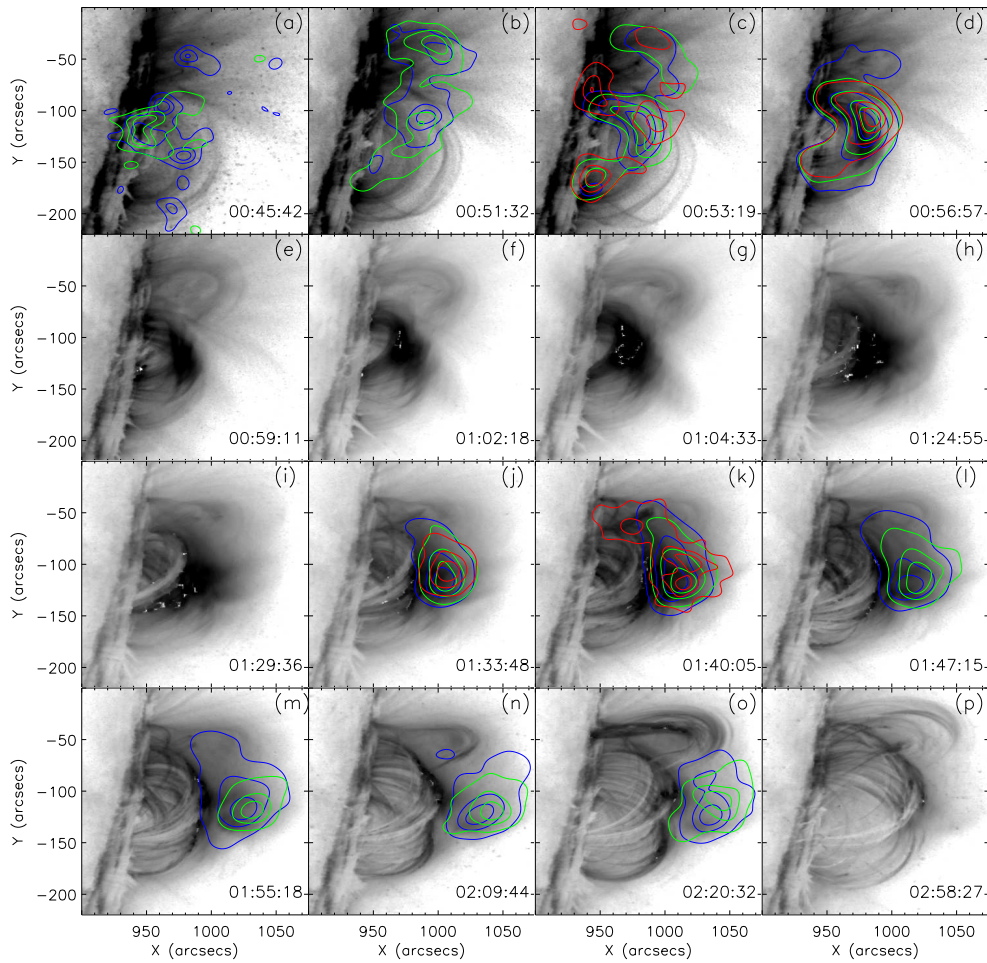


Figure 4.21: TRACE 195Å evolution of 24th August 2002 flare with corresponding RHESSI 16 s image contours overlaid with energy bands 6-12 keV (blue), 12-25 keV (green) and 25-50 keV (red). Times indicated are the start of the RHESSI time integration. Image contours are at 50, 75 and 90% of image maximum intensity. Panel (d) has an additional 25% contour for all energy bands.

mates for parameters such as temperature and density. We can use observations from RHESSI to achieve this. As we can see from the plotted lightcurves RHESSI observed the very early phase of the flare. RHESSI spacecraft night prevented observation of the flare peak, however much of the decay phase has been recorded. RHESSI observations will also allow to determine whether there is ongoing particle acceleration present in the decay phase of the flare by giving us an insight into the thermal or nonthermal nature of the electrons present in the source.

Images of the flare rise and decay phase we made using CLEAN with detectors 4 to 9 giving an angular resolution of 12". Figure 4.21 show the TRACE images with the corresponding RHESSI 16 s image contours overlaid, times indicated are

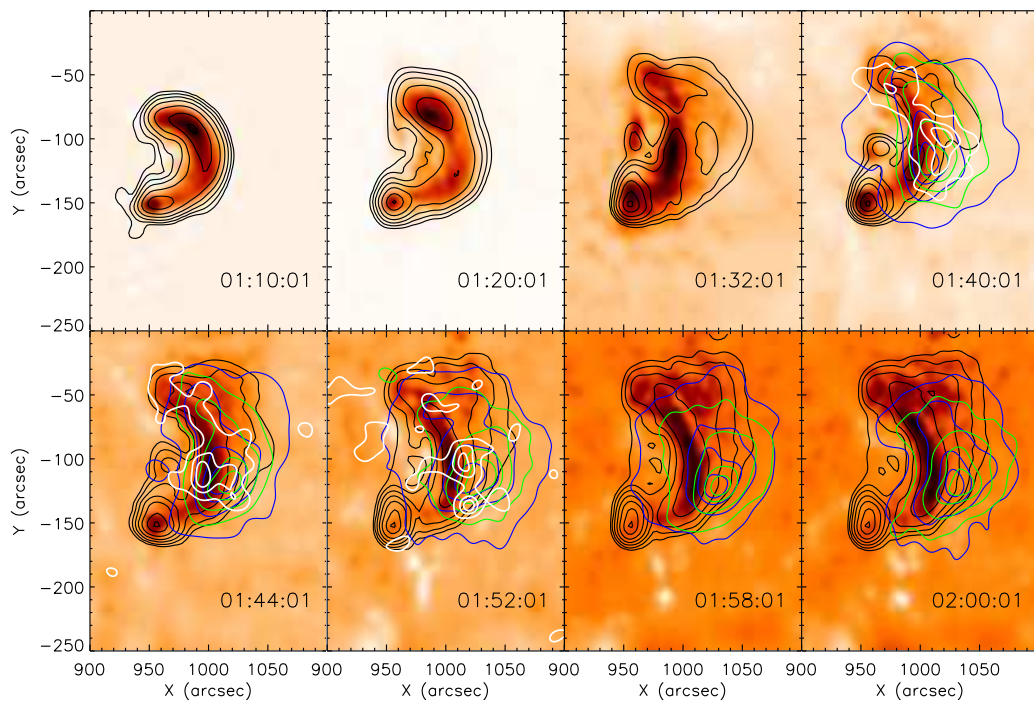


Figure 4.22: Plots show NoRH 34 GHz (redscale) brightness temperature images with NoRH 17 GHz contours overlaid (black) at 2, 4, 8, 16, 32, 64 and 96% of image maximum. RHESSI 6-12 keV (blue), 12-25 keV (green) and 25-50 keV (white) image contours are overlaid for a comparison of radio and X-ray sources during the decay phase. RHESSI contours are at 25, 50, 75 and 90% of image maximum.

the start of the RHESSI time integration. Blue shows 6-12 keV, green 12-25 keV and red shows 25-50 keV. Contours are at 50, 75 and 90% of the image maximum intensity. Panel (d) has an additional 25% contour for all energy bands. As mentioned in Chapter 3 TRACE pointing is accurate to roughly $5''$ – $10''$, cross correlation with other instruments can be carried out to improve alignment. In general the RHESSI images appear to be well aligned with TRACE features. Panel (d) shows RHESSI contours at the 25% level along the entire flare arcade which fit well with the flare arcade seen by TRACE. Also at later times where the large loop feature appears to the north, RHESSI image contours appear to match this to a good approximation.

From Figure 4.21a and b, we see at the start of the flare emission is present at 6-25 keV. From panel a it would appear that this emission could be attributed to the filament visible in TRACE images. In panel c we now see 6-12 keV emission at the looptop and along the farside loop legs. At 12-25 keV emission can be seen

from all along the flaring loop. We also have the addition of emission in the 25-50 keV energy band. From the standard flare model we would expect to see hard X-ray emission at the flare footpoints where flare accelerated electrons precipitate in the dense chromosphere and radiate Bremsstrahlung emission, see Chapter 2. As mentioned in Chapter 1 there have also been observations of coronal hard X-ray sources during flares. From panel c we can see two sources at 25-50 keV occurring at the base of the TRACE loops and a third source occurring at the looptops, slightly above the 6-25 keV emission. By 00:57 emission can be seen all along the loop for all energy bands, see panel d.

Due to RHESSI night no images are available for panels e to i. By 01:34, panel j, emission from all energy bands up to 50 keV are concentrated at the same point at the flare looptops. In panel k at 01:40 we see a small additional source at 25-50 keV which appears to be cospatial with a bright loop to the north of the main arcade. By 01:47, panel j, we see only emission up to 25 keV which is located above the bright, well-defined TRACE arcade cospatial with the hot diffuse TRACE source. This source remains above the flare loops for the remaining images. Note no RHESSI image was available at 02:58 due to another period of RHESSI spacecraft night.

For comparison of the positions of RHESSI X-ray and NoRH radio sources during the decay phase Figure 4.22 shows NoRH 34 GHz (redscale) brightness temperature images with NoRH 17 GHz contours overlaid (black) at 2, 4, 8, 16, 32, 64 and 96% of image maximum. RHESSI 6-12 keV (blue), 12-25 keV (green) and 25-50 keV (white) image contours are overlaid at 25, 50, 75 and 90% of image maximum. Time intervals chosen are the same as those in Figure 4.6. We can see that the RHESSI image contours are situated slightly above the inner loop seen in the NoRH images. All of the emission from 6-50 keV is located in a single source at the loop apex suggesting a hot soft X-ray component consistent with what we would expect in the decay phase of a flare.

4.4.2 Spectroscopy

From RHESSI images alone it is difficult to determine whether sources are thermal or nonthermal in nature. In particular it is difficult to say for definite if the 25-50 keV emission in panel c can be attributed to hard X-ray footpoint and looptop emission. From the TRACE images the flaring arcade appears to be partially occulted, if not at the nearside, then at least to some degree at the

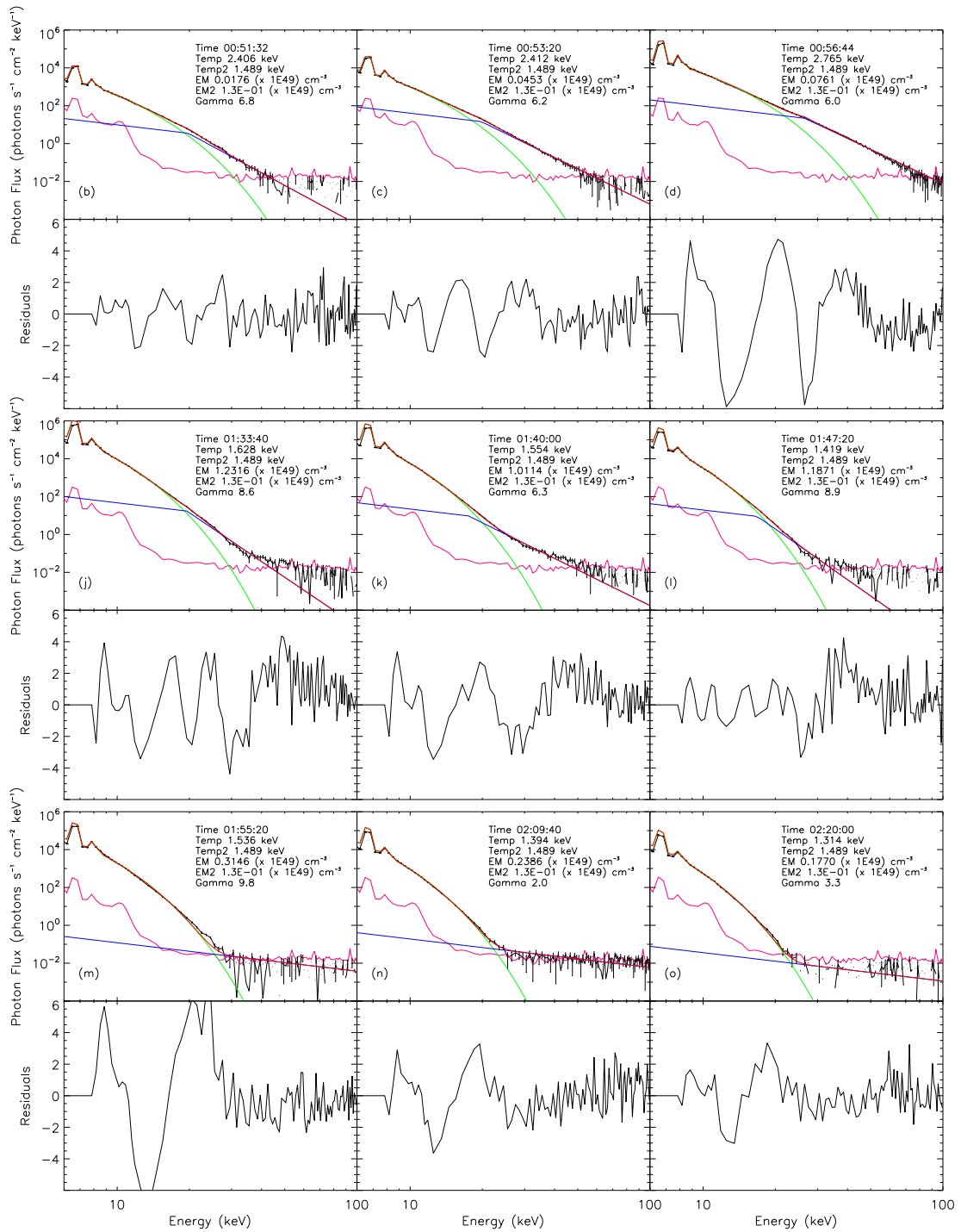


Figure 4.23: RHESSI photon spectra for time intervals corresponding to panels b, c, d, j, k, l, m, n and o of Figures 4.2 and 4.21. Black lines show the background subtracted data and pink the background emission. Plots show an isothermal (green) plus a broken powerlaw (blue) fit to the data. Red shows the overall fit function. Below each fitted spectrum the fit residuals are show.

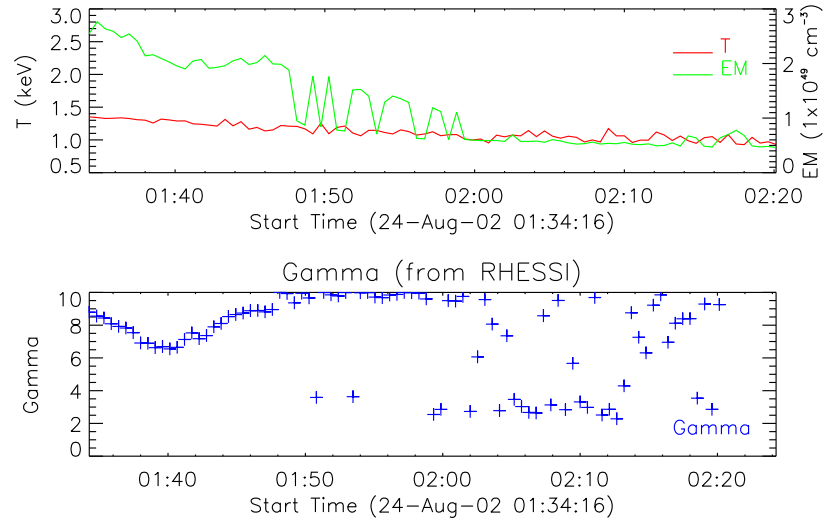


Figure 4.24: Plot shows evolution of RHESSI spectroscopy temperature, emission measure (top) and γ (bottom) fit parameters for the decay phase of 24th August 2002. The combined fit function was an isothermal plus broken power law.

farside. To help clarify this Figures 4.23 and 4.25 show fitted RHESSI spectra which correspond with the 32 s RHESSI images from Figure 4.21 (panels b, c, d, j, k, l, m, n and o indicated on plots). The fitting was carried out using counts from detectors 1, 3, 4, 6, 8, and 9. Energy bins of 0.33 keV at lower energies (6–12 keV) were used to properly fit the iron and nickel lines at 6.7 and 8.0 keV. Above 12 keV energy binning of 1 keV was used. The black lines show the background subtracted data and pink the background emission. For Figure 4.23 isothermal (green) plus broken powerlaw (blue) fit functions were used to fit the data between 8–100 keV. Red shows the overall fit function. Note the presented spectra have been converted to photon space. The thermal component is characterised by a temperature and emission measure, the values of which are stated on each plot ($1 \text{ eV} = 11,604 \text{ K}$). For the broken powerlaw component the spectral index below a freely varying break energy was fixed to 1.5. Above the break energy the spectral energy was allowed to vary, the value of which is shown on each plot. Figure 4.23 shows a different another possible fit to the data (also in photon space). Here two isothermal (light and dark green) fit functions plus a broken powerlaw (blue) were used. Values obtained for temperature, emission measure and γ are stated on each plot. Below each fitted spectrum are the fit residuals to indicate the goodness of the fit.

Firstly we discuss the isothermal plus broken powerlaw fit. The top row cor-

responds to panels b to d in Figure 4.21 taking us up to 00:57 just before RHESSI goes into night (counts were not high enough above background levels to fit at 00:45). From the thermal fit we find an increasing temperature from around 28 MK at 00:51:32 to roughly 32 MK at 00:56:44. In addition to temperature we also obtain a value for emission measure. We can see that although we find a fairly high value for temperature, this is accompanied by relatively low values for emission measures, $1.76 \times 10^{47} \text{ cm}^{-3}$ at 00:51:32 to $7.6 \times 10^{47} \text{ cm}^{-3}$ at 00:56:44, thus indicating a small quantity of hot plasma. The values obtained for γ from the broken powerlaw fit are around 6 which could be considered to be a fairly soft photon spectral index. We mentioned before the sources present at 25-50 keV in panels c and d. From these fits we can see that the 25-50 keV range still has a large thermal component but also contain a large contribution from a nonthermal fit. From this fit alone it is still difficult to separate thermal and nonthermal sources. Provided there are higher enough counts, imaging spectroscopy could resolve this uncertainty. However as these time intervals fall into the rise/impulsive phase of the flare we do not pursue that route.

The middle row of spectra refers to panels j to l in Figure 4.21. For the first 2 time intervals there is still 25-50 keV present in the images, mainly concentrated at the looptop. By 01:33:40 the temperature has dropped to around 13 MK. In contrast the emission measure has increased, now $1.2 \times 10^{49} \text{ cm}^{-3}$, indicating a large volume of plasma emitting at lower temperature than at previous times. We see now that for these times the 25-50 keV energy band is only just above the background level and is mostly dominated by a powerlaw component. The spectral index is still rather soft with values of 8 and 6 at 01:33:40 and 01:40. By 01:47:20 (panel l of Figure 4.21) the 25-50 keV emission fitted by a powerlaw component is at the background level. For times beyond this we see that the emission is entirely dominated by an isothermal component which is present up to around 25 keV. In the bottom the row the temperature is around 15 MK and the emission measure has decreased to $0.17 \times 10^{49} \text{ cm}^{-3}$ at 02:20.

Figure 4.24 shows the overall trend of temperature (red), emission measure (green) and γ (blue) fit parameters for the isothermal plus broken powerlaw fits to spectra from the flare decay phase. There is a decreasing temperature trend from 16 MK at 01:34 to 12 MK at 02:20. The emission measure also decreases over time from $2.8 \times 10^{49} \text{ cm}^{-3}$ at 01:34 to $0.5 \times 10^{49} \text{ cm}^{-3}$ at 02:20. The decrease in emission measure either indicates a decrease in the volume of emitting plasma or a decrease in the ambient plasma density. From TRACE images we observe that

the post flare arcade loops are forming at greater heights in the corona resulting in a wider, taller arcade. We would expect therefore that the soft X-ray emitting volume should remain at least fixed, if not increased over the course of the decay phase. From the 25% level contours in Figure 4.22 the source appears to increase slightly over time. Thus a decreasing emission measure suggests that the ambient density is decreasing.

From the plot of photon spectral index, we can see that from 01:34 to around 01:47 γ has a value between 6 and 9. This indicates a very soft hard X-ray spectrum. By inspecting plots of the fitted spectra we see the powerlaw component is unable to fit the data well at the highest energies. This is seen clearly in the middle 3 panels of Figure 4.23. In addition to the fitted spectra Figure 4.23 shows the fit residuals. We can see that there are large ranges over which the fit deviates considerably from the observed data. The breakdown of the fit at high energies is also reflected here. From these plots it appears that the powerlaw is fitting part of the thermal spectra and missing the powerlaw tail seen at energies of around 40-50 keV. After 01:47 the value of γ can be seen to jump around drastically. It flips between fitting the background and giving a γ value of around 3 and fitting part of the thermal spectrum, when the isothermal fit function is unable to characterise the thermal component of the flare, resulting in a much higher value of γ .

All in all the isothermal plus broken powerlaw fit function has problems fitting the entire spectrum and so we tried a number of other fit functions. We found that the addition of a second isothermal component gave a better fit to the data. Straight away we can see that the inclusion of a second isothermal fit function greatly improves the residuals for all time intervals. There are no longer large peaks and troughs in the residuals where the model overestimates or underestimates the observed data over broad energy ranges. Instead the residuals appear much more random in nature indicating a better fit.

For the first row we find temperatures up to 67 MK and 24 MK at 00:56:44 indicating with emission measures of $8.8 \times 10^{46} \text{ cm}^{-3}$ and $3.49 \times 10^{48} \text{ cm}^{-3}$ respectively. At this time there is still a powerlaw component present which has a value of 5.5 slightly harder than for the isothermal plus broken powerlaw fit. For times after RHESSI night the two temperature components have dropped to 15 MK and 30 MK with emission measure values of $5.58 \times 10^{49} \text{ cm}^{-3}$ and $8.4 \times 10^{47} \text{ cm}^{-3}$ respectively at 01:33:40. At this time the spectral index is quite hard with a value of 2.9. By 01:47:20 the spectrum is almost entirely dominated

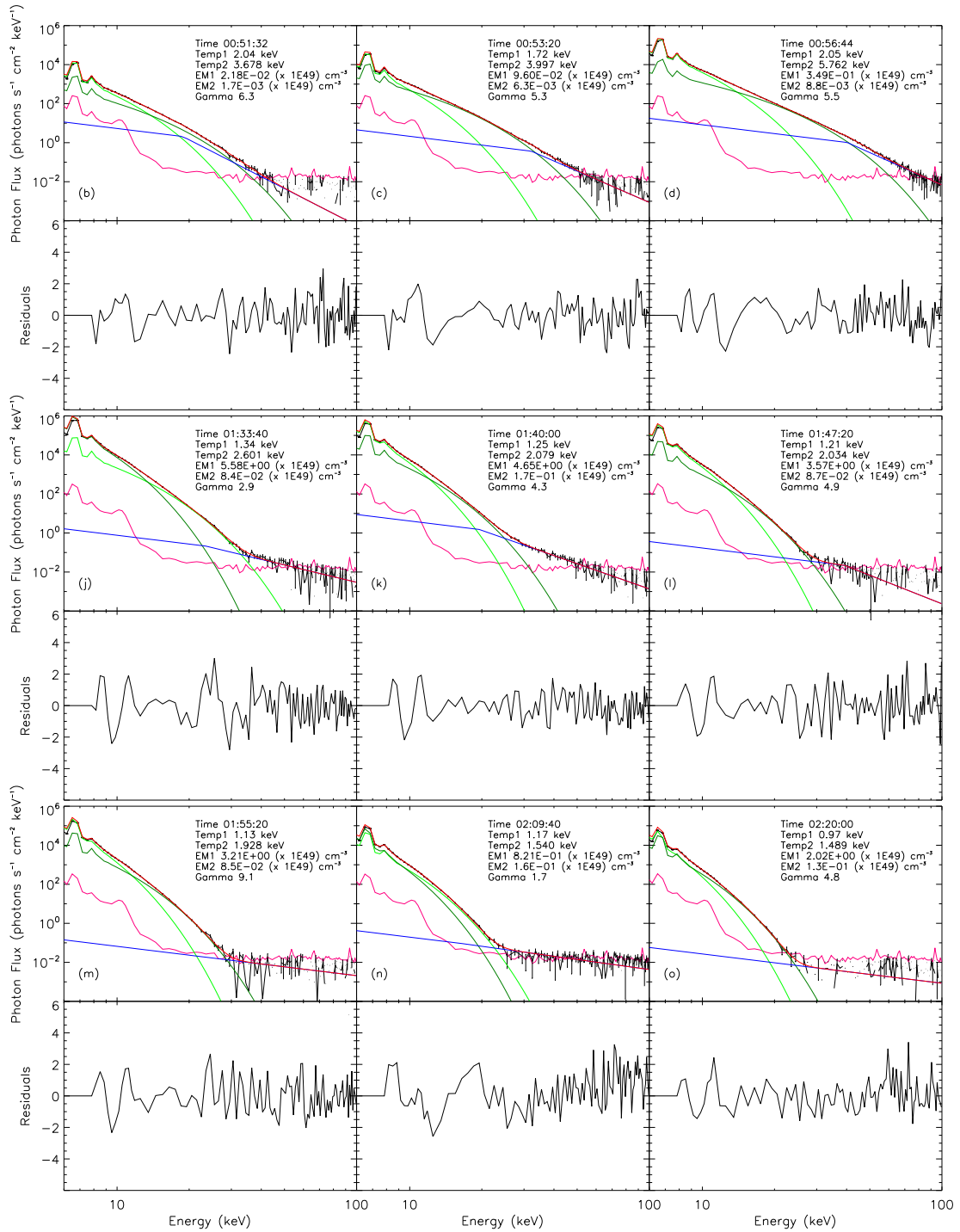


Figure 4.25: RHESSI photon spectra for 24th August 2002 for time intervals corresponding to panels b, c, d, j, k, l, m, n and o of Figures 4.2 and 4.21. Black lines show the background subtracted data and pink the background emission. Plots show two isothermal (light and dark green) plus a broken powerlaw (blue) fit to the data. Red shows the overall fit function.

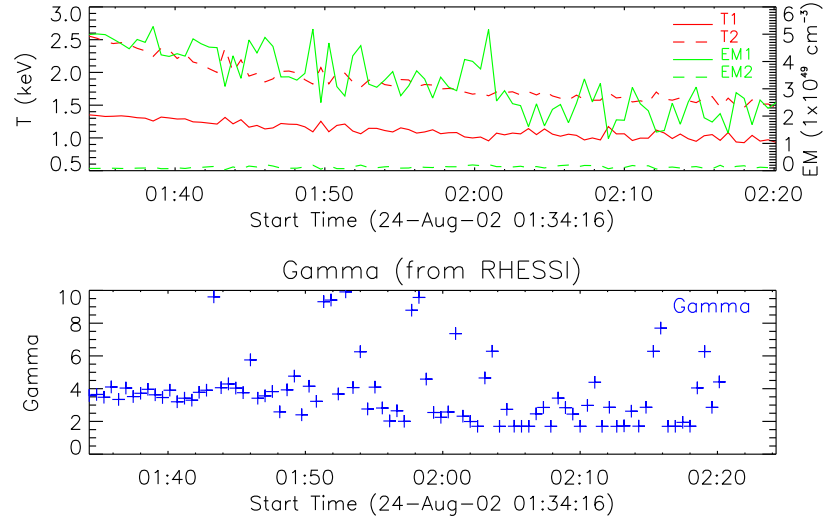


Figure 4.26: Plot shows evolution of RHESSI spectroscopy temperature, emission measure (top) and γ (bottom) fit parameters for the decay phase of 24th August 2002. The combined fit function was two isothermals plus a broken power law.

by thermal emission as with the previous fit. By 02:20 the temperature has cooled to 11 MK and 17 MK with emission measure values of $2 \times 10^{29} \text{ cm}^3$ and $1.3 \times 10^{49} \text{ cm}^{-3}$ respectively.

Figure 4.26 shows the overall trend of temperature (red), emission measure (green) and γ (blue) fitted spectral parameters for the two isothermal plus broken powerlaw fit during the flare decay phase. The corresponding temperature and emission measure from the two isothermal components are distinguished by solid and dashed lines, indicated on the plot. We see straight away that the cooler temperature component, T_1 , slowly decreases from 16 MK to 12 MK with a corresponding emission measure which also decreases from roughly $5 \times 10^{49} \text{ cm}^{-3}$ to $2 \times 10^{49} \text{ cm}^{-3}$. We note that the T_1 has a similar temperature trend to that of the thermal component in the previous isothermal plus broken powerlaw fit, but has a much greater emission measure. From this plot we also see that the addition of a second isothermal component results in a very hot temperature component, T_2 which decreases from 30 MK at 01:34 to 18 MK at 02:20. The emission measure associated with T_2 is much lower with a value of around $0.1 \pm 0.05 \times 10^{49} \text{ cm}^{-3}$ throughout the decay phase indicating a smaller volume of plasma that is emitting at high temperatures. Between 01:34 and 01:47 the value of γ lies between 3 and 4. After this point the flux at higher energies is at the background level and the fit starts to produce spurious results as it fits

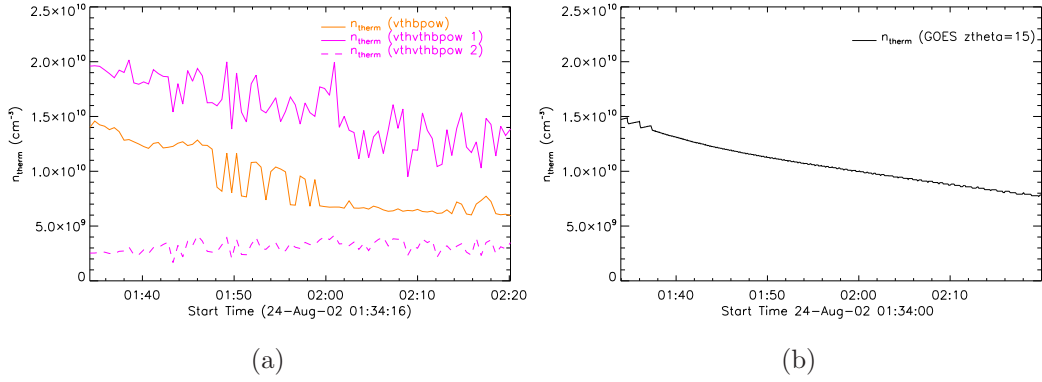


Figure 4.27: Thermal electron density calculated from RHESSI (right) and GOES (left). Orange shows the thermal density from RHESSI isothermal plus broken powerlaw fit. Pink solid shows thermal density from low temperature, high EM component of the double isothermal plus broken powerlaw fit. Pink dashed shows the corresponding thermal density from the high temperature, low EM component.

the background.

4.5 Discussion of plasma parameters

Thermal electron density

In order to model the radio emission from the loop it is necessary to determine some plasma parameters such as the ambient electron density. From RHESSI images of the decay phase the 50% contours outline a source area of around $70'' \times 70''$ situated at the looptops. Taking the volume to be a $70''$ cube and using an estimate of EM from RHESSI spectroscopy we can determine the ambient density using

$$EM = \int n^2 dV \quad (4.3)$$

Figure 4.27(a) shows the thermal density from the RHESSI isothermal plus broken powerlaw fit in orange. Pink solid shows the values calculated from the low temperature, high EM component of the double isothermal plus broken powerlaw fit. Pink dashed shows the thermal density from the high temperature, low EM component of the double isothermal plus broken powerlaw fit. As expected the values calculated from the single isothermal fit show an average of the density values determined from the high and low temperature components of the double

isothermal fit. The trend is weighted towards the higher density component as $EM = n_1^2 V_1 + n_2^2 V_2$, where n_1 is for the low temperature component and n_2 is for the high temperature component. Note we have assumed that the two temperature components are emitted from a similar volume size. It would be difficult to confirm otherwise from the available images. We have also assumed a filling factor of one. We do not present EUV spectroscopic observations to prove otherwise. However we note for example that a filling factor of 0.01 would result in a factor of 10 difference to the density value.

We can also obtain an estimate of density, in a similar manner from the EM calculated from the GOES lightcurves. Figure 4.27(b) shows the density values obtained using GOES data. In doing this we assume that GOES records the soft X-ray flux emitted from the whole arcade as it cools. From TRACE images the observed width and length of the arcade is around $75''$ and $60''$ respectively. For a viewing angle of 15° we estimate the real width and length of the arcade to be $77''$ and $230''$. This is consistent with the flaring arcade in the Bastille day flare (14th July 2000) which had a length of $250''$ (Fletcher & Hudson 2001). For an arcade of this length situated on the limb, the loops furthest round the limb are required to reach a height of around $30''$ in order to be observed above the limb. The observed height from loops at the front of the arcade is around $60''$, which we assume to be approximately accurate. Assuming all loops along the arcade reach a similar height, we expect that the entire arcade is at least partially visible above the limb. Using a measure of volume $77'' \times 230'' \times 60''$ we obtain a measure of the thermal density.

Delta

From the radio spectral index α we can determine the electron spectral index δ using the quick formula (Dulk 1985)

$$\delta = -1.1(\alpha - 1.2) \quad (4.4)$$

From Figures 4.8, 4.13 and 4.17 we can see that the values of α for the looptop and arcade source are more or less consistent with one another. In addition, Figure 4.28 shows that the looptop (dashed) and arcade source (dotted) have a similar time profile which only differs in order of magnitude, the ratio of which varies smoothly. This suggests a similar process is occurring in these two sources. It is likely that the difference in the order of magnitude is as a result of line

of sight effects due to the orientation of the arcade. As the plasma is optically thin the arcade source could be enhanced by emission from arcade loops situated in the background. The source associated with the radio loop apex is generally fainter than the arcade source and we suggest that this part of the radio loop is not enhanced by line of sight effects. Assuming that this is the case we proceed to determine δ for the looptop (LT) and southern footpoint (SFP) sources. The results are shown in Figure 4.28. For Stage 3, values from the inner loop are used to follow the evolution as the 34 GHz very quickly drops in the outer loop giving a very steep spectrum. The looptop δ remains between 3 and 4 throughout the decay phase whilst the southern footpoint source δ increases from 4 to 8 between 01:10 and 01:48 after which it slowly decreases back to 4 at 02:20.

Nonthermal electron density

Another important parameter is the nonthermal electron density N which gives the total number of electrons above a low energy cutoff E_0 . For gyrosynchrotron emission we can use approximation from Dulk & Marsh (1982)

$$\frac{\eta_\nu}{BN} \approx 3.3 \times 10^{-24} 10^{-0.52\delta} (\sin \theta)^{-0.43+0.65\delta} \left(\frac{\nu}{\nu_B} \right)^{1.22-0.90\delta} \quad (4.5)$$

and

$$\eta = \frac{T_b k \nu^2}{L c^2} \quad (4.6)$$

where L is the line of sight distance through the source and θ is the viewing angle. We can rearrange to find N . For the Dulk & Marsh (1982) expression a low energy cutoff of 10 keV was used. For consistency with model input parameters used in the following Chapter, Figure 4.28 shows the nonthermal electron density using $E_0 = 50$ keV. It is important to point out that this expression is only an approximation which, in particular, assumes that the resulting spectrum is a power law with a constant value for α . For full expressions defined in Ramaty (1969) α is frequency dependent. We discuss this further in the following Chapter. Using an arcade length of 230'' gives $L = 1.6 \times 10^{10}$ cm. For the looptop source we use $B = 150$ G. For the footpoint source we use $B = 800$ G and $B = 1000$ G, distinguished by the black and blue solid lines on Figure 4.28(bottom) respectively. These are close to values used by previous authors

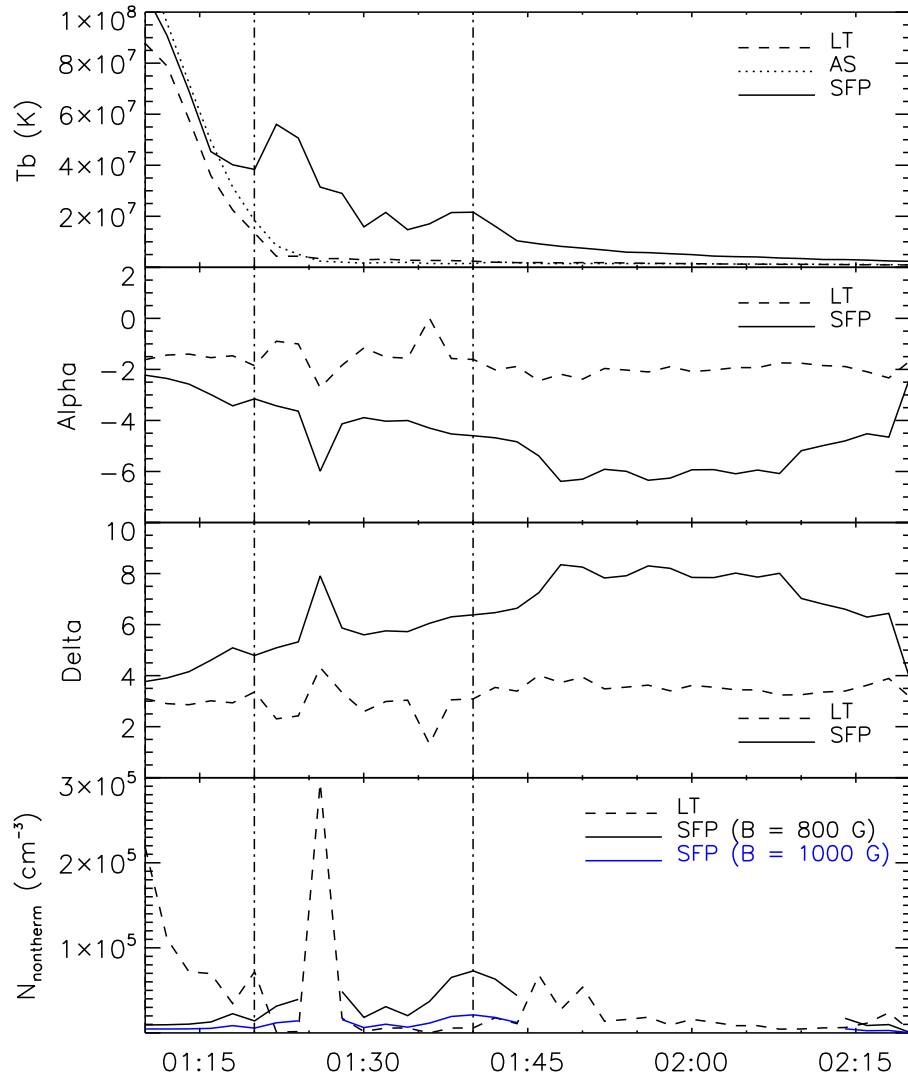


Figure 4.28: From top to bottom plots show T_b , α , δ , N_{nontherm} for looptop (dashed) and southern footpoint (solid) determined from observations with $\nu = 17$ GHz. Top plot also shows T_b for the arcade source (dotted). The looptop N_{nontherm} was calculated using $B = 150$ G. The southern footpoint N_{nontherm} was calculated using $B = 800$ G (black) and $B = 1000$ G (blue). Values of N_{nontherm} are calculated using $E_0 = 50$ keV.

(Tzatzakis et al. 2006; Reznikova et al. 2009) which were determined from MDI images from two days before the event. Equation 4.5 is only valid for $2 \leq \delta \leq 7$. For the footpoint source some values of δ exceed 7 and so we are unable to determine N . For the looptop source N decreases from around $2 \times 10^5 \text{ cm}^{-3}$ to a value of around a few times 10^4 cm^{-3} at 01:20 where it remains fairly constant

for the rest of the decay phase. N in the footpoint source increases from around $1 \times 10^4 \text{ cm}^{-3}$ to $7 \times 10^4 \text{ cm}^{-3}$ at 01:40 for the case where $B = 800 \text{ G}$ and $5 \times 10^3 \text{ cm}^{-3}$ to $2 \times 10^4 \text{ cm}^{-3}$ for $B = 1000 \text{ G}$. Although we are unable to determine values between 01:44 and 02:14 we expect that the value for N slowly decreases.

4.6 Conclusions

In this Chapter observations have been presented of a GOES X3.1 limb flare that occurred on the 24th August 2002. The flare had an associated CME which lifts off in the impulsive phase of the flare resulting in a large post flare arcade. TRACE images show that the arcade is orientated such that we are not perpendicular to the plane of the arcade loops. Using TRACE images we see the arcade forming at greater heights in the corona due to the reconnection of subsequent magnetic field lines.

Nobeyama observations of the event show a resolved loop at 17 GHz and 34 GHz. During the impulsive phase (Stage 1) a series of radio bursts are observed at radio frequencies. Observations from SONG instrument onboard CORONAS-F show corresponding hard X-ray bursts which are delayed on the order of seconds with respect to the radio bursts (Reznikova et al. 2009). Melnikov et al. (2005), Reznikova et al. (2009), and Tzatzakis et al. (2006) show that during these bursts the spatial distribution of radio brightness varies along the loop. In the rise phase of each burst the emission is dominant in the southern footpoint. At the peak of each radio burst the emission at 17 GHz is at the looptop whilst at 34 GHz the emission is situated at the footpoints. In the decay phase the footpoint emission is reduced resulting in a relative brightening of the looptop at both frequencies. The characteristics of this variation reveals information regarding the acceleration mechanisms and transport effects occurring in the loop. Each of the papers mentioned above attempts to reproduce the observations using Fokker-Planck modeling, this shall be discussed further in the following Chapter 5.

For this Chapter we concentrated on the decay phase of the flare from 01:10 to 02:20, which we separated into Stages 2, 3 and 4. We established three main sources of brightness distributed along the loop. 1) A bright source at the southern footpoint which is dominant at 17 GHz throughout most of the decay phase. At 34 GHz the footpoint dominates from around 01:20 until 01:32 after which it

fades to the level of the background. 2) A bright source situated slightly along the farside loop leg which is seen to be cospatial with the front of the flaring arcade. This source is seen to move along the radio loop as the arcade forms from west to east. 3) A fainter source situated at the loop apex. In addition to the distribution of brightness along the loop, the loop morphology changes. Between 01:10 and 01:20 (Stage 2) a single radio loop is observed. In Stage 3 a second radio loop appears below the existing radio loop. This inner loop can be seen as faint emission as early as 01:21 and becomes dominant, first at 34 GHz, at around 01:25. At 17 GHz the outer loop can be seen to extend out to $1050''$ before fading away.

The ratio of brightness between loop sources can help us understand the processes occurring during the decay phase. At 01:10 the arcade source is slightly brighter than the footpoint source at both 17 GHz and 34 GHz. At 17 GHz the arcade source emission decays more rapidly than the southern footpoint source and the footpoint can be seen to dominate from 01:16 onwards. It reaches around an order of magnitude brighter than the looptop and arcade sources during Stage 3 before fading in Stage 4. At 34 GHz the emission in the arcade source remains relatively stronger than the southern footpoint for a longer period of time than at 17 GHz. Only after 01:20 does the footpoint source dominate reaching only a factor of 3 or 4 greater in Stage 3 before the footpoint fades in Stage 4. At all times the southern footpoint emission is greater than the looptop source.

Throughout the decay phase the arcade and looptop sources show a similar trend in brightness and in spectral index suggesting that a similar process is occurring in both sources. Due to the orientation of the arcade and the presence of optically thin plasma we could interpret the difference in magnitude as line of sight effects. The arcade source could be enhanced by brightly emitting loops situated in the background whereas the looptop emission could occur from a portion of the arcade that is not enhanced by line of sight effects. As the decay phase progresses the ratio of these two sources gradually approaches unity.

The evolution in Stage 2 (01:10 and 01:20) could be interpreted as the tail end of the trend observed in the individual subpeaks during impulsive of the flare, where emission is seen at the looptop during the decay of each peak. The decay occurs more rapidly at 17 GHz. Melnikov et al. (2002b) suggested that an optically thin looptop source required an enhancement of energetic particles at the loop apex. This could be an intrinsic property of the acceleration mechanism resulting in an anisotropic or pancake distribution. Alternatively the enhancement

could be produced by trapping of energetic particles. To investigate this we can determine the trapping time for electrons of varying energy.

Trapping of particles in a loop structure occurs as a result of a converging magnetic field. Trapping is pitch angle dependent, however particles of all energies are equally trapped. Particles with a pitch angle less than a critical angle α_0 escape through the loss-cone whereas those with a pitch angle greater than α_0 are mirrored and trapped. α_0 is related to the magnetic mirror ratio R

$$R = \frac{B}{B_0} = \frac{1}{\sin^2 \alpha_0} \quad (4.7)$$

where B_0 are the magnetic field strengths at the loop apex and for the region of interest. Particles with mirror points occurring in regions with stronger field i.e. $B_{mirror} > B$ will pass through the region of interest. Particles can be scattered into the losscone by a number of processes, for example plasma turbulence, resonant wave-particle interactions and Coulomb collisions, which alter the pitch angle.

Table 4.3: Energy Loss Time (τ)

Energy	(seconds)	(minutes)
10 keV	6	0.1
100 keV	204	3.4
1 MeV	2631	43.9

Particles with a higher energy undergo fewer collisions and remain in the trap for a longer period of time. For nonrelativistic electrons, the energy loss timescale is roughly twice that of the trapping timescale due to Coulomb collisions (Benz 2002). In such a scenario, electrons can be scattered into the loss cone before losing all their energy in the trap. At relativistic energies the scattering timescale varies as the square of the energy whilst energy loss varies as energy. In this scenario, energy loss can occur before the electron is scattered into the loss-cone (Krucker et al. 2008c). Table 4.3 shows the energy loss timescales for electrons with energies of 10 keV, 100 keV and 1 MeV in a coronal density of $n = 1 \times 10^9 \text{ cm}^{-3}$. These values were calculated using an expression from Bai & Ramaty (1979).

$$\frac{\partial E}{\partial t} = 4.9 \times 10^{-9} E^{-1/2} n \quad (4.8)$$

for $E \lesssim 160$ keV

$$= 3.8 \times 10^{-10} n \quad (4.9)$$

for $E \gtrsim 160$ keV

$$(4.10)$$

$$\tau = \frac{E}{\partial E / \partial t} \quad (4.11)$$

For an X-class flare it is not unreasonable to expect particles to be accelerated up to energies as high as several MeV which, if trapped, could remain at the looptop for tens to hundreds of minutes before thermalising. We have considered here only the energy loss by Coulomb collisions however other energy loss mechanisms may also be relevant. For the electron energies considered here the Synchrotron energy loss timescales are longer than those for collisions. In addition to energy losses the electrons can be scattered into the losscone and are lost from the trap. For the highest energy electrons it is likely that energy loss will occur before escaping the trap.

Flare emission at 25-50 keV is observed at the southern footpoint in the early impulsive phase around 00:53. It is difficult to determine whether the footpoint source to the north can be attributed to the flaring arcade, or whether it is a feature of a structure the north of the arcade. There is also a source in the corona. At 00:57 emission up to the 25-50 keV band is present along the entire loop although we note that the highest value contours are situated at the looptops. By the time RHESSI images are available in the decay phase, emission up to the 25-50 keV band is concentrated in a single source in the corona, slightly above the inner loop. RHESSI spectroscopy using a double isothermal plus broken power law suggests that there is a nonthermal component present up until 01:47 with a spectral index of around 4. It should be pointed out that both the radio and X-ray emission at this time appear to be concentrated around the hot diffuse source visible in the TRACE 195Å images and is not cospatial with the more clearly defined arcade loops which we associate with emission at 10^6 K. It is likely that as the arcade loops form at greater heights in the corona the geometry is such that line of sight effects no longer result in an enhancement of the arcade source

over the looptop source as the radio emission decays. In addition it is clear that the arcade loops reach different heights, this is particularly noticeable in the late decay phase. This could explain the ratio of SFP:AS tending to one.

During the decay phase we do not observe hard X-ray emission at the footpoints but the southern footpoint still remains strong at radio frequencies. There are a number of possible scenarios. 1) The convergence of the magnetic field could be strong, resulting in a small losscone angle and allowing only a very small fraction of electrons to reach the footpoints. Such an effective trap could result in a mirror point at a height where the atmosphere is not dense enough to produce hard X-ray emission but where the field is strong enough to allow strong gyrosynchrotron radiation. For regions of strong magnetic field and high temperature, thermal gyrosynchrotron effects could contribute to the strength of the radio source. 2) A less efficient trap which allows a larger fraction of the energetic particles to escape from the trap but not a sufficiently great number to produce hard X-ray emission observable by RHESSI. A constraint would be placed on the number of escaping electrons in order to produce the radio source but not a hard X-ray source detectable by RHESSI. 3) As the flare is situated on the limb it is unclear if we are really observing the true footpoints in the chromosphere. The radio source could be produced at greater heights in the atmosphere. However in this scenario it would be difficult to explain the presence of the footpoint emission in the impulsive phase.

For the first two scenarios there must, at one point, have been some component of the distribution directed along the magnetic field line, i.e. with small pitch angle, which allowed energetic particles to reach the footpoints and create the footpoint emission observed in the impulsive phase. Reznikova et al. (2009) suggest such a scenario for the impulsive phase. We discuss this in more detail in the following chapter. From the morphology of the radio loop we are unable to distinguish loop convergence. This is most certainly due to the fact that the radio loop is not a single loop but an arcade. Also the presence of a second loop at lower heights further complicates matters. We note also that the positioning of the arcade source is seen to be along the farside radio loop leg and not at the apex. This could be due to the arcade being partially occulted such that the apex appears at an inclination to the observer. Another suggestion would be that the magnetic field is asymmetric along the loop hence resulting in an asymmetric trapping of particles.

To fully understand the evolution of this event is difficult and one must con-

sider particle acceleration versus propagation effects. Evidence for gentle particle acceleration far into the decay phase comes from the appearance of a second radio loop at around 01:21, the time of a bump in the time profile of the southern footpoint at radio wavelengths. Another such bump in the footpoint profile is seen to peak at 01:40. If we assume this to be the last major injection of accelerated particles then we could explain the presence of nonthermal hard X-ray emission at the looptops, seen until around 01:47, as trapping of energetic particles. These particles would result in thin target emission. As time progresses they will either be scattered into the losscone or thermalise in the trap resulting in the soft X-ray emission we observe at the looptop as the loop cools until the end of our analysis time frame at 02:20. A gradual flattening of NoRP radio spectrum at high frequencies, towards a spectral index of 0, suggests a move towards free-free emission seen at 17 GHz and 34 GHz.

In the following Chapter we use these observational parameters and attempt to model the radio emission during the decay phase in an attempt to understand the overall evolution of the flare.

Chapter 5

Modeling of 24th August 2002 flare

This chapter presents the method used to model the observations of radio emission from the 24th August 2002 event presented in the previous chapter. In particular we aim to model the gyrosynchrotron emission using a computational code developed by Dr Gregory Fleishman and Dr Gelu Nita (NJIT, New Jersey) (Fleishman et al. 2009; Nita et al. 2009).

As mentioned in Chapter 2 gyrosynchrotron emission is a function of magnetic field strength, nonthermal electron density and viewing angle. So far, due to its orientation on the west limb of the Sun, the flaring arcade has been treated as a single flare loop. However TRACE observations clearly show an arcade of loops rotated with respect to the observer such that we can not consider our observations to be perpendicular to the plane of the loop. In this Chapter we attempt to model the radio emission using both a simple dipole magnetic field model and a potential, force free arcade model and then compare the results. Previous authors who studied this event have restricted their analysis to short time intervals within the entire time range available by observations. In particular, previous publications have concentrated predominantly at times around the flare peak. We concentrate on examining the decay phase of the flare and investigate the long term nature of the flare evolution and in particular the contribution of thermal emission and line of sight effects to the observed flux and morphology.

In the first part of this Chapter we concentrate on how our model is set up. The computation uses a simplification to the expressions for emissivity and absorption coefficient presented in Ramaty (1969) by Petrosian (1981) and Klein (1987), the Petrosian-Klein approximation detailed in Chapter 2. Section 5.1

provides an explanation of the input and output parameters used in the calculation. Following sections discuss magnetic field models which are the basis of the 3D structure we are modeling and how this is used to determine the radio emission from the source. In the second part of this Chapter we present results from different models for varying electron distributions and spatial distributions of plasma parameters around our 3D model, the values of which are motivated from observations presented in Chapter 4.

5.1 Gyrosynchrotron Code

The computational code used for this analysis is currently provided in the form of Dynamic Link Library (DLL) files. Given a number of input parameters the code then calculates the emission and absorption coefficient from a volume element (voxel) dV , at a range of frequencies, for both the o-mode and x-mode. It is possible to chose between a DLL file which calculates gyrosynchrotron emission only or another which includes a free-free contribution. The input parameters for the calculation are given in Table 5.1.

Table 5.1: Input Parameters

ParmIn	Parameter	Units
ParmIn[0]	Area	cm ²
ParmIn[1]	Depth	cm
ParmIn[2]	Temperature	K
ParmIn[3]	ϵ	
ParmIn[4]	κ	
ParmIn[5]	E_0	MeV
ParmIn[6]	E_{\min}	MeV
ParmIn[7]	E_{\max}	MeV
ParmIn[8]	E_{break}	MeV
ParmIn[9]	δ_1	
ParmIn[10]	δ_2	
ParmIn[11]	n	cm ⁻³
ParmIn[12]	N	cm ⁻³
ParmIn[13]	B	G
ParmIn[14]	θ	degrees
ParmIn[15]	ν_{\min}	Hz
ParmIn[16]	log ν step	Hz
ParmIn[17]	Distribution	
ParmIn[18]	Number of ν steps	

The volume element is therefore Area \times Depth. Parameter 17 sets the electron distribution. Several distribution functions are available, see Table 5.2.

Table 5.2: Electron Distribution

ParmIn[17]	Distribution
2	Thermal
3	Power law over kinetic energy
4	Double power law over kinetic energy
5	Thermal/Nonthermal (power law over energy)
6	Kappa
7	Power law over momentum modulus
8	Power law over Lorentz factor
9	Thermal/Nonthermal (power law over momentum)
10	Thermal/Nonthermal (power law over Lorentz factor)

The thermal distribution is characterised by temperature T and thermal electron density n . Figure 5.1 (left) shows example thermal electron spectra and the resulting flux density spectra (right) for $n = 3 \times 10^{10} \text{ cm}^{-3}$ and $T = 3 \times 10^6 \text{ K}$ (dashed), $T = 3 \times 10^7 \text{ K}$ (solid) and $T = 3 \times 10^8 \text{ K}$ (dash-dot). Nonthermal electron spectra are characterised by a nonthermal electron density N , electron spectral index δ_1 and electron low and high energy cut offs E_{\min} and E_{\max} (Fig. credit Dr Gregory Fleishman). Figure 5.1 shows example nonthermal electron spectra over kinetic energy (left) for $N = 1 \times 10^7 \text{ cm}^{-3}$, $E_{\min} = 0.1 \text{ MeV}$, $E_{\max} = 10 \text{ MeV}$ and $\delta_1 = 2$ (dashed) $\delta_1 = 4$ (solid) and $\delta_1 = 6$ (dash-dot) and the resulting radio emission (right) (Fig. credit Dr Gregory Fleishman). For a monoenergetic electron distribution the parameter E_0 is used.

In the case of a double power law δ_1 is the spectral index below a break energy E_{break} and δ_2 is the spectral index above E_{break} . Figure 5.2 (left) shows a double powerlaw over kinetic energy with $E_{\text{break}} = 1 \text{ MeV}$, $\delta_1 = 4$ and $\delta_2 = 2$ (dashed), $\delta_2 = 6$ (solid) and $\delta_2 = 9$ (dash-dot). The dotted line shows a single powerlaw where $\delta_1 = \delta_2 = 4$. Figure 5.2 (right) shows the resulting radio emission (Fig. credit Dr Gregory Fleishman).

For a thermal/nonthermal distribution the electron spectrum is considered as a continuous function in which the thermal and nonthermal components are joined at a turnover point. For energies below the turnover the electrons are in a thermal distribution and for energies greater than the turnover are in a nonthermal power law distribution. Thus the low energy cutoff for the nonthermal distribution and

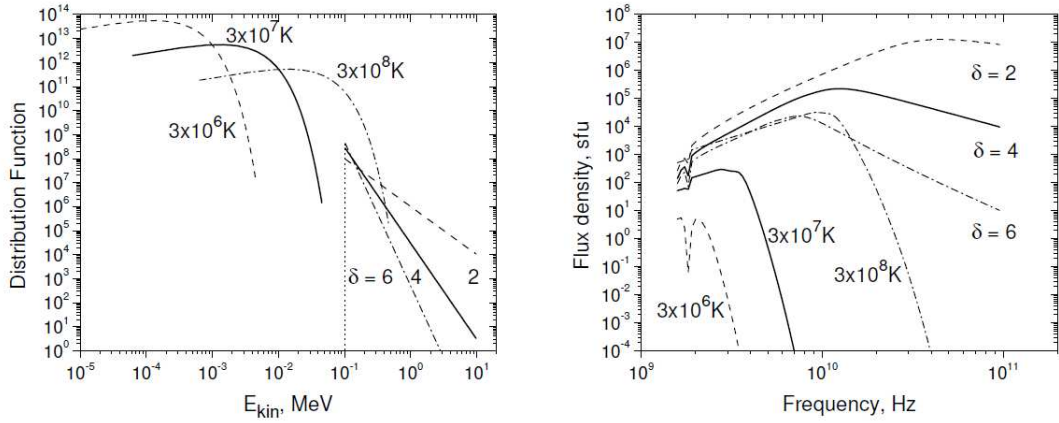


Figure 5.1: Left shows thermal electron distributions for $n = 3 \times 10^{10} \text{ cm}^{-3}$ and $T = 3 \times 10^6 \text{ K}$ (dashed), $T = 3 \times 10^7 \text{ K}$ (solid) and $T \times 10^8 \text{ K}$ (dash-dot). Non-thermal electron distribution (over kinetic energy) for $N = 1 \times 10^7 \text{ cm}^{-3}$, $E_{\min} = 0.1 \text{ MeV}$, $E_{\max} = 10 \text{ MeV}$ and $\delta_1 = 2$ (dashed) $\delta_1 = 4$ (solid) and $\delta_1 = 6$ (dash-dot). Right shows the resulting radio emission from these spectra (credit GF).

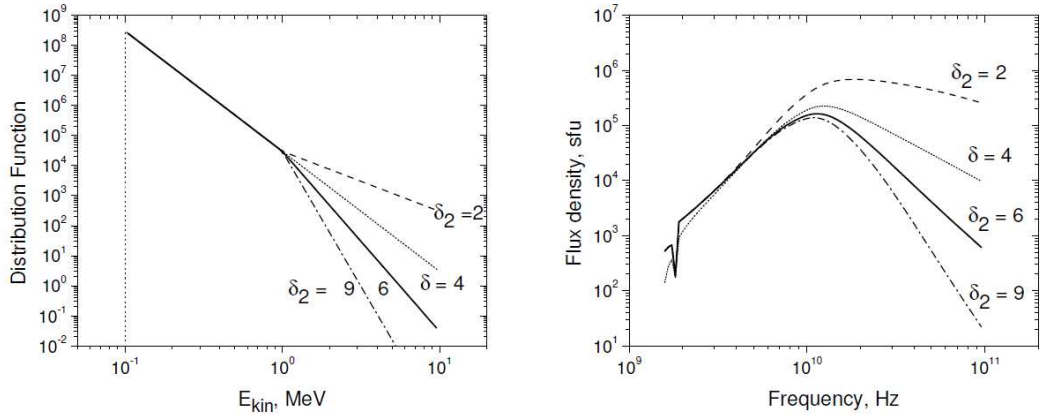


Figure 5.2: Left shows double powerlaw over kinetic energy for $E_{\text{break}} = 1 \text{ MeV}$, $\delta_1 = 4$ and $\delta_2 = 2$ (dashed), $\delta_2 = 6$ (solid) and $\delta_2 = 9$ (dash-dot). The dotted line shows a single powerlaw where $\delta_1 = \delta_2 = 4$. Right shows the resulting radio emission from these spectra (credit GF).

in turn the number of fast electrons are a function of the turning point, which is parameterised by ϵ . Figure 5.3 shows a thermal/nonthermal electron distribution for a thermal with $T = 3 \times 10^7 \text{ K}$ and nonthermal powerlaw over kinetic energy with $\delta_1 = 4$ and $\epsilon = 0.1$ (solid), $\epsilon = 0.03$ (dashed) and $\epsilon = 0.02$ (dash-dot). The point at which the thermal and nonthermal distributions meet is determined by $p_{cr}^2 = p_{th}^2/\epsilon$, where p_{th}^2 is the thermal momentum which is determined by T .

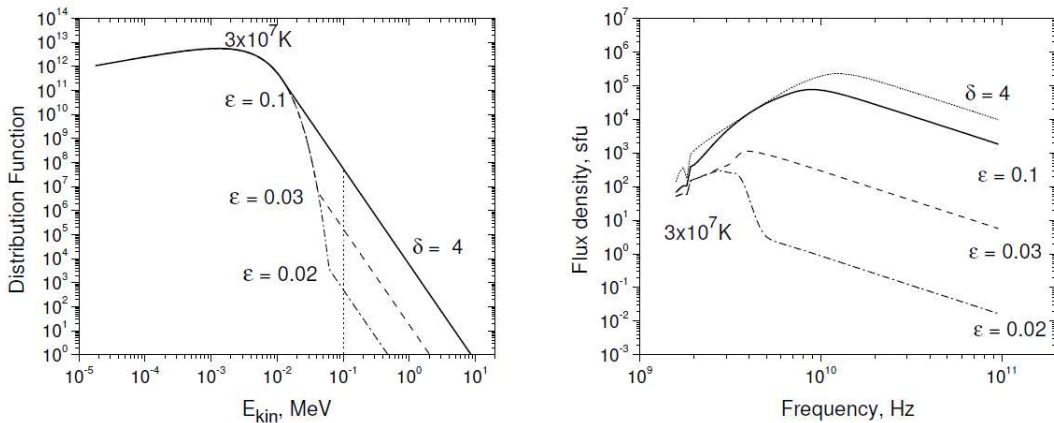


Figure 5.3: Left shows thermal/nonthermal electron distributions for a thermal with $T = 3 \times 10^7$ K and nonthermal powerlaw over kinetic energy with $\delta_1 = 4$ and $\epsilon = 0.1$ (solid), $\epsilon = 0.03$ (dashed) and $\epsilon = 0.02$ (dash-dot). Right shows the resulting radio emission from these spectra (credit GF).

A kappa distribution is also possible and is characterised by a temperature and index κ . For high electron energies and low values of κ , the electron spectrum is a power law. As $\kappa \rightarrow \infty$ the spectrum approaches a Maxwellian.

The code computes the gyrosynchrotron emission for a number of frequencies (ParmIn[18]) starting from ν_{\min} with spacing defined by ParmIn[16]. Other parameters required for the calculation are the magnetic field strength \mathbf{B} and the viewing angle θ , defined as the angle between the observer and the magnetic field in the volume dV .

5.2 Magnetic Field Model

As the magnetic field is a key parameter for gyrosynchrotron emission, in order to model the spatial structure of a radio source we are required to know something about the magnetic field strength in the source and how this varies with position. In the case of the 24th August 2002 event the radio emission clearly resembles a loop of emitting plasma. Previous authors have thus considered a simple loop model for their analysis. We therefore demonstrate the process of modeling a radio emission from a loop by considering a dipole field.

5.2.1 Dipole Field Model

As a result of the high conductivity in the corona the plasma is frozen-in to the magnetic field lines and thus observations of brightly emitting plasma trace out

the magnetic field structure in the corona. Observations show coronal loops are semi-circular in nature and we approximate them by the field produced by a buried dipole coil the central axis of which is parallel to the solar surface. Field lines resulting from this dipole can be described by (Jackson 1962)

$$\mathbf{B} = \frac{3(\mathbf{m} \cdot \mathbf{r}) - m r^2}{r^5} \quad (5.1)$$

where \mathbf{m} is the magnetic moment induced by a current in the buried dipole. The field therefore has components B_r and B_θ

$$B_r(r, \theta) = \frac{2m \cos \theta}{r^3} \quad (5.2)$$

$$B_\theta = \frac{m \sin \theta}{r^3} \quad (5.3)$$

where \mathbf{r} is defined as the distance from the dipole centre and θ is the angle with respect to the dipole central axis, see Figure 5.4. The field is symmetrical around azimuth angle ϕ .

Figure has been removed due to Copyright restrictions.

Figure 5.4: Magnetic dipole field from a buried dipole (Aschwanden 2004).

In the $r\theta$ -plane the field lines are parameterised by

$$r(r_1, \theta) = r_1 \sin^2 \theta \quad (5.4)$$

where r_1 corresponds to the distance of a given field line when $\theta = \pi/2$ (and note also when $\phi = 0$).

Before proceeding we are required to set up an appropriate coordinate system with respect to the observer. We define the xz -plane to be such that $\hat{\mathbf{x}}$ and $\hat{\mathbf{z}}$ are perpendicular to the observers the line of sight. The y axis is then defined to be parallel to the observers line of sight or the observers view is given by $\hat{\mathbf{v}} = [\mathbf{0}, \mathbf{1}, \mathbf{0}]$.

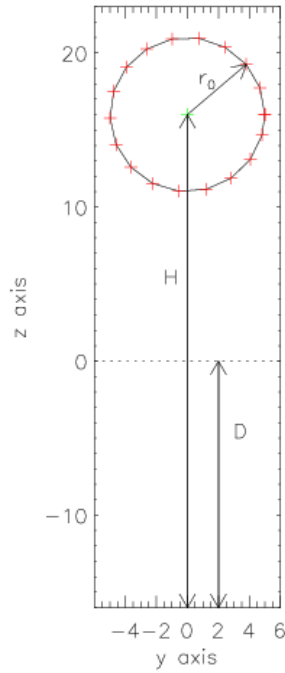


Figure 5.5: Definition of loop apex cross section in the yz -plane for a magnetic dipole model with dipole buried at depth, D . Circular cross section of radius r_0 centred at height H , the height above the dipole origin. Green cross shows loop central axis and red crosses show points at which field lines pass through the apex.

To model a simple loop we start at the loop apex. We set the loop cross section A to be circular in the yz -plane centred at height H above the field origin (i.e. the centre of the buried dipole at depth D) and of radius r_0 , see Figure 5.5. The

green cross shows the loop central axis and red crosses show points at which field lines pass through the apex. We then choose a number of points, equally spaced, around this circle (red crosses) to mark out field lines in the range $0 < \theta < 2\pi$ hence connecting them to the dipole origin and defining our loop.

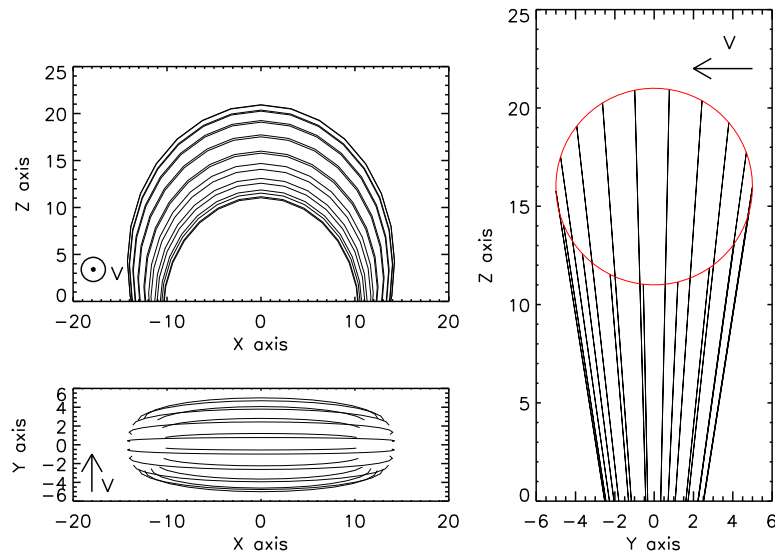


Figure 5.6: Magnetic dipole model field lines for $H = 32''$, $D = -16''$ and $r_0 = 5''$. Top left: xz -plane. Bottom left: xy -plane. Right: yz -plane. Arrows indicates the line of sight of the observer (\hat{v}). In the case of the xz -plane \hat{v} is pointing into the page. The red circle in the yz -plane represents the cross section at the loop apex.

An example dipole model is shown in Figure 5.6 for $H = 32''$, $D = -16''$ and $r_0 = 5''$. Black lines indicate a selection of field lines that define the loop structure. Plots of the xz -plane (top left), xy -plane (bottom left) and yz -plane (right) are shown. Arrows drawn on the plot indicate the direction of the line of sight of the observer (\hat{v}). In the case of the xz -plane \hat{v} is pointing into the page. The red circle in the yz -plane represents the cross section at the loop apex. Note we consider only the field above $z = 0$ i.e. the surface which represents the solar surface.

5.3 Viewing Angle

For gyrosynchrotron emission the observer's viewing angle with respect to the magnetic field is an important parameter. In the previous example the observer

is perpendicular to all field lines and we define this scenario as viewing “straight on”. In order to match observations it is essential to alter the orientation of the model. We do this by performing rotations, about the x, y and z, axis to the “straight on” model, using a series of rotation matrices.

$$R_x(\alpha) = \begin{bmatrix} 1 & 0 & 0 \\ 0 & \cos \alpha & \sin \alpha \\ 0 & -\sin \alpha & \cos \alpha \end{bmatrix} \quad (5.5)$$

$$R_y(\beta) = \begin{bmatrix} \cos \beta & 0 & -\sin \beta \\ 0 & 1 & 0 \\ \sin \beta & 0 & \cos \beta \end{bmatrix} \quad (5.6)$$

$$R_z(\gamma) = \begin{bmatrix} \cos \gamma & \sin \gamma & 0 \\ -\sin \gamma & \cos \gamma & 0 \\ 0 & 0 & 1 \end{bmatrix} \quad (5.7)$$

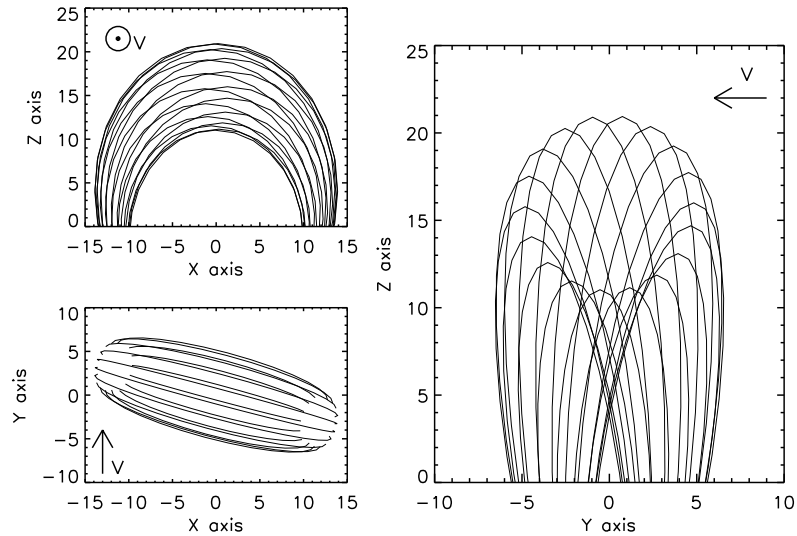


Figure 5.7: Magnetic dipole model field lines for $H = 32''$, $D = -16''$ and $r_0 = 5''$. The model has been rotated around the z axis ($\gamma = 15^\circ$) Top left: xz-plane. Bottom left: xy-plane. Right: yz-plane. Arrows indicates the line of sight of the observer (\hat{v}). In the case of the xz-plane \hat{v} is pointing into the page.

Figure 5.7 shows the standard “straight on” model for the same geometrical parameters as before rotated around the z axis, $\gamma = 15^\circ$. Plots of the xz-plane

(top left), xy-plane (bottom left) and yz-plane (right) are shown and as before arrows drawn on the plot indicate the direction of the line of sight of the observer (\hat{v}).

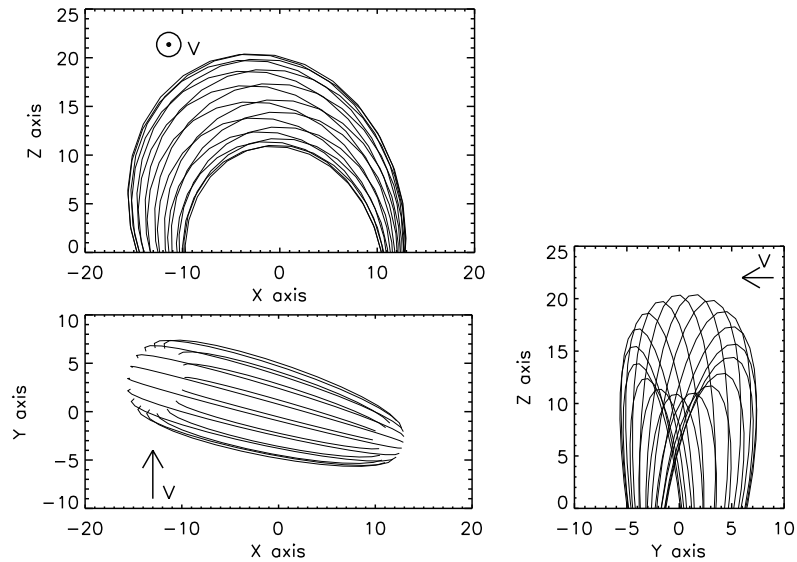


Figure 5.8: Magnetic dipole model field lines for $H = 32''$, $D = -16''$ and $r_0 = 5''$. The model had been rotated around the z and y axes ($\gamma = 15^\circ$ and $\beta = 20^\circ$) Top left: xz -plane. Bottom left: xy -plane. Right: yz -plane. Arrows indicates the line of sight of the observer (\hat{v}). In the case of the xz -plane \hat{v} is pointing into the page.

We are also interested in rotations around the y axis. Figure 5.8 shows the standard “straight on” model for the same geometrical parameters as before rotated around the z axis, $\gamma = 15^\circ$ and around the y axis $\beta = 20^\circ$. Plots of the xz -plane (top left), xy -plane (bottom left) and yz -plane (right) are shown and as before arrows drawn on the plot indicate the direction of the line of sight of the observer (\hat{v}). Rotation around the y axis has the effect of a dipole field that emerges at angle β to the vertical. The result of this is to increase the magnetic field strength in one footpoint whilst decreasing the field strength in the other. The geometry of this rotation is similar to how a dipole field would appear if the active region has rotated off the solar disk resulting in one footpoint being occulted.

5.4 Input parameters

Once the orientation of the model has been fixed with respect to the observer we can determine the input parameters required for the gyrosynchrotron calculation. It is important to remember that the input and output parameters for the DLL files are for a single voxel. In order to construct the spatial structure of the loop we must split the model into a 3-dimensional set of voxels. We do this by setting the model into a 3-dimensional mesh of cuboid shapes. We then search the mesh to find which points lie within the loop. A simple analogy is that we are constructing our loop out of a number of identical building bricks. The dimensions of cuboids in the mesh can be altered to smoothly fit the shape of the loop. This will impact on the resolution at which we determine the radio emission but will also effect the time taken to run the computation. In general we aim to use dimensions that avoid a chunky loop structure but is not so fine that the running time of the code is excessive for the results we are trying to achieve. It should be pointed out here that currently the dimensions are identical for all voxels. In theory it is possible that for voxels that lie closest to the loop outer surface, the dimensions could be decreased to give a better fit. However this complicates matters and for comparison with observations we are ultimately limited to a resolution on the order of that achieved by the recording instrument.

Now that we have our model split into individual voxels, we can determine a set of input parameters for each voxel, thus achieving information about the spatial distribution of our parameters around the loop. For each voxel we calculate the magnetic field components B_r and B_θ . These can be converted into cartesian components B_x , B_y and B_z . Figure 5.9 shows, from left to right, plots of B_x , B_y , B_z magnetic field components and B_{tot} for an xz -plane slice at step 6 through the 3D mesh (top row) and an xz -plane slice half way through the 3D mesh (bottom row). Here $B_0 = 100$ G. Note the color tables run from negative to positive values for B_y and B_z . For points found to lie outside of the model, the magnetic field components are set to zero and as such are represented by a background color equal to that of the colour table zero value.

To determine the viewing angle of the observer with respect to the magnetic field in each voxel the vector dot product is applied.

$$\theta = \cos^{-1} \left(\frac{\mathbf{B} \cdot \mathbf{v}}{|B|} \right) \quad (5.8)$$

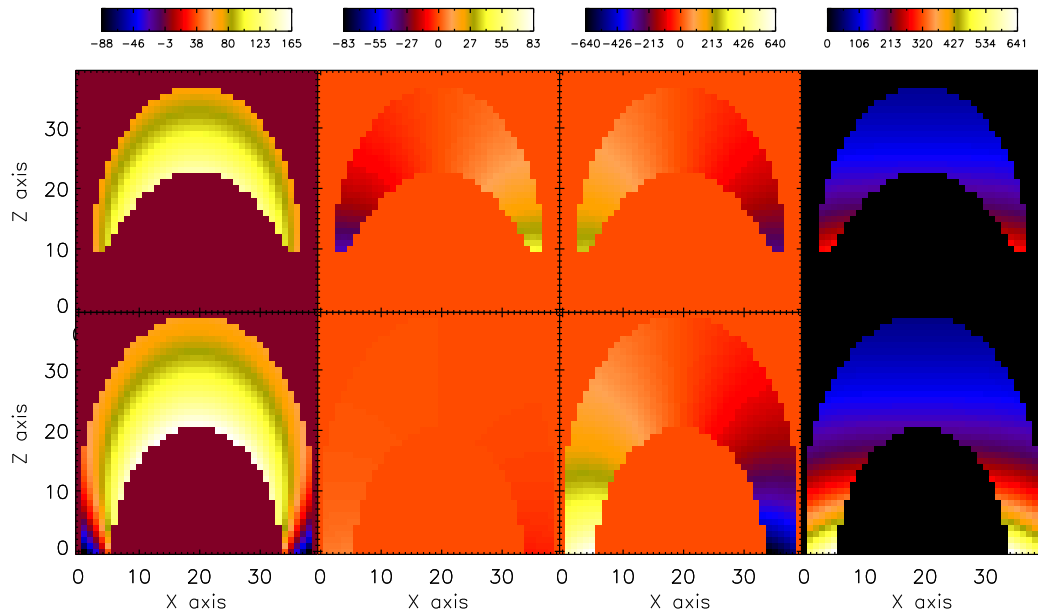


Figure 5.9: Magnetic dipole model for $H = 32''$, $D = -16''$, $r_0 = 5''$ and $B_0 = 100$ G. Top row shows an xz -plane slice at step 6 through the 3D mesh. Bottom row shows an xz -plane slice half way through the 3D mesh. From left to right, plots show B_x , B_y , B_z magnetic field components and far right shows B_{tot} . The dynamic range is scaled to the maximum and minimum values of each component for the entire model.

5.5 Radiative Transfer

Now that we have a set of parameters per voxel the gyrosynchrotron emission and absorption from each voxel can be calculated. Following this we must then determine the effects due to radiative transfer using the equations in Section 2.2.2. We sum the contribution from each voxel at each y position for a given xz position, thus giving a 2D image of the radio emission from the loop.

5.6 Arcade Model

In addition to our simple loop dipole model, TRACE observations of the 24th August flare prompted the consideration of a magnetic arcade model. This simple model is a nonpotential, force free model which is used to describe an arcade which is made of field lines with identical curvature. The magnetic field components

B_x , B_y and B_z are given by (Sturrock 1994)

$$B_x = B_{x_0} \sin(kx) \exp(-lz) \quad (5.9)$$

$$B_y = B_{y_0} \sin(kx) \exp(-lz) \quad (5.10)$$

$$B_z = B_0 \cos(kx) \exp(-lz) \quad (5.11)$$

where

$$B_{x_0} = \frac{l}{k} B_0 \quad (5.12)$$

$$B_{y_0} = \frac{\alpha}{k} B_0 \quad (5.13)$$

$$\alpha^2 = k^2 - l^2 \quad (5.14)$$

This model was primarily intended to be a nonpotential model in which the process of adding shear to the field lines increases the nonpotentiality of the model, i.e. an increase the value of α . The shear angle θ_s is given by

$$\tan(\theta_s) = \frac{B_y}{B_x} = \frac{B_{y_0}}{B_{x_0}} = \frac{\alpha}{l} \quad (5.15)$$

The model has a limit of $\theta_s = \pi/2$. We also have a condition on α , $\alpha \leq \sqrt{k^2 - l^2}$ such that $\alpha < k$ since $l > 0$. For a scenario where no shear is added $\theta_s = 0$ then $\alpha = 0$ and we have a potential field model. For our model we assume that the field is unsheared. From Equation 5.14 we therefore have $l = k$. For this scenario the field is defined by components B_x and B_z whilst $B_y = 0$. Field lines in the xz -plane can be parameterised by

$$z(x) = \frac{k}{l} \log[\sin(kx)] + z_0 \quad (5.16)$$

We define our arcade model by defining an upper and a lower field line in the xz -plane using 5.16 and projecting this back along the y axis to give an upper and lower surface that (combined with the surface $y = 0$) defines our 3 dimensional structure. The value z_0 can be altered to reduced the separation between the upper and lower surface and hence the ‘thickness’ of the arcade. Figure 5.10 shows the resulting arcade in the xz and xy plane. As with the dipole model we call this case the “straight on” view, where the model orientation to the observer has not been rotated around the z and y axes.

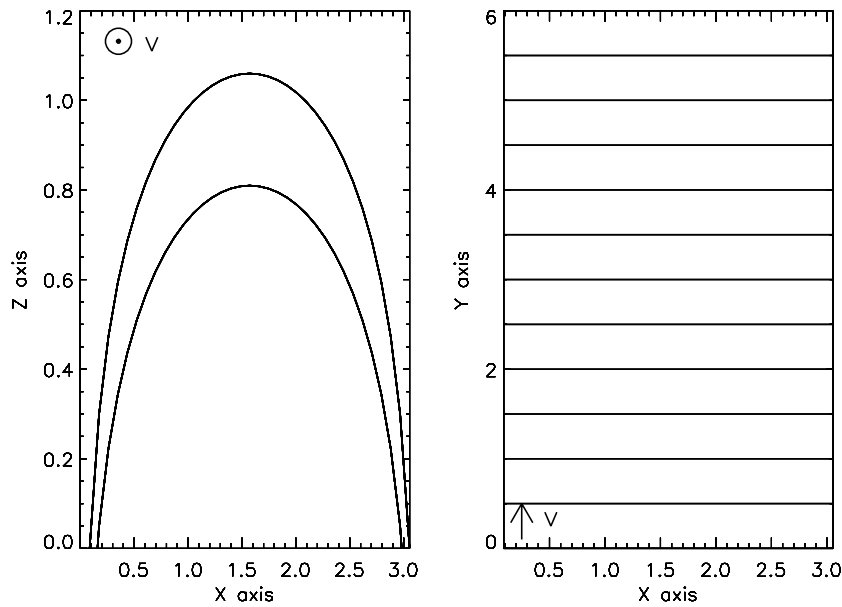


Figure 5.10: Arcade field model for $k = 1, l = 1$. Left shows an xz -plane. Right row shows an xy -plane. Arrows indicates the line of sight of the observer (\hat{v}). In the case of the xz -plane \hat{v} is pointing into the page.

As before a 3D mesh is used to separate the model into individual voxels for which we calculate the gyrosynchrotron emission and absorption coefficient and correct for radiative transfer effects along the line of sight to determine the total radio emission from the source. Figures 5.11 and 5.12 show examples of rotation around the z and y axes respectively for rotation angles $\gamma = 15^\circ$ and $\beta = 10^\circ$. Again it can be seen from Figure 5.12, that a rotation around the y axis has the effect of increasing the field strength at one footpoint, or can be seen as one footpoint being occulted.

Figure 5.13 shows plots of the magnetic field components B_x , B_z and the total

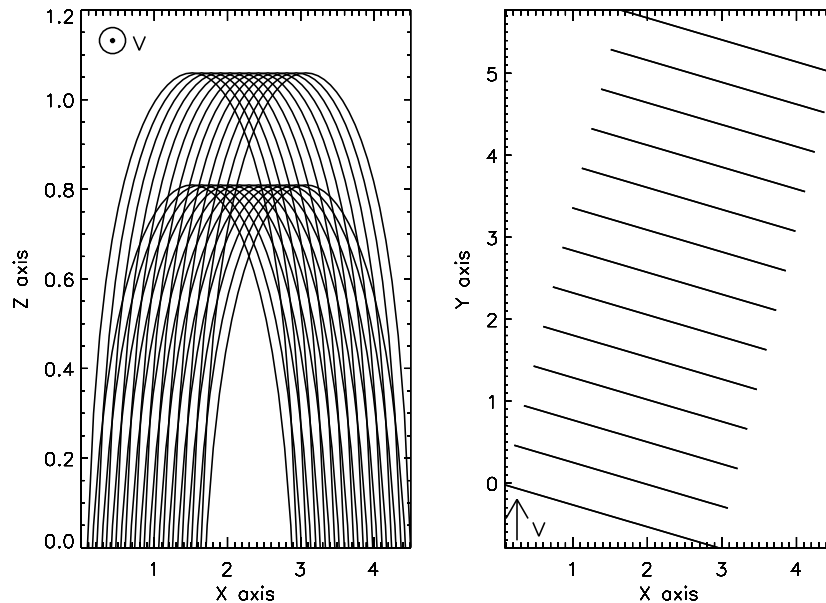


Figure 5.11: Arcade model for $k = 1$, $l = 1$ which has been rotated the z -axis ($\gamma = 15^\circ$). Left shows an xz -plane. Right row shows an xy -plane. Arrows indicates the line of sight of the observer (\hat{v}). In the case of the xz -plane \hat{v} is pointing into the page.

magnetic field strength B_{tot} for an unsheared arcade model with $k = l = 1$ for an observer viewing “straight on”. Here $B_0 = 100$ G Note for a model with no shearing and for the “straight on” viewing angle $B_y = 0$.

5.7 Modeling of 24th August 2002 Event

Following on from the findings in Melnikov et al. (2002b) where it was suggested that a dominant looptop source could be produced by an enhancement of energetic electrons at the loop apex, Melnikov et al. (2005) presented 5 flares, including the 24th August 2002 event, which displayed a temporal evolution of brightness along the loop. Each of these events showed dominant footpoint emission during the rise phase of the burst and an optically thin looptop that dominates on the rise and/or decay phase of the burst. He attempted to model the distribution of energetic electrons along the loop by solving a form of the non-stationary Fokker-Planck equation which incorporates Coulomb collisions and magnetic mirroring (Hamilton et al. 1990). The injection of energetic electrons was modeled for two scenarios: 1) injection at the loop apex (at the centre of the magnetic trap); 2)

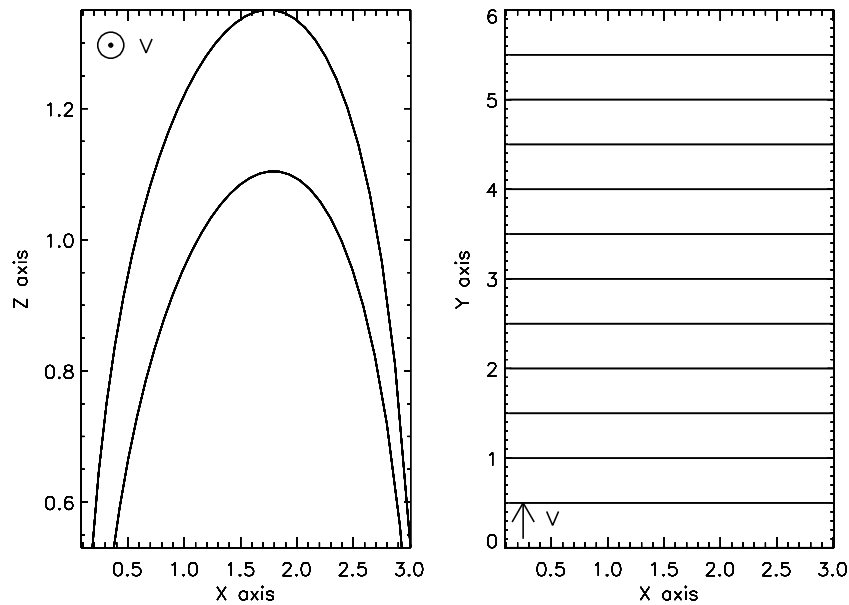


Figure 5.12: Arcade model for $k = 1$, $l = 1$ which has been rotated around the y -axis ($\beta = 10^\circ$). Left shows an xz -plane. Right row shows an xy -plane. Arrows indicates the line of sight of the observer (\hat{v}). In the case of the xz -plane \hat{v} is pointing into the page.

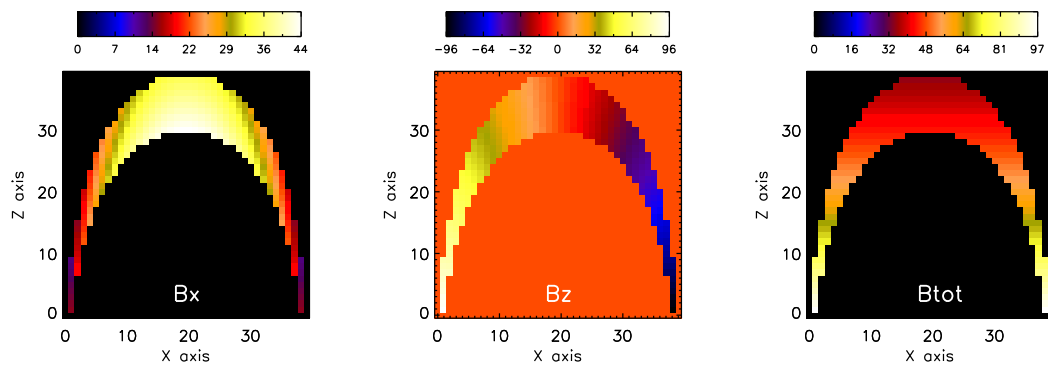


Figure 5.13: Arcade model magnetic field components for $k = 1$, $l = 1$ and $B_0 = 100$ G for the “straight on” view. Left shows B_x , middle shows B_z and right shows B_{tot} . The dynamic range is scaled to the maximum and minimum values of each component. Note also that $B_y = 0$

injection at the loop footpoints (at the foot of the magnetic trap). For looptop injection the distribution of energetic electrons along the loop does not change

significantly over time with the peak number density always located at the looptop. Conversely the evolution of electron distribution varies considerably over time for injection at the footpoints. During the rise phase the peak is located at the footpoints whilst during the decay phase the peak is located at the looptop.

Results presented by Melnikov et al. (2005) were not produced for one event in particular, but rather for events which demonstrate such brightness trends. Tzatzakis et al. (2006) extend this work to present model results specifically aimed at matching the observations of the 24th August 2002 event and in particular for a single radio burst occurring between 01:00:00 and 01:01:30. Following the method of Melnikov et al. (2005) they also use the non-stationary Fokker-Planck equation detailed in Hamilton et al. (1990), to calculate an electron distribution which is then used as an input to a gyrosynchrotron model in order to determine the brightness along the loop. For details of the best fit model we refer to the paper itself however we point out that, as before, the results imply that injection occurs at the footpoints and with an anisotropic pitch angle distribution. The best fit model was able to produce a gyrosynchrotron brightness distribution that resembles the observations during the rise and the decay phase of the burst where both 17 GHz and 34 GHz brightness peaks were located at the footpoint and then at the looptop. They were not able to match observations at the radio peak where the brightness peak is seen at the looptop for 17 GHz but at the footpoint for 34 GHz.

Another attempt to model the impulsive phase bursts was undertaken by Reznikova et al. (2009), using again the nonstationary Fokker-Planck equation approach. Using the observationally determined parameters from GOES, SONG and NoRH, they solve the Fokker-Planck equation for a number of scenarios. An asymmetric magnetic field model was used to match observations with magnetic field strengths in the southern footpoint, northern footpoint and looptop of 1000 G, 800 G and 200 G respectively. A viewing angle of $\theta = 78.5^\circ$ was used. The resulting gyrosynchrotron emission was then calculated using the full expressions (Ramaty 1969; Fleishman & Melnikov 2003). A best fit model was found for a compact source of injected electrons situated at the looptop with an anisotropic pitch angle distribution perpendicular to the magnetic field lines, pointing towards the southern footpoint. However the distribution also required a weak isotropic component in order to resemble the various features of the observations detailed in Chapter 4. The modeled distribution resembles the observations well and recreates the temporal and spatial morphology of features seen at

17 GHz and 34 GHz, including delays in the peaks of emission between looptops and footpoints and between 17 GHz and 34 GHz. The resulting output of the Fokker-Planck equation allows the number density of energetic electrons to gradually increase at the looptops and to drop off at the footpoints over course of the injection. The model shows footpoint dominated sources in the rise phase with a gradual increase of brightness at the looptop. The footpoint sources are seen to diminish in the decay phase due to electrons precipitating out more quickly at the base of the loop than compared to the looptop. The more gradual rise at 34 GHz is caused by the gradual increase of the looptop number density and the slower decay is as a result of lower energy electrons scattering into the loss cone or undergoing Coulomb collisions and thermalising at a quicker rate than higher energy electrons at the looptop. The model was also able to recreate the offset of the looptop brightness to the farside loop leg and the evolution of the optically thick southern footpoint was also matched.

5.8 Thermal distribution

Dipole

We start by showing the results from a simple thermal electron distribution. Figures 5.14 and 5.15 show the gyrosynchrotron (GS) and gyrosynchrotron plus free-free (GSFF) emission for the dipole field geometry with no rotation in the z or y axes. In line with observations, $H = 120''$, $D = 60''$ and $r_0 = 15''$. We set the magnetic field at the looptop to $B_0 = 150$ G, which gives $B \approx 800$ G at the footpoints. The ambient electron density and temperature are kept constant along the loop with $n = 1.0 \times 10^9 \text{ cm}^{-3}$ and $T = 1.0 \times 10^7$ K. Plots to the left show the resulting image at 17 GHz in S.F.U. and are scaled to the image maximum. Right shows the corresponding spectra from the looptop (green), a single footpoint (red) and the total spectra (red). The looptop and footpoint spectra are found by summing the emission from a number of pixels in these regions. The footpoint source is considered as the sum of emission in one loop leg from 0 to 8 pixels in height. The looptop emission is taken as the sum of all emission above 20 pixels in height. Also plotted for comparison, are NoRP spectra from the eight time intervals shown in Figure 4.6 during the decay phase of the flare, see Table 5.3. Straight away we can see that an entirely thermal model does not fit the observations. As expected, the dominant GS emission

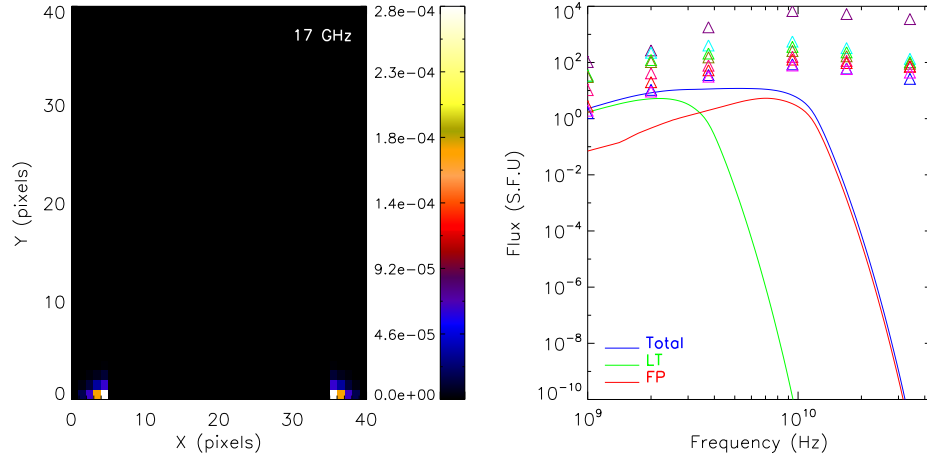


Figure 5.14: Thermal GS emission from the dipole model with $T = 1.0 \times 10^7$ K and $n_0 = 1.0 \times 10^9$ cm⁻³ ($\gamma = 0^\circ$, $\beta = 0^\circ$). Left: 17 GHz image (S.F.U). Right: looptop spectrum (green), footpoint spectrum (red), total spectrum (blue).

is situated at the loop footpoints where the magnetic field is strongest and the flux density falls off sharply at optically thin frequencies, Figure 5.14. The peak frequency of the footpoint spectrum occurs at a higher frequency than for the looptops due to the increase in B as expected from theory.

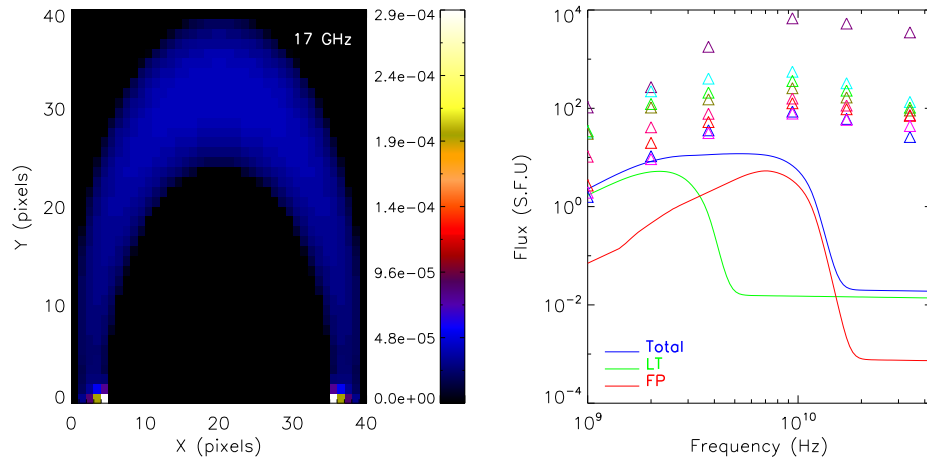


Figure 5.15: Thermal GSFF emission from the dipole model with $T = 1.0 \times 10^7$ K and $n = 1.0 \times 10^9$ cm⁻³ ($\gamma = 0^\circ$, $\beta = 0^\circ$). Left: 17 GHz image (S.F.U). Right: looptop spectrum (green), footpoint spectrum (red), total spectrum (blue).

The addition of a free-free component produces emission along the entire length of the loop as a result of the constant temperature and density, shown

Table 5.3: NoRP times

Time	Symbol	Time	Symbol
01:10	△	01:44	△
01:20	△	01:52	△
01:32	△	01:58	△
01:40	△	02:20	△

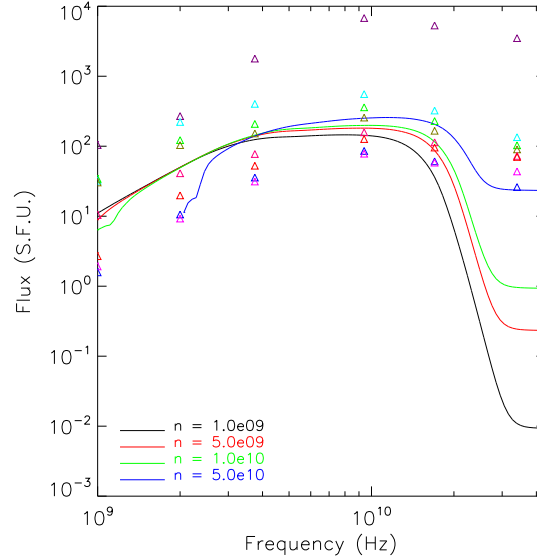


Figure 5.16: Thermal GSFF emission from the dipole model with $T = 5.0 \times 10^7$ K and $n = 1.0 \times 10^9$ cm^{-3} (black), $n = 5.0 \times 10^9$ cm^{-3} (red), $n = 1.0 \times 10^{10}$ cm^{-3} (green), $n = 5.0 \times 10^{10}$ cm^{-3} (blue) ($\gamma = 0^\circ$, $\beta = 0^\circ$).

in Figure 5.15. In order to match the NoRP flux values, in particular at higher frequencies, we are required to increase the temperature and density. Figure 5.16 shows GSFF emission for $T = 5.0 \times 10^7$ K and $n = 1.0 \times 10^9$ cm^{-3} (black), $n = 5.0 \times 10^9$ cm^{-3} (red), $n = 1.0 \times 10^{10}$ cm^{-3} (green) and $n = 5.0 \times 10^{10}$ cm^{-3} (blue). However whilst this increases the flux at the higher frequencies, images at 17 GHz show the emission concentrated at the footpoints with no looptop source and images at 34 GHz show that the entire loop is dominated by the free-free component with no compact sources at the looptop or footpoints. From Figure 5.15 we can see that the low frequency end of the spectrum is strongly suppressed for $n = 1.0 \times 10^{10}$ cm^{-3} (green). The effect is most pronounced for $n = 5.0 \times 10^{10}$ cm^{-3} (blue) at frequencies around 1 to 2 GHz.

Figure 5.17 shows the spectrum for $T = 5.0 \times 10^7$ K and $n = 5.0 \times 10^{10}$ cm^{-3} .

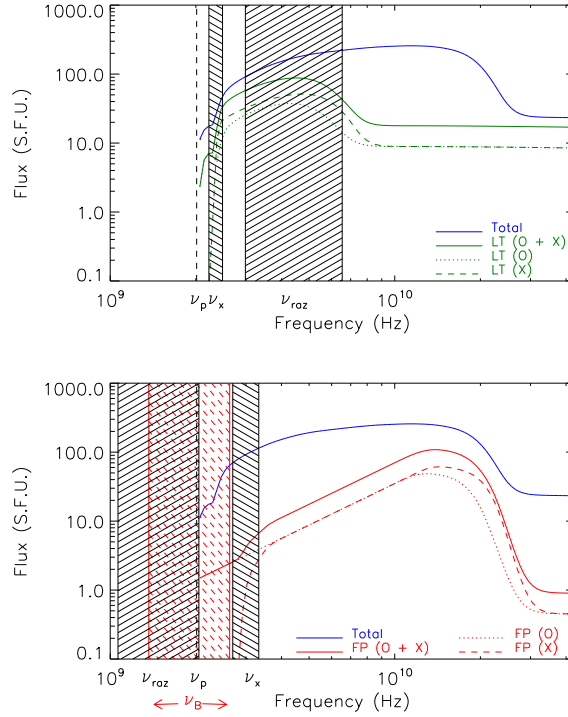


Figure 5.17: Thermal GSFF emission from the dipole model with $T = 5.0 \times 10^7$ K and $n = 5.0 \times 10^{10} \text{ cm}^{-3}$ ($\gamma = 0^\circ$, $\beta = 0^\circ$). Top: total dipole spectrum (blue), total looptop (solid green), looptop o-mode (dotted) and x-mode (dashed). Bottom: total dipole spectrum (blue), total footpoint emission (solid red), footpoint o-mode (dotted) and x-mode (dashed). The frequency ranges of relevant cut offs are over plotted.

The top panel shows the total looptop emission (solid green), the total looptop o-mode component (dotted green) and x-mode component (dashed green). The total loop emission is shown in blue for comparison. The bottom panel shows the equivalent spectra for the footpoint source. To understand the features of the spectra we have plotted the frequency ranges relevant for cutoffs in the o and x-mode. As expected o-mode experiences a cutoff at ν_p , shown as a black vertical dashed line on both plots and indicated by a label. The x-mode wave propagation experiences a cutoff at $\nu_x \approx \frac{1}{2}\nu_{Be} + (\nu_p^2 + \frac{1}{4}\nu_{Be})$. As ν_x is related to ν_{Be} (the electron cyclotron frequency) and hence depends on B it was necessary to determine an upper and lower limit to ν_x for the upper and lower limits of B in the footpoint and looptop sources. The range of ν_x is indicated on the plot by diagonal stripes inclined at 30° , and indicated by a label. The value of ν_x alters as a function of position in the loop and as such there is not a sharp cutoff in the x-mode propagation but rather a smooth decline. In addition to the cutoff

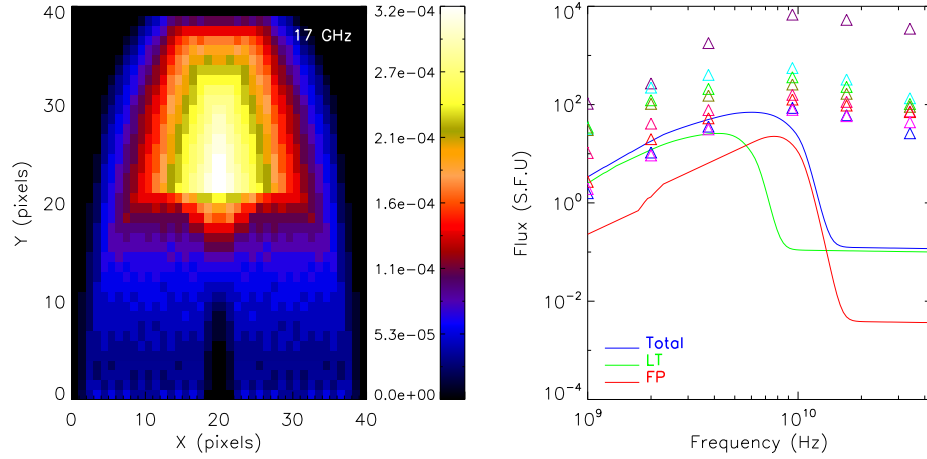


Figure 5.18: Thermal GSFF emission from the arcade model with $T = 1.0 \times 10^7$ K and $n = 1.0 \times 10^9$ cm^{-3} ($\gamma = 15^\circ$, $\beta = 0^\circ$). Left: 17 GHz image (S.F.U). Right: looptop spectrum (green), footpoint spectrum (red), total spectrum (blue).

frequencies, the estimated range of Razin suppression is plotted, indicated by diagonal stripes inclined at -30° . Also plotted for the footpoint source is the range of ν_{B_e} indicated by red diagonal strips. For the looptop source $\nu_{B_e} < 1$ GHz and is out of the range of interest. The shape of the footpoint slope to the left of the peak between around 3 GHz and 10 GHz shows the effect of free-free absorption with a slope of two. Just below 2 GHz there is a bump in the looptop spectrum. This is most likely the result of the approximations used in the Petrosian-Klein method, which is worst at low frequencies. To confirm this we would need to rerun the simulation using the full (Ramaty 1969) expressions.

Arcade

Using the arcade field model we can rotate the system to investigate the effects of line of sight enhancements. Figure 5.18 shows the GSFF emission from an arcade with footpoint magnetic field strength $B_0 = 800$ G which give a looptop field of $B \approx 150$ G. The arcade has been rotated by 15° around the z-axis ($\gamma = 15^\circ$, $\beta = 0^\circ$). The same inputs parameters are used as for Figure 5.15, i.e. $T = 1.0 \times 10^7$ K and $n = 1.0 \times 10^9$ cm^{-3} . Whilst the looptop free-free component is still relatively weak in comparison to the footpoint gyrosynchrotron emission in the dipole, rotating the arcade results in a compact source at the looptop which is brighter than the gyrosynchrotron emission at the footpoints. Despite this, the looptop source is mostly comprised of free-free emission which

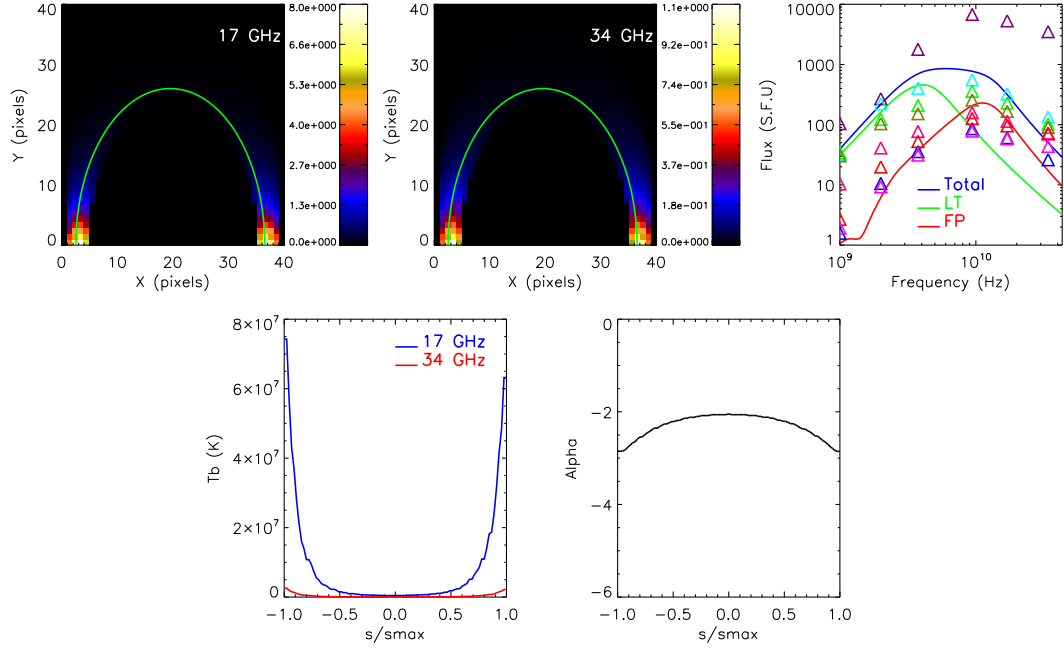


Figure 5.19: Nonthermal GS emission from the dipole model with $\delta = 4$ and $N = 1.0 \times 10^4 \text{ cm}^{-3}$ ($\gamma = 0^\circ$, $\beta = 0^\circ$). Top left: 17 GHz image (S.F.U.). Top middle: 34 GHz image (S.F.U.). Top right: looptop spectrum (green), footpoint spectrum (red), total spectrum (blue). Bottom left: T_b profiles as a function of distance s along the loop at 17 GHz (blue) and 34 GHz (red). Bottom right: alpha calculated from 17 and 34 GHz images as a function of distance s along the loop. Path s along the loop is shown in green on 17 and 34 GHz images (top left and middle).

disagrees with the negative spectral index found from observations. However this example demonstrates that effects of rotation may be important when modeling the relative brightness of footpoint and looptop emission.

5.9 Nonthermal distribution (uniform N)

Dipole

We now consider a nonthermal electron distribution. Figure 5.19 shows GS emission from the dipole field model for an electron distribution with $\delta = 4$ and $N = 1.0 \times 10^4 \text{ cm}^{-3}$ ($\gamma = 0^\circ$, $\beta = 0^\circ$). The dipole field and geometrical parameters remain unchanged from previous examples. Top left shows 17 GHz image (S.F.U.) and top middle shows 34 GHz. Both 17 GHz and 34 GHz have

been scaled to the respective image maximum. Top right shows the corresponding looptop spectrum (green), footpoint spectrum (red) and total spectrum (blue). Bottom left shows T_b profiles as a function of distance s along the loop at 17 GHz (blue) and 34 GHz (red). Bottom right shows α calculated from 17 GHz and 34 GHz images as a function of distance s along the loop. The path of s along the loop is shown in green on 17 and 34 GHz images (top left and middle).

The value of δ is kept constant at all points in the loop and as expected the gyrosynchrotron emission is concentrated at the loop footpoints where the magnetic field is strongest. From the line profile of α along the loop we can see that the footpoint emission has a steeper slope than for the looptop, similar to the trend seen from observations presented in the previous Chapter. Observations of this kind have also been reported by Yokoyama et al. (2002) and Melnikov et al. (2002a). The reason for this is connected to the electron gyrofrequency. The 17 GHz emission at the looptops is produced by electrons emitting at higher harmonics ($s = \nu/\nu_B$) than at the footpoint and can result in a softer footpoint spectrum. From the range of looptop and footpoint values for B used for modeling we find that $s_{LT} \approx 18 - 40$ and $s_{FP} \approx 6 - 12$ for 17 GHz.

In Chapter 4 we considered the radio photon spectrum to have a constant powerlaw index at optically thin frequencies and used the linear Dulk (1985) equation to relate α to δ . However it is important to remember that this is an approximation and that the full expressions from Ramaty (1969) allow α to vary for different frequencies. This can be seen in Figure 5.20(c) the details of which will be discussed later. Fleishman & Melnikov (2003) investigate the effect of an anisotropic electron distribution and find a significant differences in the value of α calculated by using the linear Dulk (1985) relation with δ . They find that the effects of anisotropy are heavily dependent on the viewing angle. For a ‘pancake’ distribution where the electrons have a transverse anisotropy, the effect is most pronounced for a quasi-parallel viewing angle and results in a steeper spectral slope in comparison to the isotropic case ($\Delta\alpha \sim 1$). The reason for this is related to the electron directivity, $\theta \sim \gamma^{-1}$ where θ defines the cone of emitted radiation and γ is the Lorentz-factor. At low energies the electron directivity is small and so the emitted radiation is only weakly sensitive to pitch-angle anisotropy. At higher energies the electrons emit into a small cone and so only a small portion of higher energy electrons emit radiation which is seen at small viewing angles to the magnetic field. Thus the intensity decreases more rapidly at high frequencies than for an isotropic case and the spectral index α is

steeper. Using the same argument, for a beam-like anisotropy the effect is most significant at quasi-perpendicular viewing angles.

Fleishman & Melnikov (2003) find that although the general trend of anisotropy holds for most cases, the overall structure of the emitted spectrum is defined by parameters such as δ , n and the optical depth τ . An important point to note is that when considering a converging magnetic field, such as that expected in a flare loop, the anisotropy of the trapped electron distribution will increase towards the footpoints due to an increase in the loss cone angle (assuming the plasma is not so dense that there is strong scattering effects).

For the 24th August event we are in the quasi-perpendicular regime at all points along the loop. Therefore, for a population of trapped electrons situated at the looptop we expect that the effects of anisotropy do not alter the value of α significantly from that of an isotropic electron distribution. However if the footpoint source is generated by a beam of electrons, then the value of α could be increased significantly leading to a softer spectrum at the footpoints. Unfortunately the current version of the code is unable to compute the emission from an anisotropic electron distribution. As such we continue our investigation with the question, can the observed footpoint spectrum be modeled with an isotropic distribution?

Figure 5.20(a) shows the total spectra for GS emission for the dipole field model with varying δ and N parameters. Figure 5.20(b) shows the corresponding loop profile of α for each set of input parameters. We see that the spectral index has a impact on the profile of α along the loop. As the value of δ decreases the contribution from higher energy electrons becomes more important and the value of α , calculated using the values of flux from 17 GHz and 34 GHz emission, flattens. In particular the change in δ can considerably alter α at the footpoints. It is helpful to see plots of α as a function of frequency, see Figure 5.20(c) for the total (solid), looptop (dashed) and footpoint (dotted) spectra respectively. The plot shows the trends for three sets of input parameters, $\delta = 4$ and $N = 1.0 \times 10^4 \text{ cm}^{-3}$ (red), $\delta = 2$ and $N = 1.0 \times 10^4 \text{ cm}^{-3}$ (black), and $\delta = 2$ and $N = 1.0 \times 10^5 \text{ cm}^{-3}$ (grey). Where the trend crosses $\alpha = 0$ (horizontal black line) indicates the peak frequency. Vertical black lines indicate 17 GHz and 34 GHz. Starting with $\delta = 4$ and $N = 1.0 \times 10^4 \text{ cm}^{-3}$ in red we see, as expected, the peak of the spectrum occurs at higher frequencies for the footpoint than the looptop. The value of α in the range 17 GHz to 34 GHz is flatter for the looptop and can be seen to vary as a function of frequency, the

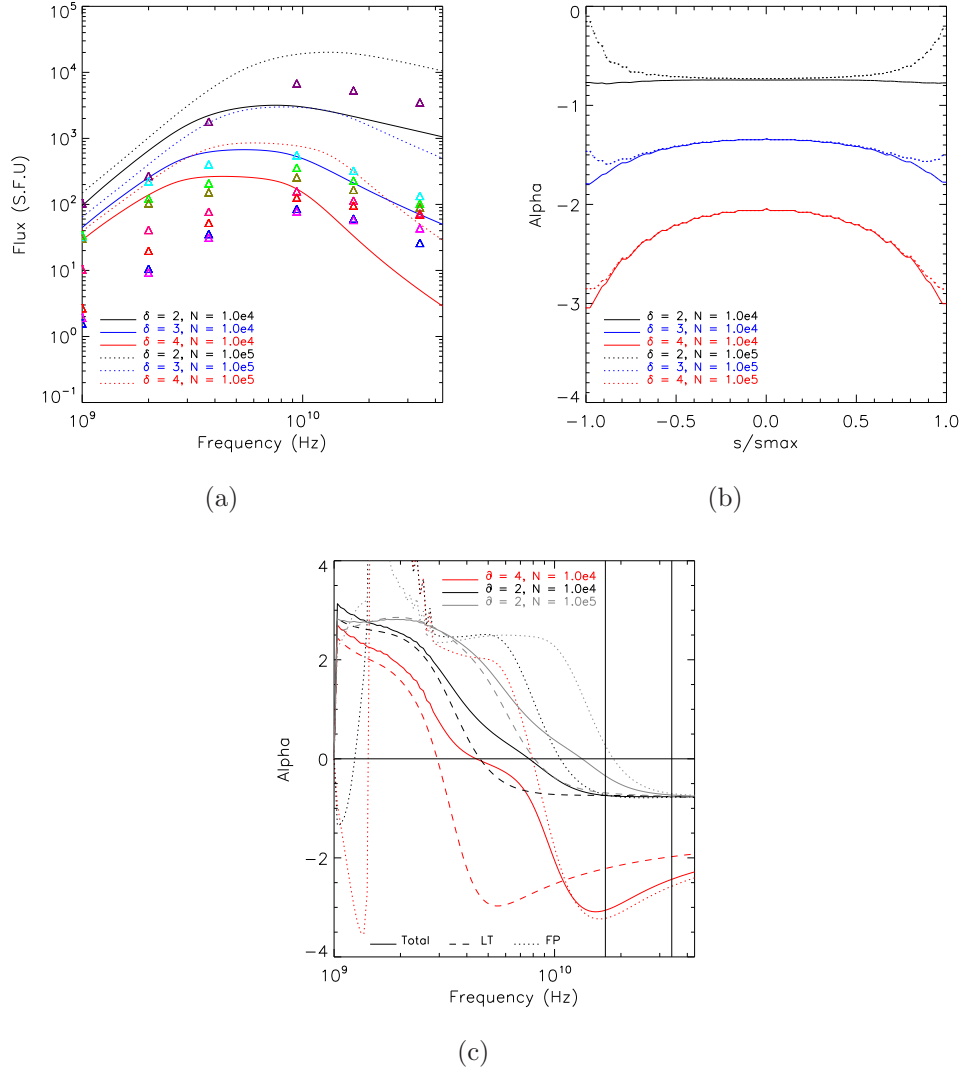


Figure 5.20: (a) Nonthermal GS total flux spectrum from the dipole model with $\delta = 2$ (black), 3(blue), 4(red) and $N = 1.0 \times 10^4 \text{ cm}^{-3}$ (solid), $N = 1.0 \times 10^5 \text{ cm}^{-3}$ (dashed) ($\gamma = 0^\circ$, $\beta = 0^\circ$). (b) Corresponding alpha calculated from 17 and 34 GHz images as a function of distance s along the loop. (c) alpha as a function of frequency for total spectrum (solid), looptop (dashed) and footpoint (dotted) for selected input parameters indicated on plot.

values of which are slightly different to that for the linear Dulk (1985) estimation of α ($\alpha = 0.9\delta - 1.22$) which equals 2.4 in this case. At higher frequencies where $\nu/\nu_B > 100$ and we approach ultrarelativistic synchrotron emission, the value of α becomes constant and we can use the approximation $\alpha = (\delta - 1)/2$. Decreasing δ to two but leaving $N = 1.0 \times 10^4 \text{ cm}^{-3}$ (black) we see that the peak of the spectra has moved to higher frequencies and for the range of interest

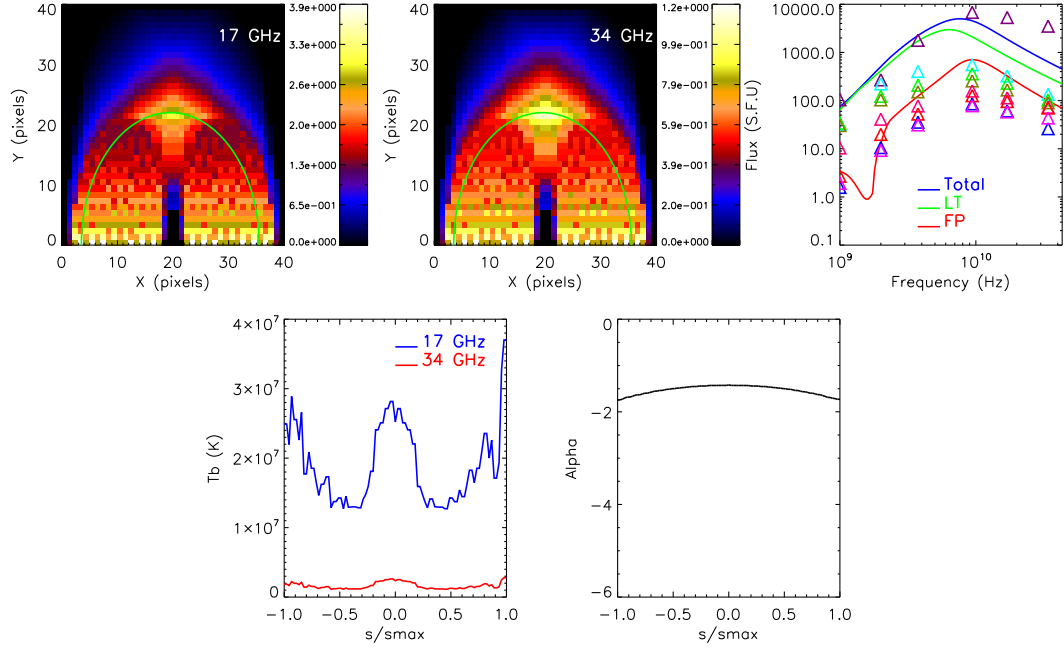


Figure 5.21: Nonthermal GS emission from the arcade model with $\delta = 3$ and $N = 1.0 \times 10^4 \text{ cm}^{-3}$ ($\gamma = 15^\circ$, $\beta = 0^\circ$). Top left: 17 GHz image (S.F.U.). Top middle: 34 GHz image (S.F.U.). Top right: looptop spectrum (green), footpoint spectrum (red), total spectrum (blue). Bottom left: T_b profiles as a function of distance s along the loop at 17 GHz (blue) and 34 GHz (red). Bottom right: α calculated from 17 and 34 GHz images as a function of distance s along the loop. Path s along the loop is shown in green on 17 and 34 GHz images (top left and middle).

the value of α is much flatter than the previous example. The value of α is fairly constant with a similar value of 0.7 for spectra from each source. From the Dulk (1985) relation $\alpha = 0.6$. If we now consider an increase in the nonthermal electron density to $N = 1.0 \times 10^5 \text{ cm}^{-3}$ for $\delta = 2$ (grey), we see that as expected the peak has once again shifted to higher frequencies. For the range of interest the looptop emission shows flat and fairly constant value for α with a similar value to the previous example. However for the footpoint source α is greater than that of the looptop source and at 17 GHz α is positive suggesting an optically thick source, although most of the range between 17 GHz and 34 GHz has a negative α . We can use these findings to constrain the values δ and N required to describe the source by a nonthermal electron distribution function.

Arcade

Although the total spectra shown in Figure 5.20(a) show some reasonable fits to the NoRP spectra, in particular the fit using $\delta = 3$ with $N = 1.0 \times 10^4 \text{ cm}^{-3}$, the resulting images show only footpoint emission and no coronal source. Using the arcade field model we investigate the line of sight effects. Figure 5.21 shows the GS emission from the arcade with $\delta = 3$ and $N = 1.0 \times 10^4 \text{ cm}^{-3}$ at 17 GHz and 34 GHz ($\gamma = 15^\circ$, $\beta = 0^\circ$). The rotation results in an enhancement of the looptop emission resulting in a source similar to what we find from observations. For the looptop the line of sight distance, L , increases from $2 \times 10^9 \text{ cm}$ for the dipole to $2 \times 10^{10} \text{ cm}$ for the arcade, whilst L at the footpoints is similar with values of around $1 \times 10^9 \text{ cm}$ for both the dipole and arcade model. In general the resulting spectral shape and α profiles for looptop and footpoint emission is similar to that for the dipole case. However the arcade emission is around one order of magnitude greater than for the dipole. This arises from a difference in source sizes between the arcade and dipole models. Here we define the footpoints as pixels 0 to 20 and 0 to 6 in the X and Y axis respectively and the looptop as emission above 13 pixels. The footpoint volume for the dipole is $1 \times 10^{27} \text{ cm}^{-3}$ compared to $5 \times 10^{27} \text{ cm}^{-3}$ for the arcade. The looptop volume for the dipole is $2 \times 10^{28} \text{ cm}^{-3}$ and the arcade $1.5 \times 10^{29} \text{ cm}^{-3}$. The increase in source volume for the arcade results in an increase of the overall flux in comparison to the same input parameters for the dipole model.

Figure 5.22(a) shows the total spectra for the same combination of input parameters as for the dipole model. For comparison we also present total spectra for two arcade models with input parameters $\delta = 3$ and $N = 1 \times 10^4 \text{ cm}^{-3}$ which are 25% smaller (green solid) and 50% smaller (green dashed) in all dimensions. Figure 5.22(b) shows a comparison of dipole and arcade models for the same input parameters with the inclusion of the 50% reduction in arcade dimensions, which can be seen to closely match the dipole spectrum. Thus to explain the spectrum with this model requires that our estimate of the arcade dimensions is reduced by a factor of two. This could be due to an error in the estimation of the length of the arcade which is viewing angle dependent. A change in viewing angle of $\pm 1^\circ$ can account for a difference in arcade length of $\pm 14''$ ($\pm 1 \times 10^9 \text{ cm}$) i.e. 6% of the total length.

The ratio of the footpoint to looptop (FP:LT) brightness varies for different input parameters. Table 5.4 shows the ratios for each combination of input pa-

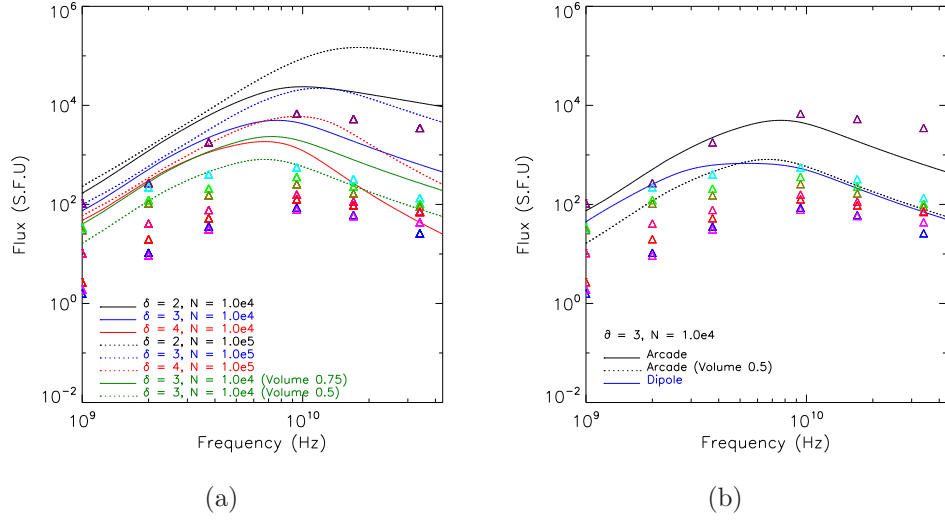


Figure 5.22: (a) Shows nonthermal GS total flux spectrum from the arcade model with $\delta = 2$ (black), 3 (blue), 4 (red) and $N = 1.0 \times 10^4 \text{ cm}^{-3}$ (solid), $N = 1.0 \times 10^5 \text{ cm}^{-3}$ (dashed). Green shows reduction of arcade volume by 25% (solid) and 50% (dashed) for $\delta = 3$ and $N = 1.0 \times 10^4 \text{ cm}^{-3}$ ($\gamma = 0^\circ$, $\beta = 0^\circ$). (b) Shows comparison of arcade and dipole spectra for $\delta = 3$ and $N = 1.0 \times 10^4 \text{ cm}^{-3}$ for the arcade (black solid), arcade with 50% volume reduction (black dotted) and dipole (blue).

Table 5.4: Arcade model FP:LT brightness ratios (17 GHz/34 GHz)

	$\delta = 2$	$\delta = 3$	$\delta = 4$
$N = 1.0 \times 10^4 \text{ cm}^{-3}$	0.57/0.55	1.31/1.07	3.75/2.34
$N = 1.0 \times 10^5 \text{ cm}^{-3}$	0.49/0.55	1.09/1.06	3.35/2.33

rameters plotted in Figure 5.22(a) at 17 GHz and 34 GHz. The main alteration to the ratio FP:LT results from changing the value of δ . As δ is lowered the ratio is also lowered. For $\delta = 2$ the looptop source dominates over the footpoints. The ratio is also slightly affected by changing N with the ratio LT:FP increasing for lower values of N .

5.10 Nonthermal distribution (Gaussian N)

In order to obtain a looptop source using the dipole model it is necessary to enhance the number of nonthermal electrons situated at the looptop in comparison to the loop footpoint. We do this by defining a Gaussian distribution of electrons centred at the apex. In order to achieve both a looptop and footpoint sources

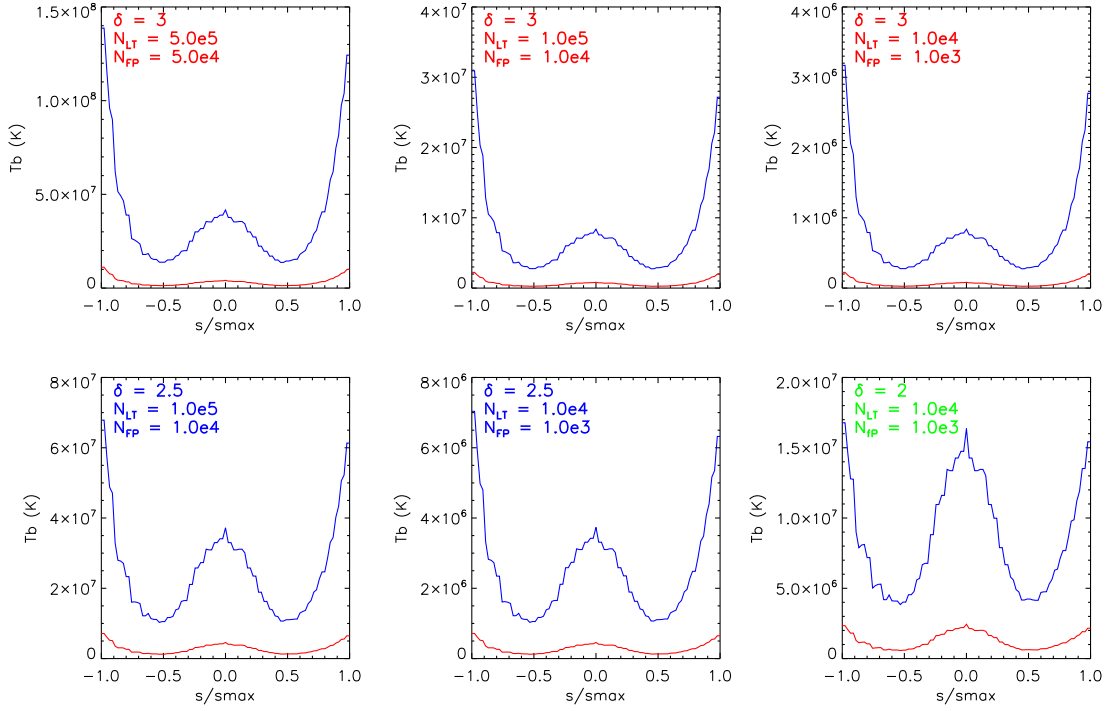


Figure 5.23: Plots of loop T_b profile at 17 GHz and 34 GHz for a series of input parameters (indicated on each plot) from a nonthermal GS distribution. FP:LT ratio can be seen in Table 5.5.

the ratio of N_{LT} to N_{FP} is important. Choosing $\delta = 3$ as a rough estimate of spectral index based on results from previous sections, we find that $N_{LT} : N_{FP}$ should be around one order of magnitude to produce both sources. For a ratio of half an order of magnitude we find that the footpoints dominate, whilst for two orders of magnitude the looptop source dominates. We find that if the value of α is changed to reflect a harder spectrum, the contribution from higher energy electrons becomes more important and the brightness of both sources increases. However, the increase in brightness is greater for the looptop source and results in a decrease in the ratio FP : LT.

Figure 5.23 shows the loop T_b line profiles for 17 GHz (blue) and 34 GHz (red) for a series of different input parameters. Table 5.5 shows the corresponding FP:LT ratio at both frequencies. We find in general for given δ , FP:LT is similar for different magnitudes of N_{LT} and N_{FP} so long as the ratio $N_{LT} : N_{FP}$ is around one order of magnitude. There is a slight increase in the brightness ratio as nonthermal densities are lowered. The ratio at 34 GHz is also found to be lower than that at 17 GHz, this agrees with the observations.

Table 5.5: Dipole nonthermal model FP:LT brightness ratios (17 GHz/34 GHz)

	$\delta = 2$	$\delta = 2.5$	$\delta = 3$
$N_{\text{LT}} = 5.0 \times 10^5 \text{ cm}^{-3}/N_{\text{FP}} = 5.0 \times 10^4 \text{ cm}^{-3}$			3.3/2.7
$N_{\text{LT}} = 1.0 \times 10^5 \text{ cm}^{-3}/N_{\text{FP}} = 1.0 \times 10^4 \text{ cm}^{-3}$		1.8/1.6	3.7/2.7
$N_{\text{LT}} = 1.0 \times 10^4 \text{ cm}^{-3}/N_{\text{FP}} = 1.0 \times 10^3 \text{ cm}^{-3}$	1.0/0.96	1.9/1.6	3.8/2.7

Figure 5.24 shows the corresponding (total) spectra for each of the nonthermal GS outputs. We find the peaks of the spectra appear to be occurring at lower frequencies than what we observe with NoRP. The positioning of the peak can be affected by several parameters i.e. B , N and L . For high B and column density NL , gyrosynchrotron self absorption can become important. An increase in the absorption coefficient κ_ν results in a change in the optical depth and the peak frequency moves to higher values. Although not relevant for the nonthermal model, there are also the effects of the ambient medium to consider. For high values of n effects such as Razin suppression become important. Frequencies close to ν_p can be absorbed by free-free absorption if the temperature is low, or by gyroresonance absorption i.e. the Maxwellian equivalent of self absorption. For the spectra presented in Figure 5.24, increasing N results in the peak moving to higher frequencies but also in an increased flux. As with the arcade model the overall emitting volume could be decreased or the magnetic field could be changed to alter the spectra as indicated in Figure 2.1. For consistency we leave both unchanged for the present discussion. Although not plotted here, the profile of α along the loop remains much the same as for previous examples with no significant steepening towards the footpoints.

5.11 Thermal/Nonthermal

During the decay phase it is expected that there is a significant contribution from thermal plasma. Using a thermal/nonthermal (TNT) electron distribution we are able to investigate the contribution of the thermal emission. As mentioned earlier the TNT distribution is described by a continuous function which matches the thermal and nonthermal components at a critical point parameterised by the input parameter ϵ via the momentum at the critical point, p_{cr}

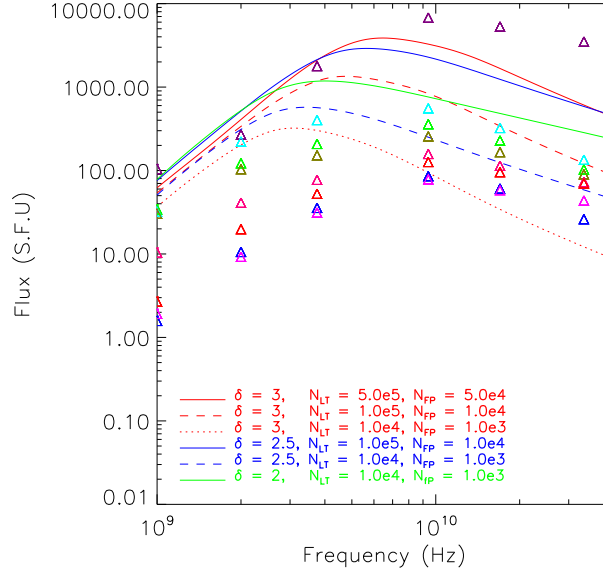


Figure 5.24: Plots of total GS emission from the dipole field model for a series of nonthermal electron distributions, with input parameters indicated on the plot, corresponding to the plots of T_b in Figure 5.23.

$$\begin{aligned} p_{cr}^2 &= \frac{p_{th}^2}{\epsilon} \\ &= \gamma_{cr}^2 - 1 \end{aligned}$$

where γ_{cr} is the Lorentz-factor at the critical point and p_{th} is the thermal momentum. For this model the parameters N and E_{min} are not directly defined for the nonthermal contribution. In Section 5.10, the electron distribution is characterised in terms of the N , the total number of nonthermal electrons above a low energy cutoff, E_{min} . In previous examples we have used $E_{min} = 50$ keV. In order to compare with previous models we are required to define the thermal and nonthermal electron densities and solve for a value of ϵ . N is related to n via

$$N = \frac{(\gamma_{cr} - 1)f(\gamma)n}{\delta_1 - 1} \quad (5.17)$$

where $f(\gamma)$ is the thermal electron distribution over the Lorentz-factor ($\gamma = E_{tot}/mc^2$). For relativistic energies the total number of thermal electrons N_{therm} is given by

$$\begin{aligned}
N_{\text{therm}}d\gamma &= nf(\gamma)d\gamma \\
&= n\frac{\gamma\sqrt{\gamma^2-1}\exp(-\gamma/\Theta)}{\Theta K_2(1/\Theta)}d\gamma
\end{aligned}$$

where $\Theta = k_B T/mc^2$ is the dimensionless thermal energy and K_ν is the modified Bessel function of order ν . For the weakly relativistic limit that we are interested in, the above expression can be reduced to

$$N_{\text{therm}}d\gamma = n\sqrt{\frac{2}{\pi}}\frac{\gamma\sqrt{\gamma^2-1}}{\Theta^{3/2}(1+15\Theta/8)}\exp\left(-\frac{\gamma-1}{\Theta}\right)d\gamma \quad (5.18)$$

For a powerlaw electron distribution the normalisation constant K_{norm} can be written as

$$K_{\text{norm}} = N_{50 \text{ keV}}(\delta_1 - 1)E_{50 \text{ keV}}^{\delta_1-1} \quad (5.19)$$

where $N_{50 \text{ keV}}$ is the total number of electrons above 50 keV. Defining N at 50 keV we can calculate K_{norm} . Using Equation 5.17 and substituting $E_{\text{cr}} = \gamma_{\text{cr}} - 1$, we can rewrite K_{norm} in terms of γ_{cr} .

$$\begin{aligned}
K_{\text{norm}} &= N_{\text{cr}}(\delta_1 - 1)E_{\text{cr}}^{\delta_1-1} \\
&= \frac{(\gamma_{\text{cr}} - 1)f(\gamma_{\text{cr}})n}{(\delta_1 - 1)}(\delta_1 - 1)E_{\text{cr}}^{\delta_1-1} \\
&= (\gamma_{\text{cr}} - 1)f(\gamma_{\text{cr}})n(\gamma_{\text{cr}} - 1)^{\delta_1-1}
\end{aligned}$$

where N_{cr} is the total number of nonthermal electrons above the cutoff energy E_{cr} . Rearranging, we can solve for γ_{cr} . Then using

$$p_{th}^2 = \frac{1}{\frac{1}{\Theta} - 1} \quad (5.20)$$

we can determine ϵ .

$$\epsilon = \frac{p_{th}^2}{\gamma_{\text{cr}}^2 - 1} \quad (5.21)$$

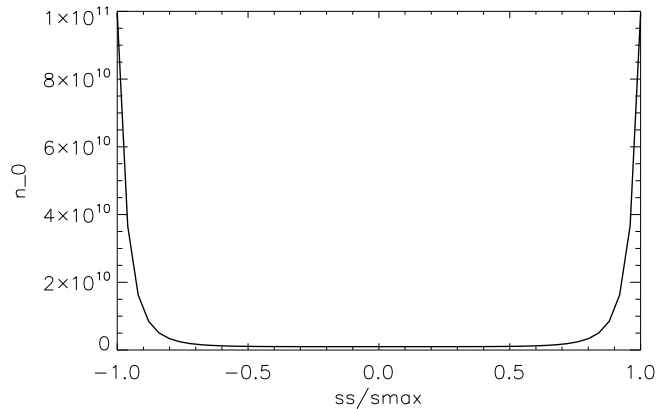


Figure 5.25: Thermal density profile as a function of distance s along the loop which models progression to greater values of n when approaching the footpoints.

Previous examples have shown that thermal gyrosynchrotron emission is dominant at the footpoints where the magnetic field is strongest. The value $1.0 \times 10^9 \text{ cm}^{-3}$ was used as an estimate of coronal density, however radio emission at 17 GHz and 34 GHz can probe down to much lower heights in the solar atmosphere where the ambient density is much higher. In order to model emission from the much denser transition region, we have defined an increase from $n = 1.0 \times 10^9 \text{ cm}^{-3}$ to $n = 1.0 \times 10^{11} \text{ cm}^{-3}$ as we approach the loop footpoints, see Figure 5.25.

Figure 5.26 shows the total GS spectra using a TNT electron distribution (red) for three sets of input parameters. The nonthermal electron density has a Gaussian distribution along the loop with values of N_{LT} and N_{FP} indicated on the plot. A temperature of $1.5 \times 10^7 \text{ K}$ was used for the thermal contribution and the profile of n along the loop is as shown in Figure 5.25. To highlight the contribution from the thermal GS component, the total spectrum resulting from a thermal population with the same input values of T and n has been plotted in green. For comparison the equivalent GS emission from a nonthermal distribution is plotted in black for the same input parameters. However note that the nonthermal distribution has a low energy cut off at 50 keV whilst the TNT model has a low energy cutoff at the critical point, which varies throughout the loop due to the spatial distribution of N and n . As N_{cr} increases, E_{cr} decreases and so we find that the looptop has lower values of E_{cr} than for the footpoint. Table 5.6 shows the values of E_{cr} for the looptop and footpoints (LT/FP) for the spectra plotted in Figure 5.26. Changing the value of E_{min} can alter the shape of the spectrum at low frequencies (Holman 2003). The effect will be strongest for

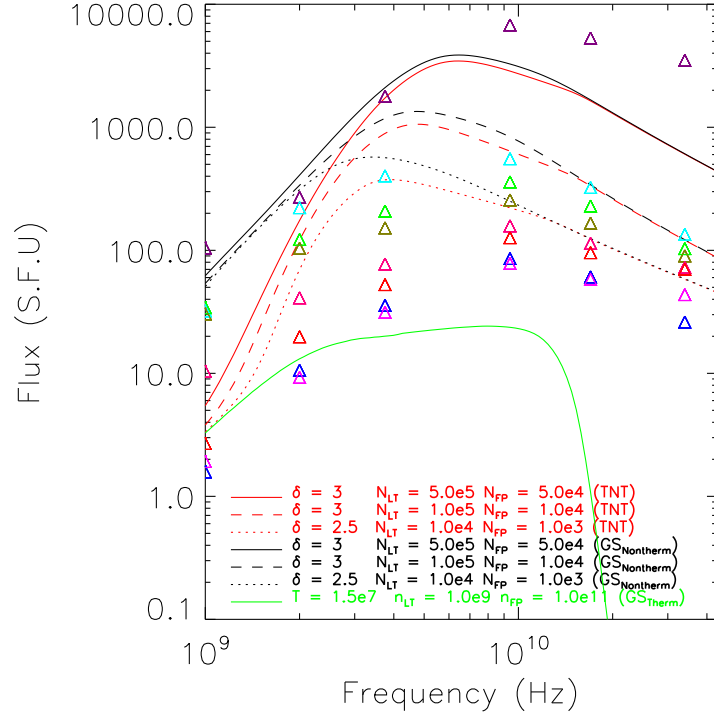


Figure 5.26: Plots show total GS spectra using a thermal/nonthermal electron distribution (red) for three sets of input parameters indicated on the plot.

higher values of N , however we expect that since the values of $E_{\min} < 100$ keV the contribution to the GS radio emission from electrons of this energy is minimal.

Table 5.6: Dipole TNT model E_{\min} (LT/FP)

	$\delta = 2.5$	$\delta = 3$
$N_{LT} = 5.0 \times 10^5 \text{ cm}^{-3} / N_{FP} = 5.0 \times 10^4 \text{ cm}^{-3}$		13/21
$N_{LT} = 1.0 \times 10^5 \text{ cm}^{-3} / N_{FP} = 1.0 \times 10^4 \text{ cm}^{-3}$		16/24
$N_{LT} = 1.0 \times 10^4 \text{ cm}^{-3} / N_{FP} = 1.0 \times 10^3 \text{ cm}^{-3}$	21/28	

It is immediately obvious that the addition of the thermal plasma affects the spectrum most at low frequencies. To highlight we use the results of the model for input parameters $\delta = 3$, $N_{LT} = 5.0 \times 10^5 \text{ cm}^{-3}$ and $N_{FP} = 5.0 \times 10^4 \text{ cm}^{-3}$ i.e. solid lines on Figure 5.26. In Figure 5.27 the looptop and footpoint sources are separated out. The top row shows the spectra from the TNT model and the bottom row shows the nonthermal model. Plots to the left show the looptop spectra plotted in dark green, separated into total (solid), x-mode (dashed) and

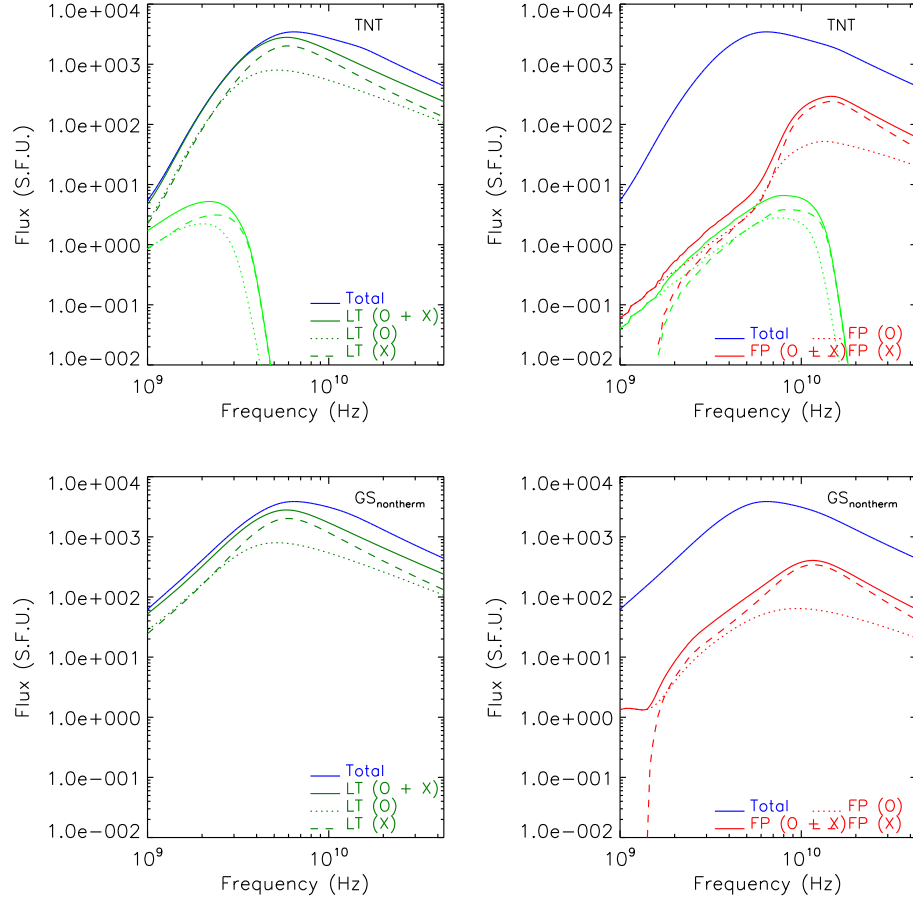


Figure 5.27: Plots show comparison of GS emission from TNT and nonthermal models with the same input parameters $\delta = 3$, $N_{LT} = 5.0 \times 10^5 \text{ cm}^{-3}$ and $N_{FP} = 5.0 \times 10^4 \text{ cm}^{-3}$ i.e. solid lines on Figure 5.26. The looptop and footpoint sources are separated out. The top row shows the spectra from the TNT model and the bottom row shows the nonthermal model. Plots to the left the looptop spectra are plotted in dark green with separated into total (solid), x-mode (dashed) and o-mode (dotted) components. Plots to the right show the equivalent footpoint spectra in red. For comparison the total loop emission is plotted in blue. For the top row, the thermal spectrum is also plotted (light green), and split into its various components.

o-mode (dotted) components. Plots to the right show the equivalent footpoint spectra in red. For comparison the total loop emission is plotted in blue. For the top row, the thermal spectrum is also plotted, and split into its various components. Although the emission from the thermal GS component is small, the addition of thermal plasma results in absorption of the nonthermal emission at low frequencies by processes such as gyroresonance absorption. The sharper

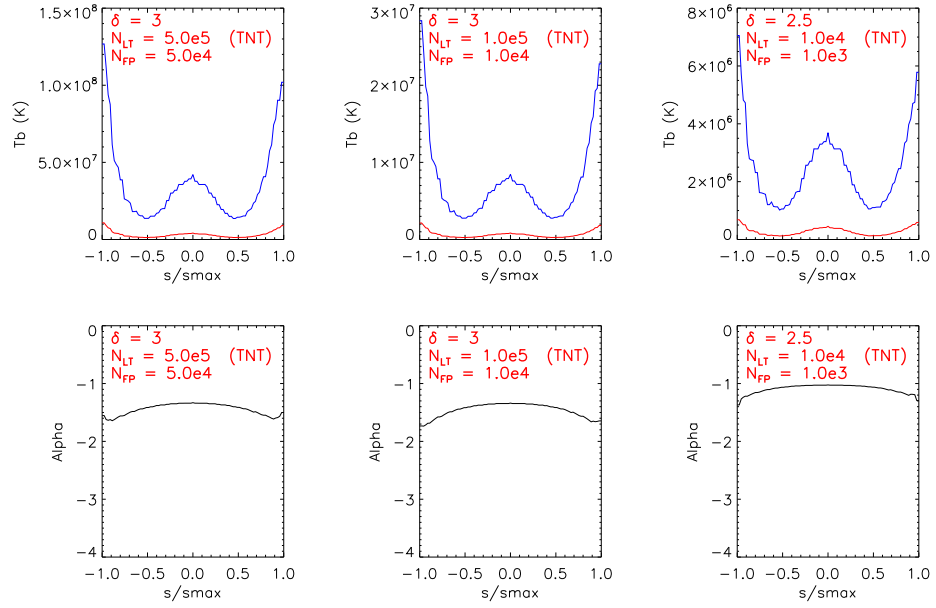


Figure 5.28: Plots of loop T_b profile at 17 GHz and 34 GHz for a series of input parameters (indicated on each plot) from a thermal/nonthermal GS distribution.

fall in the thermal/nonthermal spectrum to the left of the spectral peak is caused by the effects of the thermal plasma on the nonthermal emission. This is most noticeable for the footpoints, where the magnetic field and density is stronger and the thermal GS spectrum extends to higher frequencies. Immediately to the left of the peak falls off sharply as the nonthermal emission is suppressed by the medium and the effects of Razin suppression come into play. This results in a much steeper spectrum to the left of the peak than what we observe from NoRP. At the lowest frequencies the footpoint flux tends to that of the thermal GS spectrum, where the source is optically thick and $T_b = T_{eff}$. To the right of the peak at optically thin frequencies the spectrum is unaltered by the presence of the thermal component and for 17 GHz and 34 GHz the resulting line profiles of T_b and α along the loop are similar, see Figure 5.28 and Table 5.7.

Table 5.7: Dipole TNT vs nonthermal model FP:LT T_b ratio (17 GHz/34 GHz)

	TNT	GS _{nontherm}
$N_{LT}/N_{FP} = 5.0 \times 10^5 \text{ cm}^{-3}/5.0 \times 10^4 \text{ cm}^{-3}, \delta = 3$	3.0/2.6	3.3/2.7
$N_{LT}/N_{FP} = 1.0 \times 10^5 \text{ cm}^{-3}/1.0 \times 10^4 \text{ cm}^{-3}, \delta = 3$	3.4/2.5	3.7/2.7
$N_{LT}/N_{FP} = 1.0 \times 10^4 \text{ cm}^{-3}/1.0 \times 10^3 \text{ cm}^{-3}, \delta = 2.5$	1.9/1.5	1.9/1.6

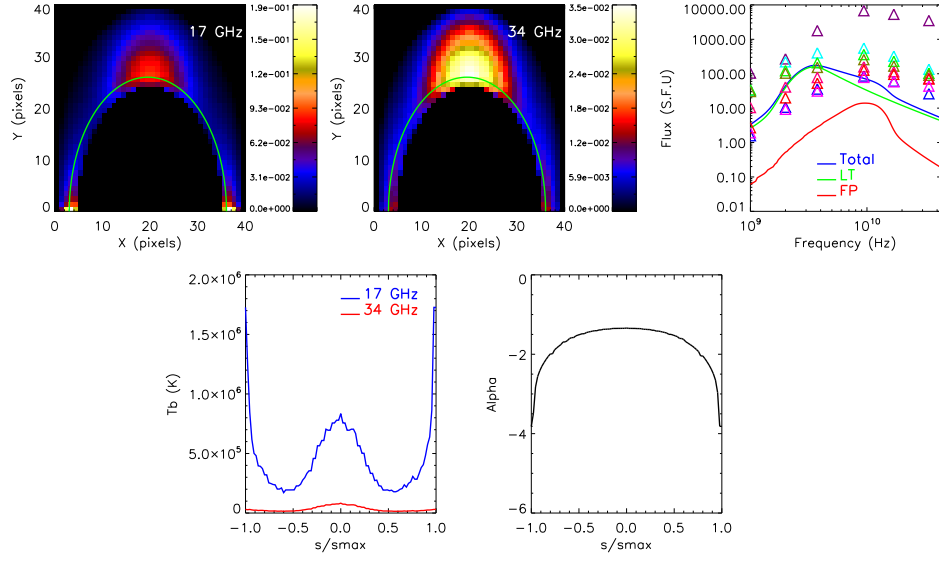


Figure 5.29: GS emission from a thermal/nonthermal electron distribution with $\delta_{\text{LT}} = 3$, $\delta_{\text{FP}} = 4$, $N_{\text{LT}} = 1.0 \times 10^4 \text{ cm}^{-3}$, $N_{\text{FP}} = 1.0 \times 10^3 \text{ cm}^{-3}$ and $T = 1.5 \times 10^7 \text{ K}$. The thermal electron density is the same as is shown in Figure 5.25 ($\gamma = 15^\circ$, $\beta = 0^\circ$). Top left: 17 GHz image (S.F.U.). Top middle: 34 GHz image (S.F.U.). Top right: looptop spectrum (Green), footpoint spectrum (red), total spectrum (blue). Bottom left: T_b profiles as a function of distance s along the loop at 17 GHz (blue) and 34 GHz (red). Bottom right: α calculated from 17 and 34 GHz images as a function of distance s along the loop. Path s along the loop is shown in green on 17 and 34 GHz images (top left and middle)

5.12 Effects of δ

Up to this point, simulations using a variety of electron distributions have been unable to produce the large difference in α that we observe between the looptop and footpoints of the flare loop. As mentioned earlier, Fleishman & Melnikov (2003) show that effects of anisotropy can account for changes in α , the magnitude of which depends on the viewing angle and on the form of the anisotropy. As the gyrosynchrotron code is currently limited to modeling isotropic distributions, we instead investigate the effect of varying δ along the loop.

Figure 5.29 shows the GS emission from a TNT electron distribution with $N_{\text{LT}} = 1.0 \times 10^4 \text{ cm}^{-3}$ and $N_{\text{FP}} = 1.0 \times 10^3 \text{ cm}^{-3}$. The thermal plasma density varies as shown in Figure 5.25 and a plasma temperature of $T = 1.5 \times 10^7 \text{ K}$ is implemented. For the nonthermal contribution the value of δ is varied from

three to four from the looptop to the footpoints respectively. Such a variation could occur due to particle trapping. In such a scenario the looptop spectrum would harden as higher energy electrons spend longer in the trap compared to those at lower energies, which are more easily scattered into the loss-cone or thermalise in the trap. Figure 5.29 top right plot shows the looptop, footpoint and total spectra for these input parameters. In the footpoint spectrum we can see the contribution for the thermal gyrosynchrotron emission dominating up to 17 GHz, after which the thermal component drops off sharply and the nonthermal emission dominates at the higher frequencies. At frequencies above 17 GHz we see that the footpoint spectrum is steeper than for the looptop emission.

Figure 5.30 shows the total loop emission for two sets of input parameters for thermal/nonthermal and nonthermal electron distributions, black and red respectively. Solid lines show $N_{LT} = 1.0 \times 10^4 \text{ cm}^{-3}$ and $N_{FP} = 1.0 \times 10^3 \text{ cm}^{-3}$ and dashed lines show a factor of five greater with $N_{LT} = 5.0 \times 10^4 \text{ cm}^{-3}$ and $N_{FP} = 5.0 \times 10^3 \text{ cm}^{-3}$. The temperature used for the TNT distribution was $1.5 \times 10^7 \text{ K}$ and the thermal density is the same as previous examples. As before, δ varies from three to four from the looptop to the footpoint. In blue the temperature is increased to $T = 2.5 \times 10^7 \text{ K}$ and two different nonthermal density profiles plotted, $N_{LT} = 1.0 \times 10^4 \text{ cm}^{-3}$ to $N_{FP} = 1.0 \times 10^3 \text{ cm}^{-3}$ to solid blue and $N_{LT} = 7.5 \times 10^4 \text{ cm}^{-3}$ to $N_{FP} = 7.5 \times 10^3 \text{ cm}^{-3}$ in dashed blue. The corresponding loop profiles of α and T_b are shown in Figures 5.31 and 5.32.

Table 5.8: Dipole TNT vs nonthermal model FP:LT T_b ratio (17 GHz/34 GHz)

	TNT	GS _{nonth}
$N_{LT}/N_{FP} = 1 \times 10^4 \text{ cm}^{-3}/1 \times 10^3 \text{ cm}^{-3}$, $T = 1.5 \times 10^7 \text{ K}$	2.0/0.37	1.2/0.39
$N_{LT}/N_{FP} = 5 \times 10^4 \text{ cm}^{-3}/5 \times 10^3 \text{ cm}^{-3}$, $T = 1.5 \times 10^7 \text{ K}$	1.3/0.37	1.2/0.39
$N_{LT}/N_{FP} = 1 \times 10^4 \text{ cm}^{-3}/1 \times 10^3 \text{ cm}^{-3}$, $T = 2.5 \times 10^7 \text{ K}$	15.4/0.37	
$N_{LT}/N_{FP} = 7.5 \times 10^4 \text{ cm}^{-3}/7.5 \times 10^3 \text{ cm}^{-3}$, $T = 2.5 \times 10^7 \text{ K}$	2.6/0.37	

Using the same approach as that in Section 5.9 and Figure 5.20(c), we plot α as a function of frequency, see Figure 5.33. On the left we compare the results from two nonthermal electron distributions which have the same spatial distribution of nonthermal electron density and have a low energy cut off at 50 keV. Plotted in black are the results for a model with a constant value of α along the loop and plotted in red are the results for a model with $\alpha_{LT} = 3$ and $\alpha_{FP} = 4$.

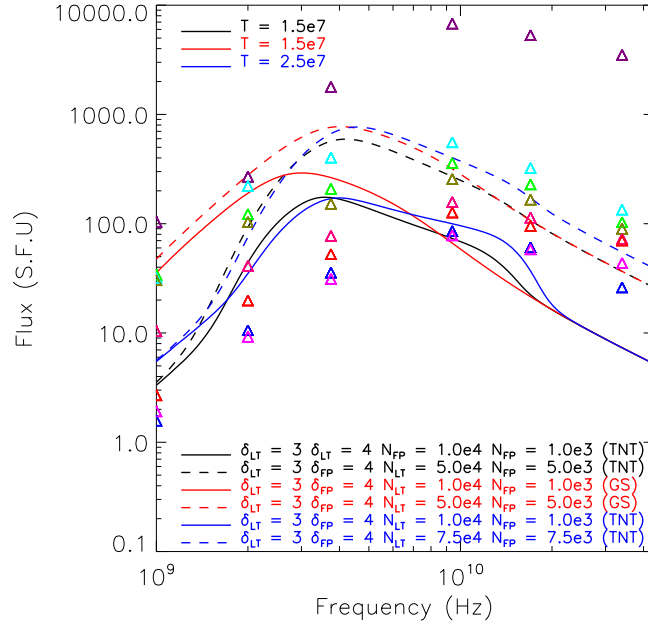


Figure 5.30: Total GS spectra from thermal/nonthermal and nonthermal electron distributions for different sets of input parameters (indicated on each plot). The values of N and δ are varied along the loop. For black TNT spectra $T = 1.5 \times 10^7$ K and red TNT $T = 2.5 \times 10^7$ K. n is varied as shown in Figure 5.25 ($\gamma = 15^\circ$, $\beta = 0^\circ$).

Solid lines represent α calculated from the total loop spectrum and dashed and dotted represent α from the looptop and footpoint spectra respectively. At the looptop the trends of α are identical with a value of ~ 1.3 calculated from the flux at 17 GHz and 34 GHz. For the footpoint α has a value of ~ 1.7 for the constant δ model while the varying δ model has a steeper footpoint spectrum with $\alpha = 2.5$. The overall spectrum for the varying δ model tends towards the trend of the constant δ model with $\alpha = 1.5$.

The main difference between the TNT model and the nonthermal model occurs at the lower frequencies, as seen in Section 5.11, where we see the absorption of the nonthermal emission by the thermal plasma. For slightly lower values of N (black solid), the thermal gyrosynchrotron emission can become important and even dominate the emission at the higher frequencies in the footpoint source. The effect of this is to produce a steeper footpoint spectrum than that from the nonthermal model (red solid). As the nonthermal electron density is increased the thermal component becomes relatively weaker and the thermal peak is not so obvious in the total spectrum (black dashed). In this scenario the TNT model

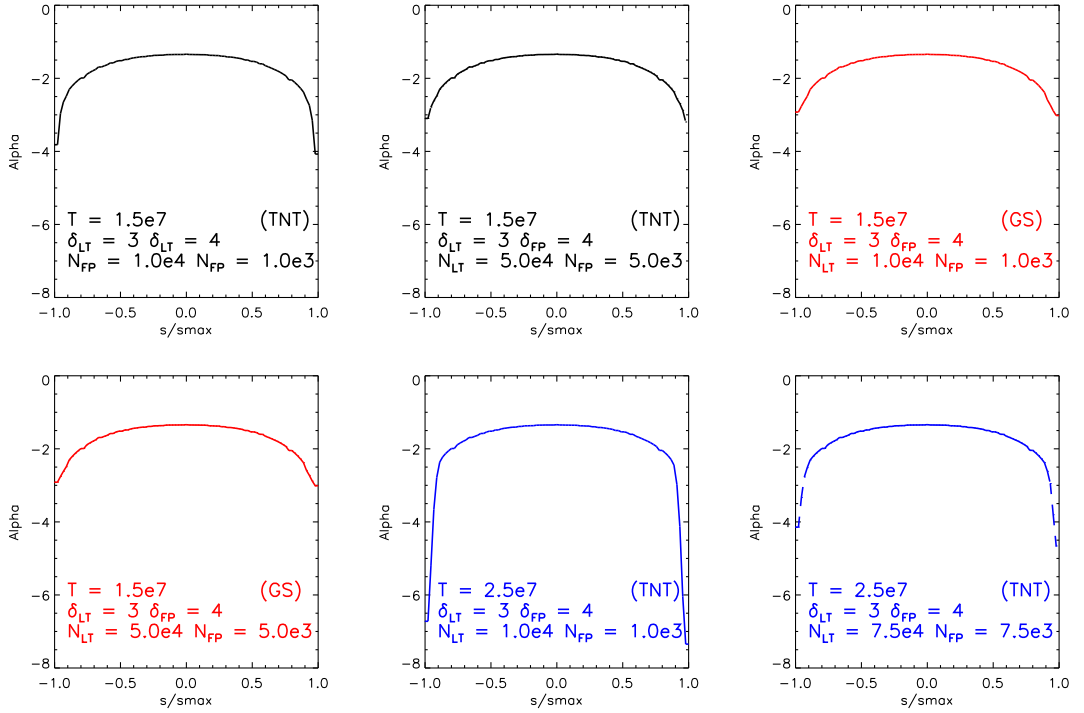


Figure 5.31: Plots of loop α profile for a series of input parameters (indicated on each plot) corresponding to spectra in Figure 5.30 from a thermal/nonthermal and nonthermal electron distributions.

tends to that of the nonthermal model (red dashed).

To increase the thermal contribution at higher frequencies requires a high plasma temperature and/or a high magnetic field value. Figure 5.34 shows loop-top (green) and footpoint (red) and total (blue) thermal spectra for temperatures ranging from 1.0×10^7 K to 2.5×10^7 K for $B_0 = 150$ G. Figure 5.34(b) shows thermal spectra from increased magnetic field models from $B_0 = 150$ G to $B_0 = 200$ G for a temperature of $T = 1.5 \times 10^7$ K.

The spectra from a TNT electron distribution with $T = 2.5 \times 10^7$ K are plotted in blue. For the lower values of N (blue solid) the thermal component is obvious, not only for the footpoint spectra but is also a prominent feature of the total loop emission. The peak of the thermal component has been shifted to higher frequencies and results in a considerable steeping of the footpoint spectrum. Figure 5.33 (right) shows a comparison between a TNT model and a nonthermal model. The presence of the thermal component results in a large change in α at the footpoints, peaking at ~ 7 at 18 GHz, before converging with that for the nonthermal model at higher frequencies. Calculating α from the

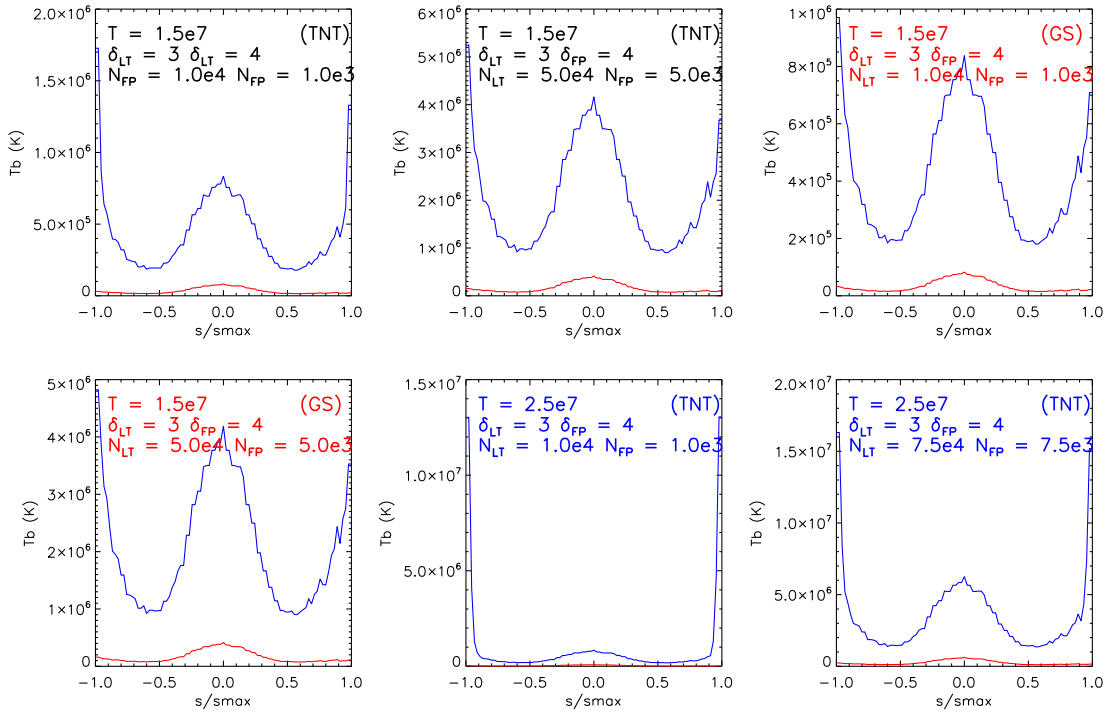


Figure 5.32: Plots of loop T_b profile at 17 GHz and 34 GHz for a series of input parameters (indicated on each plot) corresponding to spectra in Figure 5.30 from thermal/nonthermal and nonthermal electron distributions.

fluxes at 17 GHz and 34 GHz gives a footpoint and total spectrum value of 2.5 and 1.5 for the nonthermal model and 4.6 and 2.1 for the TNT model. However for the higher values of N required to roughly match the NoRP spectra at higher frequencies, the effect of the thermal component is negligible and is unlikely to be detected by the spectral resolution of NoRP.

One drawback of altering δ is that at 34 GHz the looptop emission is stronger than for the footpoint by around a factor of 2.5 for both the TNT and nonthermal models. From the observations, after around 01:32 the SFP:LT ratio at 34 GHz remains around one. With finer tuning of the variation of δ along the loop it is possible that this could be achieved for our model.

5.13 Discussion and conclusions

In this Chapter we set out to model the radio emission from a flaring arcade present in the decay phase of a flare on the 24th August 2002. In Chapter 4 we compared observations from TRACE and NoRH. NoRH images at 17 GHz

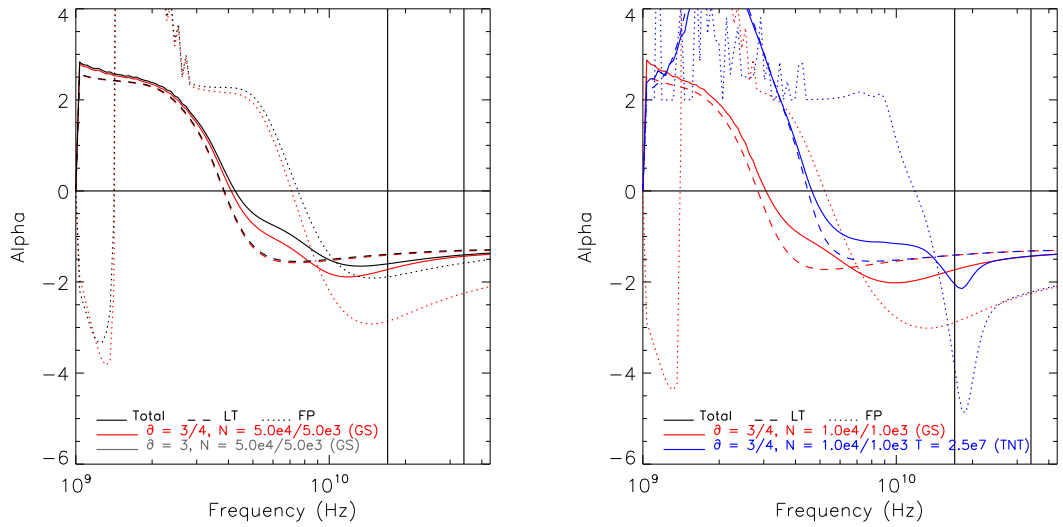


Figure 5.33: Plots of alpha as a function of frequency. Left shows the comparison of two nonthermal electron distributions which have the same spatial distribution of nonthermal electron density and have a low energy cut off at 50 keV. Plotted in black are the results for a model with a constant value of α along the loop and plotted in red are the results for a model with $\alpha_{LT} = 3$ and $\alpha_{FP} = 4$. Solid lines represent α calculated from the total loop spectrum and dashed and dotted represent α from the looptop and footpoint spectra respectively. Right shows a comparison between a TNT model (blue) and a nonthermal model (red).

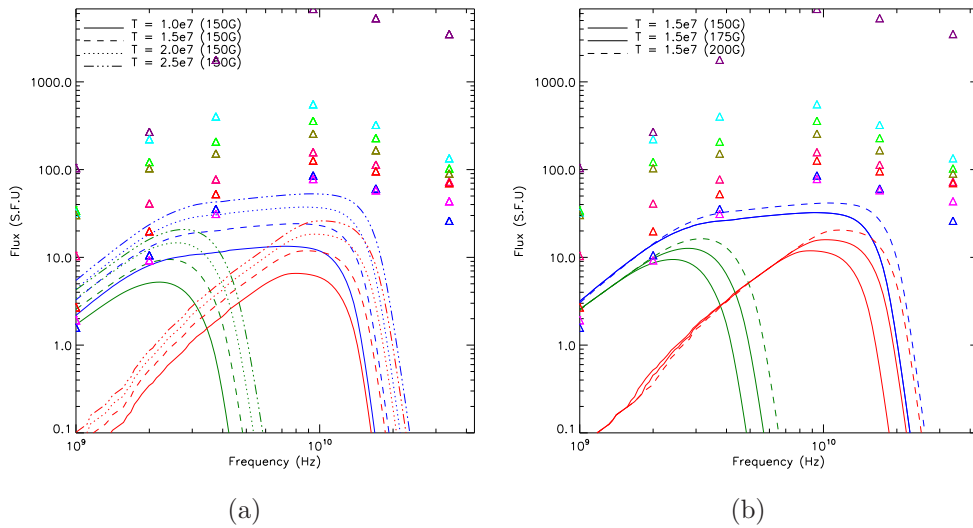


Figure 5.34: Left shows looptop (green) and footpoint (red) and total (blue) thermal GS spectra for temperatures ranging from 1.0×10^7 K to 2.5×10^7 K for $B_0 = 150$ G. Right shows thermal spectra from increased magnetic field models from $B_0 = 150$ G to $B_0 = 200$ G for a temperature of $T = 1.5 \times 10^7$ K.

and 34 GHz are unable to resolve the fine structure of individual bright loops that make up the arcade we observe from TRACE 195Å images and instead the arcade appears, for the most part, as a single radio loop. From NoRH images, determination of the radio spectral index α at all points along the loop suggests that the plasma is optically thin for this frequency range, thus a contribution from brightly emitting loops situated behind the foreground arcade loops could be contributing to the observed spatial distribution of radio brightness around the loop. In order to investigate such line of sight enhancements we chose to model two magnetic field models that act as a framework for our 3D model. 1) A simple dipole model. 2) A potential, force free arcade model.

Starting from the magnetic field structure, the model was split into a 3D set of voxels. Using a gyrosynchrotron code developed by Dr Gregory Fleishman we were able to calculate the gyrosynchrotron emission and absorption, resulting from a user defined electron distribution, for individual voxels. Then, taking into account of radiative transfer effects, the emission is summed along the line of sight and images produced for a range of frequencies between 1 GHz and 43 GHz. In addition to the gyrosynchrotron emission, an option is available to add in a free-free component. In this Chapter we investigated thermal, nonthermal and thermal/nonthermal electron distributions where the nonthermal component is given as a powerlaw over kinetic energy. Input parameters such as temperature, thermal and nonthermal electron densities, electron spectral index δ and dimensions of height, width and length were chosen using estimates from observations. From TRACE observations of the arcade we see that we are not observing in the plane of the arcade loops and for the arcade model we assume a viewing angle of 15° . Although gyrosynchrotron emission varies as a function of viewing angle, the effect for changes in viewing angle of around 15° is small compared with effect of an increased line of sight distance L through the top of the arcade. For the dipole model we stick with a viewing angle perpendicular to the central axis of the loop.

As expected, we are able to rule out the possibility that the radio emission observed is produced by an entirely thermal electron distribution. For GS emission alone the radiation is concentrated at the footpoints where the magnetic field is strongest. The addition of a free-free component produces observable emission along the entire loop length. For the dipole model with a temperature of $T = 1.0 \times 10^7$ K and low values of n (i.e. $n = 1.0 \times 10^9$ cm $^{-3}$) the GS emission dominates at the footpoints with a fainter free-free component along

the loop. Increasing n (or lowering T) can result in free-free emission dominating along the loop. However we do not observe a compact looptop component for the dipole model. Using the arcade model, line of sight effects result in a strong looptop source which dominates over the footpoint emission. It is possible that altering the temperature, density and magnetic field input parameters we could produce both a compact looptop and footpoint sources, although the looptop source would still consist of free-free emission which we know does not fit the observations for a negative spectral slope. However this example shows how line of sight effects can contribute to the morphology of the observed radio image.

Next we looked at the nonthermal electron distribution using the dipole model. As one would expect, for a constant nonthermal electron density N and electron spectral index δ at all points in the loop, the emission is concentrated at the footpoints where the magnetic field is strongest. For values of N between $1.0 \times 10^4 \text{ cm}^{-3}$ and $1.0 \times 10^5 \text{ cm}^{-3}$ and δ between two and four, the value of α is negative at all points along the loop. In general α increases as we move down the loop legs indicating a steeper spectrum, however for some combinations of input parameters i.e. low δ and high N it was found that α decreases slightly at the base of the loop legs, turning towards a flatter spectrum just at the footpoints.

For the arcade model we are able to produce an optically thin looptop source using the line of sight enhancements whilst still obtaining strong footpoint emission. For the same input parameters as the dipole, the arcade flux is around an order of magnitude higher. In order to match the NoRP from 01:20 onwards would require a rather low nonthermal electron density of less than $1.0 \times 10^4 \text{ cm}^{-3}$, a reduction in the magnetic field strength or a reduction of the arcade spatial dimensions. Reducing N and B results in a shift of the spectral peak and so in order to compare like for like with the dipole model we can reduce emitting volume of the arcade and maintain the spectral shape. To match the dipole flux we are required to reduce the height, width and length of the arcade by 50%. It is not unlikely that there is an error in the estimated arcade dimensions as they are viewing angle dependent. A change in viewing angle of $\pm 1^\circ$ can account for a difference in arcade length of $\pm 14''$ ($\pm 1 \times 10^9 \text{ cm}$) i.e. 6% of the total length. It is also worthwhile to point out that the spectral shape is slightly different for the two models. The dipole model has a much broader peak. The reason for this is the position of the peak and relative contributions from the looptop and footpoint spectra. This feature could be used as a diagnostic for the ratio of looptop to footpoint magnetic field strengths or nonthermal electron density.

However the interplay of these parameters is not straight forward and without better knowledge of the magnetic field strength this would require a more robust, statistical approach to cover the available parameter space. Furthermore, this example shows that the spectrum from a dipole field structure produces a reasonable fit to the spectrum but does not result in a looptop source. A statistical approach would therefore be required to include viewing angle and spatial dimensions as free parameters when using the arcade model to produce the looptop source via line of sight effects.

In order to produce a looptop source using the dipole model it is essential that there is a relative increase in nonthermal electron density at the apex. The ratio $N_{LT} : N_{FP}$ is important to achieve both looptop and footpoint sources and in turn for the ratio $T_{bLT} : T_{bFP}$. We find $N_{LT} : N_{FP}$ should be around an order of magnitude. For a gaussian distribution of N along the loop with such a ratio, we find that δ is also important for $T_{bLT} : T_{bFP}$. As δ is decreased the looptop source becomes relatively brighter and the ratio $T_{bLT} : T_{bFP}$ decreases. The value of N is also important, although less influential than δ , with $T_{bLT} : T_{bFP}$ increasing slightly as N is decreased.

From observations, the looptop α maintains a value between one and two whilst the southern footpoint α becomes particularly steep reaching a value of six. Nonthermal models with a constant value of δ are unable to achieve such steep footpoint spectra. By increasing the value of δ away from the apex we are able to increase the value of α at the footpoints. For $\delta_{LT} = 3$ and $\delta_{FP} = 4$, $\alpha_{LT} = 1.4$ and $\alpha_{FP} = 3$. However one drawback of this model is that the brightness ratio FP:LT drops below one at 34 GHz. Fine tuning of the variation in δ along the loop maybe able to resolve this and match the ratio of one determined from observations at 34 GHz.

Although $\alpha = 8$ for thermal gyrosynchrotron component, there is most certainly thermal emission present during the decay phase of the flare. For high values of T and B the thermal component can become important. In this Chapter we made use of the thermal/nonthermal electron distribution option. The main difference between a thermal/nonthermal model and a single nonthermal model occurs at the lower frequencies where the thermal plasma suppresses the nonthermal emission. At high frequencies the thermal plasma has a negligible effect on the nonthermal emission and the thermal/nonthermal spectrum tends to that of a nonthermal model. However for high values of T (e.g. $\sim 2.5 \times 10^7$ K) and relatively low values of N (e.g. $1.0 \times 10^4 \text{ cm}^{-3}$), the thermal component

becomes important in the footpoint sources and can even dominate the footpoint spectrum and also the total loop spectrum at frequencies between $\sim 7 - 20$ GHz. For a thermal/nonthermal model where the T is low and/or N is high (e.g. $\sim 1.0 \times 10^7$ K and $1.0 \times 10^5 \text{ cm}^{-3}$), with $\delta_{\text{LT}} = 3$ and $\delta_{\text{FP}} = 4$, α is the same as for a nonthermal model, $\alpha_{\text{LT}} = 1.4$ and $\alpha_{\text{FP}} = 3$. However if T is high and N is low (e.g. $\sim 2.5 \times 10^7$ K and $1.0 \times 10^4 \text{ cm}^{-3}$) then we find $\alpha_{\text{LT}} = 1.4$ and $\alpha_{\text{FP}} \approx 7$.

In this Chapter we set out to reproduce the radio emission from the decay phase of the 24th August. From a series of models we were able to demonstrate the importance of certain parameters for producing key features of the spatial brightness along the loop. A couple of the models produce promising results. 1) A nonthermal arcade model with a constant value for N , in which line of sight effects can account for a looptop source, although further work is required to achieve a steep footpoint spectrum. 2) A thermal/nonthermal model which displays a dominant thermal gyrosynchrotron component required to produce the steep spectrum at 17 GHz and 34 GHz. However, absorption effects at the lower frequencies result in a spectral shape that does not match NoRP observations.

The results presented have been for a static model which concentrated on roughly matching the shape and flux from NoRP. Until this point it was sufficient to choose sensible input values with results from observations in mind to explore the large parameter space. However in order to properly model the evolution of the decay phase and uncover information regarding continued acceleration, trapping effects and emission from hot thermal plasma, a different approach must be tried. For such a large parameter space in which the interplay of different parameters is complex and for an electron distribution that is evolving over time, a more robust, statistical approach is required to find a best fit to the radio spectrum. Furthermore these parameters must be able to model the spatial distribution of brightness along the loop.

Parameters such as the nonthermal electron density are an important diagnostic for evidence of continued particle acceleration or trapping in an event. From the work presented here, if line of sight effects are neglected, an enhancement of nonthermal electrons is required at the apex in order to achieve a looptop source. Straight away this is evidence for either a transverse anisotropic acceleration mechanism or anisotropy resulting from particle trapping. As Fleishman & Melnikov (2003) pointed out, anisotropy effects could be contributing to the steepening of the spectrum at the footpoints. Plans for future versions of the gy-

rosynchrotron calculation which include an option for modeling anisotropy would allow us to investigate this.

In addition to the physical plasma parameters further work is required to better match the orientation of the magnetic field and the line of sight effects resulting from optically thin radio, arcade mission. Until now we have considered only a symmetrical magnetic field. An asymmetric field will result in a change in the spatial distribution of brightness along the loop and changes in the particle mirroring which, when considering the temporal evolution, will greatly effect the spatial distribution on nonthermal electrons. For an occulted arcade, a difference in orientation to the observer will have an effect on the line of sight enhancements. Indeed we have not been able to model both a looptop source and an arcade source which we argue in Chapter 4 are the result from a combination of nonthermal looptop enhancement and line of sight effects.

It is difficult to measure the coronal magnetic field. Estimates of magnetic field can be found using gyroresonance and free-free emission, however this is only possible for a steady state magnetic field and not possible during a flare when the magnetic field undergoes major reconfiguration on short timescales. In theory, as the magnetic field strength is a key component in shaping the gyrosynchrotron spectrum, it is possible to obtain an estimate for B from spectral observations (Gary 2003). Fleishman et al. (2009) show that in principle it is possible to forward fit the gyrosynchrotron spectrum. Using the same gyrosynchrotron code as used in this Chapter, a model flare loop is created. By forward fitting the resulting spectrum at each point in the loop, they attempt to recover the original input parameters. In general the results are good and the original parameters are returned, although occasionally the fit fails where the forward fitting routine converges on a local minimum rather than a global minimum, see Fleishman et al. (2009) for details. Unfortunately for this event high resolution, radio imaging spectroscopy is not possible. Plans for the next generation of solar observing radio instruments involve a high resolution radio interferometer which will observe the Sun with subsecond cadence and cover a large frequency range with high spectral resolution. Such observations would present new opportunities to measure the coronal magnetic field which will allow us to understand more fully the processes occurring during eruptive solar events and allow us to better investigate the processes of particle acceleration and transport.

From the results presented here it is clear that modeling radio emission from a solar flare can be tricky. With a large number of free parameters and without

better spectral resolution it is difficult to find a unique solution. For this particular project further work could be carried out to fine tune and improve upon the results obtained. More thought should also be given to how the electron distribution evolves over time in order to answer questions regarding effects of trapping or continued particle acceleration.

Chapter 6

Conclusions and Future Work

In this thesis I have used observations from a number of instruments to study the Sun at different wavelengths. In particular I have used observations from the RHESSI spacecraft and ground based Nobeyama Radioheliograph and Polarimeters which together cover the X-ray and Radio emission from the Sun. The combination of X-ray and radio observations providing a particularly powerful tool for investigating the physical processes occurring during energetic solar events such as flares and jets. Hard X-ray and gyrosynchrotron emission reveal the presence of nonthermal electrons and can be used to understand acceleration mechanisms and to investigate transport effects.

In Chapter 3 we presented observations from a flare-related jet which occurred on the 22nd August 2002. At hard X-ray energies the jet is observed in the 30-50 keV energy band and RHESSI imaging spectroscopy shows a spectral index of 4.5 Co-spatial NoRH 17 GHz and 34 GHz gyrosynchrotron emission, with the RHESSI hard X-ray, supports the case for nonthermal electrons present in the jet. A Type III radio burst seen in the HIRAS spectrogram, indicating a beam of accelerated electrons, allows us to determine a local plasma density of $n = 10^{10} \text{ cm}^{-3}$ at the place where the Type III occurred, which we suggest is the location of the jet. The jet radio spectral index α has a value of 0.75 which indicates optically thick gyrosynchrotron emission. However for such jet densities and a coronal magnetic field estimate of $B = 10 \text{ G}$, it is likely that Razin suppression effects, occurring at around 20 GHz, are causing a shift in the peak of the radio spectrum to higher frequencies and as such the emission at 17 GHz and 34 GHz cannot be interpreted as optically thick.

From TRACE observations, a measurement of the jet apparent velocity was found to be $\sim 500 \text{ km s}^{-1}$. This velocity does not give a conclusive answer to

whether the jet material was accelerated due to the $\underline{J} \times \underline{B}$ force, which would have an Alfvénic velocity, or as the result of an evaporative flow, which would have a velocity similar to the sound speed. The event shows similarities to different models. For example the evolution can be compared to that described by the magnetic reconnection jet of e.g. Heyvaerts et al. (1977); Shimojo et al. (1996) where rising magnetic field interacts with the overlying corona field. In this scenario the jet emission would be produced around the reconnection region where the plasma is heated and particles are accelerated. MHD simulations have shown that hot plasma up to tens of MK can be ejected directly from the reconnection region (Moreno-Insertis et al. 2008). Another model that may be of interest is that presented in (Pariat et al. 2009), where twist from closed magnetic field is transferred to open field lines as a result of the reconnection. In this model a large fraction of the free energy previously stored in the field is released in the form a nonlinear, torsional Alfvén wave. As the wave propagates out along the newly reconnected field lines, the pressure gradient accelerates plasma in the direction of wave propagation. The Alfvén wave also compresses the plasma resulting in an increased temperature and density for the ejected material. The relaxation and untwisting of the newly reconnected field lines results in a helical jet structure that propagates out. It is not expected that this model heats the plasma to the soft X-ray temperatures observed by RHESSI, instead this model would heat the plasma to the slightly cooler temperatures seen in EUV, it is plausible that this is the twisted jet emission we observe in TRACE images. It should be noted that this model does also show plasma heating in the reconnection region but the main energy release is in the form of the Alfvén wave.

In Chapter 3 we point out that before the main ejection we observe ‘puffs’ of material moving out from around the jetting region. We associate these with small jet events prior to the main energy release and ask the question, if these pre-jet events were to result in an enhancement of the plasma density around the jetting region, could this provide a thick-target for the accelerated electrons which results in observable hard X-ray emission? Discussion has already taken place with the author of Pariat et al. (2009) and a future collaboration is planned to compare the results of the MHD simulation with observations of the 22nd August 2002 jet event. In addition to this, future postdoc work is likely to include the search for and analysis of solar X-ray and radio jets, indeed a number of possible events have already been identified.

In Chapter 4 we presented observations of a GOES X3.1 class flare that oc-

curred on the west limb of the Sun on the 24th August 2002. The event is particularly interesting to study due to its size and orientation. The event is associated with a filament eruption and a corresponding CME. TRACE 195Å images show an arcade of loops forming from west to east that we associate with a moving reconnection region or ‘unzipping’ of magnetic field lines during the liftoff of the filament. As time progresses the bright TRACE arcade loops are seen to form at greater heights in the corona due to subsequent reconnection. From TRACE images the farside, and possibly also the nearside loop footpoints, appear to be occulted and we find that we are not observing in the plane of the loops. In addition to the well defined TRACE arcade loops we also observe a diffuse source situated above the arcade which we associate with a hotter plasma component of around 10^7 K.

At radio wavelengths NoRH is unable to resolve the individual arcade loops but instead appears for the most part as a single radio loop. The loop ‘footpoints’ and looptop can be clearly separated and emission is seen along the entire loop. In addition to this the loop exhibits optically thin looptop emission. During the impulsive phase, around the time of the filament eruption, a number of radio bursts are observed and emission at 17 GHz peaks at a brightness temperature of 5×10^8 K. A number of authors have concentrated on the radio emission during these short bursts and so we concentrate our analysis on the decay phase to investigate the long term evolution of the flare.

In general the radio emission can be separated into three main sources. A mostly dominant southern footpoint source, a looptop source which is relatively faint in comparison to the southern footpoint and an ‘arcade source’ which we associate with enhanced looptop emission due to line of sight effects which is brightest at the start of the decay phase. A lightcurve of the southern footpoint shows an overall decline in emission but with a bursty profile in comparison to the smooth decay of the looptop emission. The bursty nature could suggest ongoing particle acceleration in the decay phase. A second radio loop appears at lower heights in the corona, below the original loop, first at 34 GHz and then at 17 GHz, at a time coinciding with a large bump in the footpoint spectrum which we suggest could be the result of continuing reconnection and supports the idea of ongoing particle acceleration. As time progresses the outer loop moves outwards before gradually fading as the inner loop dominates.

RHESSI coverage is unavailable for most of the flare peak due to spacecraft night although just before this happens X-ray emission is seen at all points along

the loop for energy bands up to 25-50 keV. When RHESSI data is once again available, in the decay phase, the emission is concentrated at the looptops with emission up to 25-50 keV. The source is situated slightly above the inner radio loop around the region of the hot diffuse source observed by TRACE. RHESSI spectroscopy finds evidence for the presence of nonthermal particles with a photon spectral index of around four. The nonthermal component is present for times when the 25-50 keV emission is observed at the looptops after which thermal soft X-ray emission from lower energy bands is observed until the end of our analysis time frame. The disappearance of the nonthermal component occurs around seven minutes after the peak of a final bump in the footpoint radio lightcurve. If we consider timescales for trapping based on Coulomb deflection effects, electrons with energies of around several MeV could remain trapped for around 10-15 minutes, during which they emit thin-target hard X-ray emission. A final burst of particle acceleration and trapping could therefore explain the bump in the radio footpoint lightcurve. During the decay phase no hard X-ray footpoint emission is observed. This could result from strong magnetic field convergence resulting in an efficient trap such that only a small fraction of electrons reach the footpoints and are unable to produce observable hard X-ray emission. It is also possible that the true hard X-ray footpoints are occulted. However we point out that there must at one point, have been a some component of the electron distribution parallel to the magnetic field to produce the hard X-ray emission observed along the loop just before the flare peak.

In this Chapter we wanted to determine the values for several plasma parameters to be used for modeling the observed radio emission in Chapter 5. From GOES and RHESSI the ambient plasma density was found to be around $10^9 - 10^{10} \text{ cm}^{-3}$. From RHESSI spectroscopy a best fit to the spectrum was found for a double isothermal plus broken powerlaw components. The resulting temperatures were around 10-30 MK, which agrees with the positioning of the looptop X-ray source and the hot diffuse TRACE source. From NoRH images, profiles of α along the loop revealed that all points of the loop showed optically thin emission with a looptop value for α consistently around one or two. As time progresses the footpoint spectrum steepens with α dropping from two to six before returning to two at the very end of our time frame. Using the expressions from (Dulk 1985) and an estimate of the magnetic field strength we were able to approximate values for δ and the nonthermal electron density.

In Chapter 5 we attempt to reproduce the radio emission observed in the de-

cay phase of the 24th August 2002 event. Although NoRH images appear as a single loop, TRACE images are able to resolve the structure of individual loops in an arcade. We therefore base our 3D model on two different magnetic field structures, a simple dipole model and a potential, force free magnetic arcade model. Using a mesh we split our structure into a number of voxels. Then, using a gyrosynchrotron code written and developed by Dr Gregory Fleishman, we are able to calculate the emission and absorption from individual voxels and sum the emission along the line of sight, taking into account radiative transfer effects. The physical plasma parameters estimated from observations are used as input parameters to the calculation and are varied around the loop to create different possible scenarios. We investigate the resulting emission from thermal, nonthermal and thermal/nonthermal electron distributions. For the arcade model we assume a viewing angle of 15° . Although gyrosynchrotron emission is a function of viewing angle, the effect of rotating the model by 15° is small compared with the enhanced emission due to an increased line of sight distance. For the dipole model no rotation in viewing angle is used, with the observer perpendicular to the loop central axis.

Two models in particular give interesting results. Using the arcade model and a nonthermal electron distribution with a uniform value for the nonthermal electron density, N and electron spectral index δ along the loop, we are able to produce images which have both footpoint and looptop emission. The looptop source is produced as a result of an increase in line of sight distance L through the arcade in comparison to that used for the dipole model, where the emission is concentrated only in the footpoints. However for the estimated arcade dimensions of $77''$, $231''$, $60''$ for width, length, and height respectively the total spectrum is around an order of magnitude greater than that for the dipole model. A reduction in all three dimensions of 50% produces a comparable flux. However, we do not observe a significant steepening of the α towards the footpoints.

A second model of interest is the gyrosynchrotron emission produced from a dipole model and a thermal/nonthermal electron distribution. In order to produce a looptop source is necessary to have a relative enhancement of nonthermal electrons at the loop apex. For plasma temperature of $\sim 1.0 \times 10^7$ K and nonthermal electron density of $N_{LT} = 1.0 \times 10^5 \text{ cm}^{-3}$ and $N_{FP} \approx 1.0 \times 10^4 \text{ cm}^{-3}$, the thermal/nonthermal model total loop spectrum tends towards that of a single nonthermal gyrosynchrotron model at high frequencies. In this scenario no significant increase in the footpoint α is observed. However for higher temperatures (e.g.

$\sim 2.5 \times 10^7$ K) or lower nonthermal electron density, (e.g. $N_{LT} = 1.0 \times 10^4 \text{ cm}^{-3}$ and $N_{FP} \approx 1.0 \times 10^3 \text{ cm}^{-3}$) the thermal component can become important and even dominate the spectrum at frequencies around 7-20 GHz. This dominant thermal gyrosynchrotron component can produce a much steeper spectrum at the footpoints with α reaching ~ 7 . However the presence of the thermal component results in absorption of the nonthermal emission at low frequencies and alters the shape of total loop spectrum such that it does not match that observed by NoRP. Also note worthy is a case where δ is increased towards the footpoints. This results in a steeper footpoint spectrum but for the examples shown in Chapter 5 the looptop dominates at 34 GHz.

To achieve the results presented in Chapter 5 initial parameter estimates we determined from observations and varied slightly to explore the available parameter space. The features that were important to reproduce were the presence of both looptop and footpoint sources, a steepening of the footpoint spectra and ratios of looptop to footpoint brightness. The overall loop spectra were compared with NoRP observations and we tried to roughly match the shape and the flux. The results presented puts constraints on the structure of the magnetic field and on the electron distribution of the flare accelerated, radio emitting electrons as well as for the thermal medium. We have only considered a static model but to fully understand and reproduce the evolution of the flare throughout the decay phase it is necessary to consider how the electron distribution would evolve over time. Different acceleration mechanisms should be considered for example if there continuous particle acceleration or is there discrete injections of accelerated electrons. In addition to this transport effects must be taken into consideration, in particular for this event, effects of particle trapping may be important. Further to this, the current version of the code considers only an isotropic electron distribution but Fleishman & Melnikov (2003) have shown that effects of anisotropy can considerably alter the resulting radio spectrum and are based on the line of sight of the observer.

All in all this is a tricky problem to solve and in order to fine tune the results a more robust, statistical approach is required to explore the large parameter space. The future generation of solar radio instruments will allow high resolution, high cadence imaging spectroscopy with good spectral resolution which will allow us to, in principle, forward fit the radio spectrum. Such a procedure is extremely powerful and would allow us to access information on the coronal magnetic field during flares when the field is rapidly changing.

With regards to possible future work, the work presented in this thesis has confirmed that combined X-ray and radio studies of energetic solar events can provide powerful diagnostics of electron acceleration and transport effects occurring during solar flares. Future projects could involve further work at X-ray and radio wavelengths, for both observational projects and the application of this gyrosynchrotron code to other events. One project in particular is to look at a number of coronal hard X-ray events which have corresponding radio observations to try and understand the kind of electron distribution that could produce such a source and whether the same population of electrons is producing both X-ray and radio emission. As the new solar cycle commences we are bound to find a whole host of new and interesting events to study and new questions that need answered.

Bibliography

- Alexander, D. & Fletcher, L. 1999, *Solar Physics*, 190, 167
- Alissandrakis, C. E. & Preka-Papadema, P. 1984, *Astron. Astrophys.*, 139, 507
- Antonucci, E. 1989, *Solar Physics*, 121, 31
- Aschwanden, M. J. 2004, *Physics of the Solar Corona. An Introduction (Physics of the Solar Corona)*
- Aschwanden, M. J., Nightingale, R. W., Tarbell, T. D., & Wolfson, C. J. 2000, *Astrophys. J.*, 535, 1027
- Bai, T. & Ramaty, R. 1979, *Astrophys. J.*, 227, 1072
- Bastian, T. S., Benz, A. O., & Gary, D. E. 1998, *ARA&A*, 36, 131
- Battaglia, M. & Benz, A. O. 2006, *Astron. Astrophys.*, 456, 751
- Battaglia, M., Fletcher, L., & Benz, A. O. 2009, *Astron. Astrophys.*, 498, 891
- Befki, G. 1966, *Radiation processes in plasmas*, ed. G. Befki
- Benz, A., ed. 2002, *Astrophysics and Space Science Library*, Vol. 279, *Plasma Astrophysics*, second edition
- Benz, A. O. 2008, *Living Reviews in Solar Physics*, 5, 1
- Bougeret, J.-L., Kaiser, M. L., Kellogg, P. J., et al. 1995, *Space Science Reviews*, 71, 231
- Boyd, T. J. M. & Sanderson, J. J. 1969, *Plasma dynamics*, ed. T. J. M. Boyd & J. J. Sanderson
- Brown, J. C. 1971, *Solar Physics*, 18, 489

- Brown, J. C. & Mallik, P. C. V. 2008, *Astron. Astrophys.*, 481, 507
- Brown, J. C. & Mallik, P. C. V. 2009, *Astrophys. J. Lett.*, 697, L6
- Canfield, R. C. et al. 1996, *Astrophys. J.*, 464, 1016
- Carlsson, M. 2007, in *Astronomical Society of the Pacific Conference Series*, Vol. 368, *The Physics of Chromospheric Plasmas*, ed. P. Heinzel, I. Dorotovič, & R. J. Rutten, 49–+
- Carmichael, H. 1964, *NASA Special Publication*, 50, 451
- Carrington, R. C. 1859, *Mon. Not. R. Astron. Soc.*, 20, 13
- Chifor, C., Young, P. R., Isobe, H., et al. 2008, *Astron. Astrophys.*, 481, L57
- Christe, S. et al. 2008, *Astrophys. J. Lett.*, 680, L149
- Datlowe, D. W. & Lin, R. P. 1973, *Solar Physics*, 32, 459
- Delaboudinière, J., Artzner, G. E., Brunaud, J., et al. 1995, *Solar Physics*, 162, 291
- Doschek, G. A., Feldman, U., Kreplin, R. W., & Cohen, L. 1980, *Astrophys. J.*, 239, 725
- Dulk, G. A. 1985, *ARA&A*, 23, 169
- Dulk, G. A. & Marsh, K. A. 1982, *Astrophys. J.*, 259, 350
- Emslie, A. G. 1978, *Astrophys. J.*, 224, 241
- Emslie, A. G., Miller, J. A., & Brown, J. C. 2004, *Astrophys. J. Lett.*, 602, L69
- Feldman, U., Doschek, G. A., Kreplin, R. W., & Mariska, J. T. 1980, *Astrophys. J.*, 241, 1175
- Feldman, U., Laming, J. M., Doschek, G. A., Warren, H. P., & Golub, L. 1999, *Astrophys. J. Lett.*, 511, L61
- Fisher, G. H., Canfield, R. C., & McClymont, A. N. 1985, *Astrophys. J.*, 289, 434
- Fleishman, G. D. & Melnikov, V. F. 2003, *Astrophys. J.*, 587, 823
- Fleishman, G. D., Nita, G. M., & Gary, D. E. 2009, 698, L183

- Fletcher, L., Dennis, B. R., S., H. H., & S., K. 2010, *Space Science Reviews*
- Fletcher, L., Hannah, I. G., Hudson, H. S., & Metcalf, T. R. 2007, *Astrophys. J.*, 656, 1187
- Fletcher, L. & Hudson, H. 2001, *Solar Physics*, 204, 69
- Fontenla, J. M., Avrett, E. H., & Loeser, R. 1990, *Astrophys. J.*, 355, 700
- Gabriel, A. H. 1976, *Royal Society of London Philosophical Transactions Series A*, 281, 339
- Gary, D. E. 2003, *J. Korean Astron. Soc.*, 36
- Gary, D. E. & Hurford, G. J. 1989, *Washington DC American Geophysical Union Geophysical Monograph Series*, 54, 237
- Ginzburg, V. L. & Syrovatskii, S. I. 1964, *The Origin of Cosmic Rays*, ed. V. L. Ginzburg & S. I. Syrovatskii
- Ginzburg, V. L. & Syrovatskii, S. I. 1965, *ARA&A*, 3, 297
- Golub, L., Deluca, E., Austin, G., et al. 2007, *Solar Physics*, 243, 63
- Greisen, E. W. 2003, in *Astrophysics and Space Science Library*, Vol. 285, *Astrophysics and Space Science Library*, ed. A. Heck, 109–+
- Grigis, P. C. & Benz, A. O. 2005, *Astrophys. J. Lett.*, 625, L143
- Hamilton, R. J., Lu, E. T., & Petrosian, V. 1990, *Astrophys. J.*, 354, 726
- Handy, B. N., Acton, L. W., Kankelborg, C. C., et al. 1999, *Solar Physics*, 187, 229
- Heyvaerts, J., Priest, E. R., & Rust, D. M. 1977, *Astrophys. J.*, 216, 123
- Hirayama, T. 1974, *Solar Physics*, 34, 323
- Högbom, J. A. 1974, 15, 417
- Holman, G. D. 2003, *Astrophys. J.*, 586, 606
- Hoyng, P., Duijveman, A., Machado, M. E., et al. 1981, *Astrophys. J. Lett.*, 246, L155+

- Hudson, H. S. 1991, *Solar Physics*, 133, 357
- Hudson, H. S., Canfield, R. C., & Kane, S. R. 1978, *Solar Physics*, 60, 137
- Hurford, G. J., Krucker, S., Lin, R. P., et al. 2006, *Astrophys. J. Lett.*, 644, L93
- Hurford, G. J., Schmahl, E. J., Schwartz, R. A., et al. 2002, *Solar Physics*, 210, 61
- Jackson, J. D. 1962, *Classical Electrodynamics*, ed. J. D. Jackson
- Kane, S. R. 1983, *Solar Physics*, 86, 355
- Karlický, M. 2004, *New Astronomy*, 9, 383
- Klein, K. 1987, *Astron. Astrophys.*, 183, 341
- Klein, K. & Trotter, G. 1984, *Astron. Astrophys.*, 141, 67
- Klimchuk, J. A. 2006, *Solar Physics*, 234, 41
- Kontar, E. P., Piana, M., Massone, A. M., Emslie, A. G., & Brown, J. C. 2004, *Solar Physics*, 225, 293
- Kopp, R. A. & Pneuman, G. W. 1976, *Solar Physics*, 50, 85
- Kramers, H. A. 1923, *Phil. Mag.*, 46, 836
- Krucker, S., Battaglia, M., Cargill, P. J., et al. 2008a, 16, 155
- Krucker, S., Hurford, G. J., & Lin, R. P. 2003, *Astrophys. J. Lett.*, 595, L103
- Krucker, S., Hurford, G. J., MacKinnon, A. L., Shih, A. Y., & Lin, R. P. 2008b, *Astrophys. J. Lett.*
- Krucker, S., Hurford, G. J., MacKinnon, A. L., Shih, A. Y., & Lin, R. P. 2008c, *Astrophys. J. Lett.*, 678, L63
- Krucker, S. & Lin, R. P. 2002, *Solar Physics*, 210, 229
- Krucker, S. & Lin, R. P. 2008, *Astrophys. J.*, 673, 1181
- Krucker, S., Saint-Hilaire, P., Christe, S., et al. 2008d, *Astrophys. J.*

- Kundu, M. R., Nindos, A., White, S. M., & Grechnev, V. V. 2001, *Astrophysical Journal*, 557, 880
- Lin, R. P., Dennis, B. R., et al. 2002, *Solar Physics*, 210, 3
- Mariska, J. T. & McTiernan, J. M. 1999, *Astrophys. J.*, 514, 484
- Marsh, K. A. & Hurford, G. J. 1980, *Astrophys. J. Lett.*, 240, L111
- Masuda, S., Kosugi, T., Hara, H., Tsuneta, S., & Ogawara, Y. 1994, *Nature*, 371, 495
- Melnikov, V. F., Gorbikov, S. P., Reznikova, V. E., & Shibasaki, K. 2005, in *ESA Special Publication*, Vol. 600, *The Dynamic Sun: Challenges for Theory and Observations*
- Melnikov, V. F., Reznikova, V. E., Yokoyama, T., & Shibasaki, K. 2002a, in *ESA Special Publication*, Vol. 506, *Solar Variability: From Core to Outer Frontiers*, ed. J. Kuijpers, 339–342
- Melnikov, V. F., Shibasaki, K., & Reznikova, V. E. 2002b, *Astrophys. J. Lett.*, 580, L185
- Melrose, D. B. 1968, *Astrophys. Space. Sci.*, 2, 171
- Melrose, D. B. 1986, *Instabilities in Space and Laboratory Plasmas*, ed. Melrose, D. B.
- Metcalf, T. R., Canfield, R. C., Avrett, E. H., & Metcalf, F. T. 1990, *Astrophys. J.*, 350, 463
- Milligan, R. O., Gallagher, P. T., Mathioudakis, M., & Keenan, F. P. 2006, *Astrophys. J. Lett.*, 642, L169
- Moreno-Insertis, F., Galsgaard, K., & Ugarte-Urra, I. 2008, *Astrophys. J. Lett.*, 673, L211
- Nakajima, H., Nishio, M., Enome, S., et al. 1994, *IEEE Proceedings*, 82, 705
- Neupert, W. M. 1968, *Astrophysical Journal, Letters*, 153, L59+
- Nindos, A., Aurass, H., Klein, K., & Trottet, G. 2008, *Solar Physics*, 253, 3

- Nindos, A., Kundu, M. R., White, S. M., et al. 1999, *Astrophys. J.*, 527, 415
- Nishizuka, N., Shimizu, M., Nakamura, T., et al. 2008, *Astrophys. J. Lett.*, 683, L83
- Nita, G. M., Fleishman, G. D., & Gary, D. E. 2009, in *AAS/Solar Physics Division Meeting*, Vol. 40, *AAS/Solar Physics Division Meeting*, 15.24–+
- Pariat, E., Antiochos, S. K., & DeVore, C. R. 2009, *Astrophys. J.*, 691, 61
- Parker, E. N. 1958, *Astrophys. J.*, 128, 664
- Parker, E. N. 1983, *Astrophys. J.*, 264, 642
- Parker, E. N. 1988, *Astrophys. J.*, 330, 474
- Petrosian, V. 1981, *Astrophys. J.*, 251, 727
- Phillips, K. J. H. 2004, *Astrophys. J.*, 605, 921
- Ramaty, R. 1968, *J. Geophys. Res.*, 73, 3573
- Ramaty, R. 1969, *Astrophysical Journal*, 158, 753
- Régnier, S. & Canfield, R. C. 2006, *Astron. Astrophys.*, 451, 319
- Reznikova, V. E., Melnikov, V. F., Shibasaki, K., et al. 2009, *Astrophys. J.*, 697, 735
- Savcheva, A., Cirtain, J., Deluca, E. E., et al. 2007, *PASJ*, 59, 771
- Schwartz, R. A. et al. 2002, *Solar Physics*, 210, 165
- Shibata, K. 1999, *Astrophys. Space. Sci.*, 264, 129
- Shibata, K. & Uchida, Y. 1986, *Solar Physics*, 103, 299
- Shibata, K. et al. 1992, *PASJ*, 44, L173
- Shibata, K. et al. 1994, *Astrophys. J. Lett.*, 431, L51
- Shimojo, M., Narukage, N., Kano, R., et al. 2007, *PASJ*, 59, 745
- Shimojo, M. & Shibata, K. 2000, *Astrophys. J.*, 542, 1100

- Shimojo, M. et al. 1996, PASJ, 48, 123
- Smith, D. M., Lin, R. P., Turin, P., et al. 2002, Solar Physics, 210, 33
- Sterling, A. C., Shibata, K., & Mariska, J. T. 1993, Astrophys. J., 407, 778
- Stix, M. 2004, The sun : an introduction, ed. Stix, M.
- Strong, K. T. et al. 1992, PASJ, 44, L161
- Sturrock, P. A. 1966, Nature, 211, 695
- Sturrock, P. A. 1994, Plasma Physics, An Introduction to the Theory of Astrophysical, Geophysical and Laboratory Plasmas, ed. Sturrock, P. A.
- Sui, L., Holman, G. D., & Dennis, B. R. 2006, Astrophys. J., 646, 605
- Tandberg-Hanssen, E. & Emslie, A. G. 1988, The physics of solar flares, ed. E. Tandberg-Hanssen & A. G. Emslie
- Torii, C., Tsukiji, Y., Kobayashi, S., et al. 1979, Nagoya University, Research Institute of Atmospherics, Proceedings, vol. 26, Mar. 1979, p. 129-132., 26, 129
- Török, T. & Kliem, B. 2005, Astrophys. J. Lett., 630, L97
- Trulsen, J. & Fejer, J. A. 1970, Journal of Plasma Physics, 4, 825
- Tsuneta, S., Acton, L., Bruner, M., et al. 1991, Solar Physics, 136, 37
- Tsuneta, S., Ichimoto, K., Katsukawa, Y., et al. 2008, Solar Physics, 249, 167
- Tsuneta, S., Masuda, S., Kosugi, T., & Sato, J. 1997, Astrophys. J., 478, 787
- Tzatzakis, V., Nindos, A., Alissandrakis, C. E., & Shibasaki, K. 2006, in American Institute of Physics Conference Series, Vol. 848, Recent Advances in Astronomy and Astrophysics, ed. N. Solomos, 248–252
- Uchida, Y. 1969, PASJ, 21, 128
- Švestka, Z. 1970, Solar Physics, 13, 471
- Veronig, A., Vršnak, B., Dennis, B. R., et al. 2002, Astron. Astrophys., 392, 699

- Wedemeyer-Böhm, S., Steiner, O., Bruls, J., & Rammacher, W. 2007, in *Astronomical Society of the Pacific Conference Series*, Vol. 368, *The Physics of Chromospheric Plasmas*, ed. P. Heinzel, I. Dorotovič, & R. J. Rutten, 93–+
- White, S. M., Kundu, M. R., Garaimov, V. I., Yokoyama, T., & Sato, J. 2002, *Astrophys. J.*, 576, 505
- Wild, J. P. & Hill, E. R. 1971, *Australian Journal of Physics*, 24, 43
- Yokoyama, T., Nakajima, H., Shibasaki, K., Melnikov, V. F., & Stepanov, A. V. 2002, *Astrophys. J. Lett.*, 576, L87
- Yokoyama, T. & Shibata, K. 1995, *Nature*, 375, 42
- Zarro, D. M. & Lemen, J. R. 1988, *Astrophys. J.*, 329, 456

Appendix A

Wave mode propagation in a magnetised plasma

A.1 Wave mode propagation in a Magnetised plasma

In a cold magnetised plasma, where thermal particle motion can be neglected in comparison to the bulk motion of the plasma, a number of wave modes can propagate. For an anisotropic, cold plasma the general dispersion relation describes wave propagation for all possible wave modes. To derive the dispersion relation we start with an equation for the current density \mathbf{J} .

$$\mathbf{J} = \sigma \mathbf{E} \tag{A.1}$$

Equation A.1 describes how the current density and electric field \mathbf{E} in an anisotropic plasma are related via σ , the conductivity tensor. From Maxwell's equations for electromagnetism we have Equations A.2 and A.3.

$$\nabla \times \mathbf{E} = -\frac{\partial \mathbf{B}}{\partial t} \tag{A.2}$$

$$\nabla \times \mathbf{B} = \mu_0 \mathbf{J} + \frac{1}{c^2} \frac{\partial \mathbf{E}}{\partial t} \tag{A.3}$$

Taking the curl of both sides of A.2 and using A.3 we can write

$$\mathbf{k} \times (\mathbf{k} \times \mathbf{E}) + \frac{\omega^2}{c^2} \epsilon \cdot \mathbf{E} = \mathbf{0} \tag{A.4}$$

where \mathbf{k} is the wave vector, ω is the wave frequency and ϵ the dielectric tensor.

$$\epsilon = \delta + \frac{\mathbf{i}}{\epsilon_0 \omega} \sigma \quad (\text{A.5})$$

ϵ can be represented by the matrix

$$\epsilon = \begin{bmatrix} S & -iD & 0 \\ iD & S & 0 \\ 0 & 0 & P \end{bmatrix}$$

where

$$S = \frac{1}{2}(R + L) \quad (\text{A.6})$$

$$D = \frac{1}{2}(R - L) \quad (\text{A.7})$$

$$R = 1 - \sum_s \frac{\omega_{ps}^2}{\omega^2} \left(\frac{\omega}{\omega + a_s \omega_{B_s}} \right) \quad (\text{A.8})$$

$$L = 1 - \sum_s \frac{\omega_{ps}^2}{\omega^2} \left(\frac{\omega}{\omega - a_s \omega_{B_s}} \right) \quad (\text{A.9})$$

$$P = 1 - \sum_s \frac{\omega_{ps}^2}{\omega^2} \quad (\text{A.10})$$

Equations A.8, A.9 and A.10 sum over species s . ω_{B_s} is the cyclotron or gyrofrequency and $a_s = +1$ for an ion and $a_s = -1$ for an electron. We can express Equation A.4 in terms of the refractive index $\mathbf{n} = \mathbf{k}c/\omega$.

$$\mathbf{n} \times (\mathbf{n} \times \mathbf{E}) + \mathbf{k} \cdot \mathbf{E} = 0 \quad (\text{A.11})$$

For $\mathbf{B}_0 = \hat{\mathbf{z}}B_0$ and wave propagation in the xz plane then $n = \hat{\mathbf{x}}n \sin \theta + \hat{\mathbf{z}}n \cos \theta$, where θ is the angle between \mathbf{n} and \mathbf{B} . Substituting \mathbf{n} in Equation A.11 gives

$$\begin{bmatrix} S - n^2 \cos^2 \theta & -iD & n^2 \cos \theta \sin \theta \\ iD & S - n^2 & 0 \\ n^2 \cos \theta \sin \theta & 0 & P - n^2 \sin^2 \theta \end{bmatrix} \begin{bmatrix} E_x \\ E_y \\ E_z \end{bmatrix} = 0.$$

From this we can obtain an expression for the general dispersion relation which governs the propagation of wave modes in an anisotropic cold plasma.

$$An^4 - Bn^2 + C = 0 \quad (\text{A.12})$$

where

$$\begin{aligned} A &= S \sin^2 \theta + P \cos^2 \theta \\ B &= RL \sin^2 \theta + PS(1 + \cos^2 \theta) \\ C &= PRL \end{aligned}$$

The refractive index is then given by

$$n^2 = \frac{B \pm [(RL - PS)^2 \sin^4 \theta + 4P^2 D^2 \cos^2 \theta]^{1/2}}{2A} \quad (\text{A.13})$$

and wave mode polarisation is given by

$$\frac{iE_x}{E_y} = \frac{n^2 - S}{D} \quad (\text{A.14})$$

For parallel wave propagation, $\theta = 0$ ($\mathbf{k} \parallel \mathbf{B}_0$), then solutions to the general dispersion relation are $P = 0$, $n^2 = R$ or $n^2 = L$. The later two solutions have polarisations of +1 and -1 corresponding to right and left circularly polarised wave modes respectively. $P = 0$ describes the case for plasma oscillation with polarisation of 0.

For perpendicular wave propagation, $\theta = \pi/2$ ($\mathbf{k} \perp \mathbf{B}_0$) gives solutions $n^2 = P$ and $n^2 = RL/S$ with corresponding polarisation $-D/S$ and $(P-S)/D$. For these cases the wave modes are elliptically polarised. In the case of $n^2 = P$ the electric field component is directed along \mathbf{B}_0 and as a result particle motion is also in the direction of \mathbf{B}_0 and does not feel the influence of the magnetic field. This wave mode is known as the ordinary or o-mode. For $n^2 = RL/S$ the electric field is perpendicular to \mathbf{B}_0 and as a result is influenced by the magnetic field. The wave mode is known as the extraordinary or x-mode.

Propagation of electromagnetic wave modes are subject to cutoffs ($n^2 = 0$) and resonances ($n^2 \rightarrow \infty$). For parallel propagation the R and L waves modes experience a cutoff at $\nu \approx \pm \frac{1}{2}\nu_{B_e} + (\nu_p^2 + \frac{1}{4}\nu_{B_e})$ and are subject to resonances at ν_{B_e} and ν_{B_i} respectively, where ν_{B_e} and ν_{B_i} are the electron and ion cyclotron frequencies. In the case of perpendicular propagation, the o and x-modes are subject to cutoffs at ν_p and $\nu \approx \frac{1}{2}\nu_{B_e} + (\nu_p^2 + \frac{1}{4}\nu_{B_e})$ respectively. The x-mode has a resonance at the upper and lower hybrid frequencies $\nu_U = \nu_p^2 + \nu_{B_e}$, $\nu_L = \nu_p^2 \frac{\nu_{B_e}\nu_{B_i}}{\nu_p^2\nu_{B_e}^2}$.